Electronic and magnetic properties of transition metal compounds: An x-ray spectroscopic study

by Karsten Küpper

Thesis
presented to the
Department of Physics
Universität Osnabrück

Osnabrück
June 2005

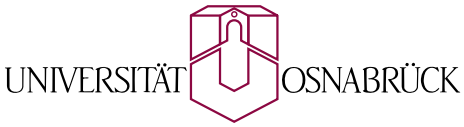

Thesis advisor:
apl. Prof. Dr. Manfred Neumann

Contents

Introduction **1**

1 Basic properties of transition metal compounds **5**
1.1 Correlated materials 5
1.2 Colossal magneto resistance (CMR) 6
1.3 Transition metal ions in crystal fields 7
1.3.1 Basic crystal properties 10
1.3.2 The Zaanen Sawatzky Allen (ZSA) scheme 11
1.3.3 Exchange interaction and orbital degeneracy 13
1.3.4 Orbital Ordering and the Kugel-Khomskii model 16

2 X-ray spectroscopic techniques **19**
2.1 Theoretical models 19
2.1.1 Band models 20
2.1.2 Short range models 23
2.2 General overview: X-ray spectroscopies 25
2.3 X-ray Photoelectron Spectroscopy (XPS) 29
2.3.1 Theoretical approaches to the photoemission process 30
2.3.1.1 Three–step model 31
2.3.1.2 One–step models 32
2.3.2 Spectral characteristics 32
2.3.2.1 Valence band spectra 32
2.3.2.2 Core–level spectra 32
2.3.2.3 Chemical shift 34
2.3.2.4 Spin–orbit coupling 35
2.3.2.5 Satellites 35
2.3.2.6 $3s$ multiplet splitting 36
2.4 X-ray Absorption Spectroscopy (XAS) 38
2.4.1 X-ray Magnetic Circular Dichroism (XMCD) 39
2.4.2 X-ray Linear Dichroism (XLD) 42
2.5 X-ray Emission Spectroscopy (XES) 43
2.5.1 Resonant X-ray Emission Spectroscopy (RXES) 44
2.5.2 Normal X-ray Emission Spectroscopy (NXES) 46
2.6 Instrumentation 47
2.6.1 The photoelectron specrometer PHI 5600ci 47
2.6.2 Synchrotron radiation based experiments 48

3 Iron compounds **53**
3.1 Why wüstite (FeO) and pyrite (FeS_2)? . . . 53
3.2 Electronic properties of FeO and FeS_2 . . . 55
3.2.1 Experimental details . . . 55
3.2.2 XPS . . . 55
3.2.2.1 Valence Band . . . 55
3.2.2.2 Fe 3*s* and Fe 3*p* core levels . . . 56
3.2.2.3 Fe 2*p* core levels . . . 58
3.2.2.4 S 2*p* and O 1*s* core levels . . . 59
3.2.3 XAS . . . 60
3.2.4 RIXS . . . 63
3.2.4.1 FeO . . . 63
3.2.4.2 FeS_2 . . . 66
3.2.5 Discussion . . . 67
3.2.5.1 XPS . . . 67
3.2.5.2 XAS . . . 68
3.2.5.3 RIXS . . . 70
3.3 Resonant Raman x-ray scattering at the S 2*p* edge of FeS_2 . . . 73
3.3.1 Introduction . . . 73
3.3.2 Experimental details . . . 73
3.3.3 Results and discussion . . . 74
3.4 Conclusions . . . 79

4 Manganites **81**
4.1 Electronic structure of A- and B-site doped manganites . . . 81
4.1.1 Introduction . . . 81
4.1.2 Experimental details . . . 83
4.1.3 Results . . . 84
4.1.3.1 XPS and XES . . . 84
4.1.3.2 XAS and RIXS . . . 87
4.1.4 Discussion . . . 89
4.1.5 Conclusions . . . 93
4.2 Orbital ordering in $La_{7/8}Sr_{1/8}MnO_3$ . . . 94
4.2.1 Introduction . . . 94
4.2.2 Experimental details . . . 95
4.2.3 Results and discussion . . . 96
4.2.4 Conclusions . . . 100

5 The double perovskite Sr_2FeMoO_6 **101**
5.1 Experimental and theoretical details . . . 103
5.2 Results and discussion . . . 105
5.2.1 Magnetic properties . . . 105
5.2.2 Valence states of Fe and Mo: XAS and XPS . . . 106
5.2.3 The valence band: XPS and XES . . . 108
5.2.4 XMCD in XAS at the Fe *L* edge . . . 114
5.2.5 Conclusions . . . 119

6 Defect oxides: The electronic structure of Li_xCoO_2 **121**
6.1 Introduction 121
6.2 Experimental Details 122
6.3 Results and discussion 122
6.4 Conclusions 127

7 Conclusions and outlook / Kurzfassung **129**

Acknowledgement / Danksagung **135**

Bibliography **139**

Curriculum Vitae **155**

List of Figures

1.1 Schematic plot showing the interplay between charge, spin and orbital degrees of freedom in $3d$ transition metal oxides. 6

1.2 The five d orbitals. In a cubic crystal field, the five-fold degeneracy is lifted to two e_g- and three t_{2g}-orbitals. 8

1.3 The energy levels of the $3d$ electrons of an Mn^{3+} ion. In a cubic crystal field, the five-fold degeneracy is lifted to two e_g– and three t_{2g}–orbitals. The Jahn-Teller distortion leads to a further splitting of both the t_{2g} and e_g states. Knowledge about the occupancy of the e_g states is a crucial point for understanding the fascinating properties of transition metal compounds. 9

1.4 The cubic perovskite unit cell. The La, Mn, and O ions are represented by white, grey and black spheres, respectively. 11

1.5 One electron (i), Mott Hubbard (ii) and charge transfer (iii) diagrams of a transition metal oxide (adapted from [25]). 12

1.6 Schematic plot of the single orbital superexchange interaction. Note that the intermediate state (ii)) has an energy larger by U compared to the ground state. There are two possible final states. 14

1.7 Schematic plot of the double-exchange interaction. Left panel: ferromagnetic spin structure, right panel: canted spin structure. 15

1.8 i) and ii): Q_3 distortion with the corresponding oxygen displacements to the filled $3z^2 - r^2$ and $x^2 - y^2$ orbitals, respectively; iii). The Q_2 distortion stabilizes in a certain superposition of $3z^2 - r^2$ and $x^2 - y^2$ orbitals. 16

1.9 Schematic representation of rod-type (left panel) and cross-type (right panel) orbital ordering. 17

1.10 Schematic plot of the **ab** plane of $LaMnO_3$, the alternating long and short Mn-O distances are labelled l and s, respectively. 18

2.1 Partitioning of the unit cell in muffin tin regions (I) and the interstitial region (II), in case of two inequivalent atoms. 22

2.2 Schematic illustration of a) x-ray absorption spectroscopy (XAS) and b) x-ray / ultraviolet photoelectron spectroscopy (XPS, UPS). 25

2.3 Schematic illustration of the core hole ionization process (left panel), followed by the Auger decay (right panel). 27

2.4 Schematic illustration of normal x-ray emission spectroscopy (NXES) (left panel) and resonant x-ray emission spectroscopy (RXES) (right panel). . . . 28
2.5 The basic principle of a photoemission experiment (adapted from [25, 67]). . . . 29
2.6 Energy level diagram for a PES experiment with a conductive sample [75]. . . . 30
2.7 Illustration of an XPS core level line [75]. . . . 33
2.8 Example for a chemical shift of the Fe $2p$ XPS core level lines of FeO. The spin-orbit coupling and satellites will be explained in Sections 2.3.2.4 and 2.3.2.5. . . . 34
2.9 Schematic illustration of a charge transfer excitation in a transition metal oxide [88, 75]. . . . 36
2.10 Example of an XMCD spectrum recorded at the Fe L edge of a ferromagnetic oxide. Upper panel: XAS spectra for right circular polarized (black line) and left circular polarized (red line) x-rays. Lower panel: The difference of both spectra gives the magnetic circular dichroism (MCD). . . . 39
2.11 Schematic representation of the XMCD process in the one electron picture. The d-band is split into spin-up and spin-down bands. Firstly the absorption of circularly polarized x-ray photons leads to a spin polarization of the photoelectrons due to the spin-orbit coupling ($j = l \pm s$). In a second step the d valence band acts as a spin detector. At the L_3 edge ($j = l + s$) left circular polarized x-rays mainly probe the unoccupied spin-up d states with respect to the direction of the magnetization. The effect reverses at the L_2 edge due to the opposite sign of the spin-orbit coupling ($j = l - s$) [100]. . . . 40
2.12 Schematic illustration of the summed XAS spectrum of a $3d$ atom (a), XMCD difference spectrum of a sample showing only a spin magnetic moment m_{spin} (b), and XMCD difference spectrum of a sample with only an orbital magnetic moment m_{orb} (c) [100]. . . . 41
2.13 Schematic diagram of the main x-ray emission lines in the K and L series (after [105]). . . . 43
2.14 Schematic representation of the RIXS process in an atomic like environment. . . . 45
2.15 Schematic diagram of the PHI 5600ci multitechnique spectrometer [114]. 47
2.16 Schematic plot of a storage ring with different insertion devices: a bending magnet and an undulator. . . . 49
2.17 Schematic drawing of an APPLE device at different settings. Upper panel: linear mode without shift (linearly horizontally polarized light). Middle panel: circular mode. The shift ($\lambda/4$) is set to the position with equal amplitudes of the horizontal and vertical magnetic fields (quarter period of the magnetic structure). Lower panel: linear mode with shift set to half period ($\lambda/2$) (linearly vertically polarized light) of the magnetic structure. Adapted from [116]. . . . 50

2.18 Typical example of an undulator beamline layout: the beamline 8.0.1 at the Advanced Light Source (ALS) at the Lawrence Berkeley Lab. . 51
2.19 Schematic plot of the SXF-spectrometer of the University of Tennessee in Knoxville [119]. 51
2.20 The Compact soft Inelastic X-ray Spectrometer (ComIXS) operating at ELETTRA [121, 122]. 52

3.1 A bulk unit cell of Pyrite: FeS_2 (blue spheres represent iron, yellow spheres sulfur). 54
3.2 Valence band x-ray photoelectron spectra of FeO (upper curve) and FeS_2 (lower curve). 56
3.3 Upper panel: XPS spectra of the Fe 3*s* and 3*p* core levels of FeS_2 and FeO. Lower panel: Fit of the Fe 3*s* region of FeO. Fit parameters: width of high spin peaks: 3.4 eV; width of low spin peaks, 4.3 eV. Branching ratio low spin / high spin: 0.42; intensity ratio charge transfer peak / parent peak: 0.25. 57
3.4 XPS Fe 2*p* core level of FeO (upper curve) and XPS Fe 2*p* core levels of FeS_2 (lower curve). 58
3.5 XPS O 1*s* core levels of FeO (upper panel) and XPS S 2*p* core level of FeS_2 (lower panel). 59
3.6 The Fe 2*p* XAS for FeO (upper panel) and FeS_2 (lower panel) compared with a crystal field multiplet calculation (dotted line) and a charge transfer multiplet calculation (dashed line). 60
3.7 RIXS of FeO (lower panel) at the selected excitation energies as indicated in the Fe 2*p* XAS (upper panel): 1: 706.0 eV; 2: 707.5 eV; 3: 709.0 eV; 4: 710.5 eV; 5: 712.0 eV; 6: 717.0 eV; 7: 719.25 eV; 8: 721.0 eV; 9: 722.5 eV and 10: 725.0 eV. 63
3.8 Resonant inelastic x-ray spectra at the oxygen edge of FeO (lower panel), at the incident photon energies indicated in the corresponding O 1*s* XAS (upper panel): 1: 527.0 eV; 2: 528.0 eV; 3: 529.3 eV; 4: 531.0 eV; 5: 533.3 eV; 6: 535.5 eV; 7: 538.5 eV and 8: 544.5 eV. . . . 64
3.9 Resonant x-ray scattering from the Fe *L* edge of FeS_2. The excitation energies are those indicated in the corresponding XAS: 1: 706.4 eV; 2: 708.0 eV; 3: 709.45 eV; 4: 711.45 eV; 5: 713.2 eV; 6: 714.7 eV; 7: 718.95 eV; 8: 720.6 eV; 9: 722.1 eV and 10: 725.9 eV. 66
3.10 A schematic plot of the density of states of FeS_2 [167]. The empty states above the gap consist of a conduction band of width ΔE_{cond}, a gap of width ΔE_{g2}, and another empty band above this. 74
3.11 X-ray absorption spectra of FeS_2 [167]: lower curve, S *L* edge; the vertical bars mark the photon energy range in which the spectra in Fig. 3.12 were taken. Upper curve: Fe *L* edge 75
3.12 Resonant inelastic x-ray emission spectra of FeS_2 at the S *L* edge [167]. Photon energy (from bottom to top): 162.3, 162.35, 162.4, 162.45, 162.5, 162.7 eV. Top curve: the inelastic EELS spectrum, recorded at an incident energy of 200 eV. 77

3.13 Summary of electronic structure: calculated partial density of Fe and S states, after Zeng and Holzwarth [147]; XPS spectrum of the valence band; Fe $2p$ and S $2p$ x-ray absorption spectra; and the Resonant Inelastic X-ray Scattering spectrum at the S $2p$ edge. 78

4.1 XPS valence band and XES spectra of the Mn $2p$ and the O $1s$ edge (plotted on a binding energy scale using the XPS core level binding energies) of $La_{1-x}Ba_xMnO_3$ ($0.0 \leq x \leq 0.55$) [194]. For $LaMnO_3$, $La_{0.8}Ba_{0.2}MnO_3$ and $La_{0.55}Ba_{0.45}MnO_3$ the experimental data are compared with the results of theoretical band structure calculations (labelled (tDOS) and (pDOS), respectively). The calculated data for $LaMnO_3$ have been extracted from Ravindran *et al.* [188], whereas the values for the Ba-doped compounds have been taken from Youn *et al.* [187]. 84

4.2 XPS valence band and the corresponding XES data of $La_{0.76}Ba_{0.24}Mn_{0.84}Co_{0.16}O_3$ (upper panel) and $La_{0.76}Ba_{0.24}Mn_{0.78}Ni_{0.22}O_3$ (lower panel) plotted on a binding energy scale [194]. For comparison also the XPS valence band of $La_{0.75}Ba_{0.25}MnO_3$ has been normalized to the Ba $5p$ XPS peak. The subtraction of the two spectra leads to a representation of the Co $3d$ and the Ni $3d$ contributions to the valence band of the corresponding sample. The XPS valence bands of $LaCoO_3$ and $LaNiO_3$ are also shown for comparison. 86

4.3 Mn $L_{2,3}$ (upper panel) and O K (lower panel) XAS regions of $LaMnO_3$ [194]. The data were recorded in total electron yield (TEY) mode. Labels A-D indicate the excitation energies of the RIXS spectra recorded at the Mn L edge. The Mn $2p$ XAS multiplet calculation has been adapted from Taguchi *et al.* [104], the O K XAS is compared with a LDA+U calculation from Wessely *et al.* [193]. 87

4.4 Mn L_3 Resonant Inelastic X-ray Scattering spectra of $La_{1-x}Ba_xMnO_3$ ($0.0 \leq x \leq 0.55$) recorded at different excitation energies near Mn L_3 edge [194]. Labels A-D correspond to the indicated features in the Mn L edge XAS spectrum (see Fig. 4.3). The RIXS spectra consist of three main features labelled $I - III$ (see text). The dashed lines represent multiplet calculations performed for Mn^{3+} ions [189]. 88

4.5 Schematic plot of the partial densities of states of O $2p$ and Mn $3d$ for the orthorhombic $GdFeO_3$ structure (upper panel) and the cubic perovskite-type structure [194]. Densities above the energy axis are majority spin states, those below are minority spin states. The values are based upon our experimental findings and the calculations of Ravindran *et al.* [188] and Youn *et al.* [187], respectively. 91

4.6 Polarization dependent XAS with $E \perp \mathbf{c}$ and $E \parallel \mathbf{c}$ and the corresponding linear dichroism (LD) recorded on the Mn L edge of $La_{7/8}Sr_{1/8}MnO_3$ at 295 K and 240 K, respectively. 96

4.7 The XLD signal recorded at the Mn L edge of a $La_{7/8}Sr_{1/8}MnO_3$ single crystal at different temperatures [211] compared with MnO_6 cluster model calculations [209]. 97

4.8 The experimental XLD recorded at 240 K [211] in comparison with a crystal field multiplet calculation (dotted line) [37] and a charge transfer multiplet calculation (dashed line) [209]. 98

5.1 A schematic picture of alternating FeO_6 and MoO_6 octahedra in an ordered double perovskite, adapted from [218]. 102

5.2 Magnetization isotherms at 4.2K, and thermal variations of reciprocal susceptibilities [19]. 105

5.3 Fe $2p$ XAS spectra (upper panel), XPS core level spectra of Fe $3s$ (lower left panel) and Mo $3d$ (lower right panel) of Sr_2FeMoO_6, compared with the spectra of some other compounds, the FeO XAS spectra has been taken from Prince *et al.* [161], the Mo $3d$ spectra of MoO_2 and MoO_3 have been adapted from Colton *et al.* [232]. 107

5.4 The XPS valence band of Sr_2FeMoO_6 (circles), compared with LDA+U calculations for different values of U (thin solid lines) [235]. The calculated total densities of states have been weighted with the corresponding photoionization cross sections [236] and broadened with the spectrometer resolution (bold lines) for direct comparison with the experiment. 109

5.5 The spin-resolved, site-projected densities of states of the LDA + U ($U = 2$ eV) calculation for Sr_2FeMoO_6 [235]. 111

5.6 The XPS valence band and XES spectra of the Fe L edge, the Mo M and the O K edges of Sr_2FeMoO_6. The calculated densities of states are also shown (thin solid lines). The XPS valence band of $SrFeO_{2.82}$ has been normalized to the Sr $4p$ XPS located around 17.5 eV of binding energy (see inset graph). The "difference spectrum" of Sr_2FeMoO_6 and $SrFeO_{2.82}$ is also shown. 112

5.7 Upper panel: the XAS spectra taken with left and right circularly polarized x-rays and the resulting MCD ($\mu_+ - \mu_-$), lower panel: the overall XAS spectrum ($\mu_+ + \mu_-$) and a two step like background function (black line). 114

5.8 The experimental XAS spectrum (upper panel) and the XMCD (lower panel) in comparison with ligand field (LF) (dotted line) and charge transfer (CT) multiplet calculations (dashed line) in O_h symmetry. . . 116

6.1 Upper panel: O $1s$ (a), lower panel: Co $2p$ (b) x-ray absorption spectra of Li_xCoO_2 [254]. The spectra labelled with 200 °C has been measured on the $Li_{0.6}CoO_2$ sample which has been heated at 200 °C for about 20 h. 123

6.2 X-ray emission O $K\alpha$ emission spectra measured at excitation energies between 529.4 and 548.9 eV. The inset graph shows the corresponding O $1s$ x-ray absorption spectrum (XAS) measured in total-electron yield mode. The vertical bars in the O $1s$ XAS and O $K\alpha$ XES spectra mark the incident photon energies [254]. 125

6.3 Valence band x-ray photoelectron spectrum and O $K\alpha$ resonant x-ray emission (RXES) and O 1s absorption (XAS) spectra of $LiCoO_2$. The XES and XAS spectra are plotted on a common energy scale based on the binding energy of the O 1s levels. The O $K\alpha$ XES spectrum is measured at the excitation energy of 530.5 eV [254]. 126

List of Tables

3.1 The crystal field parameters as used in the Fe $2p$ XAS simulations. The $3d$ spin-orbit coupling was set to zero. 61
3.2 Summary of the XPS satellite structure. 68
3.3 Input parameters and results of Coster-Kronig (CK) analysis [161]. . 72
3.4 Theoretical and experimental values of the width of the conduction band (E_{cond}) and the width of the second gap (E_{g2}) above the optical gap. 76

4.1 Type of orbital ordering of $La_{7/8}Sr_{1/8}MnO_3$ revealed by different approaches and at different temperatures [211]. 100

5.1 Comparison of previously published XMCD results with the one obtained in the present work. 115
5.2 The crystal field parameters as used in the Fe $L_{2,3}$ XAS and the corresponding XMCD multiplet calculation. The simulations were performed assuming a cubic crystal field (O_h symmetry). For the d^6 calculation, the $3d$ spin-orbit coupling was set to zero. 117

Introduction

The oxides of $3d$ metals are subject to intense studies in order to understand their electronic and magnetic properties. The high temperature superconductivity of cuprates and the colossal magneto resistance (CMR) of manganites are among the best known effects but many other interesting phenomena occur for other $3d$ metal compounds. Nowadays, one of the most striking challenges of solid state physics is to understand these intricate properties of many transition metal compounds.

While the superconductivity is dominating the research of cuprates the CMR effect has renewed the interest in the so called manganites, like manganese perovskites which were intensely studied in the 50's - 70's. Since the discovery of colossal magneto resistance [1, 2], a huge change in the electrical resistance induced by an applied magnetic field in $La_{1-x}A_xMnO_3$ (A=Ca, Sr, Ba), the manganites are subject of extensive research with respect to their remarkably rich phase diagrams as a function of temperature, magnetic field and doping.

More recently a large magneto resistance (MR) effect has been found in the double perovskite Sr_2FeMoO_6 [3]. This material is of special interest due to its high Curie temperature ($\sim$ 420 K) and a rather large MR effect already present at room temperature. Furthermore the complex properties of this CMR compound has been associated with half metallic ferromagnetism, meaning that one spin channel is metallic while the other is insulating [4, 5, 3], linking the interest to use these materials as switches or "spin-devices" (spintronics).

Another class of highly interesting transition materials are cobaltites such as $La_{1-x}Sr_xCoO_3$ or the defect oxides $Na_{1-x}CoO_2$ and $Li_{1-x}CoO_2$. The interest in the study of these materials stems partly from their practical importance as promising candidates in high performance electrodes, and partly in understanding the intriguing behavior of the spins in cobaltites. In cobalt oxides both, the valence state and the spin state can vary with temperature and even if the valence state is fixed different spin states may exist (the high-, intermediate- and low-spin state).

The systematic study of the electronic properties of transition metal oxides is a key point if one wants to understand their very interesting properties. For the analysis of the spatial distribution of the electron density and chemical bonding the methods of x-ray and photoelectron spectroscopy provide tools of unique precision, especially useful in combination with first-principles electronic structure studies. Therefore this study has been performed in order to understand the electronic structure of a number of selected transition metal compounds. Special emphasis is given to investigate the electronic structure by several complementary spectroscopic techniques in order to obtain a complete picture of the electronic properties of the compounds in question. Furthermore we compare our results with magnetic measurements and different

theoretical results. The work is structured as follows:

- In Chapter 1 the reader is briefly introduced into the rich variety of transition metal compounds. Special emphasis is given to the behavior of transition metal ions in crystal fields, the Zaanen Sawatzky Allen (ZSA) model [6] and simple exchange models like the superexchange and the double exchange [7].

- Chapter 2 contains a brief description of the experimental techniques used, namely x-ray photoelectron spectroscopy (XPS), x-ray emission spectroscopy (XES), resonant x-ray emission spectroscopy (RXES) and x-ray absorption spectroscopy (XAS). For the latter also experiments dependent on the polarization of the incident x-rays, the so called x-ray linear dichroism (XLD) and the x-ray magnetic circular dichroism (XMCD) are explained. Furthermore in this section a very short introduction into two competing theoretical models which are important for the description of x-ray spectra is given. These are on the one hand side the electron band theory or density functional theory (DFT) and on the other hand side the single impurity Anderson model (SIAM).

- The following Chapter 3 deals with a very detailed x-ray spectroscopic study of two iron containing model systems, namely wüstite (FeO) and pyrite (FeS_2). These materials are of special interest because they are very similar with respect to their crystallographic and ionic structure (Fe^{2+}) but they show a different magnetic ground state. FeO is a high spin system while for FeS_2 the ground state is low spin, that means all 6 iron $3d$ electrons occupy the 6 t_{2g} levels whereas the e_g levels are left completely empty. We find a strong dependence on the branching ratio in the Fe L edge XAS as well as in the Fe $3d \rightarrow 2p$ RXES spectra which can be explained by the different magnetic states of these materials. The results are also discussed in the light of band theory and cluster calculations.

- A comprehensive study of the electronic structure of a series of $La_{1-x}Ba_xMnO_3$ samples as well as so called double doped perovskites $La_{1-x}Ba_xMn_{1-y}TM_yO_3$ (TM = Co, Ni) is presented in Chapter 4. Besides XPS and XES we also performed XAS at the Mn L and the O K edges of the samples. Furthermore, resonant x-ray emission has been used to study intra-atomic correlation effects like dd transitions and inter-atomic effects like charge transfer excitations. We compare the experimental results again with band structure and multiplet calculations. A special effort is given to the study of orbital ordering in $La_{7/8}Sr_{1/8}MnO_3$. The experimental investigation of orbital ordering belongs to the most difficult challenges in the state of the art condensed matter physics. We present for the first time an investigation of orbital ordering on a three dimensional colossal magneto resistance perovskite by means of x-ray linear dichroism on the Mn L edge and are able to determine the predominantly type of orbital ordering.

- The next Chapter 5 deals with a detailed study of the electronic and magnetic properties of the double perovskite Sr_2FeMoO_6. A combination of structural, magnetic and spectroscopic measurements have been applied to this sample in

order to reveal a very detailed picture on the chemical composition, valence states, the magnetic and the electronic structure of this material. A whole series of band structure calculations has been performed for comparison with the experimental results. Moreover XMCD in XAS has been applied to the Fe L edge of this compound.

- In the last part (Chapter 6) the focus moves on a little bit different kind of transition metal compound, namely the defect oxide Li_xCoO_2. This kind of material is of special interest due to its application as cathode material in Li batteries. Here we present a comprehensive study of the electronic structure of these defect oxide by means of XPS, XES, XAS. A special effort is given into the study of hybridization effects between Co $3d$ and O $2p$ states by applying RXES to the O K edge of $LiCoO_2$.

- Finally, in Chapter 7 the main results achieved in the present work are summed up and an outlook is given, followed by a list containing the bibliographic references.

Chapter 1

Basic properties of transition metal compounds

In this chapter a brief state of the art review about the complex and rich properties of transition metal compounds in common is presented. The issues turned up with respect to the materials investigated in the present study are emphasized in the preface of the corresponding chapters.

1.1 Correlated materials

An electron in a solid, if bound or nearly localized on a specific atom, can be described by three attributes; its charge (e^-), spin ($S = \pm\frac{1}{2}$) and orbital. The orbital may be understood as the shape of the electron in question. If correlations between different orbitals may be neglected, solving the problem of one of the orbitals is often equivalent to solving the whole system. These orbitals hybridize to form a valence band. This so called one-electron picture ignores both intersite (like the Coulomb repulsion U) and even some intrasite correlations between the electrons (i. e., the charge transfer between O $2p$ and transition metal (TM) $3d$ states Δ). Nonetheless, the single electron approach has been very successful for the description of many of the properties of periodic solids. However, electronic correlations are responsible for some of the most fascinating properties of transition metal (TM) compounds as superconductivity or magnetism.

Strongly correlated electrons bear multiple degrees of freedom from the charge, orbital and spin sector. Strong interactions inside these sectors and/or cooperation/competition between the sectors give rise to a rich variety of different electronic and magnetic properties in dependence of the composition (different dopants) and/or the crystal structure of the compound in question such as high temperature superconductivity and colossal magneto resistance (CMR). The description of the complex interplay between the charge, spin and orbital degrees of freedom is very essential, partly in order to develop a thorough understanding of the fascinating transport properties of these compounds, and partly the electronic and magnetic phases can be controlled by utilizing cooperative response of strongly correlated electrons to external parameters as, e. g., electric/magnetic fields or pressure. One example is the

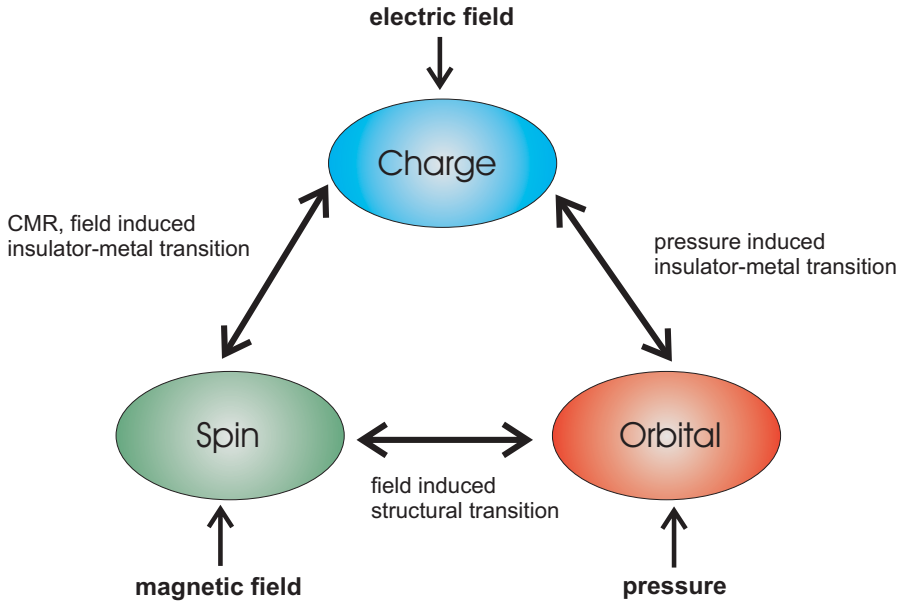

Figure 1.1: Schematic plot showing the interplay between charge, spin and orbital degrees of freedom in $3d$ transition metal oxides.

rich phase diagram of CMR manganites, which exhibits drastic phase changes dependent from parameters like temperature, doping concentration or the strength of an external magnetic field. Hence, the ability to control of all these critical phase states and transitions can be understood as being a key concept for possible technological applications of strongly correlated systems.

1.2 Colossal magneto resistance (CMR)

The so called *magneto resistance* (MR) is the change in the electrical resistance of a conductor by an applied magnetic field (H). The MR is described by equation 1.1:

$$MR = -\frac{R(H) - R(0)}{R(0)} \tag{1.1}$$

Whereas in nonmagnetic conductors, the MR is relatively small and it is due to the Lorentz force that a magnetic field exerts on moving electrons, in magnetic materials the large spin polarisation of the electrons gives rise to additional contributions and large MR effects can be obtained, sometimes even in low magnetic fields. One can distinguish between three major kinds of MR effects. The so called *Giant Magneto Resistance* (GMR) effect was firstly reported for Fe/Cr multilayers in 1989 by the sentimental works of Baibach *et al.* [8] and Grünenberg *et al.* [9]. The electrical resistance drops as the configuration of the magnetizations in neighbor Fe layers goes from antiparallel to parallel. The MR ratio reaches up to 79% at 4.2 K for these layers of 9 Å thickness.

Mid of the 90's, another type of MR effect was observed in tunnel junctions. MR of up to 40% at room temperature and 65% at 4.2 K was discovered in tunnel junctions, in which the two electrodes are ferromagnetic layers and the barrier consists of a thin insulating layer [10]. The effect, denoted as *tunneling magneto resistance* (TMR), is based on the difference in the tunneling probability between the ferromagnetic electrodes for the spin up and spin down electrons; the tunnel resistance in the parallel and antiparallel configurations are different.

In the last few years the manganese perovskites $La_{1-x}A_xMnO_3$ (A = Ca, Sr, Ba) have been the subject of intense experimental and theoretical studies due to the colossal magneto resistance effect (CMR) observed in them [11, 12, 13]. The CMR effect can reach up to several 100% or 1000%. This unusual behavior has been associated with half metallic (HM) ferromagnetism (FM) and can be explained in terms of charge carriers and local spins arising from Mn $3d$ electron states. Exchange splitting can cause one of the pair of spin-split d-bands to overlap with oxygen p bands while in the other insulating channel the Fermi level lies within the gap. The most extensive studied manganite is $La_{1-x}Sr_xMnO_3$. When La is replaced by Sr the compound remains an antiferromagnetic insulator, like the parent compound $LaMnO_3$, up to Sr concentrations of $\sim$ 10%. Between 10% and 20% doping concentration one finds a very interesting coexistence of ferromagnetic and insulating behavior in the ground state. Between 17% and 20% Sr concentration a metal to insulator transition takes place, accompanied by an increasing Curie temperature [14, 15].

A rather high Curie temperature of 340 K at Sr concentrations around 30% makes this compound to one of the most interesting candidates for possible future applications regarding sensors, hard disk storage read heads or so called spin devices. However, rather high magnetic fields, several Tesla are necessary to achieve a significant change in resistivity, a factor which is limiting possible applications. Furthermore, up to now the remarkable rich phase diagram of these compounds, especially the paramagnetic to ferromagnetic transition, the metal to insulator transition as well as the existence of a ferromagnetic insulating phase for moderate doping concentrations have not been understood thoroughly.

During the last years huge MR effects have been reported also for other types of materials as for layered systems like $La_{2-2x}Sr_{1+2x}Mn_2O_7$ [16] or the magnetic chalcogenides $Fe_{1-x}Cu_xCr_2S_4$ [17, 18]. One of the most interesting materials showing large MR is the double perovskite Sr_2FeMoO_6 [3, 19]. Due to a high Curie temperature of $\sim$ 400 K and a high magnetic saturation moment reached already at moderate magnetic fields of about 1 T this material is even more promising for future applications than the most manganites.

1.3 Transition metal ions in crystal fields

The principle quantum number n and the orbital angular-momentum quantum number l are $n = 3$ and $l = 2$ for $3d$ electrons. The angular part of the corresponding wave function can be expressed by the spherical harmonics $Y_m^2(\Theta, \Phi)$ in terms of polar coordinates with m representing the magnetic quantum number $-2 \leq m \leq 2$. In a free ion the $3d$ states are five fold degenerate since $2l + 1 = 5$. In a crystal the situation changes. In 1930, Bethe and van Vleck developed the crystal field theory

(CFT) in order to describe the electronic and chemical properties of d-metal ions in crystals [20]. Within the CFT framework a ligand ion is treated as a point charge.[1]

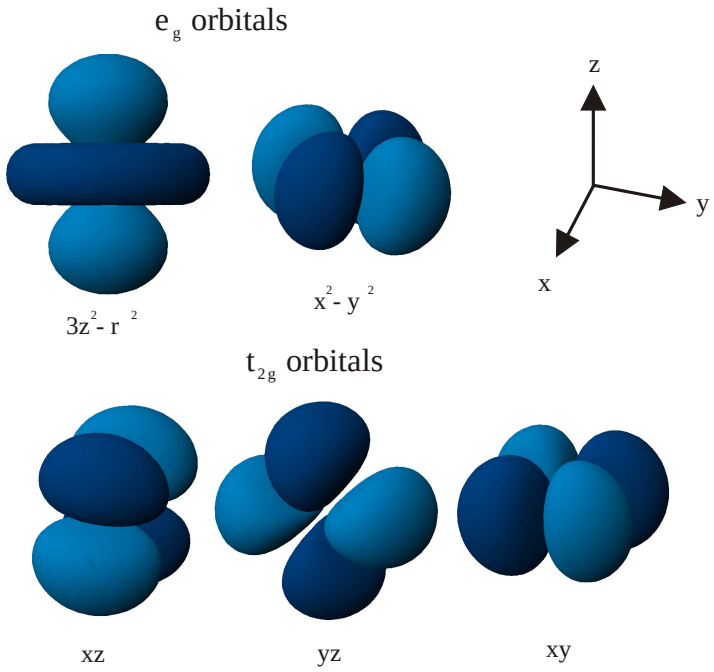

Figure 1.2: The five d orbitals. In a cubic crystal field, the five-fold degeneracy is lifted to two e_g- and three t_{2g}-orbitals.

In case of a non spherical symmetric crystal field the point charges of the ligands interact with the d-metal ion orbitals, hence the degeneracy of the $3d$ orbitals is lifted. As a general rough rule of thumb the electrostatic energy is increased for d orbitals oriented towards the region of high electron density and vice versa. In many transition metal oxides a transition metal ion is surrounded by six oxygen (O^{2-}) ions, leading to an octahedral ($\mathcal{O}$) symmetry,

$$\mathcal{H}_{3d}(\mathbf{r}) = \mathcal{H}^{TM}(\mathbf{r}) + \sum_{j=1}^{6} V^{O}(\mathbf{r} - \mathbf{R}_j) \tag{1.2}$$

where $\mathbf{r}$ denote the position of the $3d$ orbital and $\mathbf{R}_j$ the position of the the j–th vector, respectively. In a cubic crystal field the degeneracy of the $3d$ orbitals is lifted and the corresponding eigen-functions can be described as a linear combination of the spherical harmonics $Y_m^2(\Theta, \Phi)$.

The result is plotted in Fig. 1.2, and Fig. 1.3 shows the $3d$ energy levels in spherical, cubic and tetragonal (elongated along the z direction) crystal fields. In a cubic field, the two higher energy states, namely $x^2 - y^2$ and $3z^2 - r^2$ are often labelled

[1] CFT ignores covalent interactions between the metal $3d$ states and the ligand states, whereas the ligand field theory takes into account an overlap between the metal $3d$ electron and the ligand orbitals.

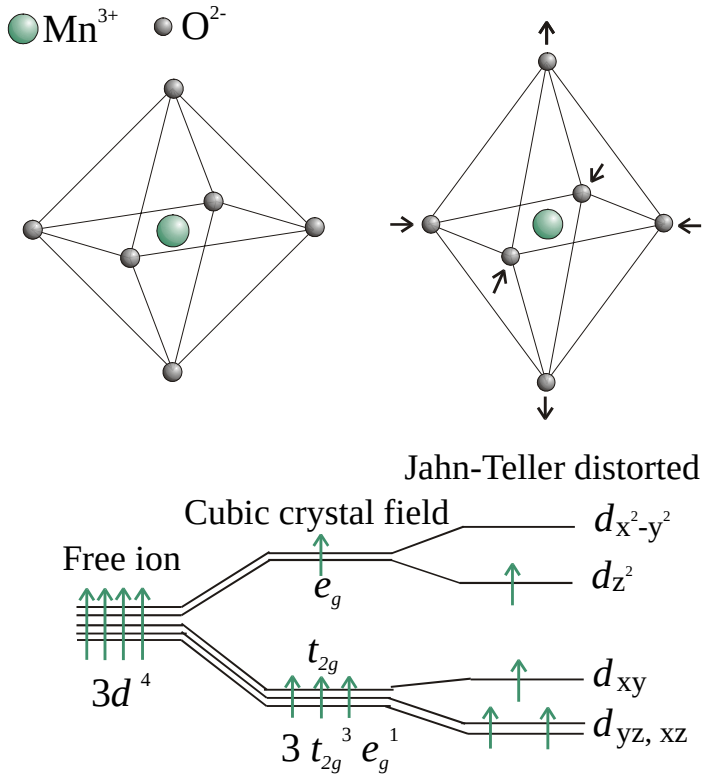

Figure 1.3: The energy levels of the $3d$ electrons of an Mn^{3+} ion. In a cubic crystal field, the five-fold degeneracy is lifted to two e_g– and three t_{2g}–orbitals. The Jahn-Teller distortion leads to a further splitting of both the t_{2g} and e_g states. Knowledge about the occupancy of the e_g states is a crucial point for understanding the fascinating properties of transition metal compounds.

as the e_g orbitals whereas the three lower energy states, xy, yz, and zx are referred as the t_{2g} orbitals, respectively. This notation is linked to the group theory, applying the symmetry operations of the octahedral point group $\mathcal{O}$ with the d orbitals Γ_d as the basis leads to the result that both the two times degenerated E and the three times degenerated T_2 irreducible representation of $\mathcal{O}$,

$$\Gamma_d = E \otimes T_2 \tag{1.3}$$

exists exactly once [21]. The e_g orbitals are directly pointing towards the oxygen ligands whereas the t_{2g} electrons are pointing between the oxygen ligands so that these electrons have an energy which is less affected by the Coulomb interactions between the TM $3d$ electrons and the oxygen $2p$ electrons than the e_g electrons. Thus, the e_g electrons have an energy raised by this Coulomb interaction. The splitting between the e_g and the t_{2g} electrons is denoted as $10Dq$. The value of the splitting is about

1−3 eV in typical TM oxides with perovskite structure. An important other symmetry is the tetragonal distortion of the regular octahedron, where the z-axis is elongated whereas the x- and y–axis are compressed (see Fig. 1.3). If one considers the simple Coulomb interaction between $3d$ states and the crystal field, the energy of the $3z^2-r^2$ orbital is reduced and the energy of the x^2-y^2 orbital is increased. Therefore a further splitting of the e_g and t_{2g} levels occurs.

Another important effect of the crystal field is the quenching of the orbital angular momentum, it vanishes. Quantum mechanically, this can be understood because the angular momentum operator $\mathbf{L}$ is an imaginary one, but the non-degenerate solutions of the time independent Schrödinger equation are real ones. More descriptive, the quenching of the orbital angular always occurs if the crystal field is much stronger than the **LS** coupling. Thus, the magnetic moment in TM oxides is usually dominated by that of the spin.

1.3.1 Basic crystal properties

The variety of properties of transition metal compounds is often due to different behavior of the $3d$ electrons, which are to large extend responsible for the complex relationship between the electronic properties and the crystal structure. One of the most important crystal structures for the transition metal oxides is the perovskite structure. The basic perovskite crystal structure, with the general chemical formula ABO_3 is plotted in Fig. 1.4, six oxygen anions and one TM cation form an octahedron.

A lot of interesting TM oxides are perovskites, like the ferroelectric titanate $SrTiO_3$ and the colossal magneto resistance manganite $La_{1-x}Sr_xMnO_3$. The ideal structure of ABO_3 fulfills the relation $r_A + r_O = \sqrt{2}(r_B + r_O)$ with r_A, r_B and r_O representing the ionic radii of A, B and O, respectively. However, in real perovkite oxides the relation

$$r_A + r_O = t\sqrt{2}(r_B + r_O) \tag{1.4}$$

with $t = 0.8 \sim 1.0$ holds, t denotes the so called "tolerance factor".

Besides the cubic perovskites there exist also two dimensional structures of the type $A_{n+1}M_nO_{3n+1}$. For instance the parent compound of the high temperature superconducting cuprates, La_2CuO_4 crystalizes in the A_2MO_4-structure ($n = 1$). The double layered CMR compound $La_{2-2x}Sr_{1+2x}Mn_2O_7$ is a manganite with $n = 2$. In such compounds not only the TMO_6 octahedrons but also TMO_5 pyramids and TMO_4 play a crucial role for the properties of the compound in question. The three dimensional perovskites correspond to this lattice with $n = \infty$.

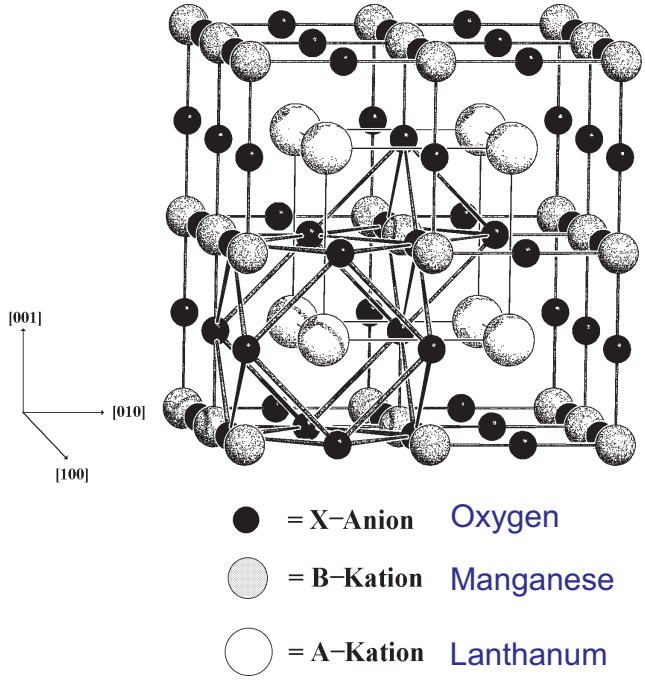

Figure 1.4: The cubic perovskite unit cell. The La, Mn, and O ions are represented by white, grey and black spheres, respectively.

1.3.2 The Zaanen Sawatzky Allen (ZSA) scheme

In 1985 J. Zaanen, G. A. Sawatzky and J. W. Allen developed a model which separates correlated systems into two general classes of materials [6]. The Mott-Hubbard theory [22] is based upon the assumption that *dd* like Coulomb exchange interactions (U) are strongly suppressed because of the high energies involved ($\sim$ 5-10 eV). This model implies that the band gap of transition metal compounds is a *dd* gap. This is correct for early transition metal compounds like Ti or V based oxides, whereas for late transition metal oxides like NiO the band gap has been found to be directly related to the electronegativity of the oxygen ligand [23]. Especially for late transition metal compounds another charge fluctuation which does not involve U becomes very important, namely the charge transfer Δ. The charge transfer can be explained as a transfer of a ligand electron into the metal d band ($d_i^n \rightarrow d_i^{n+1}\underline{L}$), where $\underline{L}$ stands for a hole in the ligand (anion) valence band. By considering both, U and Δ for transition metal compounds, within the scheme of the Anderson impurity model [24], it is possible to describe the dependence of the band gap on U and Δ qualitatively [6].

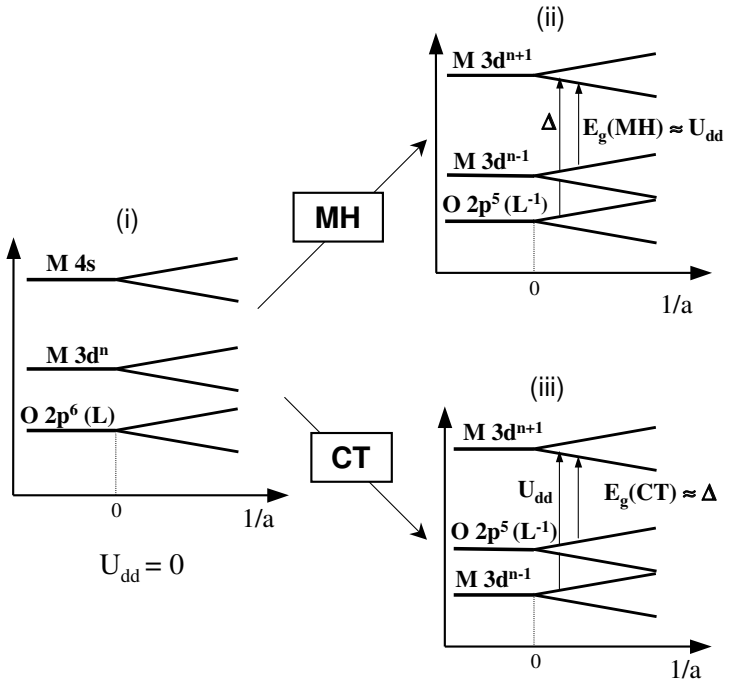

Figure 1.5: One electron (i), Mott Hubbard (ii) and charge transfer (iii) diagrams of a transition metal oxide (adapted from [25]).

A transition metal compound in question can then be associated with a particular class of material, showing properties closely related to the values of U and Δ, respectively:

- *Mott-Hubbard insulators:* The band gap E_{gap} is proportional to U. That is the case if $U \ll \Delta$. The lowest energy excitations are obtained by transferring one electron from one transition metal ion to anther one. Examples are early transition metal oxides like TiO_2, V_2O_3 and related compounds.

- *Charger transfer insulators:* E_{gap} is proportional to Δ. That is the case if $\Delta \ll U$. The lowest energy excitations are obtained by transferring one electron from the ligand atom to the transition metal ion. Examples are late transition metal oxides like CuO and related compounds.

- *Intermediate compounds:* If $\Delta \simeq U$. both, the Coulomb potential U and the charge transfer Δ have significant influence to the properties of the compound. A fine balanced competition between Coulomb and charge transfer interactions takes place. For example, manganese and iron oxides belong to this class of material.

1.3.3 Exchange interaction and orbital degeneracy

The Coulomb repulsion is one very important origin of the interactions between electrons. The Coulomb interaction between two electrons 1 and 2 can be expressed by the following equation:

$$H = \frac{1}{2}\sum_{n,m,\sigma}\langle n_1, m_1, n_2, m_2 \mid \frac{e^2}{\mid r_1 - r_2 \mid} \mid n_3 m_3, n_4, m_4\rangle a^\dagger_{n_1 m_1 \sigma_1} a^\dagger_{n_2 m_2 \sigma_2} a_{n_4 m_4 \sigma_2} a_{n_3 m_3 \sigma_1} \tag{1.5}$$

n, m and σ refer to the ionic site, the orbital and the spin quantum number, respectively, $a_{nm\sigma}$ denotes the annihilation operator. Eq. 1.5 comprises several interactions. These will be briefly introduced in the following.

Hubbard interaction

The interaction on the same orbital at the same site is often denoted as Hubbard interaction. Then Eq. 1.5 can be expressed as

$$H_U = \frac{1}{2}\sum_{\sigma}\langle n, n \mid \frac{e^2}{\mid r_1 - r_2 \mid} \mid n, n\rangle a^\dagger_{n\sigma} a^\dagger_{n-\sigma} a_{n\sigma} a_{n-\sigma} = U n^\uparrow_n n^\downarrow_n \tag{1.6}$$

with $n_{n\sigma} = a^\dagger_{n\sigma}$. In transition metal compounds, where the overlapping between the TM $3d$ and the O $2p$ states is essential, U is typically estimated to be $\sim$ 4–8 eV. U is often called the Hubbard Hamiltonian [22, 26] and is the starting point for the superexchange interaction which is discussed below.

Hund coupling

The description of the interaction between electrons from the same site but in different orbitals leads to the Hund coupling. Then Eq. 1.5 can be written as

$$H_H = K_{m_1 m_2} n_{m_1} n_{m_2} - 2J_{m_1 m_2}(\mathbf{S}_{m_1} \cdot \mathbf{S}_{m_2} + \frac{1}{4} n_{m_1} n_{m_2}) \tag{1.7}$$

where $K_{m_1 m_2}$ denotes the Coulomb interaction and the second term stands for the Hund rule coupling. In transition metal compounds $J_{m_1 m_2}$ is of the order of 1 eV. $\mathbf{S}$ refers to the spin operator of the corresponding orbital. The Hund coupling plays an important role for the so called double exchange interaction which will be introduced below.

Superexchange interaction

A lot of transition metal oxides are *Mott-Hubbard insulators*, ($U \ll \Delta$). These kind of compounds often show an antiferromagnetic and insulating behavior, the simplest model to describe these properties is the *superexchange interaction*, the starting point is given by the Hubbard Hamiltonian [22, 26]:

$$H_{SE} = -t\sum_{\langle ij\rangle\sigma}(a^\dagger_{i\sigma} a_{j\sigma} + a^\dagger_{j\sigma} a_{i\sigma}) + U\sum_i n^\uparrow_i n^\downarrow_i \tag{1.8}$$

Here each ion is assumed to have a single orbital. t denotes the hopping integral of electrons between neighboring site $\langle ij\rangle$. U is considered to be much larger than t.

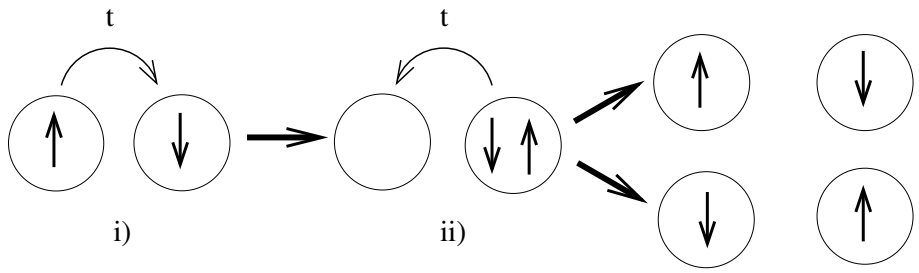

Figure 1.6: Schematic plot of the single orbital superexchange interaction. Note that the intermediate state (ii)) has an energy larger by U compared to the ground state. There are two possible final states.

Due to the Pauli principle the hopping between electrons with parallel spin is forbidden, hence the superexchange leads to an antiferromagnetic ground state. The effective exchange is:

$$H_{ex} = J_{ex} \sum \mathbf{S}_i \mathbf{S}_j, \;\; J_{ex} = \frac{2t^2}{U} \tag{1.9}$$

It is often difficult to calculate the nature of the magnetic exchange. Nonetheless, Goodenough, Kanamori and Anderson have developed some simple rules which are often able to predict the magnetic exchange correlations. The interested reader finds detailed information in References [27, 28].

However, for late transition metal oxides like nickel or copper based compounds the charge transfer Δ between the TM $3d$ electrons and O $2p$ electrons must be taken into account explicitly. For the late transition metal compounds $\Delta \ll U$ as discussed in Chapter 1.3.2. In case of an antiferromagnetic ground state the total exchange is given by

$$J_{ex} = \frac{2(t_{pd}^2 \Delta)^2}{2\Delta + U_{pp}} \tag{1.10}$$

where t_{pd} refers to the hopping amplitude between the d and p orbitals, U_{pp} is the Coulomb repulsion between the O $2p$ holes.

Furthermore the inclusion of the orbital degeneracy is essential for the description of the magnetic exchange of crystals. As discussed before the crystal structure of transition metal oxides is often reflected in the ordering of three degenerate t_{2g} orbitals and two degenerate e_g orbitals. Since the t_{2g} orbitals are pointing between the oxygen ligands there is almost no overlap between the $3d$ t_{2g} states and the O $2p$ orbitals. Hence, the hopping integral $t \to 0$, there is no hopping. On the other hand side the e_g orbitals are differently orientated and have a large overlap with the O $2p_\sigma$ orbitals, leading to strong superexchange interaction. These facts are particulary interesting for systems containing Mn^{3+} ions like many perovskite based manganites. The orbital degeneracy and the interaction between the occupied e_g orbital and the O $2p$ orbitals results in phenomena like *orbital ordering*.

Double-exchange interaction

The CMR effect is usually observed in mixed valent manganites like $La_{1-x}Ca_xMnO_3$ ($0.2 < x < 0.4$) [29]. This composition shows metallic ferromagnetic behavior,

whereas the "parent compounds" $LaMnO_3$ (Mn 3+) and $CaMnO_3$ (Mn 4+) are antiferromagnetic insulators. Historically Zener, Anderson and Hasegawa, and de Gennes studied the relation between ferromagnetism and the metallic state [7, 30, 31]. Supposing neighboring Mn^{3+} ($t_{2g}^3\, e_g^1$ configuration) and Mn^{4+} ($t_{2g}^3\, e_g^0$ configuration) states. Following the Hund coupling the (itinerant) e_g electron located at the Mn^{3+} site may move to the empty e_g states of the Mn^{4+} ion, this interaction is ferromagnetic. Antiferromagnetic interaction is inhibited by the Hund coupling. Thus, ferromagnetism and metallic behavior occur cooperatively in CMR manganites.

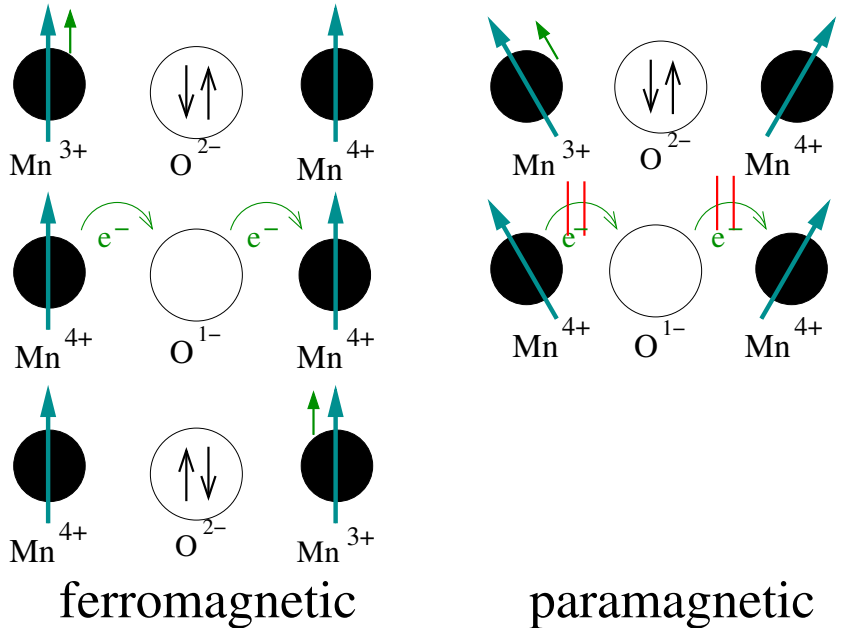

Figure 1.7: Schematic plot of the double-exchange interaction. Left panel: ferromagnetic spin structure, right panel: canted spin structure.

Considering the strong Hund coupling between the localized t_{2g} electrons and the itinerant e_g electron the hopping integral for an electron between neighboring sites $\langle ij \rangle$ is given by:

$$t_{ij} = t \cos \frac{\Theta_{ij}}{2} \tag{1.11}$$

Θ_{ij} denotes the orientation of the spin (of the e_g electron) at site i with respect to the (localized) spin of the t_{2g} electrons at site j. Note that the (ferromagnetic) electron hopping prefers $\Theta = 0$ whereas (antiferromagnetic) superexchange prefers $\Theta = \pi$ (Fig. 1.7). We then obtain the following Hamiltonian describing the double exchange:

$$H_{DE} = \sum_{\langle ij \rangle} t \cos \frac{\Theta_{ij}}{2} a_i^\dagger a_j - J_H \sum_i \mathbf{S}_i \cdot \mathbf{S}_j \tag{1.12}$$

De Gennes [31] proposed that for a small carrier concentration ($x \ll 1$) in $La_{1-x}Ca_xMnO_3$ a canted spin structure, like indicated in the right panel of Fig. 1.7, occurs.

1.3.4 Orbital Ordering and the Kugel-Khomskii model

As mentioned before, in the rare-earth perovskites $RMnO_3$ (R stands for a rare earth metal), the Mn^{3+} ion has the d^4 configuration. In octahedral symmetry, the d-levels split into three t_{2g} and two e_g levels. In the case of Mn^{3+} three t_{2g} electrons and one e_g electron is occupied ($t_{2g}^3 e_g^1$). According to the *Jahn-Teller theorem* a further lowering of the symmetry, induced by a (e.g. tetragonal) distortion of the crystal will lift the degeneracy of the e_g levels. In particular the most extensively studied perovsite, i.e. $LaMnO_3$ shows a *cooperative* Jahn-Teller distortion. This means that a *long range ordering* is established throughout the whole crystal. Under this conditions the cooperative Jahn-Teller phase is accompanied by a long range ordering of the orbital degree of freedom, i.e. the occupation of the energetically lower lying e_g orbital.

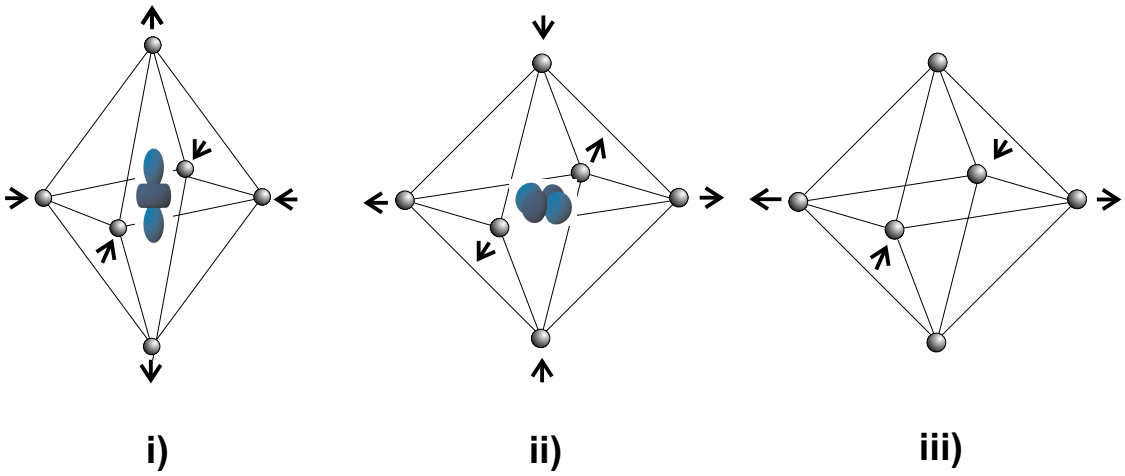

Figure 1.8: i) and ii): Q_3 distortion with the corresponding oxygen displacements to the filled $3z^2 - r^2$ and $x^2 - y^2$ orbitals, respectively; iii). The Q_2 distortion stabilizes in a certain superposition of $3z^2 - r^2$ and $x^2 - y^2$ orbitals.

This kind of collective ordering is often called *orbital ordering*. For $LaMnO_3$ a *rod-type* orbital ordering, the $3x^2 - r^2$ and $3y^2 - r^2$ orbitals are arranged in the **ab** plane of the crystal in an alternating way, has been proposed by theory [32] and experiment [33]. In perovskites there are two types of distortions associated with the Jahn-Teller effect. These are the so called Q_2 and Q_3 distortion (see Fig. 1.8). The Q_3 distortion represents a tetragonal elongation or contraction along the crystal **c**-axis, resulting in an elongated or contracted MnO_6 octahedron, respectively. In this case, either the $x^2 - y^2$ or the $3z^2 - r^2$ orbital will be filled preferentially. If a Q_2 distortion takes place, the elongation (contraction) of the **c**-axis is usually accompanied by the contraction (elongation) of the **a** or **b** axis, leading to an orthorombic distortion in the crystal. In this case a certain superposition of the $x^2 - y^2$ and the $3z^2 - r^2$ orbitals is obtained, resulting, e.g. in a rod-type or cross-type orbital ordering (Fig. 1.9)[2].

[2]Bernd J. Zimmermann is acknowledged for drawing Fig. 1.9

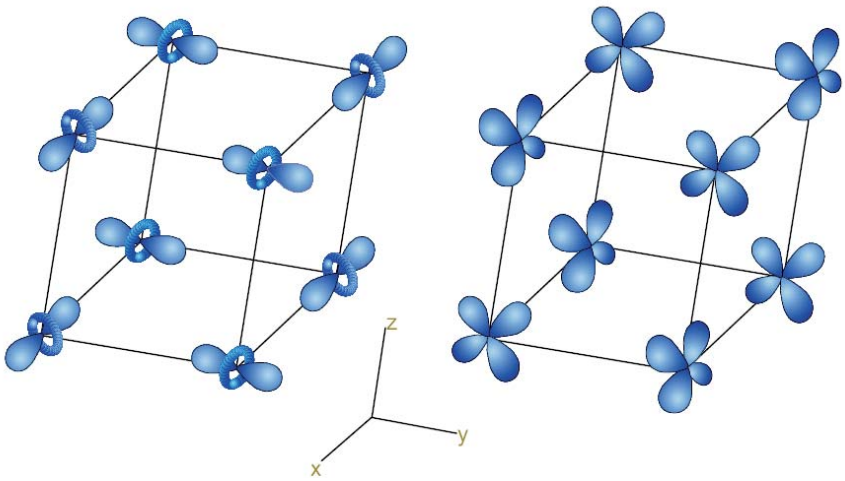

Figure 1.9: Schematic representation of rod-type (left panel) and cross-type (right panel) orbital ordering.

In $LaMnO_3$ the cooperative Jahn-Teller effect is dominated by a Q_2 distortion with alternating long and short Mn–O bond length in the **ab** plane of the crystal and a medium out of plane (apical)Mn–O bond length in **c** direction. The overall Jahn-Teller distortion of $LaMnO_3$ also comprises a Q_3 contribution: $LaMnO_3$ is found to be an *A–type* antiferromagnetic insulator (the ferromagnetic **ab** planes are antiferromagnetically coupled along the **c** axis) and has a distorted cubic perovskite structure: the octahedra are elongated and tilted, the d-type Jahn-Teller distortion (the elongated axes of the octahedra are parallel along the **c** axis) is accompanied by the $GdFeO_3$-type distortion, caused by the tilting of the MnO_6 octahedra.

One can analyze the type of orbital ordering within the framework of the crystal field theory, considering also the Jahn-Teller effect and the Coulomb exchange U_{dd} between the TM ions (this model is often called *exchange model* or *Kugel-Khomskii model*) [32]. On the Mn^{3+} sites of cubic manganite perovskites , e_g electrons of $3z^2-r^2$ type are preferentially occupied if the Mn-O bond is elongated along the z-direction; and e_g electrons of x^2-y^2 type are preferentially occupied if the Mn-O bond length is contracted along the z-direction. Following this model the Jahn-Teller distorted phase of $LaMnO_3$ is dominated a rod-type orbital ordering: thus the $3x^2-r^2$ and $3y^2-r^2$ orbitals are alternately arranged in a non-orthogonal way on two sublattices. However, since the Zaanen, Sawatzky and Allen model [6] (chapter 1.3.2) it is widely accepted that magnetic and orbital ordering in TM oxides are influenced not only by the usual exchange U_{dd} between two TM sites but also by the charge transfer from a ligand to a TM site, Δ. The Kugel-Khomskii model does not consider charge transfer. Very recently, Mostovoy and Khomskii, have renewed the theoretical discussion of the underlying mechanism of orbital ordering [34]. They find that the exchange (Kugel-Khomskii) model only describes Mott- Hubbard insulators correctly, since the model does not include the charge transfer energy between the TM d and the O p states. It is obvious that for systems, where $\Delta \sim U_d$ like in manganites it is not trivial if

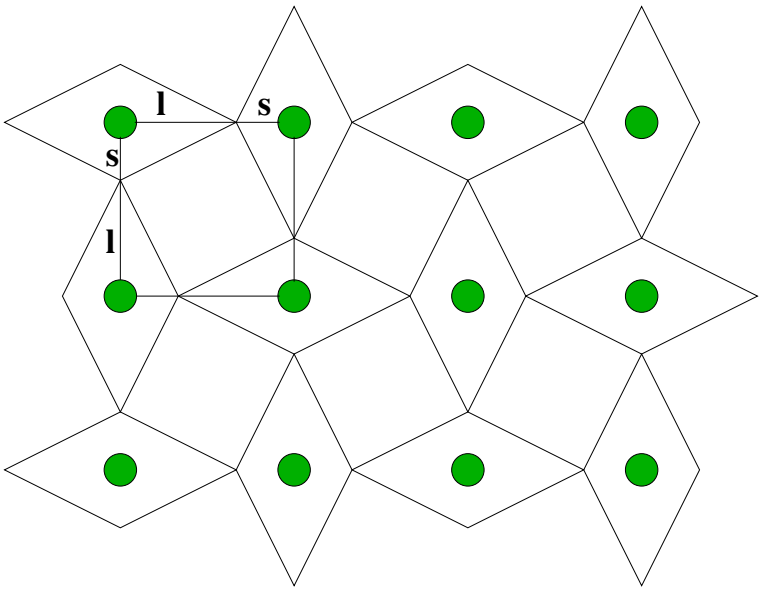

Figure 1.10: Schematic plot of the **ab** plane of $LaMnO_3$, the alternating long and short Mn-O distances are labelled l and s, respectively.

the charge transfer or the Coulomb interaction is dominant, and the type of orbital ordering is stabilized by a fine balance between these different exchange interactions.

The direct experimental investigation of orbital ordering is a very difficult task. Especially due to this fact most available techniques, as accurate crystal structure determination can only lead to an indirect probe of the orbital ordering. In particular Resonant X-ray Scattering (RXS) on the Mn K edge is dominated by the ($1s \rightarrow 4p$) dipole transition, and information about the orbital ordering of the $3d$ states can only be obtained by analyzing the interactions between Mn $3d$ and $4p$ electrons. Up to now even the interpretation of the origin of this interaction is controversial [35, 36]. X-ray linear dichroism, applied to the Mn L edge ($2p \rightarrow 3d$ transition) is a promising tool to investigate the type of orbital ordering much more directly, particularly in Jahn-Teller distorted manganites [37]. A more detailed introduction into XLD will be given in chapter 2.4.2.

Chapter 2

X-ray spectroscopic techniques

The experimental methods used in this work to investigate the electronic structure are reviewed in this chapter. The aim is to give a state of the art brief review on the employed techniques including theoretical and practical details. The issues which turned up to be relevant in the presented studies are emphasized.

2.1 Theoretical models

Actually, there is no unified theory available which can describe the intricate electronic and magnetic properties of transition metal compounds. There are basically two different approaches available. On the one hand side, the single particle, or band model is able to describe delocalized electron states, like for instance the total and partial densities of the valence band. Band-like properties ever arise from strong mixing and hybridization between the metal and the ligand orbitals in a solid.

On the other hand side this approach often fails to describe core excitations like the L edge NEXAFS spectra in transition metal oxides. For such spectra another kind of approach, the so called Cluster- or Multiplet models are often used successfully in order to describe the electronic structure in a localized picture. A typical example of more localized states is the Coulomb interaction between the $3d$ electrons in transition metal compounds, leading to a more ionic character of the compound in question. Therefore multiplets become important if a *direct* transition to a partly filled d band occurs. Therefore, spectra of transition metals based upon $2p \rightarrow 3d$ excitations are often dominated by multiplet effects whereas spectra of the much more delocalized ligand edges (i.e. the O $1s$ edge) are not or only weakly affected by multiplet effects.

At present it is not possible to describe a particular transition metal compound in question merely in the band- or the multiplet-picture. A fine balanced competition between different interactions, which lead either to a more localized or delocalized behavior of the electrons has to be considered in order to describe the electronic structure of these class of material properly.

2.1.1 Band models

The electronic band structure is usually derived using the density functional theory (DFT) developed by Hohenberg and Kohn [38]. The DFT employs the Born-Oppenheimer approximation, that means that the positions and atomic numbers of the nuclei are considered to be fixed (or frozen) in comparison to the much lighter electrons [39]. Within the DFT formalism one derives the eigenfunctions $\phi_i(\mathbf{r})$ by solving the Kohn-Sham equation [40]:

$$\left[-\frac{\hbar^2}{2m}\nabla_i^2 + V_{eff}(\mathbf{r})\right]\phi_i(\mathbf{r}) = \epsilon_i\phi_i(\mathbf{r}) \tag{2.1}$$

where V_{eff} represents the effective periodic potential of the crystal lattice, comprising the classical coulomb exchange potential, the coulomb exchange parameter due to an external potential (the ion lattice) V_{ext} and one external potential which can be understood as being due to exchange and correlation effects V_{xc},

$$V_{eff} = \frac{e^2}{4\pi\epsilon_0}\int d\mathbf{r}'\frac{\rho(\mathbf{r}')}{|\mathbf{r}-\mathbf{r}'|} + V_{ext}(\mathbf{r}) + V_{xc}(\mathbf{r}) \tag{2.2}$$

where the exchange and correlation term is is given by

$$V_{xc}(\mathbf{r}) = \frac{\delta V_{xc}(\mathbf{r})[\rho]}{\delta\rho} \tag{2.3}$$

Following the theorem of Kohn and Sham [40] the *exact* ground state density $\rho(\mathbf{r})$ of an N-electron system can be formulated as follows:

$$\rho(\mathbf{r}) = \sum i\phi_i(\mathbf{r})^*\phi_i(\mathbf{r}) \tag{2.4}$$

as stressed above, the Kohn-Sham theorem describes the electronic structure of a solid in question *exactly* except the Born-Oppenheimer approximation. However, there is a crucial point, the exchange-correlation potential V_{xc} is unknown. Further approximations have to be made at this point. There are several approximations that can be employed [41] in order to reduce the insoluble many–particle problem to a soluble one–electron equation, in the following we will present briefly some widely used approaches.

The Hartree–Fock (HF) approximation:

A historically and well established approximation is the Hartree–Fock (HF) approximation, the HF exchange term can be written as follows:

$$V_H(\mathbf{r})\phi_i(\mathbf{r},\mathbf{r}') = \sum_i\int d\mathbf{r}'\rho'_{HF}(\mathbf{r},\mathbf{r}')\frac{e^2}{|\mathbf{r}-\mathbf{r}'|} \tag{2.5}$$

where

$$\rho'_{HF}(\mathbf{r},\mathbf{r}') = \frac{\phi_i^*(\mathbf{r})\phi_i(\mathbf{r}')\sum_{i'}\phi_{i'}^*(\mathbf{r}')\phi_{i'}(\mathbf{r})}{|\phi_i(\mathbf{r})|^2} \tag{2.6}$$

One difficulty of the Hartree–Fock formalism is that the exchange potential V_{HF} depends on the solution $\phi_i(\mathbf{r})$ itself. The correlation interaction between the electron with different spins is not considered, therefore different ways to take into account correlation effects have to be considered. In general, HF overestimates the band gap essentially.

The local (spin) density of states approximation (LSDA):

In this approximation the exchange–correlation potential $V_{LDA}(r)$ in Eq. 2.7 is approximated by a homogeneous electron gas with the density $n(\mathbf{r})$:

$$V_{LDA}(\mathbf{r}) = \int d(\mathbf{r}')\rho_{xc}(\mathbf{r},\mathbf{r}')|\frac{e^2}{|\mathbf{r}-\mathbf{r}'|} \tag{2.7}$$

$$n(\mathbf{r}) = \sum_l |\phi_i(\mathbf{r})|^2 \tag{2.8}$$

In order to make possible the calculation of spin–density waves or antiferromagnetic states, the local spin–density approximation has been developed (LSDA) [41]. Here, one introduces the spin–dependent electron densities, $\mathrm{n}_\uparrow(\mathbf{r})$ and $\mathrm{n}_\downarrow(\mathbf{r})$, so that the exchange correlation energy (Eq. 2.9) is replaced by (Eq. 2.10):

$$\int dr V_{LDA}(\mathbf{r})n(\mathbf{r}) \tag{2.9}$$

$$\int d\mathbf{r}[n_\uparrow(\mathbf{r}) + n_\downarrow(\mathbf{r})]V_{LDA}[n_\uparrow(\mathbf{r}), n_\downarrow(\mathbf{r})] \tag{2.10}$$

An essential problem of the LSDA scheme is that it calculates all $3d$ transition metal monoxides to be metallic, in contrast to the experimental results. In general, LSDA calculates a too small gap for a lot of transition metal compounds, since it does not consider the on site correlation effects between the $3d$ TM electrons, hence the bonding strength between the TM $3d$ and the ligand states is overestimated.

During the last few years several approaches have been undertaken in order to overcome the limitations of the LDA scheme. For instance, within the generalized gradient approximation (GGA) V_{LDA} is replaced by a potential depending also on the gradient of the corresponding electron density (∇n) [42]. A number of different alternative formulations of the exchange correlation potential within the GGA exist, e.g. the widely used formulation of Perdew-Wang [43].

Another possibility to consider the correlation effects is the inclusion of U_{dd} into the LDA Hamiltonian, with good results for many TM compounds [44, 45],

$$V_{LDA+U}(\mathbf{r}) = V_{LDA}(\mathbf{r}) + U\sum_{m'}(n_{m'-\sigma} - n^0) + (U-J)\sum_{m'}(n_{m'-\sigma} - n^0) \tag{2.11}$$

The difficulty of this approach is related to the way of choosing U. One possibility is to calculate the value of U first with LDA and then to include it into a LDA + U calculation. However, it is not certain if this value of U represents the "correct" correlation strength. Therefore the comparison with corresponding experimental results is very important.

The (linear) augmented plane wave (LAPW) method:

In order to solve the Kohn-Sham equations for a *real* system one has to introduce a basis set of wavefunctions which reduces the infinite set of one electron equations into a (*efficient*) solvable set of equations but does not carry too much properties from the basis function (*unbiased*), what would lead to a poor approximation of the eigenfunctions.

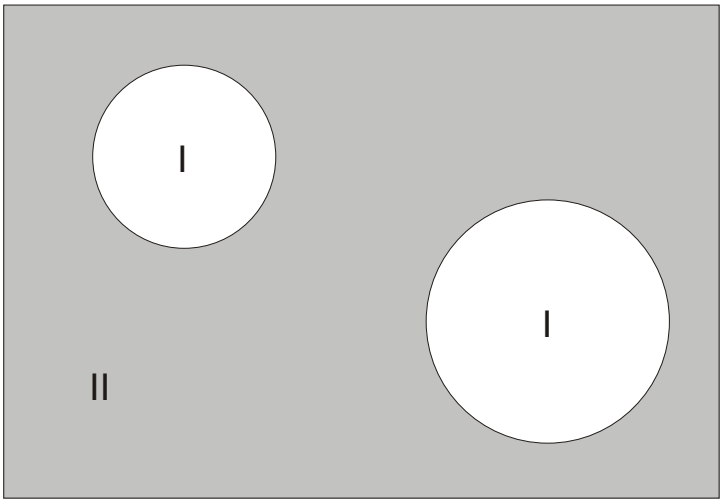

Figure 2.1: Partitioning of the unit cell in muffin tin regions (I) and the interstitial region (II), in case of two inequivalent atoms.

A number of different realizations are available, such as the use of spherical waves, fixed basis sets like the linear combination of atoms (LCAO) or linearized versions, such as linearized muffin tin orbitals and linearized augmented plane waves (LAPW). The LAPW formalism is known to be among the most accurate methods in order to calculate the electronic structure of crystals. Since a lot of results in this thesis are compared with band structure calculations using LAPW a brief overview is following.

The LAPW adaption is achieved by dividing the space into two different regions (Fig. 2.1). Around each atom a sphere (*muffin tin sphere*) is drawn, then the part occupied by the spheres is often called *muffin tin region (I)*. The empty space outside the spheres is defined as *interstitial region (II)*. Inside the spheres a *linear combination* of radial functions times the spherical harmonics Y_m^l is applied whereas one describes the interstitial region with help of a plane wave expansion. The Kohn-Sham equations can then be solved by expansion with the LAPW basis set. A very detailed description of the LAPW method has been written by Shingh [46]. The LAPW method is used within the WIEN2k computer package [47].

2.1.2 Short range models

Hubbard and Anderson impurity models:

In transition metal compounds it costs energy to transfer an electron from one metal atom to another: The two electrons repel each other due to the strong two-electron $3d$ Coulomb integrals (U_{dd}), comparable to the strength of the electron band width. In the case of $2p$ XPS or XAS core level spectra (L edges) the single particle approximation breaks down due to the strong overlap of $2p$ core wave functions and the $3d$ valence wave functions. The $2p$ core level spectra of transition metal oxides are often dominated by these *multiplet effects*, and therefore the spectra do not reflect the density of states. The $2p$ core level spectra of these correlated systems can be better described by so called Hubbard models [22, 26, 48]. This kind of model is based upon the approximation that all repulsions between electrons can be neglected, except they are localized on the *same* atomic site. The electron correaltion strength is expressed by the on site Coulomb interaction U_{dd}. Hubbard models usually consist only of the TM $3d$ and the O $2p$ states.

The so called single Anderson impurity model [24] goes beyond this point by including interactions around one specific metallic site of the compound in question. It comprises the U_{dd}, the energy positions of the localized and delocalized states ϵ_d and ϵ_p, as well as the hopping terms t_{pd} and t_{pp} [49, 50]. The model may be subject to further extensions. The single Anderson impurity model and related models are important in order to achieve a proper description of XPS and XAS core level spectra of transition metal compounds. Recently this kind of model has been also successfully applied to resonant inelastic x-ray scattering of $4f$ systems [51]. For $3d$ systems the situation is more difficult due to the strong hybridization strength between the TM and the O sites, also the single metal-ion approximation may break down. There the Anderson impurity model is often not so applicable as it is for the description of XAS or XPS core level spectra [51].

The TML_6 cluster model:

Different realizations of the single Anderson impurity model are known [52, 53]. For transition metal compounds the single transition metal site TML_6 (TM = transition metal ion, L = ligand ions) cluster model, also called crystal field multiplet model (CFM), has been proven be very useful [54, 55]. It is furthermore based upon to the crystal field theory introduced in Chapter 1.

The basic starting point to calculate core-level spectra within the *ligand field model* (LFM) is the atomic multiplet theory [56]. Dipole transitions from the ground state can only reach a limited subset of final states, thereby providing a fingerprint for the specific ground state. The atomic Hamiltonian is given by:

$$\begin{aligned} H_{atom} = \frac{1}{2} \sum_{\nu_1,\nu_2,\nu_3,\nu_4} g_{\nu\nu}(\nu_1,\nu_2,\nu_3,\nu_4) a^\dagger_{\nu_1} a^\dagger_{\nu_2} a_{\nu_3} a_{\nu_4} \\ + \sum_{\nu_1,\nu_2,c_1,c_2} g_{\nu\nu}(\nu_1,c_1,c_2,\nu_2) a^\dagger_{\nu_1} a^\dagger_{c_1} a_{c_2} a_{\nu_2} \\ + \sum_{\nu_1,\nu_2} \xi(\nu_1,\nu_2) a^\dagger_{\nu_1} a_{\nu_2} + \sum_{c_1,c_2} \xi(c_1,c_2) a^\dagger_{c_1} a_{c_2} \end{aligned} \tag{2.12}$$

Here, ν and c denote the valence states and the core states, respectively. ξ is the spin-orbit interaction, $g_{\nu\nu}$ the multipole Coulomb interaction between the valence states and finally $g_{\nu c}$ is the multipole Coulomb and exchange interaction valence and core states. Atomic multiplet theory has, e.g. been used to calculate the Mn $2p$ XAS spectra of dilute manganese in silver, which unambiguously displays the atomic Hund rule $3d^5$ ground state [57].

In the CFM an additional term which is due to the crystal field strength is added to the atomic Hamiltonian,

$$H_{crystalfield} = \sum_{\nu_1,\nu_2} D_{\nu_{1,2}} a^\dagger_{\nu_1} a_{\nu_2} \tag{2.13}$$

where $D_{\nu_{1,2}}$ is the electrostatic field coupling the atomic representations within the point group symmetry of the system. It shall be noted that the code developed by B. T. Thole, G. van der Laan and P. H. Butler is allowing calculations in any point group [58]. In particular important for transition metal compounds is the octahedral (O_h) and the tetragonal distorted octahedral symmetry (D_{4h}) (see Chapter 1.3). The $2p$ XAS of a lot of $3d$ transition metal compounds have been found to be in excellent agreement with the corresponding crystal field theory [59]. This approach is particulary successful for ionic compounds.

Charge transfer multiplet theory:

As mentioned before the late transition metal compound are often dominated by hybidization or charge transfer effects between the metal and the ligand states. Therefore the combination of the crystal field multiplet theory and the impurity Anderson model is a very important step in the understanding of core level spectra of late transition metal oxides. The corresponding Hamiltonian is given by:

$$\begin{aligned} H_{IAM} = \sum_{k,\nu} \epsilon_k a^\dagger_{k,\nu} a_{k\nu} + \epsilon_\nu \sum_\nu a^\dagger_\nu a_\nu + \sum_c a^\dagger_c a_c + \frac{V}{\sqrt{N}} \sum_{k,\nu} (a^\dagger_\nu a_{k\nu} + a^\dagger_{k\nu} a_\nu) \\ + U_{\nu\nu} \sum_{\nu>\nu'} a^\dagger_\nu a_\nu a^\dagger_{\nu'} a_{\nu'} - U_{\nu c} \sum_{\nu,c} a^\dagger_\nu a_\nu (1 - a^\dagger_c a_c) \end{aligned} \tag{2.14}$$

Here, the summations over ν and c represent the summation over the spin and orbital quantum numbers. The ligand band (ϵ_k), the valence level (ϵ_ν) and the core level (ϵ_c) interact with each other via the valence level-ligand hybridization (V), the Coulomb interaction between valence electrons ($U_{\nu\nu}$) and the core-hole potential ($U_{\nu c}$).

The impurity Anderson model, or *charge transfer multiplet model* has been successfully applied to a number of late transition metal compounds like NiO and $NaCuO_2$ [60, 61].

2.2 General overview: X-ray spectroscopies

Nowadays spectroscopic techniques, based upon the interaction of light with matter, are widely used in order to probe the electronic structure of all kinds of atoms, molecules and solid compounds. Since it is possible to obtain information about the chemical and physical properties of the sample in question it is clear that x-ray spectroscopic techniques belong to the most powerful tools in modern physics and chemistry. One may separate the electrons into two "classes". The valence electrons, energetically located close to the Fermi level are responsible for the chemical bonding between the atoms of a molecule or crystal, and their spatial and energetic distribution to the occupied and unoccupied states are closely related to the properties of the compound in question. The core level electrons are spatially localized at a specific atom and hence energetically well separated from each other. Nonetheless the x-ray spectra of core level states can contain important information about the chemical environment of the specific atom, i.e. the valence state of the corresponding ion.

In general, x-ray spectroscopic techniques may be divided into two types, the one which are described by an one-step process, i.e. x-ray photoelectron spectroscopy (XPS), ultra-violet photoelectron spectroscopy (UPS) and x-ray absorption spectroscopy (XAS). Usually the excitation of an electron is followed by decay processes. Two-step spectroscopies are Auger electron emission or x-ray emission spectroscopy (XES). The electronic transitions between core and valence levels often fall into the so called soft x-ray region (between 20 eV and 2000 eV), hence radiation covering this range is extremely useful for various electronic structure studies.

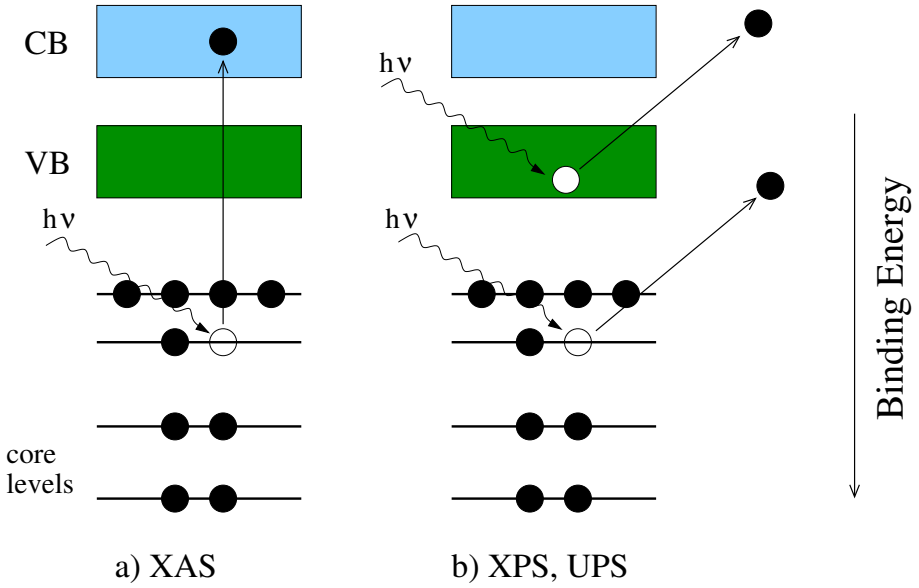

Figure 2.2: Schematic illustration of a) x-ray absorption spectroscopy (XAS) and b) x-ray / ultraviolet photoelectron spectroscopy (XPS, UPS).

Fig. 2.2 illustrates the mentioned x-ray spectroscopic techniques based upon one-step processes. In x-ray absorption spectroscopy (XAS) one measures the absorptivity of a material as a function of incident x-ray energy $h\nu$ [55]. As a result a core electron

is promoted to an empty state just above the Fermi level. The atomic like behavior of core holes makes XAS as powerful element sensitive technique. A knowledge of the nature of the core level as well as the matrix element for the transition will reveal information of the unoccupied density of states of the material. The dipole selection rule for photon-excited transitions states that the change in the angular momentum quantum number (ΔL) is ± 1, while the spin is not changed. For ligand spectra like those from the oxygen $1s$ edge ($L = 0$) this means that only oxygen p character ($L = 1$) can be reached. To first order, we can therefore view the resulting O $1s$ XAS spectrum as an image of the oxygen p projected unoccupied density of states. However, for the transition metal $2p$ edges multiplet effects are often dominating the spectrum, and thus these do not represent the projected unoccupied DOS.

X-ray absorption measurements performed in the electron-yield mode typically have a surface sensitivity of approximately 100 Å, so surface issues are not nearly as important as they are in photoemission.

Today the technique of x-ray photoelectron spectroscopy (XPS) is very important and widely used to probe the occupied electronic density of states. Historically the experiment is based upon the *photoelectric effect*, which was discovered in 1887 by Hertz and Hallwachs [62, 63]. In the following years Thomsons experiments led to the discovery of the electron before in 1905 A. Einstein formulated the quantum hypothesis for electromagnetic radiation [64]. For this discovery he won the Nobel Prize in Physics in 1921. Later, between 1960 and 1980 K. Siegbahn *et al.* developed a new type of spectrometer which was able to resolve electron binding energies of elements and their shifts [65]. Since core level XPS is sensitive to the chemical environment, this technique is sometimes also called *ESCA* (Electron Spectroscopy for Chemical Analysis). In 1986 K. Siegbahn was awarded with the Nobel Price in Physics for his work. Dependent wether one uses ultra violet or x-ray radiation as excitation source the technique is named ultra violet photoelectron spectroscopy (UPS) or x-ray photoelectron spectroscopy (XPS). UPS or XPS are able to probe the distribution of the occupied densities of states, hence photoelectron spectroscopy is a complementary technique with respect to XAS. The above mentioned techniques are all based upon a one-step, or first order optical process referring to the fact that first order perturbation theory is a suitable approach in order to describe their properties.

However, after a core hole is created the *excited core state* will decay rapidly by a transition of an electron from higher lying shells into the core hole on the femtosecond time scale. This recombination may be either a non-radiative Auger electron decay resulting in the emission of an Auger electron or a x-ray photon is emitted (fluorescence). This decay mechanisms are schematically plotted in Figs. 2.3 and 2.4.

In case of an Auger electron decay the core hole is filled by ejection of another electron from a higher energy state [66]. The description of this process follows the nomenclature XYZ. Here X refers to to the core hole's shell, Y stands for the shell from which the electron decay starts and Z labels the shell from where the Auger electron is emitted. In Auger spectroscopy, the X, Y and Z are usually named K for the $1s$ levels, L_I, L_{II} and L_{III} for $2s$, $2p_{1/2}$ and $2p_{3/2}$, M_I, M_{II}, M_{III}, M_{IV} and M_V for $3s$, $3p_{1/2}$, $3p_{3/2}$, $3d_{3/2}$ and $3d_{5/2}$, respectively. For example, the $KL_{II}L_{III}$ line corresponds to the case when a hole from the $1s$ shell is filled by an electron from the

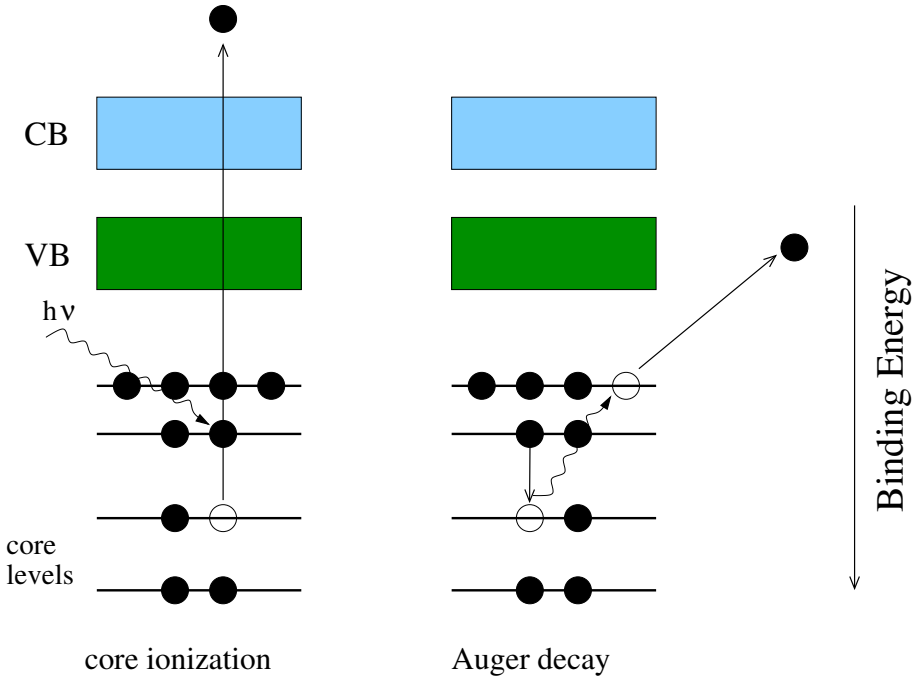

Figure 2.3: Schematic illustration of the core hole ionization process (left panel), followed by the Auger decay (right panel).

$2p_{1/2}$ shell and the resulting energy is taken by an electron from the $2p_{3/2}$ shell, which is emitted as Auger electron. A special case is if the initial and final hole states are on the same shell, but in different orbitals (for example, $L_I L_{III} M_I$), then the process is of so called *Coster–Kronig* type [67]. One can easily distinguish between electrons resulting wether from the XPS process or either from an Auger electron decay by using different excitation energies. The XPS lines will appear at the same binding energy whereas the Auger lines will occur shifted by $|h\nu_1 - h\nu_2|$.

For lighter elements the Auger electron decay is usually dominating by factor 100-1000 over the fluorescence decay in the soft x-ray region [68], which is nowadays mostly named (soft) x-ray emission spectroscopy (XES) [69]. Thus XES, which probes the energy distribution of photons emitted by the compound in question, was for a long time limited to the high energy range (several keV), where strong electron sources are used as excitation source. However, during the last 10-15 years the availability of synchrotron radiation sources delivering monochromatized photons in the soft x-ray range with a very high intensity and brilliance changed the situation, and XES in the soft x-ray range is becoming a more and more important technique to probe the projected partial occupied densities of states (PDOS). When the excitation energy is far above the corresponding ionization (absorption) threshold the decay process is also denoted as *normal x-ray emission spectroscopy* (NXES). In this case NXES can be understood as being a two-step process, independent from the energy of the incident photon. The overall decay process can be described as spontaneous x-ray emission in a dipole transition between two electronic states.

The possibility of tuning the monochromatized synchrotron radiation below or

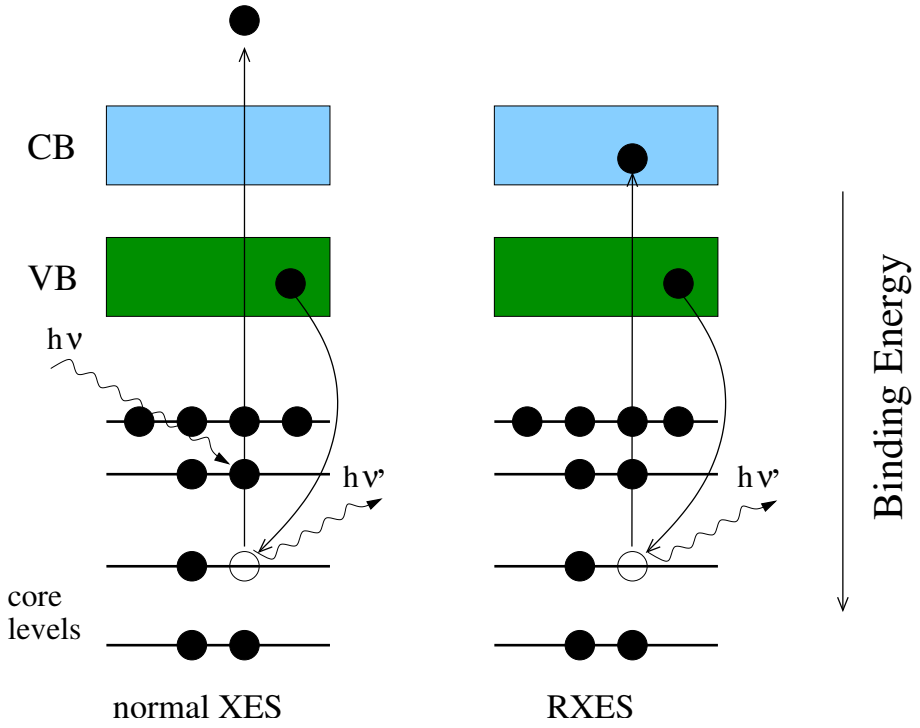

Figure 2.4: Schematic illustration of normal x-ray emission spectroscopy (NXES) (left panel) and resonant x-ray emission spectroscopy (RXES) (right panel).

close to an absorption threshold enables to perform *resonant x-ray emission spectroscopy* (RXES) [51]. During resonant excitation an electron is promoted from a core state to an unoccupied state located at (or just above) the Fermi energy (see Fig. 2.4). In contrast to XPS, RXES is a charge neutral technique, the number of electrons in the ground and the final state is the same for the excited atomic site. Furthermore, XES and RXES are rather bulk sensitive, x-ray emission probes the sample to depths of tens or hundreds of nm. The intermediate state in RXES corresponds to the final state of XAS. For a proper description RXES must be treated as a coherent absorption-emission one-step process. In this context RXES is also called *resonant inelastic x-ray scattering*. The emission features can be then understood as being due to coherent (*resonant elastic x-ray scattering* (REXS)) and inelastic "RIXS-loss features" which can be associated with the difference in energy between initial and final state. The RIXS cross section is described by the Kramers-Heisenberg equation [70, 71]. The possibilities in the study of correlated systems by means of RIXS go from Coulomb interactions on high energy scales over charge transfer excitations to lower excitation energies, especially regarding optically inaccessible bands, such as *dd* transitions [72, 73, 74].

2.3 X-ray Photoelectron Spectroscopy (XPS)

In Fig. 2.5 the principle of the photoelectron spectroscopy (PES) experiment is plotted. For a free atom or molecule the maximum kinetic energy of the photoelectron is given by

$$E_{kin,max} = h\nu - \Phi \tag{2.15}$$

where $h\nu$ denotes the energy of the exciting photon and Φ the work function of the solid, respectively.

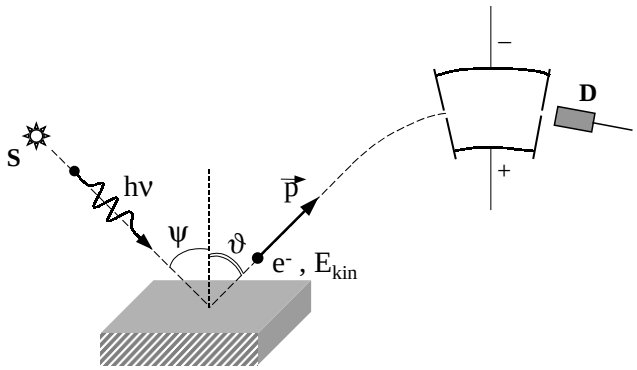

Figure 2.5: The basic principle of a photoemission experiment (adapted from [25, 67]).

Equation 2.15 describes the photomession process for valence electrons located energetically close or at the Fermi energy E_F. If core level electrons are emitted the binding energy of these electrons has to be taken into account,

$$E_{kin,max} = h\nu - E_{B,eff} - \Phi \tag{2.16}$$

here $E_{B,eff}$ is the effective binding energy of the emitted electron. The work function is a characteristic for the material. Since the reference of the binding energy is by definition the Fermi energy E_F the spectra must be calibrated by Φ. For conductive materials the work function of the material corresponds to that of the spectrometer (Φ_{spec}), which is known.

The binding energy for a conductive sample can then described by the following equation:

$$E_B^F = h\nu - E_{kin} - \Phi_{spec} \tag{2.17}$$

Knowledge about the binding energy is a crucial point in photoelectron spectroscopy since it is material specific.

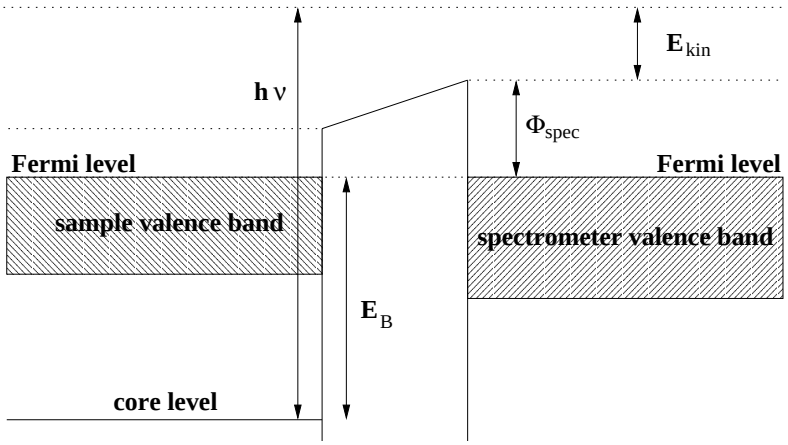

Figure 2.6: Energy level diagram for a PES experiment with a conductive sample [75].

2.3.1 Theoretical approaches to the photoemission process

A precise description of the photoemission process requires a full quantum mechanical approach. A system comprising N electrons can be described by two wave functions Ψ_i and Ψ_f, corresponding to the initial and final state, before and after the emission of an electron, respectively. The transition probability (which is dominating the photocurrent intensity) fulfills Fermi's Golden rule, by assuming that the perturbation H^* to the $N-1$ electron system in the final state is small,

$$\omega \sim \mid \langle \Psi_f \mid H^* \mid \Psi_i \rangle \mid^2 \delta(E_f - E_i - h\upsilon) \tag{2.18}$$

where the δ function ensures energy conservation. The interaction Hamiltonian H^* can be expressed by the following equation.

$$H^* = \frac{e}{2mc}(\mathbf{A}\cdot\mathbf{P} + \mathbf{A}\cdot\mathbf{P}) - e\Phi + \frac{e^2}{2mc^2}|\mathbf{A}|^2 \tag{2.19}$$

Here e and m refer to the charge and the mass of the electron, c denotes the speed of light, $\mathbf{A}$ and Φ are the vector and the scalar potential of the incident radiation, finally $\mathbf{P}$ is the momentum operator. A more simple form of equation 2.19 can be obtained by neglecting the two-phonon process (the $|\mathbf{A}|^2$ term) and by assuming the radiation wave length $\gg$ atomic distances. The vector potential can then be expressed $\mathbf{A}(\mathbf{r},t) = \mathbf{A}_0 \exp(\mathbf{kr} - \omega t)$ [76].

For high energy spectroscopy it may be assumed that the photoelectron is so fast that there is only negligible interaction between the emitted electron with the remaining $(N-1)$ electron system [76]. This so called *sudden approximation* splits the final state into two configurations:

$$\Psi_i(N); E_i(N) \rightarrow \Psi_f^k(N-1); E_f^k(N-1) \; + \; \xi^k(1); E_{kin}^k. \tag{2.20}$$

Here $\xi^k(1)$ denotes the wave function of the emitted photoelectron. The binding energy is then given by

$$E_B^k = E_f^k(N-1) - E_i(N). \tag{2.21}$$

In the *frozen–orbital approximation* the orbitals are assumed to be unmodified during the photoemission process and the binding energy in equation 2.21 can be calculated from Hartree–Fock wave functions for the initial and the final state (Koopman's theorem: "*for a closed shell molecule the ionization potential of an electron in a particular orbital is approximately equal to the negative of the orbital energy calculated by an SCF* (self–consistent field) *ab initio method*") [77]. The binding energy is then given by the negative one-electron energy of the orbital from which the electron has been expelled by the photoemission process:

$$E_B^k \simeq \epsilon^k \tag{2.22}$$

This approximation does not take into account some important effects, since after photoemission the orbitals in the excited system will be different as compared to the inital state. There is an intra–atomic relaxation related to the reorganization of the orbitals in the same atom and, additional, an extra–atomic relaxation connected with the charge flow from the crystal to the ion where the hole was created during photoemission [25]. Hence, additional to the orbital energy in 2.22 one has to take into account the relaxation (reorganization) energy (E_{relax}). The correlation effects, which are related to the fact that the electrons motions are not independent, but correlated (E_{corr}).

2.3.1.1 Three–step model

In this model, based upon the ideas of Berglund and Spicer [78], the photoelectron process is considered as consisting of three separate steps:

1. The local absorption of the photon and the photo–excitation of the electron;

2. The propagation of the electron through the sample to the surface. Some of the excited photoelectrons suffer energy losses during the transport through the surface; for high energies these scattering process is dictated by electron–electron interaction, whereas low energies lead to dominating electron-phonon interaction. A very important parameter is the *inelastic mean free path* λ, which reflects the mean distance between two inelastic impacts of the electron propagating through the crystal [79]:

$$\lambda(E) = \frac{E}{E_{plas}^2 \beta \ln(\gamma E)} \tag{2.23}$$

   Here E denotes the electron energy, E_{plas} is the plasmon energy of a free electron gas, finally β and γ are parameters. In the soft x-ray energy range ($\sim$ 100 – 1000 eV) the mean free path may be approximated by $\lambda \propto E^p$, p ranging from 0.6 to 0.8 [80].

3. The penetration of the photoelectron through the surface and emission into the vacuum of those electrons whose kinetic energy normal to the surface is high enough to overcome the potential barrier. The other electrons are reflected back.

2.3.1.2 One–step models

The three step model is very descriptive and illustrative, however it turned out not to be a useful approach for computational simulation of PES spectra. Here the so called *one step models*, which consider the whole photoemission process as a single step, are heavily used. Different models have been developed, one of the most recent approaches is a relativistic one–step theory [76]. If one uses characteristic crystal potentials as input data one-step models are an appropriate tool for the simulation of XPS spectra [81].

2.3.2 Spectral characteristics

For PES, the spectroscopic notation of a state is usually given by nl_j, where n and l are the principal and orbital quantum numbers and $j = l \pm s$ ($s = 1/2$). For a given principal quantum number, l can have n values: 0, 1, 2, 3,... $(n-1)$ and the corresponding levels are denoted as *s, p, d, f,...,* respectively.

2.3.2.1 Valence band spectra

XPS is well known to be a powerful probe of the occupied density of states (DOS). This region is usually denoted as *valence band*, located between 0–20 eV binding energy. Since the valence electrons are involved in the chemical bonding of the solid they are usually delocalized, thus the valence band comprises a superposition of the occupied states of all elements involved. One possibility to analyze the valence band is the comparison with first principles DOS calculations. Another, or complementary approach is the comparison with site sensitive XES spectra, reflecting the corresponding partial DOS. In this case certain features in the XPS valence band can be directly assigned to elemental components.

2.3.2.2 Core–level spectra

In contrast to the valence band the core level spectra (> 20 eV) appear as sharp and intensive lines in the XPS spectrum. These spectra are mostly energetically well separated and allow a fast identification of the chemical components. The line width is defined as the full width at half maximum and is a convolution of three distinct contributions [82]; the natural line width of the core level γ_n, the line width of the excitation source γ_e and the analyzer resolution γ_a.
The overall FWHM is given by:

$$\gamma = \sqrt{\gamma_n^2 + \gamma_e^2 + \gamma_a^2} \tag{2.24}$$

The natural line width is dominated by the uncertainty principle $\Delta E \Delta t \geq h$. With h as the Planck constant τ representing the core hole lifetime the natural width can be determined, $\gamma_n = h/\tau$. Typical core hole lifetimes vary in the range of $10^{-14} - 10^{-16}$ seconds.

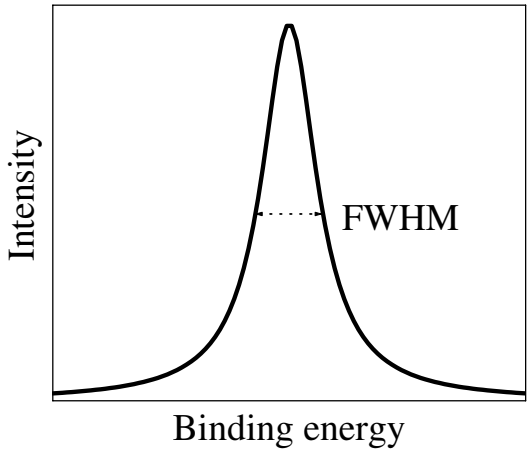

Figure 2.7: Illustration of an XPS core level line [75].

For metals, the lines show often a rather pronounced tail (asymmetry) to higher binding energies, what can be explained by screening effects produced by the conduction electrons. This so called *Doniach–Sunjic line shape* [83] is given by:

$$I(E-E_0) = \frac{\Gamma(1-\alpha)\cos[\pi\alpha/2 + (1-\alpha)\arctan(E-E_0)/\gamma]}{[(E-E_0)^2+\gamma^2]^{(1-\alpha)/2}} \tag{2.25}$$

Here E_0 denotes the center of the energy distribution curve for the core line, Γ is the Γ function, α and γ are parameters.

Background correction

Due to the inelastic scattering only photoelectrons from the very surface layers of a solid are emitted without perturbation, others may lose a part of their energy and end up at a lower kinetic energy in the spectrum, giving rise to a *background*, also called *secondary spectrum*. For quantitative analysis of the XPS spectra, the true peak areas and their shapes need to be determined. In a very simple analysis one may subtract a linear background. Another very common background correction was proposed by Shirley [84]; a Shirley background eliminates contributions to the data from the scattering of low-energy electrons. A right-to-left integration between the two endpoints of the spectrum in question is performed, generating an integrated background curve. This new curve is then adjusted so that the amplitude of each endpoint corresponds to the amplitude of the corresponding data points in the original curve.

In the Tougaard algorithmn the measured spectra $j(E)$ is considered to consist of the photoelectron spectra $F(E)$ and the background [85]:

$$j(E) = F(E) + \lambda(E)\int_E^\infty K(E, E-E')j(E)dE' \tag{2.26}$$

Here $K(E, E-E')$ denotes the probability that an electron with the energy E loses the energy $(E-E')$ during a mean free path travel. The loss function $\lambda(E)K(E, E-E')$ can be described for many materials with a reasonable approximation by

$$\lambda(E)K(E, E-E') \simeq \frac{B(E-E')}{[C+(E-E')^2]^2} \tag{2.27}$$

This loss function using the parameters B=2886 eV^2 and C=1643 eV^2 leads to a good agreement for spectra of metals like Ag, Au or Cu. Also for transition metal oxides a satisfactory description of the background is achieved. However, for Si and a number of insulating compounds the Tougaard approximation fails since the influence of the band gap is not sufficiently considered [86].

2.3.2.3 Chemical shift

The core level binding energy may be strongly dependent on the oxidation state (up to several eV), this effect is called *chemical shift*. The sensitivity of XPS to different chemical environments is another important and valuable feature of this technique. The chemical shift is a result of a change in the Coulomb and exchange potential dependent on the chemical environment. For instance, a Fe 2p electron in Fe metal feels a weaker Coulomb interaction with the nucleus than a Fe 2p electron in FeO. Thus, in FeO the bonding of the Fe 2p electron is stronger than in the Fe metal, resulting in a higher binding energy (Fig. 2.8).

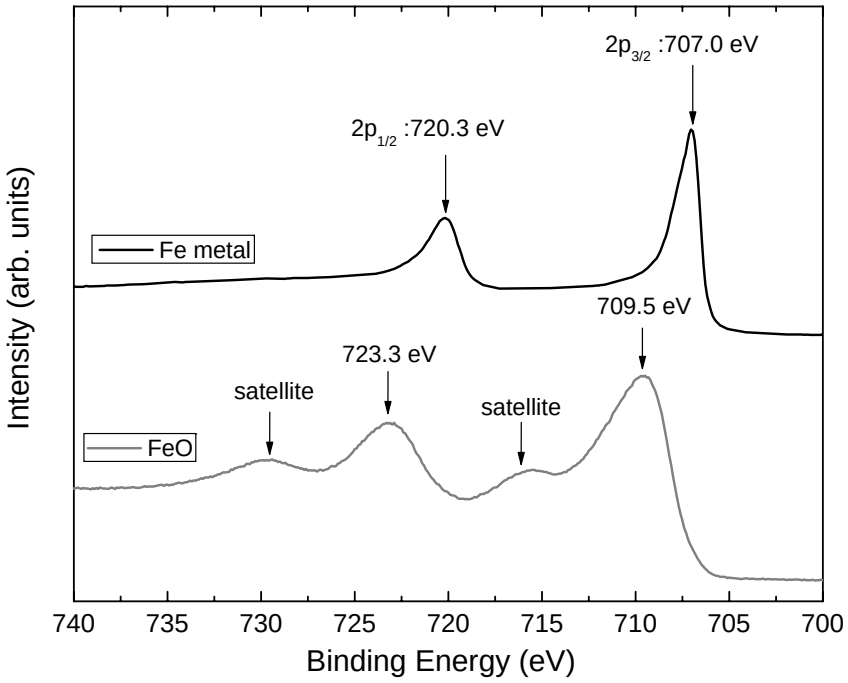

Figure 2.8: Example for a chemical shift of the Fe 2p XPS core level lines of FeO. The spin-orbit coupling and satellites will be explained in Sections 2.3.2.4 and 2.3.2.5.

The chemical shift can be understood in the framework of the *charge potential model*, where a core hole binding energy is considered to depend on the potentials created by the valence electrons of the corresponding atom and also depends on the potential created by the electrons of the surrounding atom [87]. In principle one has to extend Eq. 2.17:

$$E_{B,eff} = E_B(atom) + \Delta(E_{chem} + E_{Mad}) \tag{2.28}$$

Here $\Delta E_{chem} = Kq_A$ denotes the chemical shift which is connected to the potentials created by the valence electrons of the corresponding atom. K stands for interaction between the valence and the core electrons, q_A refers to the shift relative to a reference state. ΔE_{Mad} denotes the Madelung term and sums up the influence of all potentials created by the other atoms of the molecule or solid. The overall chemical shift is then given by,

$$E_{B,eff} = E_B(atom) + Kq_A \sum_{B \neq A} (\frac{q_B}{R_{AB}}) \tag{2.29}$$

where the last term sums the potential at atom A due to the surrounding atoms B. It shall be noted that this is a purely electrostatic model with an empirical parameter K.

The chemical shift can theoretically be simulated by alternative approaches. Core level spectra can be simulated by applying self consistent calculations based upon the non-relativistic Hartree-Fock formalism or the relativistic Dirac-Fock-formalism [81]. In particular for transition metals core level spectra multiplet effects are often dominating the spectrum. Then the usage of a short range model is necessary to obtain a suitable simulation of the spectrum.

2.3.2.4 Spin–orbit coupling

Except the lines from s levels, XPS core level lines are doublets. The doublet character of the core lines arises through the spin–orbit $(j-j)$ coupling. In the $j-j$ coupling, the total angular momentum of one electron (j) is given by the sum of the electronic spin and angular momenta $(j = l + s)$, two possible energy levels for the electrons are possible: $j = l + s$ and $j = l - s$. Therefore, except for s levels $(l = 0)$, for each state (nl) there will be a double-line (doublet) in the XPS spectrum: $nl_{l+1/2}$ and $nl_{l-1/2}$, respectively, of which relative intensities are given by:

$$\frac{I_{(l+1/2)}}{I_{(l-1/2)}} = \frac{l+1}{l} \tag{2.30}$$

For example, for $l = 1$ (p levels), the relative intensities of the corresponding doublet, $p_{3/2}$ and $p_{1/2}$ (Fig. 2.8) are $2:1$, whereas for $l = 2$ (d levels), $I_{5/2}/I_{3/2}$= 3/2.

2.3.2.5 Satellites

Due to the fast photoemission process the $(N-1$ electron) excited state leads to a number of additional features. Hence, the XPS spectra comprise not only the main line corresponding to the lowest excited state but also a number of additional lines,

the *satellites*. There may be as well *extrinsic* satellites present, which are due to *inter-atomic* excitations, and *intrinsic* satellites, which can be explained with *intra-atomic* relaxations.

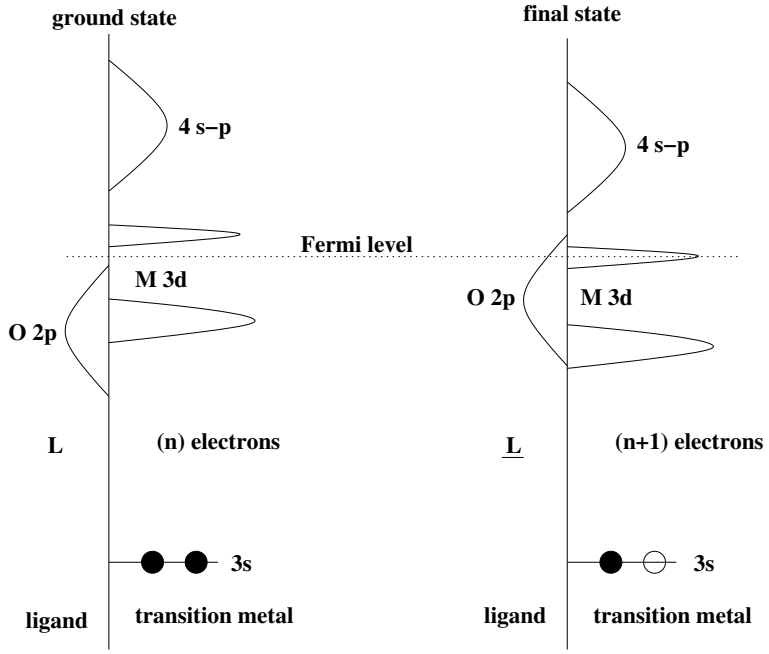

Figure 2.9: Schematic illustration of a charge transfer excitation in a transition metal oxide [88, 75].

Simultaneously with the removal of a core electron during the photoemission process, a second electron can be transferred to another orbital with higher energy in a *shake–up* process or can be completely removed in a *shake-off* process [89]. The energy necessary for these processes is supplied from the kinetic energy of the photoelectron produced during the initial ionization. Therefore, the corresponding satellites in the XPS spectrum will appear on the high binding (low kinetic) energy side of the main peaks.

For metallic samples the relaxation leads to quantified excitations in the conduction electron system, so called *plasmons* are created.

Fig. 2.9 shows the principle of a *charge transfer* excitation. In many TM oxides like NiO [88] the $2p_{3/2}$ and $2p_{1/2}$ lines are accompanied by additional peaks, the so called charge-transfer satellites (see also the satellites in Fig. 2.8). L refers to the ligand shell (oxygen, for TM oxides), and the charge-transfer process is a transfer of one electron from the ligand $2p$ (L) to the metal $3d$ shell: $3d^nL \rightarrow 3d^{n+1}L^{-1}$. The energy required by this extrinsic charge transfer process (Δ) is

$$\Delta = E(3d^{n+1}L^{-1}) - E(3d^nL). \tag{2.31}$$

2.3.2.6 $3s$ multiplet splitting

Multiplet (exchange) splitting of the core level lines can occur for systems with unpaired electrons in the valence levels. If one considers the photoemission from

the $3s$ core levels of transition–metal compounds, the spin $s = 1/2$ of the core hole created during photoemission can couple parallel or antiparallel to the total spin of the valence electrons (S). The core line will then split and the exchange splitting (ΔE_s) can be written according to the van Vleck theorem [90]:

$$\Delta E_s = \frac{2S+1}{2l+1} G^2(3s, 3d) \tag{2.32}$$

where $G^2(3s, 3d)$ is the Slater exchange integral and l is the orbital quantum number ($l = 2$). The binding energy of the state with spin $(S + 1/2)$ is lower than the binding energy corresponding to $(S - 1/2)$. The intensity ratio for the two peaks is given by:

$$\frac{I_{S+1/2}}{I_{S-1/2}} = \frac{S+1}{S} \tag{2.33}$$

More than 30 years ago it has been found that there are spectra for which the van Vleck theorem is not fulfilled: the multiplet intensities ratio was higher than that predicted by equation 2.32, whereas the value of the splitting was about two times smaller than expected [91, 92]. This discrepancy has been associated to intra-atomic "near–degeneracy" correlation effects [93]. Due to inter–atomic correlation effects like charge transfer the model usually fails to describe the XPS $3s$ spectra of late transition metal compounds where the charge transfer, to large extends dominates the electronic properties of the compounds [94]. Nonetheless the above phenomenological description often can be used as a valuable "diagnostic" tool for the analysis of the magnetic ground state. State of the art treatment of the $3s$ multiplet splitting is based upon full multiplet calculations [95].

For the other core levels ($l \neq 0$), the multiplet splitting is more complex because an additional spin–orbit splitting occurs in the spectra.

2.4 X-ray Absorption Spectroscopy (XAS)

In x-ray absorption spectroscopy (XAS) a core electron is excited into an empty state (conduction band). Thus, XAS is a powerful probe of the unoccupied part of the electronic structure. Like XPS, XAS leads to valuable information of the chemical composition, XAS is furthermore sensitive with respect to the local symmetry (e.g. the symmetry of a crystal field around a TM ion) of the probed element. The transition probability is described, like the XPS process, by Fermi's Golden Rule:

$$I_{XAS} \sim \mid \langle \Psi_f \mid \hat{e}r \mid \Psi_i \rangle \mid^2 \delta(E_f - E_i - h\upsilon) \tag{2.34}$$

Hence, the intensity of the XAS in equation 2.34 is proportional to the squared dipole matrix element $\hat{e}r$ between the initial Ψ_i and the final state Ψ_f. Due to the dipole selection rules only transitions which change the angular momentum quantum number (l) by one, $\Delta l = \pm 1$, occur in the XAS process. While the spin is conserved, $\Delta s = 0$, the orbital momentum of the z-component has to change by zero or one, $\Delta m \pm 1, 0$. In particular, $\Delta m = +1$ for left circular polarized light and $\Delta m = -1$ for right circular polarized light.

In this thesis special attention is given to the XAS of TM $2p \rightarrow 3d$ transitions. Fig. 2.10 illustrates a (polarization dependent) XAS spectrum recorded on the Fe L edge of an oxide. Like in the XPS the spectrum is seperated due to the spin-orbit interaction into $2p_{3/2}$ and $2p_{1/2}$ levels. The shape of XAS spectra is predominantly governed by the contributions by the transitions into the empty $3d$ states (continuous line). However, even unoccupied s and p states contribute to the spectrum by means of a flat energy dependent two-step like function (dashed line). In case of the quantitative analysis of dichroic spectra this background function with relative step heights $2:1$, according to the occupation of the $2p_{3/2}$ and the $2p_{1/2}$ core states [96], has to be subtracted.

The XAS process is followed either by an Auger decay process or the emission of a photon. In the soft x-ray region the Auger process is dominating the decay and the Auger yield is usually around 99 % or higher compared to the fluorescence. Therefore one possibility to measure an signal which is proportional to the XAS signal is to measure the drain current from the sample, the *total electron yield (TEY)*. Analogous to the XES one can also use the emitted photons to probe the XAS (*partial fluorescence yield (PFY)*). However, the XAS spectra recorded by means of PFY often suffer due to strong saturating effects like self-absorption.

The XAS can be divided into two spectral regions, the so called *near edge x-ray absorption fine structure (NEXAFS)* which reflects excitations of the photoelectron into the unoccupied states, and the so called *extended x-ray absorption fine structure (EXAFS)*. Here the photoelectron is excited into the continuum and its scattering with the environment with the absorber leads to characteristic features in the XAS, usually at photon energies well above the corresponding NEXAFS threshold. A more general and comprehensive treatment of x-ray absorption spectroscopy can be found in Ref. [97].

2.4.1 X-ray Magnetic Circular Dichroism (XMCD)

After its first verification in 1987 by Schütz *et al.* [98], the technique of x-ray magnetic circular dichroism (XMCD) in XAS has become more and more a widely used tool as probe for the *element-specific* characterization of magnetic materials. The growing interest in XMCD stems partly from the growing availability of tunable high brilliance x-rays (synchrotron) and partly from the unique possibility to analyze the magnetic moments not only element specific, but also separated into their spin and orbital contributions.

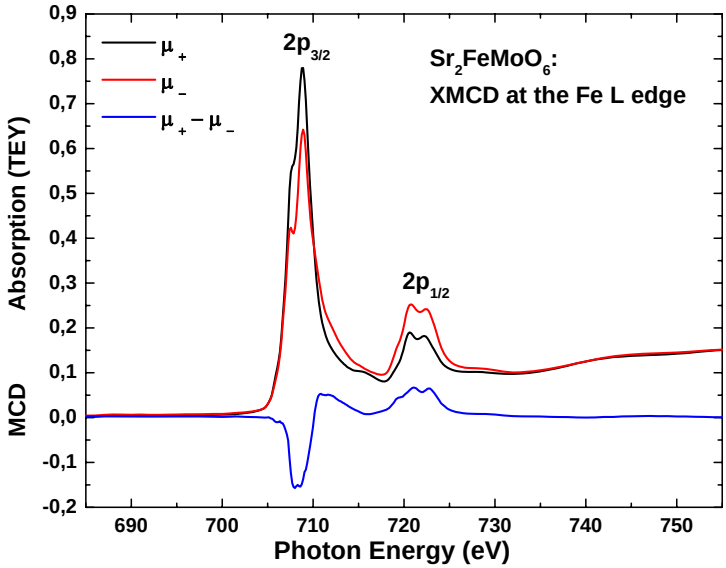

Figure 2.10: Example of an XMCD spectrum recorded at the Fe L edge of a ferromagnetic oxide. Upper panel: XAS spectra for right circular polarized (black line) and left circular polarized (red line) x-rays. Lower panel: The difference of both spectra gives the magnetic circular dichroism (MCD).

Fig. 2.10 shows a typical example of a XMCD spectrum on a TM L edge. If $2p \rightarrow 3d$ transitions are excited by circularly polarized x-rays, these transitions show a spin polarization due to transition selection rules [99]. Dependent on the light helicity more electrons of one spin direction are excited to the unoccupied $3d$ states than of the other spin direction. If in a ferromagnet the spins aligned, e.g. in an external magnetic field and both spin polarizations coincide in sign the XAS signal will be higher for one spin direction than for the opposite one (see Fig. 2.11). It is noteworthy that the spin polarization exhibits opposite sign for $2p_{3/2} \rightarrow 3d$ and for $2p_{1/2} \rightarrow 3d$ transitions. Thus, for a fixed sample magnetization the absorption at the L_3 peak ($2p_{3/2} \rightarrow 3d$) is higher for right circular polarized x-rays whereas the opposite situation is found at the L_2 peak ($2p_{1/2} \rightarrow 3d$) (see Fig. 2.10).

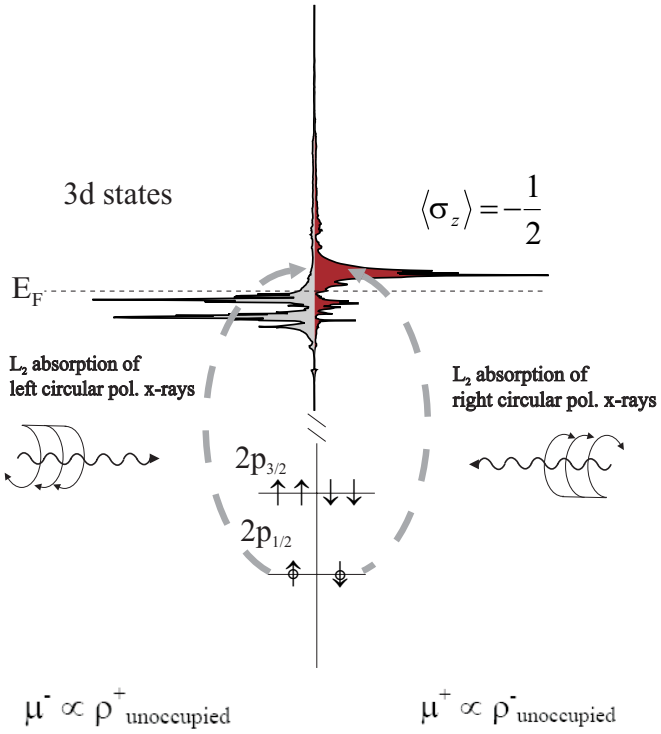

Figure 2.11: Schematic representation of the XMCD process in the one electron picture. The d-band is split into spin-up and spin-down bands. Firstly the absorption of circularly polarized x-ray photons leads to a spin polarization of the photoelectrons due to the spin-orbit coupling ($j = l \pm s$). In a second step the d valence band acts as a spin detector. At the L_3 edge ($j = l + s$) left circular polarized x-rays mainly probe the unoccupied spin-up d states with respect to the direction of the magnetization. The effect reverses at the L_2 edge due to the opposite sign of the spin-orbit coupling ($j = l - s$) [100].

Sum rules

The spin polarization of the $2p \rightarrow 3d$ transitions can be used to probe the unoccupied $3d$ states spin selective, and thus to reveal the spin magnetic moment. Since the orbital momentum is directly connected with the absorption of a circular polarized photon by the relationship $\Delta m = \pm 1$ the XMCD also contains valuable information about the orbital magnetic moment. Both the $2p_{3/2} \rightarrow 3d$ and for $2p_{1/2} \rightarrow 3d$ transitions exhibit the same sign and magnitude of orbital polarization, whereas the spin polarization of the $2p_{1/2} \rightarrow 3d$ transitions is of twice the magnitude and opposite sign compared to that of the $2p_{3/2} \rightarrow 3d$ transitions.

An illustrative description is plotted in Fig. 2.12. The schematic XMCD difference spectrum shown in panel b corresponds to a sample which only exhibits a spin orbital moment m_{spin}, and no orbital moment. In this case the spectrum comprises two features of different sign but equal intensities, corresponding to the L_3 and L_2 edges, respectively. The higher spin polarization of the L_2 edge compensates its lower

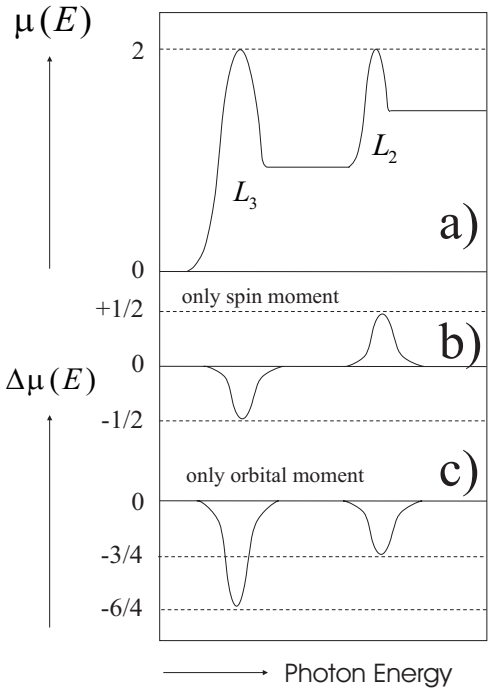

Figure 2.12: Schematic illustration of the summed XAS spectrum of a $3d$ atom (a), XMCD difference spectrum of a sample showing only a spin magnetic moment m_{spin} (b), and XMCD difference spectrum of a sample with only an orbital magnetic moment m_{orb} (c) [100].

intensity, so that its peaks exhibit equal heights. The other special case is a sample with only an orbital magnetic moment m_{orb}, but no spin magnetic moment (panel c of Fig. 2.12). In that case the difference curve consists of two features with same sign, and due to the equal orbital polarization the intensity of the L_3 peak is twice as high as the one of the L_2 peak. A spectrum of a sample showing both, m_{orb} and m_{spin} can be understood as being a linear superposition of the two cases discussed.

An experimental XMCD spectrum recorded at a TM L edge can be unambiguously decomposed into its orbital and spin moment. By applying the so called *XMCD sum rules*, which have been found by Thole and Carra *et al.* [101, 102, 96] based upon the magneto optical sum rules:

$$m_{orb} = - \frac{4\int_{L_3+L_2}(\mu_+ - \mu_-)\,d\omega}{3\int_{L_3+L_2}(\mu_+ + \mu_-)\,d\omega}(10 - n_{3d})$$

$$m_{spin} = - \frac{6\int_{L_3}(\mu_+ - \mu_-)\,d\omega - 4\int_{L_3+L_2}(\mu_+ - \mu_-)\,d\omega}{\int_{L_3+L_2}(\mu_+ + \mu_-)\,d\omega} \times (10 - n_{3d})\left(1 + \frac{7\langle T_z\rangle}{2\langle S_z\rangle}\right)$$

Here m_{orb} and m_{spin} represent the orbital and spin magnetic moment in units of μ_B/atom, respectively. n_{3d} is the number of occupied $3d$ electrons of the corresponding transition metal ion, whereas L_3 and L_2 denote the integrals over the L_3 and the L_2 edge, respectively. $(\mu_+ - \mu_-)$ and $(\mu_+ + \mu_-)$ stand for the MCD spectrum and the summed XAS spectra (see also Fig. 2.12, upper panel), finally $\langle T_z \rangle$ and $\langle S_z \rangle$ denote the expectation value of the magnetic dipole operator and the half of m_{spin} in Hartree atomic units. In the bulk of cubic crystals the last two values can be usually neglected.

The sum rules are based on a number of simplifications, firstly they are based upon the consideration that the $2p \rightarrow 3d$ transitions take place on free atoms. Many particle effects are neglected. Furthermore, a complete energetic separation of the L_3 and L_2 edges is necessary in order to determine the corresponding integrals exactly. This is particularly difficult for less than half filled $3d$ transition metals, i.e. Ti, V and Cr. Whereas a sum rule analysis is leading to more or less exact results for the late and intermediate $3d$ transition metal ions (deviations between 8% and 30% for Ni and Mn, respectively), deviations of 80% and more for Ti and V indicate the breakdown of the spin sum rule.

2.4.2 X-ray Linear Dichroism (XLD)

In a more general formulation, the x-ray absorption intensity of *linear polarized x-rays* directly probes the quadrupole moment of the local charge around the absorbing atom through a search-light-like effect. A quadrupole moment exists in all cases where the local charge has a symmetry lower than cubic. The absorption intensity is at a maximum if the x-ray electric field vector is aligned along the direction of maximum charge (hole) density in the atomic volume surrounding the absorbing atom, e.g. along an empty molecular orbital. The *x-ray linear dichroism* (XLD) effect provides, e.g. the basis for the determination of the orientation of chemisorbed molecules on surfaces and the orientational order in polymers or liquid crystals. In case of a single crystal the XLD difference spectrum is determined by subtracting the XAS for light polarization parallel ($\mathbf{E} \parallel \mathbf{c}$) from the XAS for light polarization perpendicular ($\mathbf{E} \perp \mathbf{c}$) to the high symmetry $\mathbf{c}$-axis of the crystal. The measured angular dependence determines the quadrupole moment or order parameter of the charge distribution of the selected orbital [97, 103].

The ability of XLD to detect the uniaxial electron density of electron clouds is also highly interesting for the investigation of orbital ordering in transition metal oxides like manganites (see Chapter 1.3.4). Here the spatial symmetry of the occupied orbitals is lower than that of the crystal. In the case of orbital ordering the orthogonal set of twofold degenerate e_g states is either $(3z^2 - r^2, x^2 - y^2)$, $(3x^2 - r^2, y^2 - z^2)$, $(3y^2 - r^2, z^2 - x^2)$, or a suitable superposition of them. Unlike resonant x-ray scattering (RXS), XLD observes not the modulation wave vector of the $3d$ orbital order but the superposition of the $3d$ electron distributions of the A and B sublattices. Furthermore RXS is usually applied to the Mn K edge ($1s \rightarrow 4p$ transition), and it is still under discussion wether RXS at the Mn K edge reveals the orbital ordering in manganites or is more sensitive to the Jahn-Teller distortion [36]. XLD, applied to the L edge is a very promising tool to reveal direct information about the type of orbital ordering, e.g. in manganites. However, one must distinguish between two cases. If the orbits

are arranged in an orthogonal way alternately in the A and B sublattices of a cubic crystal, there is no uniaxial anisotropy and thus, no XLD can be expected. This is for example the case for the $4f$ antiferro-orbital ordering in CeB_6. On the other side, for $LaMnO_3$ the orbital ordering is accompanied by the Jahn-Teller distortion, thus the twofold degenerate e_g orbitals are alternately arranged in a *non-orthogonal* way in the two sublattices, this means one can expect to observe a XLD signal for $LaMnO_3$, as predicted by theory [37, 104].

2.5 X-ray Emission Spectroscopy (XES)

As already mentioned, two additional processes can simultaneously occur with the photoionization. The ions produced during the photoemission process can relax by emitting x-ray radiation (*fluorescence*) or by the ejection of a second electron (*Auger process*), which has been briefly introduced in Chapter 2.2. We now want to discuss the x-ray emission process in more detail.

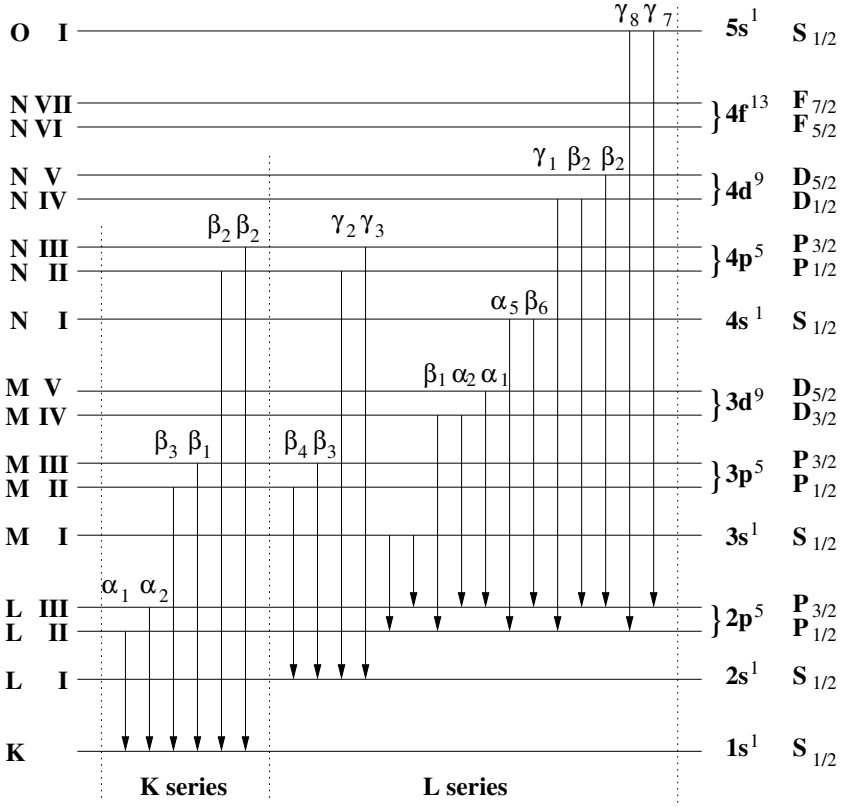

Figure 2.13: Schematic diagram of the main x-ray emission lines in the K and L series (after [105]).

The x-ray emission is dominated following dipole selection rules: $\Delta l = \pm 1$ and $\Delta j = \pm 1; 0$, if one only considers the electric dipole vector of the radiation. The probability of ion relaxation via dipolar emission is more than two times larger than that corresponding to the electric quadrupoles or to the magnetic dipole vector, therefore

the last two can be often neglected, particularly in the case of normal x-ray emission spectroscopy (NXES) [105].

2.5.1 Resonant X-ray Emission Spectroscopy (RXES)

Taking into account the excitation by means of a photon, XES is a so called *'photon in - photon out'* spectroscopy. Let us consider the x-ray scattering process in which a photon with energy Ω and a corresponding wave vector $\mathbf{k}_1$ excites a material and as a result another x-ray photon with energy ω and wave vector $\mathbf{k}_2$ is emitted due to the electron-photon interaction in the material: Then the overall x-ray scattering cross section is described by the Kramers-Heisenberg equation [70, 51]

$$F(\Omega,\omega) = \sum_f \left| \sum_m \frac{\langle f|T|m\rangle\langle m|T|i\rangle}{E_i + \Omega - E_m - m\Gamma_m} \right|^2 \cdot\delta(E_i + \Omega - E_f - \omega) \tag{2.35}$$

where $|i\rangle$ and $|m\rangle$ represent the initial state and the intermediate state with energies E_i and E_m, respectively while $|f\rangle$ and E_f stand for the final state configuration and energy. The transition operator is denoted by T, and Γ describes the spectral broadening which is due to the core lifetime (in the final state). It can be seen from equation 2.35 that RIXS is a second order process comprising the x-ray absorption from $|i\rangle$ to $|m\rangle$ and the x-ray emission process from $|m\rangle$ to $|f\rangle$. If the final state $|f\rangle$ is the same as the initial state $|i\rangle$, then the spectrum described by equation 2.35 corresponds to resonant elastic x-ray scattering (REXS), while if $|f\rangle$ is not the same as $|i\rangle$, it gives the resonant inelastic x-ray scattering (RIXS). If both cases are combined, $F(\Omega,\omega)$ describes the overall resonant x-ray emission spectrum (RXES).

For the analysis of XAS and RXES for semiconductors and ionic insulators the energy-band theory (Chapter 2.1.1) has been successfully applied. Considering the Kohn-Sham equation, the optical transition matrix element is constant and the momentum selection rule can be disregarded, equation 2.35 is reduced to

$$F(\Omega,\omega) \propto \int d\epsilon \, \frac{\rho(\epsilon)\rho'(\epsilon + \Omega - \omega)}{(\epsilon - \epsilon_L - \omega)^2 + \Gamma^2} \tag{2.36}$$

where ρ and ρ' denote the partial occupied and unoccupied densities of states, respectively [106]. This model was used to describe the C $1s$ RIXS of highly oriented graphite [107]. In this and similar cases it was possible a band-mapping by means of RIXS.

However, the energy-band model could not be often used successfully to describe the RIXS of d and f electron systems. The single impurity Anderson model (Chapter 2.1.2) is widely used to analyze first order core level spectra, i.e. XAS and XPS of f- and d-electron systems. The applicability of the Anderson impurity model to RIXS has been furthermore confirmed for many f electron systems like for La compounds or Ce oxides [108, 109].

In $3d$ transition metal compounds the situation is more complex. The $3d$ wave function of a transition metal ion is more extended than the $4f$ wave function of a

rare earth, thus the $3d$ electrons are more sensitive to the local atomic arrangement around the transition metal element. In these systems, the electronic structure characterized by the dual nature of delocalized and localized states, and the Anderson impurity model has turned out to be not as applicable as it is for the description of XAS and XPS. The localized atomic like intermediate states are reflected by low energy excitations in RXES spectra, these can be often described within the Anderson impurity model.

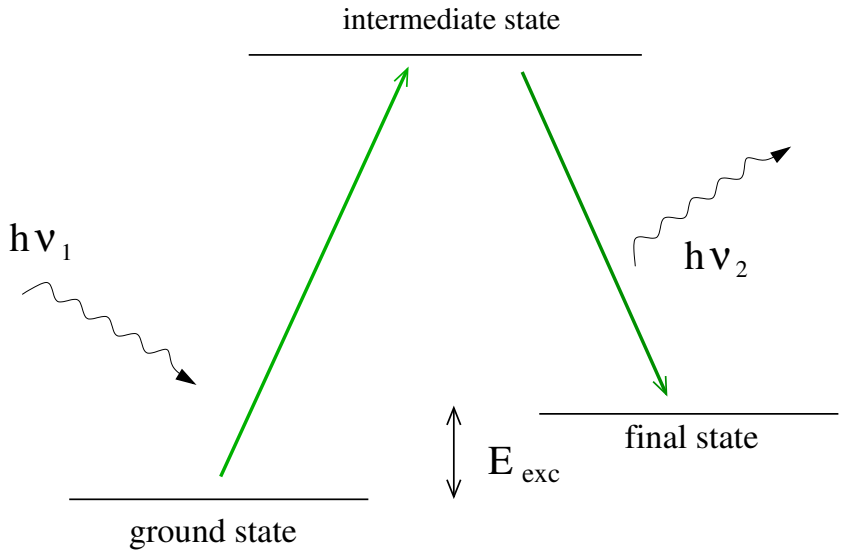

Figure 2.14: Schematic representation of the RIXS process in an atomic like environment.

Figure 2.14 visualizes the RIXS process by an energy level diagram. Because two (virtual) dipole transitions are involved in the RIXS process the final state has the same parity as the initial state, as a consequence so called crystal-field excitations between d-orbitals of different symmetry (more commonly denoted as dd-excitations) are allowed. Besides the low energy excitations the RIXS spectra of $3d$ transition metal oxides also comprise charge transfer (CT) excitations, which are due to transitions between delocalized ligand and localized transition metal atom states [51, 25]. One difficulty within the cluster model is the strength of the hybridization between the transition metal $3d$ states and the O $2p$ states. If it is strong, one may have to take into account many configurations d^n, $d^{n+1}\underline{L}$, $d^{n+2}\underline{L}^2$, ..., in order to obtain a satisfactory agreement between experiment and theory. It may also happen that the single metal ion approximation breaks down and one has to take into account the periodic arrangement of metal ions in a large cluster model considering many transition metal ions. In this context it is noteworthy that both theoretical approaches, the band theory [110] as well as an extended cluster model [111] have been successfully used to describe the Ti $2p$ RIXS of TiO_2.

Energy conservation is valid during the whole RIXS process, one obtains information about the ground state of the system via the intermediate core excited states. Due to the energy conservation rule the excitation energy of the final state E_{exc} is

given by Eq. 2.37:

$$h\nu_2 = h\nu_1 - E_{exc} \tag{2.37}$$

Here $h\nu_2$ and $h\nu_1$ denote the energies of the scattered and incident photons, respectively. Interestingly enough, the energy of the intermediate state does not occur in equation 2.37. As a result, the spectral broadening is not related to the life time of the intermediate state [112]. The overall resolution of the spectra is only limited to the experimental setup, i.e. beamline (monochromator) plus spectrometer.

2.5.2 Normal X-ray Emission Spectroscopy (NXES)

The Kramers-Heisenberg equation can also be used to describe normal x-ray emission spectroscopy (NXES), if one assumes the incident photon energy Γ to be well above the x-ray absorption threshold. With a sufficiently large Ω, a core electron is excited by the incident photon to a high-energy continuum, namely into the photoelectron state $|\phi_\epsilon\rangle$ with energy ϵ. In this case the spectral shape does not depend on Ω, in NXES the core hole creation is correlated with the x-ray emission process. It is often possible to describe NXES within the energy-band model. By taking into account a one-electron approximation equation 2.35 reduces to

$$F(\Omega,\omega) = \rho t^2 \sum_m \frac{|\langle\rho_f|t|\rho_m\rangle|^2}{(\omega - \epsilon_m + \epsilon_f)^2 + \Gamma_m^2} \tag{2.38}$$

The NXES spectrum gives the partial DOS, which is symmetry-selected by the dipole transition $|\langle\rho_f|t|\rho_m\rangle|^2$, broadened by the lifetime broadening Γ_m of the intermediate state.

In the present work mainly the TM L ($3d \rightarrow 2p$ transitions) and O $K\alpha$ ($2p \rightarrow 1s$ transitions) edges are used to obtain information about the TM $3d$ and O $2p$ partial DOS and to interpret the valence band XPS spectra of the investigated transition metal compounds. In order to bring the XPS and XES spectra to the same energy scale one measures the ionization energy of the inner orbital level involved in the XES by XPS (for example, TM $2p$ and O $1s$ when one studies the TM L and O $K\alpha$ XES). Then, the corresponding XES can be easily correlated to the binding energy scale by building the difference.

2.6 Instrumentation

2.6.1 The photoelectron specrometer PHI 5600ci

All XPS measurements presented in this work have been performed with a PHI 5600ci multitechnique spectrometer produced by the Perkin Elmer Cooperation [113]. The figure below shows a schematic diagram of this spectrometer.

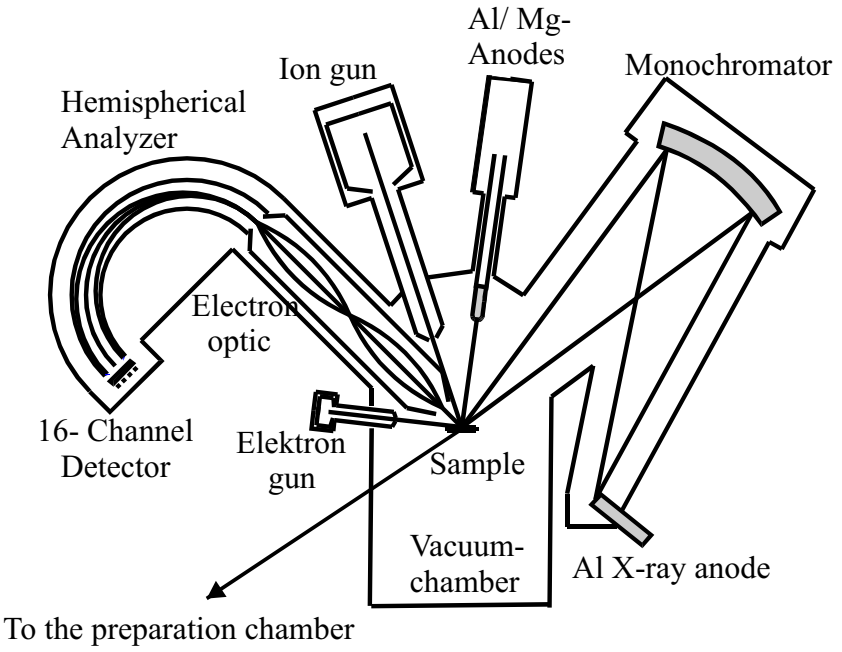

Figure 2.15: Schematic diagram of the PHI 5600ci multitechnique spectrometer [114].

The PHI 5600ci is equipped with a dual Mg/Al x-ray anode. The energies of Al $K\alpha$ and Mg $K\alpha$ radiations are 1486.6 eV and 1253.6 eV and their half–widths for the unmonochromatized radiation are 0.85 eV and 0.7 eV, respectively. $K\alpha$ indicates that an electron has been ejected from the K shell and the radiation is due to an electron from the L shell that occupies the hole created in the K shell. If the Al $K\alpha$ radiation is monochomatized by using an appropriate quartz crystal, the half width is reduced to ~ 0.3 eV, the crystal–sample–analyzer angle is fixed to 90°.

After ejection the electrons are filtered by an 11 inches hemispherical analyzer with respect to their kinetic energy. First the electrons are focussed with help of an electronic lens system, then the kinetic energy is reduced to a certain pass energy E_p, this is necessary to ensure a constant absolute resolution for the whole spectrum. If the analyzer is operated in the so called constant analyzer transmission (CAT) mode only electrons with the energy $E_p \pm \Delta E$ may pass the analyzer, ΔE denotes the absolute energy resolution. The usage of small pass energies increases the absolute energy resolution of the recorded spectra but also reduces the overall intensity of the XPS signal.

Since the electrons, which leave the excited sample, shall reach the analyzer without being scattered on a gas molecule the main chamber is requested to be kept under

ultra high vacuum (UHV). Furthermore XPS is a rather surface sensitive technique and UHV conditions are also required in order to keep the sample surface free of contamination. A pressure of about 1×10^{-9} mbar assures that XPS measurements can be performed for several hours without taking care of surface contamination. The UHV is produced by a combination of different vaccum pumps: rotation pumps are necessary to create vacuum conditions in which turbomolecular pumps can work, with help of these on can reach a vacuum of around 1×10^{-8} mbar, for even better vacuum conditions ion getter pumps as well as titanium sublimation pumps are necessary. In order to get a contamination free surface different preparation techniques are available. With help of a sputter gun one may bombard the sample surface with argon ions, accelerated to max. 4.5 kV. Sputtering may be appropriate for metallic surfaces, however, for most compounds and especially oxides sputtering, even if only low acceleration potentials of a few hundret volts are used, may cause a dramatic change of the sample surface stoichiometry. Hence, it is better to either scrape the sample surface under UHV conditions, this is often successful for inter–metallic compounds. For oxidic materials the best sample preparation is to fracture the sample in situ using grippers.

2.6.2 Synchrotron radiation based experiments

In order to perform XAS, XES, and RXES experiments one needs high intensity and tunable x-ray sources. NXES experiments may be also performed by using strong electron excitation sources, the x-rays created by the bremsstrahlung is characteristic for the compound in question and may be analyzed by different types of crystal monochromators and multichannel detectors. However, this technique is limited by the fact that the major part of the kinetic energy of the exciting electrons is dissipated as heat rather than x-ray photon flux. State of the art XAS and (R)XES are usually performed with the high brilliant and tunable light produced at synchrotron radiation (SR) facilities [115].

Storage ring and Insertion devices

SR is produced by accelerating electrons to almost the speed of light; at relativistic velocities charged particles emit electromagnetic radiation in form of a narrow intense cone tangentially to the path of the particles. The electrons are then forced by a series of magnets into a circular path in the so called *storage ring*. The energy loss of the electrons, which is due to the emitted radiation, can be compensated by using an oscillating electric field in a *radio frequency* (RF) cavity. Different types of magnetic structures are available to bend the electron beam and subsequently to deviate the SR into the beamlines and experiments. The two most common insertion devices are the *bending magnets* and the *undulators*. Fig. 2.16 shows a schematic plot of a storage ring and the two different type of insertion devices.

A dipole, or bending magnet simply bends the electrons in a single curved trajectory, a rather narrow cone of radiation is produced. The spectrum is continuous over a wide energy range, e.g. 100-1000 eV. In contrast an undulator comprises alternating strong permanent magnets of opposite polarity. The electrons oscillate through

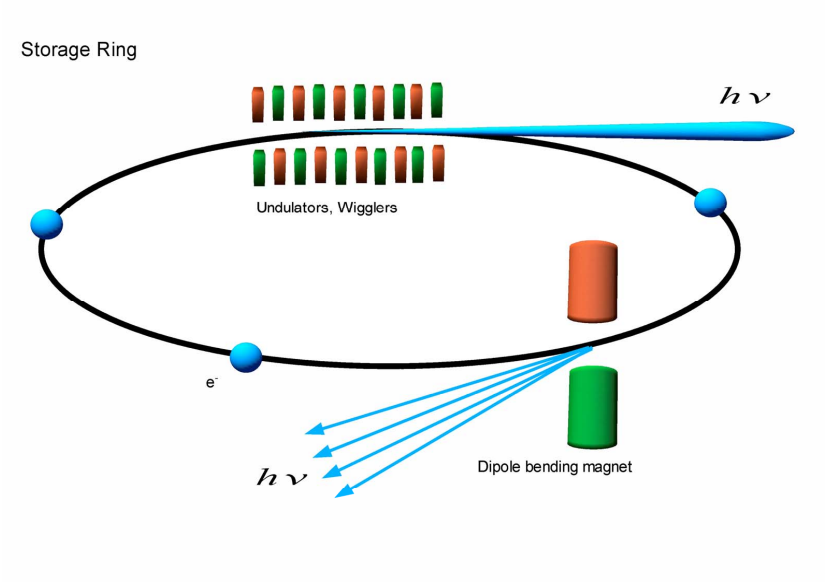

Figure 2.16: Schematic plot of a storage ring with different insertion devices: a bending magnet and an undulator.

this periodic magnetic structure, at each pole coherent x-ray pulses are emitted by the oscillating electrons which lead to constructive interference. The overall emitted radiation is a very intense and narrow cone with small angular and spectral widths (usually ranging over a region of a few electron volts). Thus, the undulator spectrum consists of sharp peaks, called harmonics. The desired energy for the experiment can be chosen by varying the magnetic field strength between the poles. This is realized by changing the distance, or gap, between the upper and lower row of permanent magnets. Such a setup of an upper and lower row of permanent magnets leads to an almost 100% linearly and horizontally polarization. In order to perform experiments in dependence of the polarization, especially if circular polarized radiation is required, a combination of two undulators can be applied.

In contrast to a standard planar undulator the so called APPLE-type elliptical polarizing insertion device comprises horizontally separated magnet rows (see Fig. 2.17)[1]. The shifting of these rows produces a helical field at the position of the electron beam causing an elliptical or even circular trajectory. Consequently, elliptically or circularly polarized radiation is emitted. To change the polarization while staying at a fixed photon energy, both gap and shift have to be varied.

Beamline and endstation

After the radiation has been generated by the insertion device it has to be linked to the experiment. Firstly the desired excitation energy has to be chosen. In case of an

[1]Bernd J. Zimmermann is acknowledged for drawing Fig. 2.17

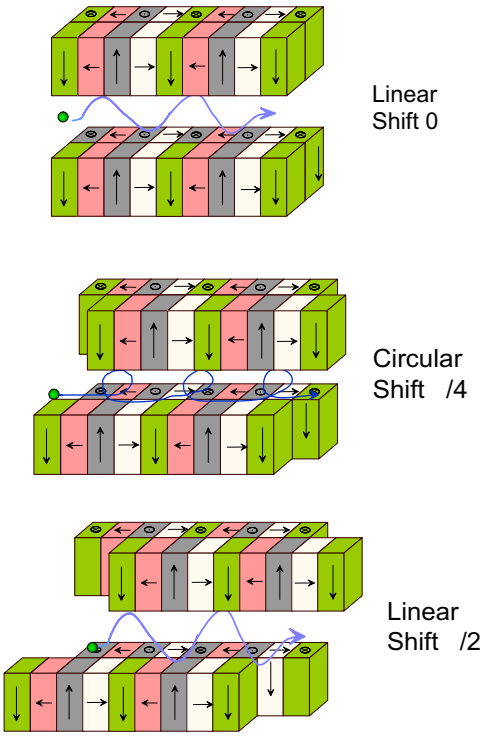

Figure 2.17: Schematic drawing of an APPLE device at different settings. Upper panel: linear mode without shift (linearly horizontally polarized light). Middle panel: circular mode. The shift ($\lambda/4$) is set to the position with equal amplitudes of the horizontal and vertical magnetic fields (quarter period of the magnetic structure). Lower panel: linear mode with shift set to half period ($\lambda/2$) (linearly vertically polarized light) of the magnetic structure. Adapted from [116].

undulator this is done firstly by choosing the right gap, then a further monochromatization is achieved by using a series of high precision optical elements as a monochromator. In order to reflect the x-rays these gratings have to be aligned in very grazing incidence angles. For the XAS and (R)XES experiments performed in this work two different types of x-ray monochromators have been used; the plane grating monochromator (PGM) and the spherical grating monochromator (SGM) [117]. The monochromator of a beamline is usually followed by a further exit slit and a refocussing unit which focusses the incoming light onto the sample surface. In Fig. 2.18 a typical beamline layout is presented.

The results presented in this work have been obtained by using a number of different beamlines equipped with complementary experimental endstations. Most of the (R)XES measurements and the corresponding XAS have been performed at the beamline 8.0.1 at the Advanced Light Source (ALS), Lawrence Berkeley National Laboratory, Berkeley, USA. The beamline is based upon a 50 mm period length undulator providing linearly polarized photons in the horizontal plane of the laboratory. The generated radiation can be monochromatized by three interchangeable SGMs [118]. The spectral resolution (typically $E/\Delta E$ has been set to around 1000-3000)

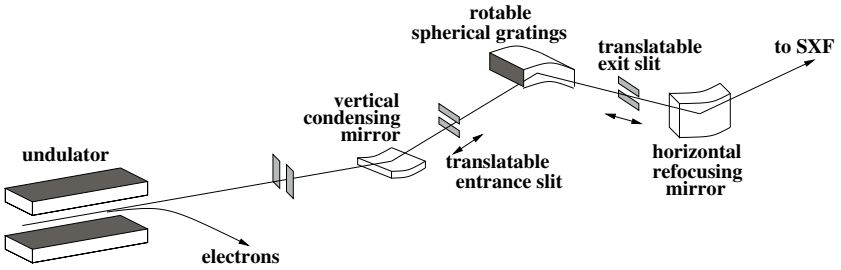

Figure 2.18: Typical example of an undulator beamline layout: the beamline 8.0.1 at the Advanced Light Source (ALS) at the Lawrence Berkeley Lab.

can be selected with help of the entrance and exit slits. The spectra were recorded using the soft x-ray fluorescence (SXF) endstation of the University of Tennessee in Knoxville and the Tulane University in New Orleans (Fig. 2.19) [119]. It has a variable spectrometer entrance slit, the emitted photons arising from the sample fluorescence are analyzed by four interchangeable gratings which are in a Rowland geometry with a multichannel plate detector.

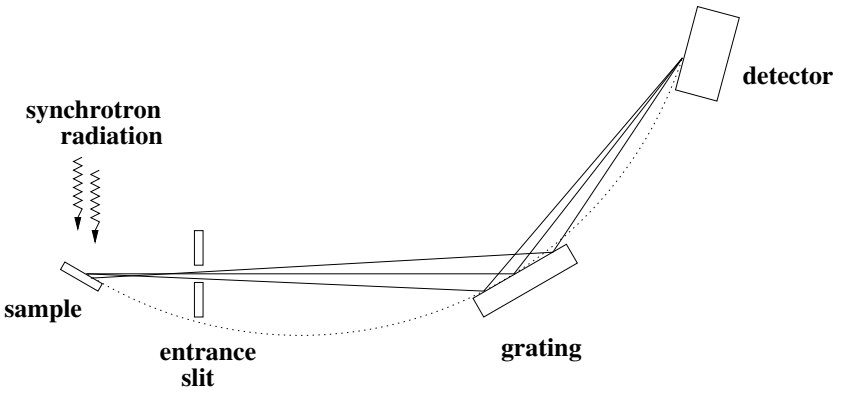

Figure 2.19: Schematic plot of the SXF-spectrometer of the University of Tennessee in Knoxville [119].

Some complementary XES measurements, in particular on B-site doped Lanthanum manganites were carried out at the ID 12 at BESSY II in Berlin. This beamline comprises a similar undulator with a period length of 41 mm and a PGM [116]. As endstation the ROtatable Spectrometer Apparatus (ROSA) equipped with a soft x-ray spectrometer developed by Nordgren *et al.* was used [120].

Further RXES measurements on pyrite and a number of dichroic experiments in XAS and RXES on selected CMR compounds were performed at the Beamline of Advanced diCHroism (BACH) at ELETTRA, Sincrotrone Trieste, Trieste, Italy. Here two APPLE type helical undulators deliver x-rays over a wide range from 20-2000 eV with variable polarization, and the generated radiation can be monochromatized by four interchangeable SGMs [123]. In contrast to the "conventional" multi channel detectors another type of soft x-ray spectrometer is available, tho so called *Compact Inelastic X-ray Spectrometer* (ComIXS). This spectrometer is based upon a charged couple device (CCD) as a detector, providing very high count rates and the possibility

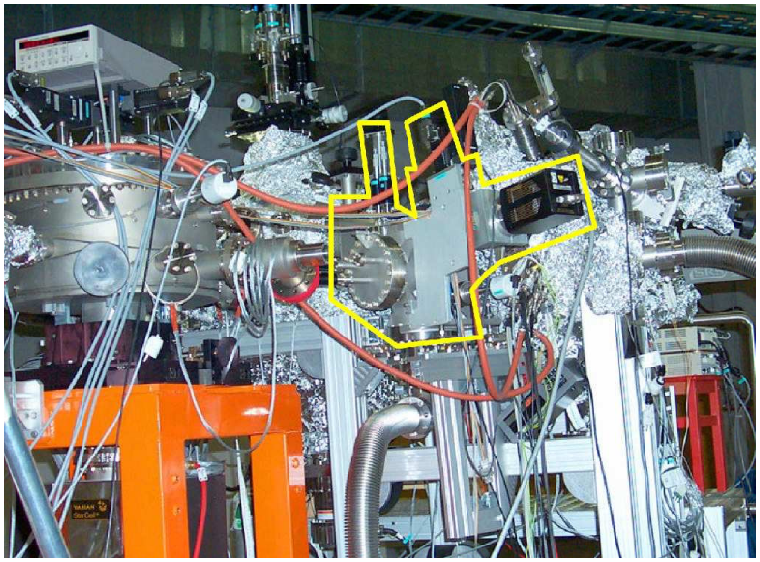

Figure 2.20: The Compact soft Inelastic X-ray Spectrometer (ComIXS) operating at ELETTRA [121, 122].

to keep the spectrometer gratings very compact (see also Fig. 2.20). For a further improvement a new generation of CCD detector is necessary since the actual spectral resolution is limited by the pixel size of the CCD detector plate.

Some XMCD experiments under high magnetic fields were performed at beamline 4.0.2 at the ALS, based upon a 5.0-cm-period elliptical polarization undulator (EPU5). The polarization is user selectable; linear polarization continuously variable from horizontal to vertical; left and right elliptical (or circular) polarization in an energy range of 50-1900 eV. The radiation is monochromatized with a variable-included-angle PGM. The XAS experiments were carried out using a cryostat enabling to perform measurements at low temperatures down to 2 K and magnetic fields up to 6 T [124].

Finally, some defect oxides Li_xCoO_2 were probed by means of XAS at the Russian German Laboratory at BESSY II. Radiation in a wide energy range of 30-1500 eV is produced by a dipole magnet, the desired photon energies can be selected by two interchangeable PGMs. The endstation provides XAS, XPS and RPES experiments [125].

Chapter 3

Iron compounds

3.1 Why wüstite (FeO) and pyrite (FeS_2)?

In the present work core level excitation studies of iron monoxide, FeO, which are compared with isovalent FeS_2 are reported. These compounds have been probed at the Fe L and other edges by several core spectroscopies, namely Near Edge X-ray Absorption Spectroscopy (NEXAFS), Resonant Inelastic X-ray Scattering (RIXS) and X-ray Photoemission Spectroscopy (XPS). These two materials have many similarities (both cubic or nearly so, same oxidation state, comparable semiconducting gaps) but their magnetic properties are very different.

FeO is cubic with rock salt structure, antiferromagnetic and is typically non-stoichiometric. The Fe^{2+} ions with configuration d^6 are are in the high spin state and located in identical octahedral sites. The electronic configuration in cubic symmetry is $(t_{2g}\uparrow)^3(e_g\uparrow)^2(t_{2g}\downarrow)^1$, which in rhombohedral symmetry becomes $(a_{1g}\uparrow)^1(e_g^{'}\uparrow)^2(e_g^{''}\uparrow)^2(a_{1g}\downarrow)^1$ [126]. Simple LDA theory predicts that it is a metal but in reality it is an insulator. More sophisticated treatments reproduce this result [126, 127, 128], but there is still some discussion about whether it is a charge transfer or Mott-Hubbard insulator, or an intermediate case. The value of the gap obtained from optical absorption has been reported to be 0.5 eV [129] but most other authors quote a value of 2.4 eV [128, 130, 131]. FeO has been studied by NEXAFS at the oxygen K and Fe L edges [132, 133, 134, 135], EELS [136], and photoemission [137, 138].

FeS_2 or pyrite (also known as fools' gold) is cubic with four formula units per unit cell, and is non-magnetic. Iron pyrite (FeS_2) crystallizes in the pyrite structure with space group $Pa\bar{3}$ (T_h^6), and the unit cell contains four formula units [139, 140, 141].

The iron pyrite crystal structure can be derived from the NaCl structure with one sub-lattice occupied by Fe^{2+} ions and the other sub-lattice occupied by the centers of gravity of disulfide (S_2^{2-}) ions. The iron atoms are coordinated by six sulfur atoms and the FeS_6 octahedra are linked by common corners, due to the formation of the sulfur pairs. The sulfur atoms are tetrahedrally surrounded by one sulfur and three iron atoms. The band gap is about 0.95 eV [142], but it is not clear if it is direct or indirect. The sulphur is arranged in pairs surrounded by 6 Fe atoms; the Fe atoms (d^6, low spin state, $S = 0$) are octahedrally coordinated by the sulphur dimers. The material is a chalcogenide like the oxides, but different in several ways: the questions to be answered are whether it is more or less covalent than the oxides,

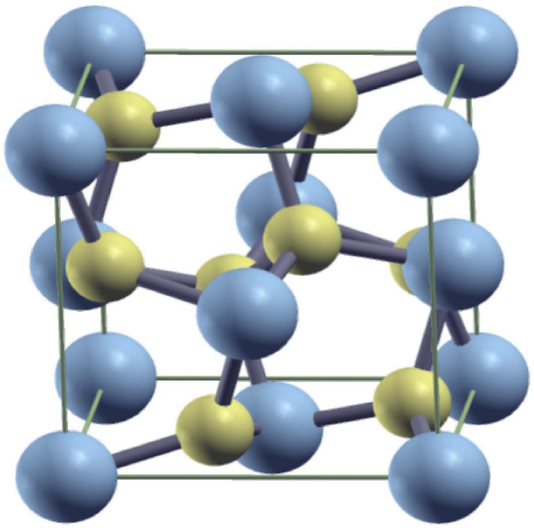

Figure 3.1: A bulk unit cell of Pyrite: FeS_2 (blue spheres represent iron, yellow spheres sulfur).

and whether the Fe d states are localized or band-like. X-ray absorption spectra at the Fe L edge have been reported [143, 144, 145], as well as a number of band structure calculations [146, 147, 148, 149]. Some x-ray emission data has also been reported by Kurmaev *et al.* [148] while Suga *et al.* [150] have reported both NEXAFS and resonant photoemission of FeS_2 at the Fe L edges.

The interest in the study of the electronic structure of these two materials stems partly from their practical importance in mineral science, solar cells (FeS_2), and biomedical applications (FeO), and partly in understanding the influence of different magnetic ground states to the electronic properties of these ferrites and transition metal compounds in common.

3.2 Electronic properties of FeO and FeS_2

3.2.1 Experimental details

The samples were both single crystals, a synthetic crystal of FeO and a natural mineral crystal of FeS_2, and the crystalline quality was verified by Laue radiography. The NEXAFS and RIXS measurements were performed at beamline 8.0.1 of the Advanced Light Source, Berkeley, USA [119]. Linearly polarized p light was incident on the sample and emission was measured along the electric vector of the incident light. This geometry minimizes diffuse elastic scattering, since the Brewster angle in the soft x-ray range is very close to 90° so that the reflectivity for p light is very nearly zero. For x-ray absorption, the photon energy resolution was set to 0.3 eV, and for x-ray emission 0.7 eV. The measured total resolution on the elastic peak (spectrometer + incident photons) at the Fe L edge was 1.6 eV in second order of the spectrometer. Emitted photon energies at the iron edge were calibrated to the Fe metal L_α normal emission maximum at 705.0 eV, and at the oxygen K edge to the emission from MgO at 525.0 eV. The energy scale of the monochromator was calibrated by measuring the NEXAFS spectrum of iron metal and calibrating the onset to the XPS binding energy at 706.8 eV. The accuracy of this procedure was limited by the surface cleanliness of the iron metal, which was cleaned by scraping in UHV. Samples were prepared by scraping with a diamond file under vacuum.

The XPS measurements were carried out in the Dept. of Physics, Osnabrück, using a PHI 5600CI multi-technique spectrometer with the total energy resolution (photons + analyser resolution) set to 0.35 eV. Samples were prepared by fracturing in vacuum.

3.2.2 XPS

3.2.2.1 Valence Band

Valence band spectra of both compounds are shown in Fig. 3.2. The spectrum of FeO is in good agreement with Sangaletti and Parmigiani [151], and we label the features in the same way. The overall shape shows some small differences with respect to the spectrum of Zimmerman *et al.* [152], with lower intensity in our spectra at the top of the valence band.

The spectrum of FeS_2 is in good agreement with that of Kurmaev *et al.* [148] For FeS_2, the valence band can be divided into three main regions. The first region is characterized by an intense, narrow peak between the top of the valence band and about 2 eV, and the second by states spanning the energy range from 2 eV to about 9 eV. The third region consists of the S 3s states split into antibonding and bonding sub-bands arising at 13 eV and 16 eV, respectively. The sharp peak immediately below the Fermi level comprises mainly Fe 3d states of t_{2g} character, with a minor contribution of S 3p character. The main contribution to the DOS in the energy region between 2 eV and 9 eV comes from the disulfide ions.

The FeO spectrum has recently been calculated by Takahashi and Igarashi [127] within both the LDA+U and Hartree-Fock approximations. They predicted 3 components in the upper part of the valence band, labelled by them a_1, a_2 and a_3.

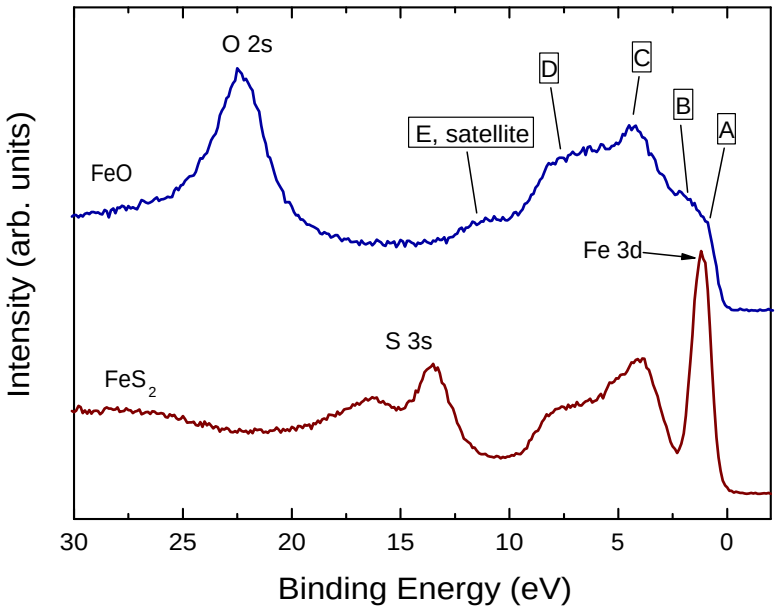

Figure 3.2: Valence band x-ray photoelectron spectra of FeO (upper curve) and FeS_2 (lower curve).

We identify their highest energy peak, a_1, which consists of nearly pure Fe $3d$ t_{2g} minority-spin states, with feature A; this corresponds to the band labelled a_{1g} by Mazin and Anisimov [126]. Feature B is identified with their peak a_2 and consists of majority-spin e_g states strongly hybridized with oxygen p states; the label is the same in rhombohedral symmetry [126]. One can identify the third peak C at about 4 eV with their feature a_3, which consists of t_{2g} majority spin states of Fe $3d$ character. This gives a valence band exchange splitting between peaks A and C of about 3 eV. The rest of the valence band down to about 8 eV binding energy consists of mixed Fe and O states. There is also a satellite, E, around 11 eV, labelled by them d. The peak at 22 eV is due to emission from the O $2s$ orbital.

3.2.2.2 Fe $3s$ and Fe $3p$ core levels

The Fe $3p$ spectra of the two compounds are shown in Fig. 3.3. The spectra of both compounds consist of a broad main line with unresolved $3p_{1/2}$ and $3p_{3/2}$ components. The full width at half maximum of the $3p$ peak of FeS_2 is 2.6 eV while the FeO line is broader, 4.2 eV, due to unresolved multiplet splitting, and the satellite structure of FeO appears to be better resolved than in the paper of Zimmerman *et al.* [152]. Both lines show satellite structure which is summarized in table 3.2.

The Fe $3s$ photoemission spectra of FeO and FeS_2 are also shown in Fig. 3.3 (upper panel). For the FeS_2 spectrum, the scale of the off-resonant spectra published

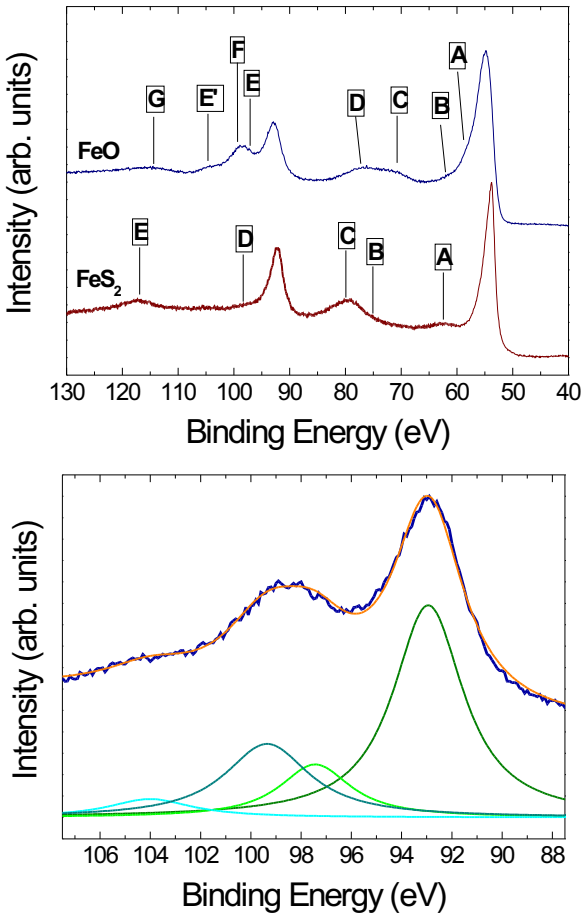

Figure 3.3: Upper panel: XPS spectra of the Fe 3*s* and 3*p* core levels of FeS_2 and FeO. Lower panel: Fit of the Fe 3*s* region of FeO. Fit parameters: width of high spin peaks: 3.4 eV; width of low spin peaks, 4.3 eV. Branching ratio low spin / high spin: 0.42; intensity ratio charge transfer peak / parent peak: 0.25.

by Suga *et al.* [150] is too small to determine the degree of agreement while the FeO spectrum agrees with the data of Sangaletti and Parmigiani [151] and Zimmerman *et al.* [152]. Note that due to configuration interaction there is strong mixing of the $3p^{-2}3d^{n+1}$ states with the $3s-1$ state [153].

The FeS_2 3*s* level shows a rather broad main line (width 2.7 eV) with a weak satellite *D* extending to about 8 eV below the maximum of the main line, and another satellite *E* at 25 eV from the main line. The Fe 3*s* spectrum of FeO consists of two well separated peaks assigned to the high spin state ($3s^1 3d^6 \underline{L}$) labelled 3*s* and low spin ($3s^1 3d^6 \underline{L}$) state, peak *F*, in which the 3*s* core electron is coupled parallel and antiparallel respectively to the majority spin 3*d* electrons. Since the Néel temperature is 200 K, the existence of exchange splitting at room temperature is an indication of short range magnetic ordering at room temperature. Additionally, a weak satellite assigned by Sangaletti and Parmigiani [151] to charge transfer excitations is visible

as peak $E^{'}$. We fitted the peaks in a manner similar to these authors and constrained the charge transfer energy to be the same for both peaks, with the widths of each pair of spin states equal. We obtained the values for the exchange splitting and charge transfer excitations shown in table 3.2, and the fit parameters shown in the caption. The magnitude of the splitting is proportional to the number of unpaired d electrons, i. e., proportional to the total spin S, and the predicted relative intensities are given by the relation $S/(S+1)$. The experimental integrated intensity ratio is 0.51 compared with the theoretical value of 2/3.

3.2.2.3 Fe $2p$ core levels

Figure 3.4 shows the Fe $2p$ photoelectron lines of FeS_2 and FeO.

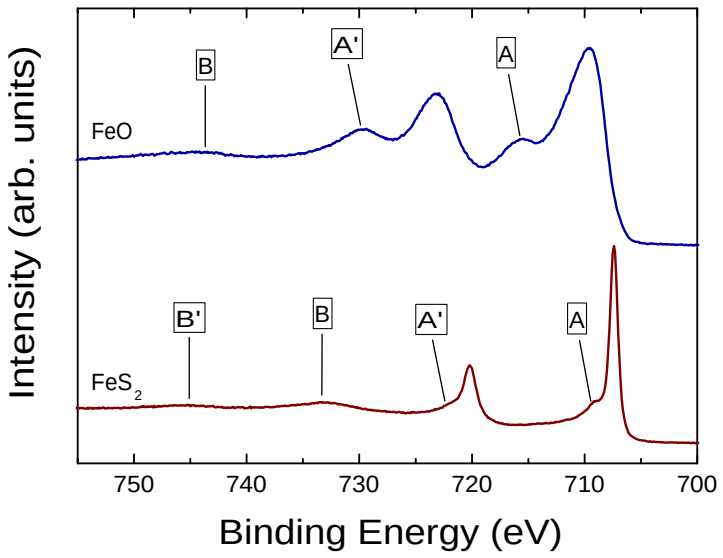

Figure 3.4: XPS Fe $2p$ core level of FeO (upper curve) and XPS Fe $2p$ core levels of FeS_2 (lower curve).

The $2p_{3/2}$ and $2p_{1/2}$ emission lines consist of single narrow peaks of widths 1.0 eV and 1.6 eV respectively. We observe weak satellites (A and $A^{'}$) as tails on the high-binding energy sides of the main peaks, at about 1.7 eV relative binding energy, and broad spin-orbit split peaks B and $B^{'}$ at 25 eV. Bocquet *et al.* [154] also observed a broadening towards higher binding energy and attributed this to bulk satellite structure, although the energy position did not match well their calculated position of about 5 eV relative to the main peak. This tail has alternatively been attributed to surface states of Fe(II) and Fe(III) ions created on the cleavage surface by the rupture of Fe-S and S-S bonds [155, 156]. The use of a single photon energy in the present study does not allow us to distinguish between these assignments, however we cannot rule out the possibility that inelastic losses due to *dd* excitations are also

present in this spectrum. The main peaks can be fitted with a Voigt function, having a Gausssian width of 0.45 to 0.50 eV (accounting for experimental resolution and phonon broadening), and Lorentzian widths of 0.7 and 1.1 eV for the $2p_{3/2}$ and $2p_{1/2}$ lines respectively.

The $2p$ XPS spectrum of FeO is much broader (thr $2p_{3/2}$ line 5.5 eV), due to multiplet splitting, with two main bands corresponding to the spin-orbit split components and two main satellites, Fig. 3.4 and table 3.2. The spectrum is rather better resolved than that of Zimmerman *et al.* [152] The feature at 35 eV below the $2p_{3/2}$ line (labelled $B^{'}$) is clearly resolved and was assigned to oxygen KLL Auger emission by Bocquet *et al.* [154] who used Mg $K\alpha$ radiation. However it is clearly observed in the present spectrum with Al $K\alpha$ excitation, as in the spectrum of Zimmerman *et al.* , so it appears to be a loss rather than an Auger peak. Furthermore, it does not have a spin-orbit split component around 13 eV higher binding energy so we assign it to a loss involving the $2p_{1/2}$ line, with a loss energy of 21 eV. The corresponding loss peak of the $2p_{3/2}$ line is obscured by the 6.5 eV satellite of the $2p_{1/2}$ line.

3.2.2.4 S $2p$ and O $1s$ core levels

The S $2p_{3/2}$ and $2p_{1/2}$ doublet lines of FeS_2 are observed at 162.7 eV and 163.9 eV binding energy, respectively, Fig. 3.5.

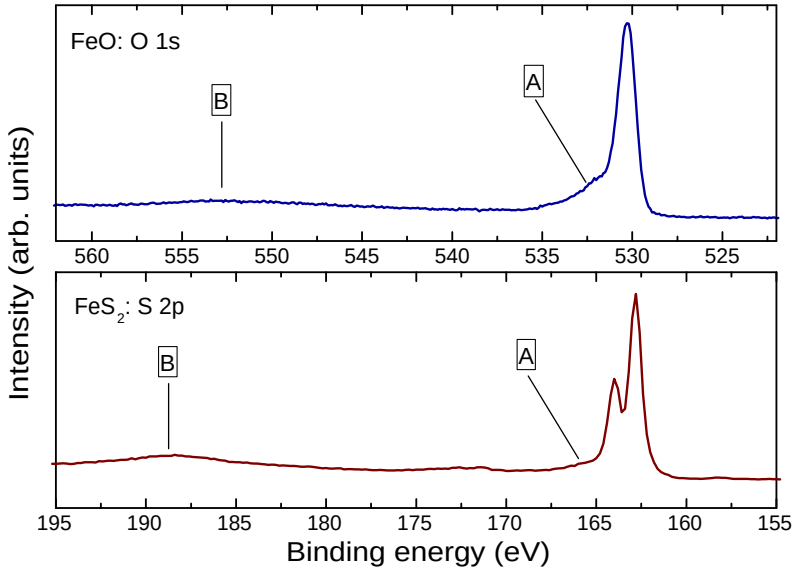

Figure 3.5: XPS O $1s$ core levels of FeO (upper panel) and XPS S $2p$ core level of FeS_2 (lower panel).

Due to the high kinetic energy of the photoelectrons (∼1223 eV), the spectrum is not very surface sensitive, so traces of surface sulfur [155, 156] are not visible in

the present spectrum. The feature labelled A corresponds to a loss of 2 eV and is assigned to interband transitions, which may be either intrinsic to the photoemission process, or due to losses during transmission to the surface. The plasmon peak B is also visible at 25 eV.

The O 1s spectrum of FeO is shown in Fig. 3.5. It agrees reasonably well with that of Sangaletti and Parmigiani [151]: the main peak has the same width but the feature A is a little stronger in the present spectrum. This is assigned to surface defects.

3.2.3 XAS

Figure 3.6 displays the NEXAFS spectrum of FeS_2 and FeO at the Fe L edges.

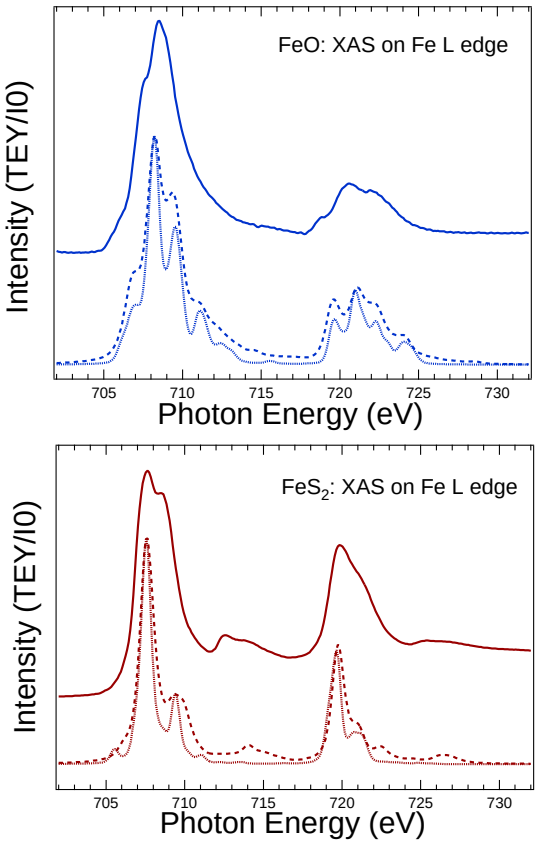

Figure 3.6: The Fe 2p XAS for FeO (upper panel) and FeS_2 (lower panel) compared with a crystal field multiplet calculation (dotted line) and a charge transfer multiplet calculation (dashed line).

The FeO spectrum is much better resolved than the EELS spectrum of Colliex *et al.* [136], and is a little better resolved than the NEXAFS spectrum reported by Crocombette *et al.* [133]. In particular it consists of a small shoulder at

about 706 eV, a main asymmetric peak at 708-709 eV and a tail at 711 eV, representing excitations from the Fe $2p_{3/2}$ core level. The calculations of Crocombette *et al.* indicate that the spectrum is the sum of many multiplets and they predicted the observed features, although the asymmetry in the main peak was expected to be reversed, that is, more intense at lower energy. Like in the spectrum obtained by Crocombette *et al.* there is a weak structure at about 715 eV, which is not predicted by the calculations; this may be a satellite structure, due for instance to a spin flip transition as in [157]. The second main structure starting at around 718 eV consists of excitations from the $2p_{1/2}$ core level to empty d states. Again our spectra are better resolved than those of Crocombette *et al.* and agree reasonably well with their calculations: four peaks are predicted, and three are resolved.

The Fe L near edge x-ray absorption spectrum of iron sulfide is also shown in Fig. 3.6. It is similar to that of Mosselmans *et al.* [143] and Thole and van der Laan [145], but considerably better resolved. The spectrum resembles that of Suga *et al.* [150].

Since the $2p$ core hole wave function has a large overlap with the $3d$ wave function the $2p$ absorbtion is determined by the transition probability $3d^n \rightarrow 2p^5 3d^{n+1}$. This strong overlap of the wave function also is responsible for the multiplet effect that makes the $2p$ x-ray absorption line shapes to be given, in first approximation, by the $2p^5 3d^7$ final state in case of a Fe^{2+} ion. This wave function overlap is an atomic effect that can be very large. It creates final states that are found after the vector coupling of the $2p$ and $3d$ wave functions. Thus, the analysis of $2p \rightarrow 3d$ XAS with help of single particle band structure calculations is limited. In order to identify the electronic interactions accounting for the experimental data, full multiplet calculations on O_h symmetry within the ligand field approximation as well as the charge transfer approximation were carried out. The calculations were performed by using the TT-multiplets computer program [59, 55]. The results of these calculations are also plotted in Fig. 3.6.

Table 3.1: The crystal field parameters as used in the Fe $2p$ XAS simulations. The $3d$ spin-orbit coupling was set to zero.

Compound	Type of calculation	10 Dq (eV)	Δ (eV)	Slater-Condon (% of atomic)
FeO	ligand field	1.2	-	80 %
FeS_2	ligand field	2.1	-	80 %
FeO	charge transfer	1.0	4.0	80 %
FeS_2	charge transfer	1.5	4.0	80 %

Table 3.1 sums up the parameters used for the simulation of the Fe $2p$ XAS spectra of FeO and FeS_2. A series of calculations with varying the crystal field parameter 10 Dq from 1.0 eV and 2.4 eV was performed. In case of the presented calculations, for FeO the crystal field strength has been set to 1.2 eV in the ligand field approach, and for FeS_2 to 2.1 eV. For the charge transfer calculations, crystal field parameters of 1.0 eV and 1.5 eV for FeO and FeS_2 were used, the energy difference Δ between the

$3d^6$ and $3d^7\underline{L}$ configuration was set to 4.0 eV. For all calculations the Slater-Condon parameters were reduced to 80% of their calculated (atomic) Hartree-Fock values in order to account for intra-atomic relaxation effects. The calculated features were convoluted with a 0.3 eV FWHM Lorentzian to take into account the experimental broadening.

Abrupt changes in the spectra are indicative of spin transitions [61], for small and moderate crystal fields the configuration has high spin, however, if the crystal field strength exceeds the energy gain of the spin pairing, the spin state changes to low spin (in the case of divalent Fe). For Fe^{2+} this transition occurs at 10 $Dq = 2.0$ eV in the ligand field approach and at 1.5 eV within the charge transfer approximation.

3.2.4 RIXS

3.2.4.1 FeO

Figure 3.7 presents an overview of x-ray emission spectra taken at the Fe L edge of FeO for selected incident photon energies.

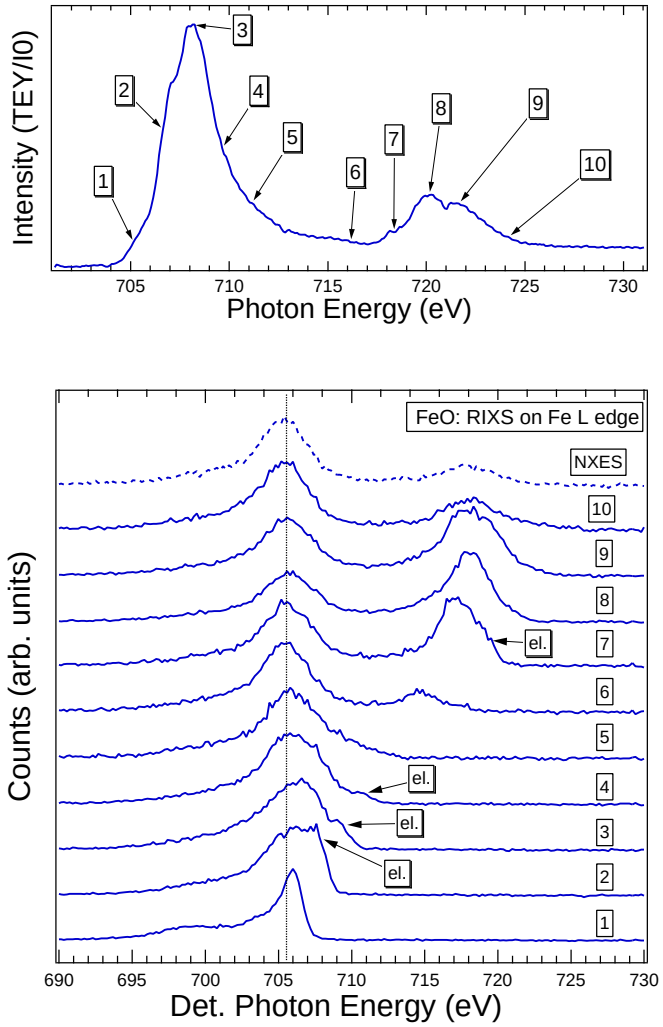

Figure 3.7: RIXS of FeO (lower panel) at the selected excitation energies as indicated in the Fe $2p$ XAS (upper panel): 1: 706.0 eV; 2: 707.5 eV; 3: 709.0 eV; 4: 710.5 eV; 5: 712.0 eV; 6: 717.0 eV; 7: 719.25 eV; 8: 721.0 eV; 9: 722.5 eV and 10: 725.0 eV.

At the first four energies, and the sixth energy, the elastic peak is visible as a partly resolved shoulder or clear peak. As the incident photon energy increases from below threshold, $2p_{3/2} \rightarrow 3d$ transitions are first excited and x-rays of corresponding energy are emitted, converging to L_α radiation above threshold. At higher excitation energy, $2p_{3/2} \rightarrow 3d$ transitions are excited and a second emission peak converging to L_β grows in. The lower energy L_α radiation continues to be emitted due to weak

direct excitation of $2p_{3/2}$ holes, but mostly due to Coster-Kronig (CK) transitions, which leave a hole in the $2p_{3/2}$ level. However the intensity of the second L_β peak at the maximum of the absorption resonance (spectra 8 and 9) is higher than the intensity of the first peak. For FeS_2, the relative intensities are inverted, these data are analyzed in detail below.

At highest energy, 730 eV, the spectrum corresponds to normal, non-resonant fluorescence. The L_α/L_β spin orbit splitting is 12.5 eV, significantly smaller than the XPS value of 13.5 eV. This is not surprising as the XPS spectrum consists of many multiplets, while the emission spectrum consists of the projection of the valence density of states on the core holes.

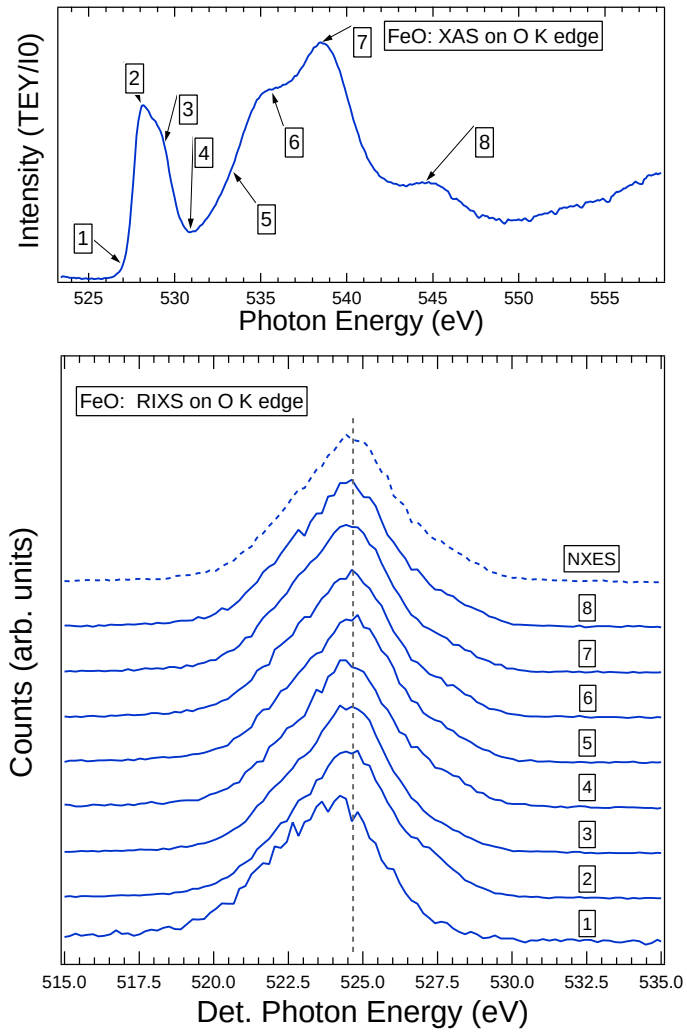

Figure 3.8: Resonant inelastic x-ray spectra at the oxygen edge of FeO (lower panel), at the incident photon energies indicated in the corresponding O 1*s* XAS (upper panel): 1: 527.0 eV; 2: 528.0 eV; 3: 529.3 eV; 4: 531.0 eV; 5: 533.3 eV; 6: 535.5 eV; 7: 538.5 eV and 8: 544.5 eV.

The NEXAFS spectrum of oxygen in FeO was also measured, Fig. 3.8. It is

similar to that of Wu *et al.* [134] in overall shape, but we see an additional shoulder on the high energy side of the first main peak and the second main band is weaker with respect to the first structure in the present data.

The emission spectra at the oxygen edge, Fig. 3.8, show little structure and apart from the lowest energies, do not change much with incident photon energy. Only at threshold, 529.7 eV, is the maximum of the spectrum shifted about 0.5 eV to lower energy. The spectra taken under resonant Raman scattering conditions and off-resonance ("normal emission") are rather similar. On the maximum of the first absorption peak at 530.8 eV, a small increase in energy on the high energy side is probably due to the elastic peak. Above these energies, the spectral shape is constant and only the intensity changes significantly, proportionally to the absorption coefficient, and the spectra resemble the normal fluorescence taken well above threshold at 561 eV.

3.2.4.2 FeS_2

The emission spectra in Fig. 3.9 were taken at the resonance energies indicated in the corresponding XAS spectrum, and above threshold (730 eV).

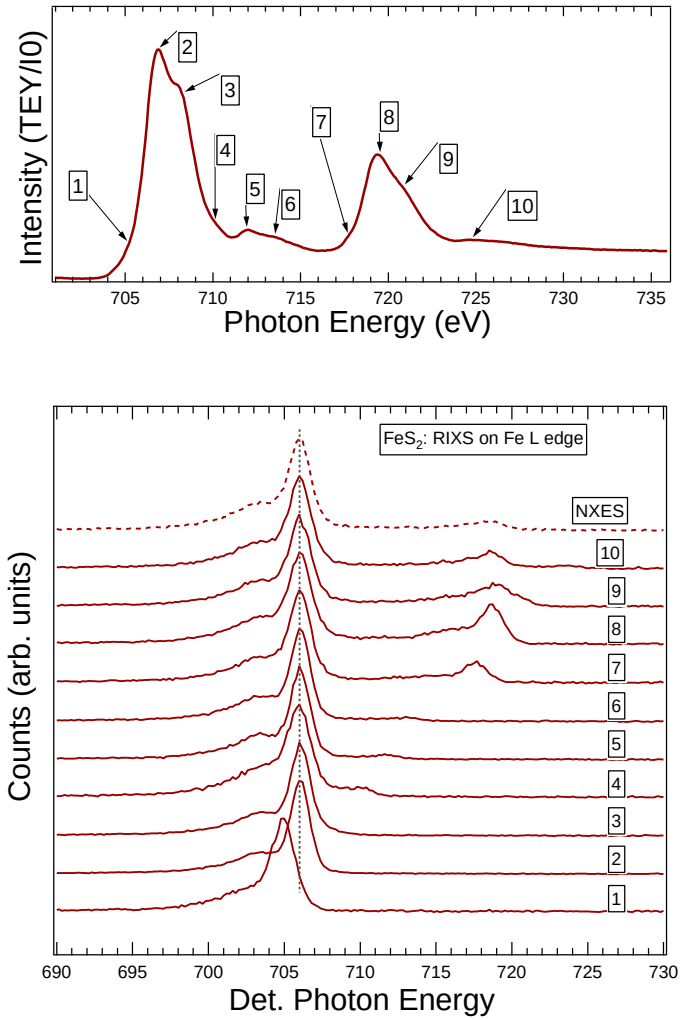

Figure 3.9: Resonant x-ray scattering from the Fe L edge of FeS_2. The excitation energies are those indicated in the corresponding XAS: 1: 706.4 eV; 2: 708.0 eV; 3: 709.45 eV; 4: 711.45 eV; 5: 713.2 eV; 6: 714.7 eV; 7: 718.95 eV; 8: 720.6 eV; 9: 722.1 eV and 10: 725.9 eV.

The structure around 712 eV is due to decay of $2p_{3/2}$ holes and converges to L_α emission while the feature around 725 eV is due to decay of $2p_{1/2}$ holes and converges to L_β emission. The weaker peaks indicated by markers between these static structures are due to elastic scattering. Note that the L_β peak on the maximum of the $2p_{1/2}$ absorption has a maximum intensity of about half of the L_α peak (spectrum 8). This is in strong contrast to the data of FeO presented above.

3.2.5 Discussion

3.2.5.1 XPS

The Fe $3p$ and $3s$ photoelectrons of FeS_2 and FeO have high kinetic energy, ∼1400 eV, and are thus characteristic of the bulk rather than the surface. The spectra show an inelastic loss or satellite tail, peaks A and D of FeS_2 and A and B of FeO in Fig. 3.3, over an energy range of 8 eV. Since the lifetime widths of these states are rather large it can not be expected to resolve fine structure, but this result suggests that the additional structure observed in the Fe $2p$ spectra (∼770 eV kinetic energy) may not be entirely due to emission from surface states, but may contain a component due to satellite or loss structure. One can assign these structures to interband transitions, occurring either in the photoexcitation process (shake up) or during transport of the photoelectron to the surface (loss peaks).

The $3s$ and $3p$ core levels both show satellites at 25 eV, while the $2p_{1/2}$ peak shows a satellite at 21 eV (the 20-25 eV loss region of the $2p_{3/2}$ peak overlaps the $2p_{1/2}$ peak). These structures, and the broad loss peak at 30 eV binding energy in the valence spectrum, have been assigned to bulk plasmons by Suga *et al.* [150]; however the energy is different for the $2p_{1/2}$ core level. Although the loss peaks are diffuse, there is a clear difference of several eV in the positions of the maxima. We assign this to differences in the core localization between inner and outer core levels. In addition the $3p$ peak shows a weak structure B around 18 eV which is tentatively assigned to a multiplet.

The $2p$ core level XPS spectra of FeO are in generally good agreement with the published spectra, with few exceptions. Like Sangaletti and Parmigiani [151], one does not observe the $2p_{1/2}$ satellite at 11.4 eV reported by Zimmerman *et al.* [152] in the present study but the existence of the broad, high energy satellite at 21 eV can be confirmed. Since also similar satellites of the $3s$ and $3p$ levels are observed, this feature does not appear to be a feature related to multiplet structure. The assignment of Zimmerman *et al.* to a plasmon loss is plausible, but one should point out that the energy loss and width is also consistent with an oxygen $2s$-conduction band inelastic loss.

While Bocquet *et al.* [154] assigned the $2p$ main lines of FeO to $d^7\underline{L}$ final states, and the $2p$ satellites to d^6 final states, the more recent calculations of Zimmerman *et al.* concluded that these were only the main characters. Due to configuration interaction, the main line has significant d^6 and $d^8\underline{L}^2$ character while the satellite has significant $d^8\underline{L}^2$ character mixed with the main configuration.

Table 3.2: Summary of the XPS satellite structure.

Compound	Satellite	XPS Main line	Energy with respect to maximum of the main line (eV)	Assignment
FeS_2	A	Fe $3p$	8.7	Shake up, inelastic loss
FeS_2	B	Fe $3p$	18.0	Multiplet
FeS_2	C	Fe $3p$	25.5 ± 0.5	Plasmon
FeS_2	D	Fe $3s$	0.0 - 8.0	Shake up, inelastic loss
FeS_2	E	Fe $3s$	25.5 ± 1.0	Plasmon
FeS_2	A, A'	Fe $2p$	1.7	d^6 final state (main line $d^7\underline{L}$)
FeS_2	B, B'	Fe $2p$	21.0	Plasmon
FeS_2	A	S $2p$	2.0	Interband transitions
FeS_2	B	S $2p$	25.0	Plasmon
FeO	A	Fe $3p$	3.5	Multiplet
FeO	B	Fe $3p$	5.5 - 9.0	Multiplet
FeO	C	Fe $3p$	17.0 ± 1.0	Multiplet
FeO	D	Fe $3p$	22.0 ± 1.0	Plasmon
FeO	E, E'	Fe $3s$	4.4	d^6 final state (main line $d^7\underline{L}$)
FeO	F	Fe $3s$	6.4	Exchange splitting
FeO	G	Fe $3s$	22.0 ± 1.0	Plasmon
FeO	A	Fe $2p_{3/2}$	5.9	d^6 final state (main line $d^7\underline{L}$)
FeO	A'	Fe $2p_{1/2}$	6.5	d^6 final state (main line $d^7\underline{L}$)
FeO	B	Fe $2p_{1/2}$	21.0	Plasmon [152]
FeO	A	O $1s$	1.0 - 5.0	Defects
FeO	B	O $1s$	22.0	Plasmon [152]

3.2.5.2 XAS

Turning now to the XAS spectroscopy, for FeS_2, Mosselmans *et al.* [143] and Suga *et al.* [150] have previously discussed the Fe $2p$ edge absorption spectrum. Many calculations of the band structure exist, but some only calculate the near gap region, while those of Zeng and Holzwarth [147] and Zhao *et al.* [146] extend up to 10-15 eV above threshold. Both of these calculations predict a substantial gap in the density of unoccupied states above the empty Fe d states, while Eyert *et al.* [149] predict a gap beginning at 4 eV above the top of the valence band, but did not calculate the width of the gap. The first peak in the absorption spectrum is due to transitions to the conduction band, and is strong because the lower part of this band has mainly Fe $3d$ character. One can interpret the weak peaks labeled 5 and 6 in Fig. 3.9 as due to transitions to this second band. Mosselmans *et al.* [143] assigned this peak to a satellite structure due to hybridization, an explanation similar to the argument

of Bocquet *et al.* [154] for XPS satellites. However one may do a first interpretation with help of band structure calculations for the following reasons: (1) the two-peak structure is replicated for the Fe $2p_{1/2}$ curve, peak 10 of Fig. 3.9; (2) in the spectra of Mosselmans *et al.* [143], an analogous peak appears at the Fe K edge, suggesting mixing of Fe states. This second unoccupied band has mainly Fe s character according to Zhao *et al.* [146], or mainly S p character according to Zeng and Holzwarth [147]. In either case the Fe $2p$ absorption is expected to be weak, and this is indeed the case. The energy difference between the bottom of the conduction band and the onset of this band, about 5-6 eV, is consistent with the S L absorption spectrum, which indicates a similar gap. The experimental value of the gap of about 6-7 eV in the density of unoccupied states is in better agreement with the calculations of Zeng and Holzwarth [147], 6 eV, or Eyert *et al.* [149], than Zhao and Callaway [146], about 10 eV.

Regarding to the multiplet calculations, as already mentioned due to the large $2p-3d$ core hole wave function overlap the $2p$ x-ray absorption spectra of $3d$ TM metal compounds can often not be described properly within the single particle picture. The reason for this discrepancy is not that the density-of-states is calculated wrongly, but that one does observe a spectrum comprising overlapping band-like and multiplet-like effects, sometimes the multiplet-effects can be very strong and dominate the spectrum. The dotted lines in Fig. 3.6 represent the results of the ligand field calculation, the corresponding input parameters are collected in Table 3.1. For FeO, the crystal field strength was set to 1.2 eV. Furthermore, Fe^{2+} has a partly filled t_{2g} ground state $^5T_2$, and thus may be affected by $3d$ spin-orbit coupling. Simulations with and without $3d$ spin-orbit coupling have been performed and it has been found that the simulation without spin-orbit coupling matches the experimental spectrum better. An overall good agreement between the ligand field simulation and the experimental spectrum for FeO is found. Some deviations are found for the pre-peaks the L_3 and L_3 edges located around 706 and 719 eV, the calculated intensity is higher than the experimental one. In case of the charge transfer calculation also the the $3d^7\underline{L}$ configuration has been included into the calculation (dashed line). The calculated spectrum resembles that of Crocombette *et al.* [133], small differences may be explained by the way the ligand hole is treated in the different computer codes[1]. By increasing the crystal field strength to 2.0 eV the spin state of the simulated spectrum changes from high spin to low spin. The calculated ligand field spectrum resembles that of van der Laan and Kirkman [61], the main features of the experimental spectrum of FeS_2 are also reproduced. However, the calculated intensity of the two large shoulders at the L_3 and the L_2 is essentially too low. The same fact is found in corresponding charge transfer simulation, however, the features located in between the L_3 and L_2 edges as well as the tail which follows the L_2 absorption edge are somewhat better reproduced within the charge transfer approach. Thus, the shoulders as well as the smaller features may not only consist out of multiplet effects. Hence, the additional analysis of the FeS_2 XAS by means of band structure calculations as describes in the beginning of this section is justified.

[1]The TT-multiplets program considers the ligand hole as having d symmetry, whereas, cluster programs take into account the real p-ligand states.

3.2.5.3 RIXS

With regard to the resonant x-ray emission spectra, the symmetry allowed excitations for the resonant scattering process are *dd* (monopole) and *ds* (quadrupole) excitations localized on the Fe atoms for atomic-like symmetry. Specifically, in octahedral symmetry, the core p states belong to the irreducible representation t_1, while the d states split into t_{2g} and e_g bands. In x-ray absorption, transitions from $2p$ (t_1) states to both of these bands are dipole allowed; similarly, for x-ray emission, transitions from t_{2g} and e_g bands to the core hole (t_1) are permitted. Thus we expect final states with a hole in a t_{2g} or e_g band, and an electron in a previously unoccupied t_{2g} or e_g band. The long tail of excitations covering about 5 eV below the main emission line is broader than would be expected from t_{2g} to e_g Fe *dd* transitions only. We therefore conclude that the occupied $3d-e_g$ states of the valence band participate in these transitions, although all calculations agree that this part of the valence band, from about 2 to 7.5 eV, have mainly S $3p$ character. The present results suggest strong covalency and that the Fe $3d$ states are strongly hybridized in this region.

At higher energy, the spectra correspond to normal fluorescence emission, and can be interpreted in terms of the projection of states of d character on the $2p$ core hole. The overall shape is consistent with the calculated band structure: an intense high energy peak due to the t_{2g} states, and a weak broader band due to the e_g states, as discussed by Kurmaev *et al.* [148]. The valence band photoemission spectrum can be seen as a measurement of the total density of states, while the normal emission spectrum can be seen as the measurement of the density of states projected on the core hole. In Fig. 3.2 XPS and XES are compared and this illustrates that the strong peak in the valence band indeed corresponds to Fe $3d$ states, while the second main peak has less Fe character.

For FeO, the RIXS resonant spectra excited close to the absorption threshold (1) shows an inelastic loss at 2.2 eV below the elastic recombination peak (el.), which can be interpreted in the light of the band structure calculations of Mazin and Anisimov [126]. The 2.2 eV band corresponds to transitions from the uppermost occupied band minority spin a_{1g} band, (derived from t_{2g}) to the second unoccupied band; the theoretical energy difference is 2.3 eV. For the broad band at 4-9 eV, the band structure calculations predict that the third unoccupied band lies at 3.4-4.2 eV above the highest occupied d band, and is followed by other bands. Furthermore the deeper lying occupied t_{2g} derived majority spin bands may also participate in this broad transition, as in the case of FeS_2.

The emission spectra at excitation energies further above threshold are again interpreted in terms of the projection of the density of states of the valence band on the $2p$ core hole site. The excited electron is expected to be no longer spin polarized well above threshold so that holes with both minority and majority spin character are created. In addition a range of multiplets are created with various couplings between the core hole and valence angular momentum. The fluorescence then arises from many valence to core transitions, and both the L_α and L_β emission have a width of about 10 eV. This suggests that the d character of the valence band, although higher in some bands, is spread over a similar range. This conclusion supports the interpretation of the valence band photoemission given some time ago by Bagus *et al.* [137].

As noted above, the branching ratios of L_α to L_β emission on excitation at the

L_2 edge are very different for FeS_2 and FeO. A related effect has been observed for Heusler alloys [158], in which the intensity of L_α emission on L_3 excitation and L_β emission on L_2 excitation has been related to their ferromagnetic properties. The present observation of a large difference suggests a relation between the spin state and the L_2/L_3 emission branching ratio for L_2 excitation, in a way similar to how the spin state and absorption branching ratio were related by Thole and van der Laan [145]. Clearly the difference in the L_α/L_β ratio is due to differences in the Coster-Kronig (CK) rate for the two samples, with a much faster rate for FeS_2.

One can consider a simplified, one-electron LS coupling picture, and the case of fully spin polarized valence and conduction bands. The initially excited $2p$ electron will be of minority spin. In the CK process a $2p_{1/2}$ core hole decays to a $2p_{3/2}$ hole and the energy liberated ($2p$ spin-orbit splitting) promotes a valence electron to an unoccupied state. However the CK process cannot fill the core hole with a spin conserving transition as the valence band consists of majority spin electrons only. Similarly the electron promoted from the valence band to the conduction band must undergo a transition that does not conserve spin. As spin-flip processes are generally weaker than spin conserving ones, this qualitative argument illustrates how in a system that is not completely polarized, the CK transition probability is reduced.

We therefore suggest a general rule for resonant emission at the L_2 edge, similar to the branching ratios in absorption: the L_α/L_β emission branching ratio is higher for high spin ground states than for low spin ground states. Thus not only x-ray absorption but also resonant emission can be used to characterize the magnetic state of a material. This argument and the rule are analogous to those of Yablonskikh *et al.* [158] who discussed the ratio of L_β emission intensity for excitation at the L_2 edge to L_α emission intensity for excitation at the L_3 edge. To analyze in detail the L_α/L_β intensity ratio and the CK lifetime, we assume a simple model based on equation (1) of Magnuson *et al.* [159]. The contribution due to directly excited $2p_{3/2}$ core holes and that due to CK derived core holes is summed incoherently. We assume that the probability for creation of $2p_{3/2}$ holes across the L_2 absorption peak is constant and equal to the absorption cross-section just before the L_2 peak. Then we integrate the emission intensity over a range of 15 eV of each of the two emission bands, L_α and L_β, and assume this is proportional to the total emission cross-section. We adapt the equation of Magnuson *et al.* by omitting the factor 2 for the statistical branching ratio, and adding a term that describes the L_α emission due to CK decay. The ratio of x-ray emission intensities, L_α/L_β for the two edges is:

$$I_X^{Ratio} = \frac{\sigma^{3/2}\,\Gamma_X^{3/2} + \sigma^{1/2}\,\Gamma_{CK}^{1/2}\,\Gamma_X^{3/2}\;/\;(\Gamma_X^{1/2} + \Gamma_A^{1/2} + \Gamma_{CK}^{1/2})}{\Gamma_X^{3/2} + \Gamma_A^{3/2}} \Big/ \frac{\sigma^{1/2}\,\Gamma_X^{1/2}}{\Gamma_X^{1/2} + \Gamma_A^{1/2} + \Gamma_{CK}^{1/2}} \quad (3.1)$$

where Γ represents a transition rate, the superscripts indicate the $2p_{1/2}$ or $2p_{3/2}$ holes; the subscripts indicate that the lifetime is for X-ray emission, Auger or CK processes; and the symbols σ are absorption cross-section. Following Magnu-

son *et al.* [159], we use the approximation , so that:

$$\begin{aligned} I_X^{Ratio} =& \frac{\sigma^{3/2}\,\Gamma_X^{3/2} + \sigma^{1/2}\,\Gamma_{CK}^{1/2}\,\Gamma_X^{3/2}\ /\ (\Gamma_A^{1/2} +\ \Gamma_{CK}^{1/2})}{\Gamma_A^{3/2}} \Big/ \frac{\sigma^{1/2}\,\Gamma_X^{1/2}}{\Gamma_A^{1/2} +\ \Gamma_{CK}^{1/2}} \\ =& \frac{\sigma^{3/2}\,\Gamma_A^{1/2} +\ \Gamma_{CK}^{1/2}\ + \sigma^{1/2}\,\Gamma_X^{1/2}}{\sigma^{1/2}\,\Gamma_A^{3/2}} \end{aligned} \tag{3.2}$$

The values of Γ calculated by Yin *et al.* [160] are given in table 3.3. We can estimate the value for FeS_2 from the difference in the Lorentzian part of the XPS widths of the two spin-orbit split components, $1.1 - 0.7 = 0.4$ eV, which is rather smaller than their value of 0.58 eV.

Table 3.3: Input parameters and results of Coster-Kronig (CK) analysis [161].

Parameter	FeS_2	FeO
$\Gamma_{CK}^{1/2}$ [160]	0.58 eV	-
$\Gamma_{CK}^{1/2}$ (calculated)	-	0.28 eV
$\Gamma_A^{1/2}$ [160]	0.35 eV	0.35 eV
$\Gamma_A^{3/2}$ [160]	0.55 eV	0.55 eV
$\sigma^{3/2}$ (L_2 edge)	0.21 arb. units	0.11 arb. units
$\sigma^{1/2}$ (L_2 edge)	0.72 arb. units	0.58 arb. units
Branching ratio $I(L_2)/I(L_3)$, expt.	2.1	0.74
Branching ratio (calulated)	2.4	-

We assume that their other values are an adequate approximation and calculate the expected branching ratio: we obtain a value of 2.4 compared with the measured value of 2.1, which is reasonable. For FeO the XPS peaks are very broad due to multiplet splitting, so we cannot obtain any information about lifetime broadening. In this case we assume that the Auger decay rates are the same as the atomic values of Yin *et al.* [160] since Fe is in the same valence state, i.e., it has the same number of electrons. All of the difference is assigned to the difference in relative cross sections and Coster-Kronig rates. Using the measured relative cross-sections and branching ratio we calculate the Coster-Kronig rate and find a value of 0.28 eV, much lower than the values for FeS_2. Thus the significant lowering of the Coster-Kronig rate by the existence of magnetic ordering is about half the non-magnetic rate.

3.3 Resonant Raman x-ray scattering at the S $2p$ edge of FeS_2

3.3.1 Introduction

In resonant inelastic x-ray scattering (RIXS), an incident photon is inelastically scattered from a target and a photon of lower energy is detected. Under Resonant Raman conditions, this gives rise to loss features characteristic of excitations from the ground state and is thus a powerful method for investigating low energy excitations of a wide range of materials [162, 163]. Since the final state of the system does not contain a core hole, the relaxation effects which can complicate core level photoemission are absent.

In this paper we apply RIXS to iron pyrite, FeS_2, at the sulfur $2p$ edge. This material is cubic and non-magnetic (in contrast with many other iron compounds, such as the oxides) and has been widely studied both theoretically and experimentally. A previous RIXS study reported the L edge emission spectra of this compound, but not resonant Raman scattering at the S $2p$ edge [148]. Many theoretical band structures have been reported [148, 164, 146, 147, 149, 165, 166], which agree in the general description of the electronic structure. The top of the valence band is composed mainly of Fe $3d$ states, while the bottom of the conduction band is composed mostly of S $3p$ states. Theory confirms the experimental finding that the material is semiconducting, and a second gap is predicted about 3 to 4 eV above the valence band.

Figure 3.10 shows a scheme of the electronic structure. There are some differences in the theoretical calculations: Zhao et al obtain a width of about 7 eV for this second gap, while Zeng and Holzwarth and Muscat *et al.* obtain values of about 3 eV. The material has also been studied by NEXAFS (near edge x-ray absorption spectroscopy) at the S L edge [168] and by Fe L edge NEXAFS [143, 145, 144, 150, 161] (see also Chapter 3.2).

As mentioned above, a previous study [148] did not find Raman scattering, although recently there have been a couple reports of this effect in transition metal compounds, all of which are oxides [169, 170, 171]. To date dispersion of the loss features in the soft x-ray range has been observed mainly at metal and O $1s$ edges and we wished to determine whether this occurred for other anions, such as disulphide.

3.3.2 Experimental details

The measurements were performed at the BACH beamline [122], at Elettra, Trieste, using the COMIXS spectrometer [121]. The total resolution for x-ray emission, measured from the width of the elastic peak was set to 0.4 eV. The emitted photon energy was calibrated to 148 eV for the maximum of the L_3M_1 emission peak and the incident photon energy was calibrated to this value by observing the difference between the elastic and inelastic peaks. The incident light was p polarized, that means linearly polarized in the horizontal plane with the sample surface in the vertical plane. The XPS and electron energy loss spectra (EELS) were measured with a PHI 5600 CI multi-technique spectrometer with a total resolution of about 0.6 eV.

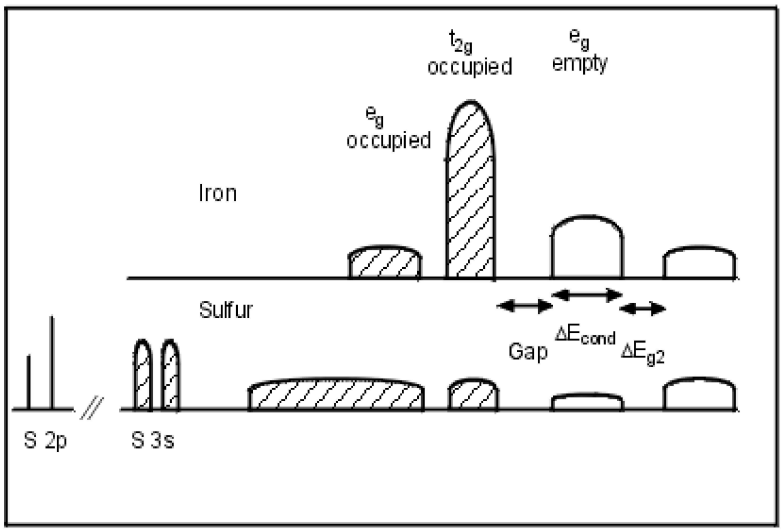

Figure 3.10: A schematic plot of the density of states of FeS_2 [167]. The empty states above the gap consist of a conduction band of width ΔE_{cond}, a gap of width ΔE_{g2}, and another empty band above this.

For this experiment the sample was prepared by fracturing in situ.

3.3.3 Results and discussion

The NEXAFS spectrum at the S L edge is shown in Fig. 3.11 and is similar to the spectrum of Li *et al.* [168] except that the high energy features are more intense in the present spectrum. The Fe L edge spectrum [161] is shown for comparison and has been shifted to align the onsets. The NEXAFS spectrum shows four main features, labelled A to D in Fig. 3.11, of which the first two show clear spin-orbit splitting of the S $2p_{1/2} - 2p_{3/2}$ core levels. Li *et al.* [168] assigned the states labelled A to S $3s$ like states, and the states B to "the antibonding S $3s$-like states at the conduction-band minimum". However the $3s$ states form a bonding-antibonding pair at 13−15 eV binding energy, so it is unlikely that they participate in the conduction band. We assign peak A to states at the minimum of the conduction band, and peak B to the second band above the conduction band. The character is indeed probably s like, but selection rules require only that they bands be of t_{2g} or e_g symmetry for the transition from $2p$ core states (which belong to t_1 in octahedral symmetry) to be allowed.

We note that there is a substantial gap between the two bands. Assuming the spectrum consists of a superposition of essentially similar L_3 and L_2 spectra that are simply shifted in energy by the spin-orbit splitting, we can estimate the width of the

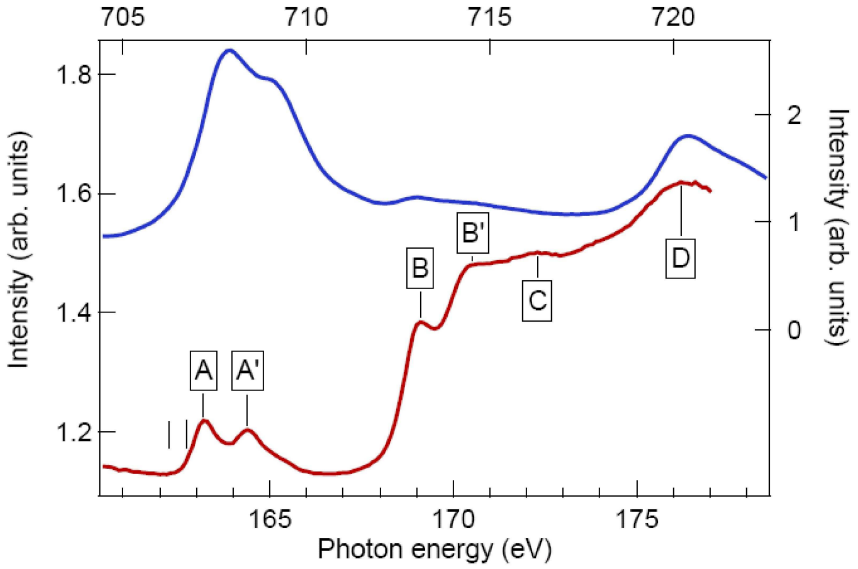

Figure 3.11: X-ray absorption spectra of FeS_2 [167]: lower curve, S L edge; the vertical bars mark the photon energy range in which the spectra in Fig. 3.12 were taken. Upper curve: Fe L edge

conduction band to be 2.4 eV and the width of the second gap above the optical gap to be about 3 eV. These values are summarized in Table 3.4 together with more recent theoretical estimates. Best agreement is found with the calculations of Zeng and Holzwarth [147] and Muscat *et al.* [166].

The comparison with the Fe L_3 edge absorption spectrum in Fig. 3.11 shows that a feature also occurs at the same energy above the onset of absorption, but is much weaker. We have argued elsewhere [161] that this indicates that the peak in the Fe spectrum is not a satellite due for instance to two-hole or multiplet excitations [143], but is a feature of the band structure. It is clear that feature B has only very weak Fe character, and much stronger S character: it is predicted to have either mainly Fe s character,[146] or mainly S p character [147], or mainly S $3d$ character [166].

Peaks C and D were assigned by Li *et al.* [168] to empty S $3d$-like states of e_g and t_{2g} symmetry. They are not observed in the Fe L edge spectrum: peak C is in any case very weak, while peak D overlaps the Fe L_2 edge, and is obscured.

RIXS spectra were taken across the resonance and in general are similar to those of Kurmaev *et al.* [148] and so are not shown here. Resonant spectra taken close to the onset of absorption, Fig. 3.12, were different. The spectra are plotted on a loss energy scale, and the elastic scattering peak is very strong at this incident

Table 3.4: Theoretical and experimental values of the width of the conduction band (E_{cond}) and the width of the second gap (E_{g2}) above the optical gap.

E_{cond} (eV)	E_{g2} (eV)	Reference
2.4	7.0	5
3.3	2.8	6
3.3		7
2.5		12
2.6	3.5	9
2.8		8
2.4	3.0	Present work, experimental

energy. Elastic scattering is in this case mostly due to diffuse scattering associated with surface roughness, that is, microfacets that are aligned at the specular angle. The scattering angle in the present experiment is 60°, far from the Brewster angle (scattering angle $\sim$ 90°), at which the reflectivity is zero for p polarized light. In their previous study, Kurmaev *et al.* [148] used a scattering angle of 90° so that the elastic peak was very weak. Weak inelastic loss peaks can be distinguished near the elastic peak. The energy loss is constant over a range of 0.3 to 0.4 eV of the incident beam, that is, the loss peak disperses with the elastic peak, while at higher energy the emitted energy is constant. There is a peak close to the elastic peak with a loss energy of 1.9 eV and a width of 0.9 eV, and a broad loss peak at about 14 eV due to $L_{2,3}M_1$ emission. The latter is very broad so that it is difficult to observe small energy changes, but it does not appear to show a constant energy loss, that is, it is due to incoherent scattering. The present results show that resonant Raman conditions can be established in a narrow energy range close to the S $2p_{3/2}$ threshold. At lower energy, there is insufficient intensity to observe the loss peak, while at higher energy the peak is stationary in energy. We identify this peak by comparison with available band structure calculations. All calculations which explicitly show the band structure (and not just the density of states) predict that the conduction band minimum is located at the Γ point. This band has S *sp* character - indeed its parabolic shape and dispersion suggest an *s*-like band. We assign the weak x-ray absorption at the onset of $2p$ threshold to transitions from $2p$ states to these states at the bottom of the conduction band. Emission is then assigned to final states with a hole in the flat t_{2g} band and an electron in the previously unoccupied e_g band. This picture implies that the system is correlated as this one-electron final state does not correspond to the one-electron intermediate state with an electron in the *sp* band. Muscat *et al.* have recently drawn attention to the importance of correlation in this system [166].

In a resonant photoemission spectroscopy study of graphite [107] it was possible to extract band structure information, but this does not appear to be the case for FeS_2. If the behaviour were similar, the present results imply that there exist roughly parallel valence and conduction bands of S character, which would explain the constant energy loss. However such bands cannot be distinguished in published band

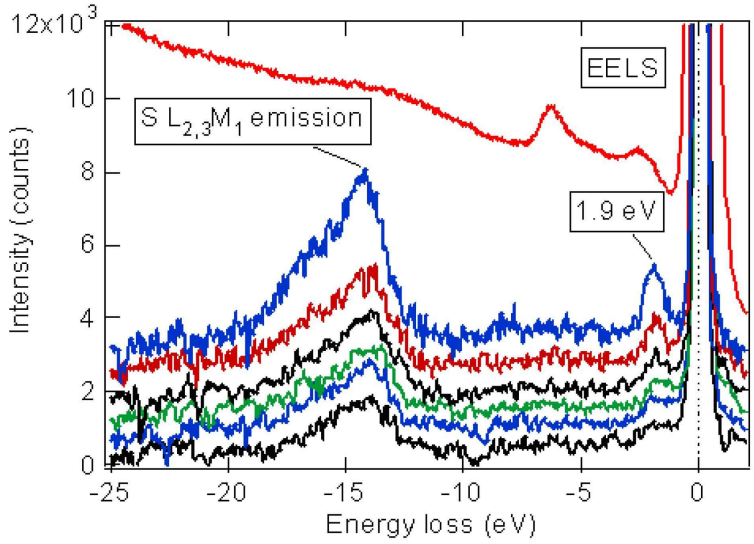

Figure 3.12: Resonant inelastic x-ray emission spectra of FeS_2 at the S L edge [167]. Photon energy (from bottom to top): 162.3, 162.35, 162.4, 162.45, 162.5, 162.7 eV. Top curve: the inelastic EELS spectrum, recorded at an incident energy of 200 eV.

structure calculations. Rather, the difference appears to be due to the fundamentally different electronic structures. Graphite has strongly delocalized valence and conduction bands, and under resonant x-ray scattering conditions, the spectral peaks show clear dispersion. Pyrite has a more complicated electronic structure in which the S states are more delocalized and the Fe states more localized. It appears that the existence of correlation has the effect of masking one electron-behaviour. If this is generally true, and many more studies are needed to test this idea, then it means that the technique reported in ref. [107] may be restricted to wide band materials.

In comparison the EELS spectrum in Fig. 3.13 shows losses at 2.6 and 6.25 eV, with a weak structure at 4.3 eV. EELS measures electronic transitions without restrictions due to momentum conservation or site selectivity. The first loss peak is at higher energy than the loss peak observed in RIXS and is likely to be dominated by Fe dd transitions, as these constitute the highest joint density of states. However other transitions may be present, such as non k-conserving transitions that shift the center of gravity of the peak. The advantage of RIXS in terms of selectivity is clear.

The calculations of Zeng and Holzwarth predict that the occupied t_{2g} band is overwhelmingly (about 90 %) of Fe d character while the unoccupied e_g band is predicted to be mainly (about 75 %) of Fe character. However since we observe

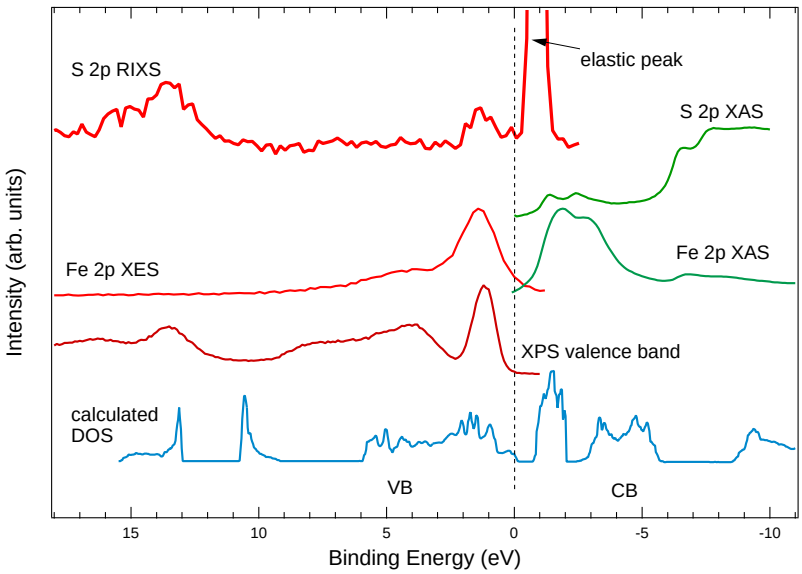

Figure 3.13: Summary of electronic structure: calculated partial density of Fe and S states, after Zeng and Holzwarth [147]; XPS spectrum of the valence band; Fe $2p$ and S $2p$ x-ray absorption spectra; and the Resonant Inelastic X-ray Scattering spectrum at the S $2p$ edge.

a loss peak, the density of states at the S $2p$ hole is significant. The binding energy of the t_{2g} band extends from the top of the valence band to about 1 eV, while the e_g band is centered at about 1.5 eV. Thus the sum of the one-electron energies, 1.5−2.5 eV, covers the experimental value of 1.9 eV and the width of 0.9 eV is approximately as expected. We conclude that excitonic effects are not strong and that the present final state, if not the scattering process, can be described in a one-electron picture. The electronic structure is summarized in Fig. 3.13, where the digitized calculated spectra of Zeng and Holzwarth [147] are compared with spectroscopic measurements of the density of occupied (XPS and RIXS) and unoccupied (NEXAFS) states. The inelastic loss correlates well with the main peak seen in XPS, although in XPS the peak is due mainly to Fe d states.

3.4 Conclusions

We have reported photoemission and photoabsorption spectra of FeS_2 and FeO that are generally in good agreement with most recent results, with some spectra showing marked improvement in resolution. The assignment of peaks such as plasmons has been confirmed, while alternatives have been suggested for others, for example for the $2p$ satellite structure. The plasmon energies are 21-25 eV for both compounds and all core levels. We have shown that pyrite shows a high degree of covalency in the emission spectra, and we have assigned the losses observed. The very different ratios of L_α to L_β integrated intensity for L_2 excitation of the two compounds has been explained in terms of the magnetic structure of FeO, which inhibits Coster-Kronig processes. We propose that this is a general rule, like those proposed by Yablonskikh *et al.* [172] for the ratio of L_α intensity for L_3 excitation to L_β intensity for L_2 excitation, and by Thole and van der Laan for x-ray absorption. Excitations of the valence d electrons to unoccupied states have been located at 1.0 eV and over a band of 4-5 eV for FeS_2, while for FeO they lie at 2 and 4-9 eV. The density of states projected on the Fe $2p$ and oxygen $1s$ core holes have been determined from NXES.

In summary, by setting up resonant Raman conditions over a narrow energy range near the S $2p$ threshold we are able to probe Fe dd excitations between the valence and conduction band, via the hybridization of the Fe states with sulfur states. The results, and the S $2p$ edge NEXAFS, can be interpreted in the light of published band structure calculations.

Chapter 4

Manganites

4.1 Electronic structure of A- and B-site doped manganites

4.1.1 Introduction

The lanthanum manganese perovskites of the type $La_{1-x}A_xMnO_3$ (A=Ca,Sr,Ba) display a remarkably rich phase diagram as a function of temperature, magnetic field and doping that is due to the intricate interplay of charge, spin, orbital and lattice degrees of freedom. This competition of different phases on the nanoscale has been the subject of many studies during the last few years [12, 13, 173]. The variety of properties is often due to different behavior of $3d$ electrons, which may be more or less localized, giving rise to intra-atomic correlation effects of varying strength. Moreover they may either experience the orbital degeneracy compatible with a given crystal space group or lift this degeneracy, due to the Jahn-Teller distortion. These types of behavior are to a large extent mediated by Mn $3d$ − O $2p$ hybridization, thus establishing a link to the chemistry of the compound in question. In a cubic crystal the Jahn-Teller distortion leads to a lowering of the symmetry and thus a splitting of the e_g level. Its occupation, influenced by doping and energetic position, strongly influences the hybridization between the Mn $3d$ and the O $2p$ states, which is crucial for understanding the family of colossal magnetoresistance compounds. In the last few years, studies of these compounds were stimulated by the discovery of colossal magnetoresistance (CMR), a huge negative change in the electrical resistance induced by an applied magnetic field [1, 2]. This behavior has been associated with half metallic ferromagnetism, meaning that one spin channel is metallic while the other is insulating [4, 5]. The spin polarized Mn $3d$ electrons are the charge carriers.

$La_{1-x}Ba_xMnO_3$ is the first reported CMR model compound [1] with a Curie temperature of around 340 K [174]. The crystal structure changes from orthorhombic through rhombohedral ($x > 0.13$) to cubic ($x > 0.35$), and the system shows ferromagnetic behavior for Ba-concentrations $x \geq 0.15$. It also undergoes a metal to insulator transition at $x \approx 0.20$ [175, 174]. This system has been subjected to intense investigation of its crystallographic and magnetic properties [175, 176], various phase transitions [174, 177, 178] and spin dynamics [179] during the last few

years. Also the effect of Mn-site doping leads to remarkable magnetic transport phenomena since B-site doping with another 3d-element like Fe, Co, or Ni has a direct influence on the magnetic transport and exchange properties of the compound [180]. In particular, $La_{1-x}Ba_xMn_{1-y}Co_yO_3$ is of interest since the Co substitution leads to a strong ferromagnetic Mn^{4+}-O-Co^{2+} interaction. For single crystals of $La_{0.74}Ba_{0.26}Mn_{1-y}Co_yO_3$ it has been found that the Curie temperature decreases with increasing Co content whereas the magnetoresistance shows sharp maxima, especially at a Co concentration of around 16% [181]. Recently some photoemission spectra of these compounds have been reported, revealing the divalent character of the Co ions in $La_{0.74}Ba_{0.26}Mn_{1-y}Co_yO_3$ [182, 183].

Nonetheless, in particular for the A- and B-site doped compounds, very few x-ray spectroscopic data are available up to now. However, for the analysis of the spatial distribution of the electron density and chemical bonding the methods of x-ray and photoelectron spectroscopy provide a tool of unique precision, especially useful in combination with first-principles electronic structure studies. Several electronic structure studies have been reported, which nonetheless leave a number of essential questions unanswered. A number of spectroscopic techniques, mostly x-ray photoelectron spectroscopy (XPS) and x-ray absorption spectroscopy (XAS) have been applied to $La_{1-x}A_xMnO_3$ (A=Ca,Sr) [184, 185]. Although the band structure of $LaMnO_3$ and $La_{1-x}A_xMnO_3$ (A=Ca,Sr,Ba) has been also studied theoretically by several local spin density approximation (LSDA) studies [185, 186, 187, 188], the importance and strength of correlation effects are still a controversial subject. For example, one of the most recent works comes to the conclusion that the stabilization of the cubic phase is more important for ferromagnetism in hole doped compounds than the double-exchange mechanism [188].

Element and site specific resonant inelastic x-ray scattering (RIXS) spectroscopy [107, 51] is also a powerful tool to investigate the electronic structure of transition metal compounds. XAS is the starting point for RIXS measurements since an excitation energy close to an absorption threshold leads to very different decay states than those at higher excitation energies (20-30 eV above the XAS edge) which instead results in normal x-ray emission spectroscopy (XES). This reflects the partial density of states which is symmetry-selected by the dipole selection and broadened by the lifetime broadening. During resonant excitation an electron is promoted from a core state at (or just above) the Fermi energy. The emission features can be understood as being due to coherent elastic scattering and inelastic loss features which can be associated with the difference in energy between initial and final state. The RIXS cross section is described by the Kramers-Heisenberg equation [70, 71]. The possibilities in the study of correlated systems by means of RIXS go from Coulomb interactions on high energy scales over charge transfer excitations to lower excitation energies, especially regarding optically inaccessible bands, such as *dd* transitions [72, 73, 74].

The $2p$ transition metal (TM) oxides belong to the most interesting materials for RIXS since the interpretation of the TM $2p \rightarrow 3d \rightarrow 2p$ RIXS data is controversial and leads to the limitations of both the band model and the Anderson impurity model. Butorin *et al.* reported RIXS spectra of MnO to be due to low-lying *dd* and charge transfer excitations, which can be described by an atomic multiplet calculation [72]. Furthermore the Mn $2p \rightarrow 3d \rightarrow 2p$ RIXS spectra of $La_{0.5}Ca_{0.5}MnO_3$ have been

interpreted within a charge transfer multiplet approach [189]. On the other hand side Kurmaev *et al.* found that the effect of interatomic hybridization between Mn 3*d* and O 2*p* states is present over the whole valence band in $Pr_{0.5}Sr_{0.5}MnO_3$, leading to a more itinerant electronic structure [190]. For this kind of system, RIXS leads to an observation of structural features in the occupied part of the valence band, and RIXS measures the joint DOS for vertical transitions [190, 191, 167]. Very recently, the Mn $2p \rightarrow 3d \rightarrow 2p$ RIXS in $La_{1-x}Na_xMnO_3$ has been interpreted as well in the band picture [192].

We present here, for the first time a detailed x-ray spectroscopic study of $La_{1-x}Ba_xMnO_3$ ($0.2 \leq x \leq 0.55$) and the mentioned A- and B-site doped manganites using of a number of complementary spectroscopic techniques, namely XPS, XES, XAS and RIXS. The results are analyzed along the questions stated above, compared with measurements on undoped $LaMnO_3$ and discussed in the light of both available band structure calculations [186, 187, 188, 193], as well as cluster model calculations [72, 104].

4.1.2 Experimental details

High quality $La_{1-x}Ba_xMnO_3$ ($0 \leq x \leq 0.55$) polycrystals were produced by solid state reaction at the Moscow State Steel and Alloys Institute. X-ray analysis was used to check the structural quality and single phase nature of the specimens. $La_{0.76}Ba_{0.24}Mn_{0.84}Co_{0.16}O_3$ and $La_{0.76}Ba_{0.24}Mn_{0.78}Ni_{0.22}O_3$ single crystals were grown by the flux melt method [181].

The XAS, XES and RIXS data of $La_{1-x}Ba_xMnO_3$ were performed at room temperature at beamline 8.0.1 at the Advanced Light Source, Berkeley, using the x-ray fluorescence end station of the University of Tennessee at Knoxville [119]. Linearly polarized light with polarization in the horizontal plane was incident on the sample whose surface was vertical. Emission was measured along the electric vector of the incident light in the horizontal plane, that is, at a scattering angle of 90°. This geometry minimizes diffuse elastic scattering from the surface, since the Brewster angle in the soft x-ray range is usually very close to 45° so that the reflectivity for $\overrightarrow{p}$ light is very nearly zero. Photons with an energy of 520-670 eV are provided to the end station via a spherical 925 lines/mm grating monochromator. The Mn, Co and Ni $3d \rightarrow 2p$ and O $2p \rightarrow 1s$ XES spectra were obtained with a 1500 lines/mm, 10 meter radius grating. The spectra were calibrated using a reference sample of pure Mn metal and MgO, respectively. Mn 2*p* and O 1*s* x-ray absorption spectra were measured with the same experimental conditions in total electron yield mode. Samples were scraped in air with a diamond file in order to reduce surface contamination just before mounting them in the transfer chamber.

The XES spectroscopy on the $La_{0.76}Ba_{0.24}Mn_{0.84}Co_{0.16}O_3$ and $La_{0.76}Ba_{0.24}Mn_{0.78}Ni_{0.22}O_3$ single crystals was performed at the undulator based beamline ID12-2, using the rotatable spectrometer apparatus (ROSA) at BESSY II, Berlin.

XPS valence bands were recorded using a PHI 5600CI multi-technique spectrometer with monochromatic Al Kα ($h\nu = 1486.6$ eV) radiation of 0.3 eV FWHM, and with the sample at room temperature. The resolution of the analyzer is 1.5 % of the pass energy, i.e., 0.35 eV, giving an overall resolution of about 0.6 eV. All spectra were obtained using a 400 μm diameter analysis area. The samples were fractured

in situ. The survey spectrum taken directly after breaking the samples shows only low contamination by hydrocarbons, and C $2p$ states should have no influence on the valence band spectra. The spectra were calibrated against the Au $f_{7/2}$ signal from Au-foil (E_B=84.0 eV) [113]. During all measurements, the pressure in the main chamber was kept below $1 \cdot 10^{-9}$ mbar.

4.1.3 Results

4.1.3.1 XPS and XES

In order to study the influence of Ba-doping on the Mn $3d$ – O $2p$ hybridization we performed XES measurements on the Mn $2p$ and the O $1s$ edge of undoped $LaMnO_3$ and all of the Ba-doped compounds.

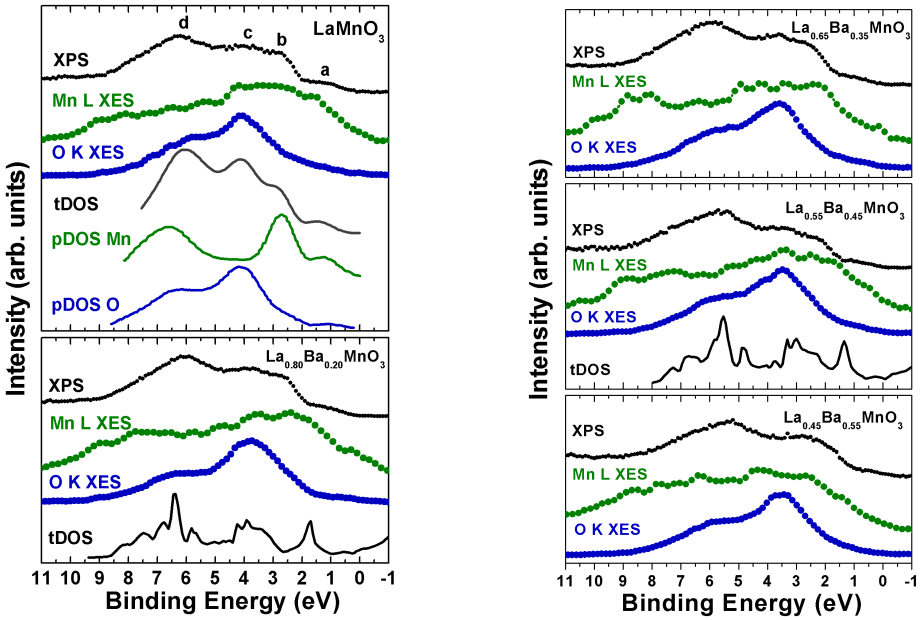

Figure 4.1: XPS valence band and XES spectra of the Mn $2p$ and the O $1s$ edge (plotted on a binding energy scale using the XPS core level binding energies) of $La_{1-x}Ba_xMnO_3$ ($0.0 \leq x \leq 0.55$) [194]. For $LaMnO_3$, $La_{0.8}Ba_{0.2}MnO_3$ and $La_{0.55}Ba_{0.45}MnO_3$ the experimental data are compared with the results of theoretical band structure calculations (labelled (tDOS) and (pDOS), respectively). The calculated data for $LaMnO_3$ have been extracted from Ravindran *et al.* [188], whereas the values for the Ba-doped compounds have been taken from Youn *et al.* [187].

The results are shown in Fig. 4.1. The Mn $2p$ and O $1s$ XES spectra and the theoretical results [188, 187] have been plotted on a binding energy scale for comparison. The Mn $2p$ and O $1s$ XES spectra overlap in a large part of the valence band, indicating significant hybridization between Mn $3d$ and O $2p$ states. The valence band region consists of four distinct features labelled $a - d$, which, for the undoped

$LaMnO_3$, are in excellent agreement with the theoretical results. From the Mn $2p$ XES spectra, band a just below the Fermi level can be attributed to Mn $3d$ states, and moreover theory reveals band a to be due to Mn e_g electrons [188]. Feature b is located at a binding energy of 2.5 eV and mainly formed by Mn t_{2g} states whereas band c around 4 eV can be associated with overlapping Mn $3d$ t_{2g} and O $2p$ states. Finally, feature d (6 eV) is composed of by hybridized Mn $3d$, O $2p$ and La $4d$ bands. Doping with Ba^{2+} leads to a shift of features $b-d$ towards the Fermi level. According to the calculations [188, 187] band b shifts from 2.5 eV in $LaMnO_3$ to around 1.8 eV in $La_{0.8}Ba_{0.2}MnO_3$ and to approximately 1.4 eV binding energy in $La_{0.60}Ba_{0.40}MnO_3$. Feature c moves closer to E_F from 4 eV in the valence band of $LaMnO_3$ to $\sim$ 3.6 eV in the case of $La_{0.8}Ba_{0.2}MnO_3$ and finally to around 3.2 eV at higher Ba-concentration while for the band d a slight shift from 6 eV ($LaMnO_3$) to 5.5 eV for the valence band of $La_{0.60}Ba_{0.40}MnO_3$ is predicted [187]. These shifts are also present in the experimental results. Feature b moves closer to the Fermi level from 2.5 eV binding energy in $LaMnO_3$ to 2 eV in the case of $La_{0.55}Ba_{0.45}MnO_3$, a smaller shift than the calculated one but detectable. The experimental data also reveal that feature b becomes broader with increasing doping concentration, which may indicate that the Mn t_{2g} states are somewhat less localized at higher hole concentration. In the case of feature c one can observe a shift from 4.5 eV to 3.5 eV at higher doping concentration (x=0.45, 0.55). Also band d shows a resolvable shift from around 6 eV ($LaMnO_3$) to 5.5 eV in the XPS valence band spectra for compounds with higher Ba concentrations. The Mn $2p$ XES show a broad structure between the Fermi level and 5 eV comprising valence band features $a-c$. The maximum intensities of the O $1s$ XES spectra, mainly comprising band c, show a shift from 4.5 eV for $LaMnO_3$ to 3.5 eV, degenerate with the Mn t_{2g} states, for $La_{0.45}Ba_{0.55}MnO_3$.

Fig. 4.2 displays the XPS valence band and the XES spectra of $La_{0.76}Ba_{0.24}Mn_{0.84}Co_{0.16}O_3$ and $La_{0.76}Ba_{0.24}Mn_{0.78}Ni_{0.22}O_3$, respectively. All spectra were normalized to the Ba $5p$ peak. The valence band region of these materials consist, as for $La_{1-x}Ba_xMnO_3$ of four distinct bands ($a-d$) spanning the energy range from E_F to about 11 eV. However, the intensity ratios of the bands $a-c$ in the valence bands of the Mn-site doped samples show significant differences compared to $La_{0.75}Ba_{0.25}MnO_3$. The valence band of $La_{0.76}Ba_{0.24}Mn_{0.84}Co_{0.16}O_3$ shows higher intensities for bands $a-c$ compared to the reference spectrum, while feature d is of approximately the same intensity in both spectra. In Fig. 4.2 we present also a difference spectrum of the valence spectra of $La_{0.76}Ba_{0.24}Mn_{0.84}Co_{0.16}O_3$ and $La_{0.75}Ba_{0.25}MnO_3$, which can be associated, to a large extend, with the Co $3d$ contribution to the Co-doped sample. The high intensity of band a in the Co-doped compound is a clear indication of the presence of Co $3d$ e_g states near E_F, whereas the Co t_{2g} states probably mainly contribute to the features b and c over an energy range of 2 - 4.5 eV on a binding energy scale. A more detailed discussion with respect to the Co concentration dependence in this kind of material can be found elsewhere [183]. The XPS valence band of $La_{0.76}Ba_{0.24}Mn_{0.84}Co_{0.16}O_3$ is also compared with the Mn $2p$, Co $2p$, and O $1s$ XES measurements. As for $La_{1-x}Ba_xMnO_3$ the XES experiment reveals strongly overlapping Mn $3d$ and O $2p$ denities over the whole valence band region. The Co $2p$ XES also suggests hybridization and charge transfer between Co $3d$ and O $2p$ bands over a large region of the valence band.

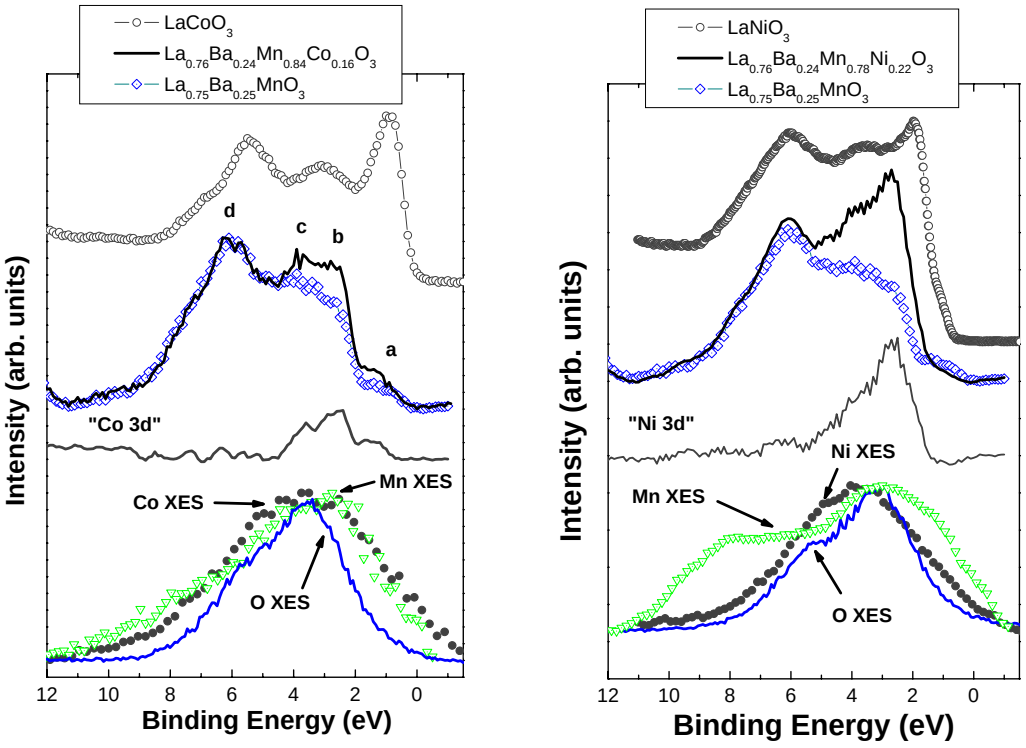

Figure 4.2: XPS valence band and the corresponding XES data of $La_{0.76}Ba_{0.24}Mn_{0.84}Co_{0.16}O_3$ (upper panel) and $La_{0.76}Ba_{0.24}Mn_{0.78}Ni_{0.22}O_3$ (lower panel) plotted on a binding energy scale [194]. For comparison also the XPS valence band of $La_{0.75}Ba_{0.25}MnO_3$ has been normalized to the Ba $5p$ XPS peak. The subtraction of the two spectra leads to a representation of the Co $3d$ and the Ni $3d$ contributions to the valence band of the corresponding sample. The XPS valence bands of $LaCoO_3$ and $LaNiO_3$ are also shown for comparison.

In the case of $La_{0.76}Ba_{0.24}Mn_{0.78}Ni_{0.22}O_3$, band a shows a significantly lower intensity compared to that of $La_{0.75}Ba_{0.25}MnO_3$, suggesting a lower occupation of the e_g states around E_F. Features b and c are much more pronounced for the Ni-doped compound. Finally, band d has the same intensity for both compounds. We also derived the difference spectrum between the valence band spectra of the Ni-doped compound and $La_{0.75}Ba_{0.25}MnO_3$, the difference reflects the Ni $3d$ contributions to the valence band of $La_{0.76}Ba_{0.24}Mn_{0.78}Ni_{0.22}O_3$. The net spectrum suggests a large contribution of Ni $3d$ states, spanning the energy range of around 1.5 - 5 eV. Also the comparison with the XPS valence spectrum of $LaNiO_3$ confirms that the Ni $3d$ states contribute the valence band at lower binding energies than the Mn $3d$ states except the e_g levels near E_F. The Mn $2p$ and O $1s$ XES spectra again indicate strong hybridzation effects between Mn $3d$ and O $2p$, spanning the energy range from 1 eV to about 9 eV. Also the Ni $2p$ XES, which reaches its maximum intensity at around 3.5 eV, suggests a significant overlapping with O $2p$ states, mainly between 2 eV and 7 eV.

4.1.3.2 XAS and RIXS

In Fig. 4.3 we present the XAS spectra of the Mn $L_{2,3}$ edge and the O K edge of $LaMnO_3$.

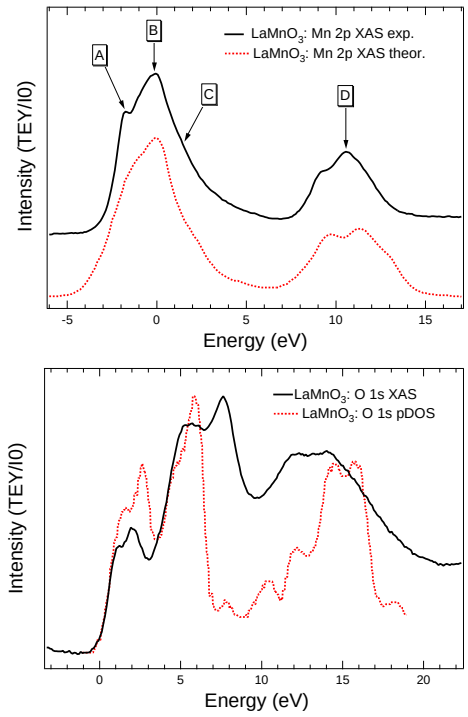

Figure 4.3: Mn $L_{2,3}$ (upper panel) and O K (lower panel) XAS regions of $LaMnO_3$ [194]. The data were recorded in total electron yield (TEY) mode. Labels A-D indicate the excitation energies of the RIXS spectra recorded at the Mn L edge. The Mn $2p$ XAS multiplet calculation has been adapted from Taguchi *et al.* [104], the O K XAS is compared with a LDA+U calculation from Wessely *et al.* [193].

The Mn $L_{2,3}$ XAS spectra, which are dominated by transitions to Mn $3d$ states but also contain contributions from Mn $4s$ states, consist of two broad multiplets due to the spin-orbit splitting of the Mn $2p$ core hole. $2p$ edge XAS spectra of TM oxides can be understood in the framework of atomic multiplet theory [56], since the XAS structures are affected by the core hole wave function. The Mn $2p$ XAS spectra (Fig. 4.3) can be compared with ligand-field multiplet calculations for Mn^{3+} in D_{4h} crystal symmetry [195]. However, excellent agreement is achieved with recently reported model calculations of a $(MnO_6)^{10-}$ cluster based upon a charge transfer model in D_{4h} symmetry [104]. Following the argumentation of Taguchi *et al.* the ground state can be described as a superposition of 73.6% $3d^4$ states and 26.4% $3d^5\underline{L}$ charge-transfer states. Hole doping with Ba leads to a change of the chemical environment, and consequently to a chemical shift of the maxima of the Mn L_3 edge towards higher photon energies, as it has been previously observed in $La_{1-x}Sr_xMnO_3$ [196].

In the case of XAS on the ligand K edge the situation is different. The O K edge spectra are dominated by transitions to O $2p$ states hybridized with Mn $3d$ states

and Mn 4*s* contributions [188]. The spectra consist of two features, the first of which is located at photon energies around 528 eV while the second one is a broad features between 531 and 535 eV. For $LaMnO_3$ we find that two prominent peaks are present in the low energy feature. This result can be described accurately with single-particle calculations [188].

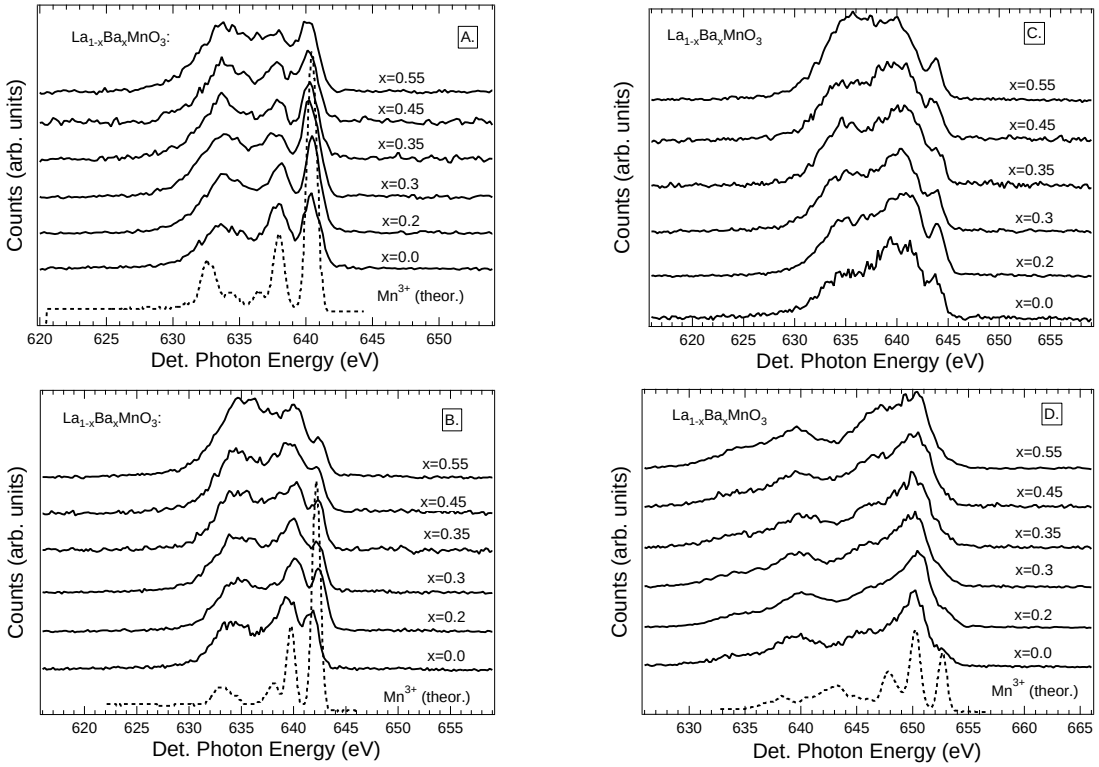

Figure 4.4: Mn L_3 Resonant Inelastic X-ray Scattering spectra of $La_{1-x}Ba_xMnO_3$ ($0.0 \leq x \leq 0.55$) recorded at different excitation energies near Mn L_3 edge [194]. Labels A-D correspond to the indicated features in the Mn L edge XAS spectrum (see Fig. 4.3). The RIXS spectra consist of three main features labelled $I - III$ (see text). The dashed lines represent multiplet calculations performed for Mn^{3+} ions [189].

Figure 4.4 shows the RIXS spectra taken at the Mn L_3 edge of $La_{1-x}Ba_xMnO_3$ ($0.2 \leq x \leq 0.55$), and Fig. 4.4 displays the RIXS results recorded at the Mn $L_{2,3}$ edge; labels A-D correspond to the excitation energies as marked in the XAS spectrum (Fig. 4.3). The RIXS spectra depend strongly on the incident photon energy and Ba concentration. The emission spectra corresponding to excitation energies A and B consist of three main resonant features labelled $I - III$. Feature I can be associated with the elastic recombination peak whereas features II and III represent resonant loss features, which appear at constant energy with respect to the elastic recombination peak. In the case of peak II a fixed energy loss of around 2.5 eV below the elastic peak is observed while peak III is a rather broad structure 6-9 eV below the recombination peak. At higher excitation energies above the Mn L_3 threshold

(C) the emission spectra contain more non-resonant features which contribute to the spectra as dispersing features. If the excitation energy is increased to the Mn L_2 edge, the elastic peak almost disappears while the loss feature located 2.5 eV below the recombination peak shows a strong resonance. Also the second loss feature appears, while one can observe normal emission due to transitions from the Mn 3d states to the Mn $2p_{3/2}$ level (Fig. 4.4). One can now identify the features with the help of the results shown above. The XPS spectra (Fig. 4.1) show a sharp increase in intensity with a maximum at 2.5 eV on a binding energy scale which is due to more or less localized (dependent on hole concentration) Mn t_{2g} states of the majority spin band. Hence, loss feature II may be associated with intra atomic Mn dd transitions between occupied and unoccupied Mn 3d states. Taking the XPS and XES results (section 4.1.3.1), feature III can be attributed to excitations from the occupied Mn 3d e_g and t_{2g} bands hybridized with O 2p states to the Mn e_g states in the conduction band. With increasing hole concentration x the intensity of the charge transfer feature (III) increases. These findings are consistent for the RIXS spectra labelled A. and B., and furthermore it can also be seen from the spectra recorded with excitation energies above the Mn L_3 edge (C.) that the intensity of emission features corresponding to inter-atomic transitions increases with increased hole doping. The spectra taken at excitation energy D., on the maximum of L_2 absorption show an intensity ratio of L_β to L_α of about 0.5. This is consistent with the results of Yablonskikh *et al.* [172] on Mn based Heusler alloys, where it was found that magnetic ordering decreases the L_α/L_β branching ratio.

Also the multiplet calculations [189] (Fig. (4.4)) reproduce the RIXS spectra of $LaMnO_3$ rather well. Features II and III can be described as *local dd* transitions and O 2p $\rightarrow$ Mn 3d charge transfer excitations within the Anderson impurity model. A more detailed discussion can be found in section 4.1.4.

4.1.4 Discussion

The XPS valence bands of $La_{1-x}Ba_xMnO_3$ ($0 < x < 0.55$) (Fig. 4.1) consist of four distinct bands. A weak feature is due to Mn e_g states near E_F, followed by a sharp increase in intensity around 2.5 eV binding energy, which is attributed to localized Mn t_{2g} states. The spectra reveal a broadening of the Mn t_{2g} states in the valence band with higher Ba concentration. This finding is consistent with recent band structure calculations [187, 188]. The O $K\alpha$ XES maximum intensities (Fig. 4.1) show a shift towards E_F (from $\sim$4.5 eV to $\sim$3.5 eV) with higher doping concentration. This places the oxygen and Mn states closer in energy, and hence hybridization between the Mn t_{2g} states and O 2p states in the valence band is expected to be stronger with higher Ba concentration.

Features $a-c$ of the XPS valence band of $La_{0.76}Ba_{0.24}Mn_{0.84}Co_{0.16}O_3$ show a significantly higher intensity. The Co contributes to band a with 3d e_g like states and bands b and c with 3d t_{2g} like states. In contrast to the trivalent Co ions in $LaCoO_3$ (XPS valence spectrum also shown in Fig. 4.2), the divalent Co ions in this compounds are not in a low-spin state but have a non zero magnetic moment, inducing also a negative Co^{2+}-O-Mn^{4+} superexchange interaction. The Co 2p XES spectrum is in reasonable agreement with this result, indicates however a somewhat broader

contribution of Co 3d states between 1-8 eV on a binding scale. According to theory [197] some Co 3d states are also present around 5-7 eV, hybridized with O 2p states, which contribute to the Co 2p XES spectrum. Furthermore the XES spectrum is influenced by lifetime broadening effects. The Mn 2p and O 1s XES spectra lead to results similar to $La_{1-x}Ba_xMnO_3$. This is also the case for $La_{0.76}Ba_{0.24}Mn_{0.78}Ni_{0.22}O_3$, whereas the Ni 2$p$ XES experiment suggests the presence of Ni 3d states from about 1.5 eV to 7 eV. This is in reasonable agreement with the "Ni 3d" difference spectrum (Fig. 4.2) which indicates that Ni 3d states contribute to the valence band in a region of 1.5-5 eV. In comparison with the XPS valence band $LaNiO_3$ and band structure calculations for $LaNiO_3$ [198] and $LaMn_{1-x}Ni_xO_3$ [199] one can draw the conclusion that the Ni 3d in this kind of compound are more localized than Mn 3d states and lead to a weaker occupancy of e_g like states near E_F. Magnetic measurements for this specific compound are not known to us. However, experiments on other manganites have shown that Ni doping at the Mn-site induces the metal insulator transition at low concentrations, a few percent, but also leads to a decrease of Curie temperature and magnetic moment at higher concentrations [180, 199]. The lowering of the e_g state occupancy as well as the weaker interaction of the Ni 3d states with the O 2p states in the valence band region suggest that one may find similar magnetic properties for $La_{0.76}Ba_{0.24}Mn_{0.78}Ni_{0.22}O_3$. In contrast Co doping leads to a stronger occupancy of the e_g like states near E_F, which may be an explanation for the intricate magnetic transport properties, resulting in sharp magnetoresistance maxima in $La_{0.74}Ba_{0.26}Mn_{1-y}Co_yO_3$ around a Co concentration of $y = 0.16$. On the other hand side the interaction of the divalent Co ions and Mn^{4+} ions may lead to a decrease of the Curie temperature in these compounds [181].

In Fig. 4.5 we present a schematic plot of the partial densities of the Mn 3d and O 2p states for the orthorhombic crystal structure of undoped $LaMnO_3$, and the cubic perovskite structure, which is found for highly doped $La_{1-x}Ba_xMnO_3$ ($x > 0.35$) [175]. For the orthorhombic phase, an energy gap between the highest occupied Mn e_g band (spin up) and the lowest unoccupied Mn e_g band (unpolarized) is found, followed by a localized band comprising Mn t_{2g} states (spin up) around 2 eV which is mixed with some Mn e_g derived states. At higher binding energies ($\sim 3 - 9$ eV) the valence band comprises mainly unpolarized O 2p states hybridized with some Mn 3d states. For the cubic crystal structure the gap between the Mn e_g bands near E_F closes and the compound becomes metallic. The Mn t_{2g} states are still more or less localized. However, they contribute to a broader region of the valence band ($\sim 1 - 3$ eV binding energy) compared to the orthorhombic structure. Furthermore O K XES data reveal a stronger hybridization between Mn t_{2g} and O 2p bands while theory predicts almost no overlap between Mn t_{2g} and Mn e_g bands in the valence band.

A preliminary interpretation of the RIXS spectra at the Mn L edge of $La_{1-x}Ba_xMnO_3$ is possible by considering the XPS, XES and band theory [190, 192]. RIXS spectra recorded at excitation energies below and at the Mn L_3 edge (Fig. 4.4) consist of three features. Feature I can be associated with the elastic recombination peak while feature II is due to intra-atomic dd transitions between occupied Mn t_{2g} and unoccupied Mn e_g states. Finally, feature III can be attributed to inter-atomic transitions between hybridized O 2p - Mn 3d bands in the valence band and Mn 3d bands in the

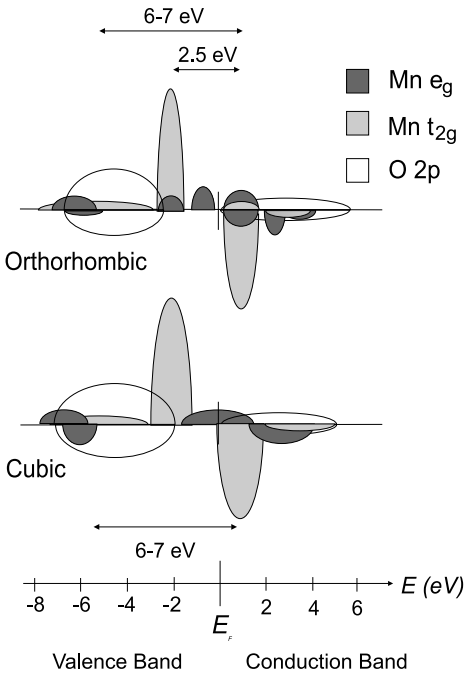

Figure 4.5: Schematic plot of the partial densities of states of O $2p$ and Mn $3d$ for the orthorhombic $GdFeO_3$ structure (upper panel) and the cubic perovskite-type structure [194]. Densities above the energy axis are majority spin states, those below are minority spin states. The values are based upon our experimental findings and the calculations of Ravindran *et al.* [188] and Youn *et al.* [187], respectively.

conduction band.

The selection rules for RIXS (with cubic and orthorhombic symmetry) state that all dd transitions are allowed: $t_{2g} - t_{2g}$, $e_g - e_g$, $t_{2g} - e_g$ and $e_g - t_{2g}$. Transitions from occupied Mn e_g states (spin down, hybridized with O $2p$) to unoccupied Mn t_{2g} states are likely to make a significant contribution as they have a large density of unoccupied states, making the transition strong, and the energy range in the one-electron schematic covers an appropriate range. This is especially the case for the cubic phase (Fig. 4.5) where a significant density of e_g electrons (spin down) is present at a binding energy of around 6 eV due to covalent interaction between Mn e_g and O $2p$ states [188]. Thus, feature III can be explained as a superposition of a transition between occupied and unoccupied majority states (charge transfer) and minority states (covalent interaction).

The Mn t_{2g} − O $2p$ hybridization becomes much stronger in cubic symmetry, or at higher doping concentration. Consequently the relative intensity of feature III compared to the intensity of feature II increases. One can now come to the conclusion that hole doping in lanthanum manganites leads to more hybridization between Mn $3d$ and O $2p$ bands in the valence band. In RIXS this development can be investigated directly, the relative intensity of the intra-atomic dd transitions between Mn $3d$ bands compared to the intensity of the inter-band transitions of heavily mixed Mn $3d$ − O $2p$ bands decreases with increasing hole doping concentration. This finding may support

the point of view that the importance of correlation effects has been exaggerated, and furthermore we show that hole doping leads to stronger Mn $3d$ − O $2p$ hybridization compared to the undoped compound.

Fig. 4.4 also shows the results of a charge transfer multiplet calculation of a Mn^{3+} ion in D_{4h} symmetry [189]. Also within the Anderson impurity model the RIXS loss features of $LaMnO_3$ can be reproduced rather well. The calculated spectra comprise the elastic recombination peak, local dd transitions located around 2.5 eV below the elastic peak, followed by O $2p \rightarrow$ Mn $3d$ charge transfer excitations [189]. The 2.5 eV loss feature is rather good reproduced by the multiplet calculation, which are as well as the charge transfer band. The 2.5 eV loss feature shows a similar behavior and energy position in all samples, showing different magnetic ground states and a metal to insulator transition in dependence of the Ba concentration. This is a rather substantial indication for a local dd excitation and consequently for the presence of correlation effects. Nonetheless, the 2.5 eV loss peak is also present and even resonating at excitation energy B, corresponding to the maximum of the Mn L_3 absorption. For this energy and those recorded at higher excitation energies the excitonic states begin to overlap with the ordinary Mn L_α emission, representing at least parts of the occupied densities of states. This is also the case with increasing doping concentration, since the contribution of the charge transfer band and transitions between hybridized Mn $3d$ and O $2p$ is increasing, leading to an even more extended Mn $3d$ wave function of the compound in question. To fully understand the Mn $2p$ RIXS of $La_{1-x}Ba_xMnO_3$ would require full multiplet calculations for a Mn^{4+} system, or even calculations within an extended cluster model. For systems with a not so localized $3d$ wave function also a simulation of these spectra with the restricted joint DOS (that is a convolution of vacant $3d$ DOS in a narrow energy interval with the occupied $3d$ DOS) would be an interesting approach. This is beyond the scope of the present work. It should be mentioned that both theoretical approaches have been successfully used to describe the Ti $2p$ RIXS of TiO_2 [110, 111].

4.1.5 Conclusions

We have presented a detailed x-ray spectroscopic study of the A-site doped CMR compound $La_{1-x}Ba_xMnO_3$ as well as for the A- and B-site doped manganites $La_{0.76}Ba_{0.24}Mn_{0.84}Co_{0.16}O_3$ and $La_{0.76}Ba_{0.24}Mn_{0.78}Ni_{0.22}O_3$. XPS and XES data reveal hybridization between Mn $3d$ states and O $2p$ states in the valence band, and this hybridization becomes stronger with increasing Ba concentration due to the broadening of the Mn t_{2g} states and the shift of the O $2p$ states towards E_F. In $La_{0.76}Ba_{0.24}Mn_{0.84}Co_{0.16}O_3$ the Co $3d$ states mainly contribute at lower binding energies between 0.5-5 eV to the valence band, including the states near E_F. Doping with Ni leads to a lower occupancy of the e_g states near E_F, and the Ni $3d$ states are rather localized between 1.5-5 eV.

The Mn $2p$ XAS results of $LaMnO_3$ are in excellent agreement with recent cluster model calculations assuming D_{4h} symmetry [104]. A chemical shift with increasing Ba concentration was observed, indicating the changing chemical environment of Mn.

RIXS spectra, which have been performed at the Mn $L_{2,3}$ edges consist of three main features, which can be associated with the elastic recombination peak and two loss features. The peak located around 2.5 eV below the elastic peak can be associated with a local Mn dd transition in agreement with multiplet calculations, the second feature can be assigned to charge transfer transitions. Since the loss features remain present at excitation energies at the Mn $L_{2,3}$ XAS maxima they represent parts of the joint DOS, with the states projected on the Mn site. With increasing Ba concentration the hybridization between O $2p$ and Mn t_{2g} states becomes stronger, which can be directly investigated by RIXS: the intensity of the corresponding peak increases with increasing Ba concentration. In summary, we have shown that colossal magneto resistance manganites can be understood as being moderately correlated systems, in which hybridization effects like charge transfer and also covalent interaction between the Mn and O states for both occupied and unoccupied states may play an important role with respect to their unusual phenomena and transport properties.

4.2 Orbital ordering in $La_{7/8}Sr_{1/8}MnO_3$

4.2.1 Introduction

Systems showing an orbitally degenerate state have attracted much attention, since a preferential occupation of the d-orbitals may lead to long rage orbital ordering. This ordering strongly influences the bonding between the transition metal (TM) ions and the oxygen ligand in the compound which determines both the magnetic interactions and electronic properties.

Among these compounds, $LaMnO_3$, an A-type antiferromagnetic insulator with a Néel temperature of 140 K, is of special interest as the parent compound of colossal magnetoresistance (CMR) compounds which are the possible magnetic materials for applications in the next generation of magnetic data storage read heads [12, 200, 201]. Doping by a moderate number of holes by Sr-doping doping between 10% and 20% leads to a very interesting temperature dependent competition between ferromagnetism and a cooperative Jahn-Teller distorted phase in $La_{1-x}Sr_xMnO_3$ ($0.1 < x < 0.2$) [202, 15, 14].

In particular, around a hole concentration of $x \approx 0.125$, $La_{1-x}Sr_xMnO_3$ is a compound showing a fascinating combination of Jahn-Teller distortion, orbital ordering, and ferromagnetism [203, 204]. $La_{7/8}Sr_{1/8}MnO_3$ undergoes a phase transition from a slightly orthorhombic distorted phase at high temperature into a cooperative Jahn-Teller distorted phase upon cooling at around 270 K, induced by a contraction of the $\boldsymbol{c}$-cell parameter [14, 205]. If T decreases through T_c around 180 K, the ferromagnetic order suppresses the cooperative Jahn Teller distortion and the system undergoes another transition into a ferromagnetic phase. In a cubic crystal the Jahn-Teller distortion leads to a lowering of the symmetry and thus a splitting of the e_g level. Its occupation, influenced by doping and the energetic position, strongly influences the hybridization between the Mn $3d$ and the O $2p$ states, which is crucial for the understanding of the underlying physics of the family of CMR manganites. In the case of $La_{7/8}Sr_{1/8}MnO_3$, the $(c/\sqrt{2})/a$ ratio is reduced from 0.993 to 0.986 in the cooperative orbital ordered phase, this contraction is accompanied by an elongation of the $\boldsymbol{b}$-cell parameter, resulting in an orthorhombic Q_2-type Jahn-Teller interaction, which stabilizes in a certain superposition of $(3r^2 - z^2)$ and $(x^2 - y^2)$ orbitals (Chapter 1.3.4) [32].

Whereas the magnetic properties of CMR manganites, such as spin or charge ordering have been subject to intense studies, i.e., by means of electron or neutron diffraction analysis, the direct investigation of orbital ordering is known to be a difficult task. The orbital ordering in $La_{7/8}Sr_{1/8}MnO_3$ has been studied by resonant x-ray scattering (RXS) on the Mn K edge by Endoh *et al.* [206] and Geck *et al.* [207]. There are some differences in detail. Endoh *et al.* find evidence for a new type of orbital ordering, the hybridization of $d_{(x^2-z^2)-(y^2-z^2)}$ and $d_{(3x^2-r^2)-(3y^2-r^2)}$ in the low temperature ferromagnetic phase (below 145 K), but do not find any indication for orbital ordering in the cooperative Jahn-Teller distorted phase [206]. On the other hand side, Geck *et al.* find that the cooperative Jahn-Teller distorted phase (270 K - 170 K) shows a rod-type $(3x^2 - r^2)/(3y^2 - r^2)$ orbital ordering similar to that investigated in $LaMnO_3$ using the same experimental technique [207]. RXS on the Mn K edge leads to Mn $1s \rightarrow 4p$ transitions, which means that this technique

allows only an indirect probe of the Mn $3d$ spatial distribution [33]. In the case of orbital ordering the outermost Mn $3d$ orbitals are not orthogonal and arranged in two sublattices, so that x-ray linear dichroism (XLD) on the Mn L (Mn $2p \rightarrow 3d$ transition) edge is able to probe the type of the uniaxial $3d$ electron distribution directly, which has been shown by multiplet calculations [37, 104, 208]. Moreover, very recently, the orbital ordering in the *single layered* compound $La_{1.5}Sr_{0.5}MnO_4$ has been investigated by using XLD on the Mn L edge (Mn $2p \rightarrow 3d$) [209]. In contrast to the common view of rod-type $(3x^2 - r^2)/(3y^2 - r^2)$ orbital ordering these experiments suggest that the orbital occupation of the Mn e_g states is dominated by a cross type $(x^2 - z^2)/(y^2 - z^2)$ orbital ordering.

We report here for the first time soft XLD measurements on the Mn L edge of the *cubic crystal* $La_{7/8}Sr_{1/8}MnO_3$ at room temperature and in the cooperative Jahn Teller distorted phase. In comparison with the recently published results and the available theory we find strong indications that a predominantly cross type $(x^2 - z^2)/(y^2 - z^2)$ orbital ordering is present in the three dimensional CMR manganite $La_{7/8}Sr_{1/8}MnO_3$.

4.2.2 Experimental details

A $La_{7/8}Sr_{1/8}MnO_3$ single crystal was grown by the floating zone method at the Moscow State Steel and Alloys Institute, Russia. X-ray diffraction (XRD) was used to check the structural quality and single phase nature of the specimens. The chemical composition was determined by Microprobe analysis. The crystal was carefully polished with a diamond paste and oriented with help of back reflection Laue patterns. No substantial admixtures of twin domains could be identified at room temperature. By cooling the sample below $T_{JT} \approx 270$ K one introduces a collective Jahn Teller distortion and consequently anisotropy into the crystal. The temperature dependent XRD measurements indicated that the $\boldsymbol{a}$ and $\boldsymbol{b}$ axis might be interchanged in parallel plates of the crystal. This is also in agreement with recent results of Alejandro *et al.* who found that if twinning in the *ac* and *bc* planes of $La_{7/8}Sr_{1/8}MnO_3$ is present, it is small[205]. Twinning in the *ab* plane has no essential influence on the XLD signal, as discussed below. The XLD spectroscopy was performed at the Beamline for Advanced diCHroism (BACH) at ELETTRA, Italy [122, 210]. The incident angle of the beam was 75° from the sample surface normal and the *c*-axis of the crystal, which was oriented perpendicular to the polished [001] surface. Hence, for a vertically polarized incoming beam, the $\boldsymbol{E}$-vector of the light was orientated perpendicular to the $\boldsymbol{c}$-axis of the crystal, whereas the $\boldsymbol{E}$-vector of horizontally polarized light was orientated nearly parallel to the $\boldsymbol{c}$-axis. The linear dichroism was then determined by subtracting the two XAS spectra from each other.

4.2.3 Results and discussion

Figure 4.6 displays the polarization dependent Mn L edge XAS spectra and the corresponding linear dichroism (LD), recorded at different temperatures, respectively, at 295 K and 240 K.

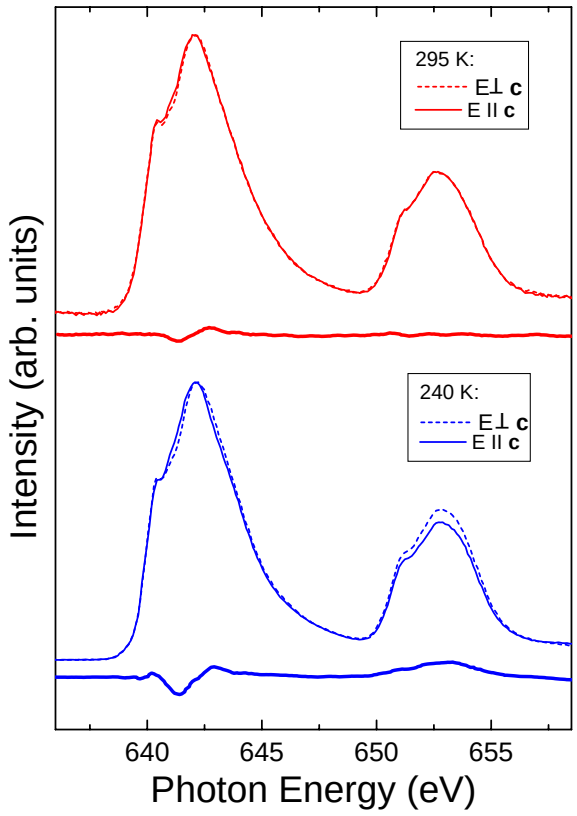

Figure 4.6: Polarization dependent XAS with $E \perp \mathbf{c}$ and $E \parallel \mathbf{c}$ and the corresponding linear dichroism (LD) recorded on the Mn L edge of $La_{7/8}Sr_{1/8}MnO_3$ at 295 K and 240 K, respectively.

At room temperature, $La_{7/8}Sr_{1/8}MnO_3$ is in a paramagnetic, pseudocubic, incoherent Jahn-Teller distorted phase, and thus no LD signal can be expected. Indeed, the LD signal (Fig. 4.7) for the measurement at room temperature is very small. If the sample is cooled below a temperature of around $T_{JT} = 270$ K, $La_{7/8}Sr_{1/8}MnO_3$ undergoes a phase transition into a coherent Q_2 - type Jahn Teller distorted, orbital ordered phase, induced by a significant contraction of the c-cell parameter from 7.79 Å (295 K) to 7.74 Å (240 K). Highly distorted MnO_6 octahedrons undergo a long-range ordering, accompanied by orbital ordering of the outermost Mn $3d$ valence electrons. Hence, a strong LD can be observed by measurements recorded at 240 K (Fig. 4.7). Very recently, it has been shown that even in the case that the $\boldsymbol{a}$ and $\boldsymbol{b}$ axis show twinning and are interchanged in parallel plates of the crystal, the averaged XLD

signal over the two sublattices is observed [208]. Thus XLD is suitable for the investigation of the orbital ordering even in crystals with this kind of twinning. With the present result we have shown that XLD, applied to the Mn L edge, can probe the presence of orbital ordering in *three dimensional CMR manganites*.

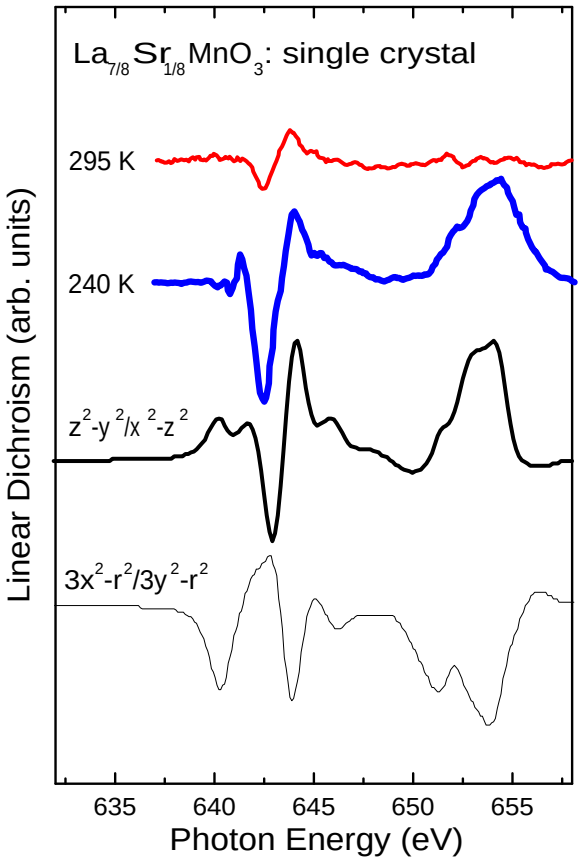

Figure 4.7: The XLD signal recorded at the Mn L edge of a $La_{7/8}Sr_{1/8}MnO_3$ single crystal at different temperatures [211] compared with MnO_6 cluster model calculations [209].

In Figure 4.7 we compare the measured Mn L edge linear dichroism (LD) spectra at different temperatures with calculated spectra, with the $(x^2 - z^2)/(y^2 - z^2)$, and the $(3x^2 - r^2)/(3y^2 - r^2)$ orbitals occupied, respectively [209]. The comparison with the calculations shows a very good agreement with the calculated LD spectra of Mn^{3+} ions with the $(x^2 - z^2)$ / $(y^2 - z^2)$ orbitals occupied [209]. The cluster model calculations of Huang *et al.* have been performed based upon a model for an Mn^{3+} ion in a cubic crystal field [37, 209] and one can qualitatively compare the present results for $La_{7/8}Sr_{1/8}MnO_3$ with these calculations. Furthermore it is generally believed that the MnO - planes (and the MnO_6 octahedra) have a very similar structure in layered and three dimensional systems [212]. Hence, the cooperative Jahn-Teller distorted phase of $La_{7/8}Sr_{1/8}MnO_3$ is probably accompanied by a cross type $(x^2 - z^2)/(y^2 - z^2)$

orbital ordering. Fig. 4.8 displays a comparison of the experimental XLD signal with different multiplet calculations [37, 209]. Both approaches reproduce the correct sign of the XLD spectrum, and the overall integrated intensity is positive. In the crystal field approximation one finds a feature between the Mn L_3 and the Mn L_2 edge which is not present in the experiment. By including charge transfer in the calculation, and assuming an admixture of the ground state configuration $3d^5\underline{L}$, an almost perfect fit with the experimental data is obtained.

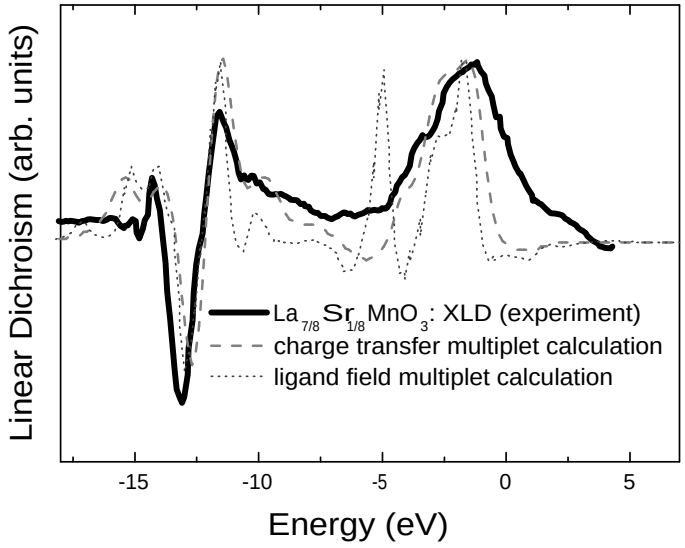

Figure 4.8: The experimental XLD recorded at 240 K [211] in comparison with a crystal field multiplet calculation (dotted line) [37] and a charge transfer multiplet calculation (dashed line) [209].

The result above can not be explained within the framework of the widely used exchange model or Kugel-Khomskii model [32]. Dabrowski *et al.* derived the Mn-O bond length for the very similar compound $La_{0.87}Sr_{0.13}MnO_3$ by means of a temperature dependent Rietveld analysis. They found the Mn-O bond length in the cooperative Jahn Teller distorted phase in the $x-y$ - plane (equatorial) to be 2.04 Å and 1.94 Å, respectively, whereas the Mn-O in (apical) z-direction is determined to be 1.97 Å. For $La_{0.11}Sr_{0.89}MnO_3$ a similar situation was found [14]. Two short Mn-O bonds and one elongated Mn-O bond are present in moderately doped three dimensional $La_{1-x}Sr_xMnO_3$. Applying the exchange model [32], one would expect a rod-type $(3x^2-r^2)/(3y^2-r^2)$ orbital ordering. This is in contrast to the result of the soft XLD measurement on the Mn L edge of $La_{7/8}Sr_{1/8}MnO_3$, which strongly indicates the presence of a predominantly cross-type $(x^2-z^2)/(y^2-z^2)$ orbital ordering (Fig. 4.7), as discussed above. A possible reason for this may be that the exchange interaction model is based upon an effective Hubbard model, considering

only the Coulomb exchange between the degenerate d-electron states. This model describes Mott Hubbard insulators, where $\Delta >> U_{dd}$ (Δ represents the charge transfer energy and U_{dd} the Coulomb exchange between the transition metal (TM) $3d$ electrons, respectively), in a correct way.

However, it is clear that the ground states of charge transfer insulators are strongly influenced by hopping of electrons between ligand and TM ions (Δ), whereas the usual exchange involves the electron transfer from one TM site to another one. The magnetic and orbital ordering in the ground state may strongly depend on the ratio U_{dd}/Δ [34]. For Mn based oxides one finds an intermediate behavior ($\Delta \approx U_{dd}$), this means that electronic transfer interactions between Mn ion and oxygen ligand play an essential role for the mechanism of the orbital ordering. Mostovoy and Khomskii find in a very topical and recent paper that the type of the ground state in charge transfer insulators is essentialy different from that of Mott Hubbard insulators [34]. The charge transfer interaction is furthermore of purely electronic origin, independent of any electron-lattice interaction, and in general present in all TM oxides. For charge transfer insulators with one hole per TM site the occupation of $(x^2 - y^2)$ like orbitals is preferred. Therefore in materials like $La_{7/8}Sr_{1/8}MnO_3$, where ($\Delta \approx U_{dd}$), the type of orbital ordering can not be determined by merely taking into account the Coulombic consequences of the electron-lattice interaction, but it is stabilized by a fine balance between electron-lattice and the electron-hole interactions. Thus, a predominantly cross type $(x^2 - z^2)$ / $(y^2 - z^2)$ orbital ordering, as indicated by the XLD measurements, is probably present.

However, it should be mentioned that an admixture of $(3x^2 - r^2)$ / $(3y^2 - r^2)$ orbitals decreases the integrated intensity of the XLD signal, but does not lead to a major change of the spectral shape [208]. Therefore an admixture of $(3x^2 - r^2)$ / $(3y^2 - r^2)$ orbits into the $(x^2 - z^2)$ / $(y^2 - z^2)$ orbits can not be excluded. However, XLD at the Mn L edge is in any case able to distinguish between predominantly rod-type $(3x^2 - r^2)$ / $(3y^2 - r^2)$ and predominantly cross-type $(x^2 - z^2)$ / $(y^2 - z^2)$ orbital ordering.

To fully understand the Mn L edge XLD and the orbital ordering of $La_{7/8}Sr_{1/8}MnO_3$, complementary x-ray scattering experiments on the Mn L edge would be very helpful, since this technique is also able to probe the type of orbital ordering in manganites directly. This has been demonstrated very recently for the half doped single layered manganite $La_{1.5}Sr_{0.5}MnO_4$ [213, 214]. However, there are no soft x-ray scattering experiments on $LaMnO_3$ or other *three dimensional* CMR manganites known up to now.

Table 4.1: Type of orbital ordering of $La_{7/8}Sr_{1/8}MnO_3$ revealed by different approaches and at different temperatures [211].

	Type of orbital ordering	Technique
Endoh *et al.* [206]	Hybridization of $d_{(x^2-z^2)-(y^2-z^2)}$ and $d_{(3x^2-r^2)-(3y^2-r^2)}$ in the low temperature ferromagnetic phase (below 145K), no orbital ordering in the cooperative Jahn Teller distorted phase	RXS on the Mn K edge
Geck *et al.* [207]	$(3x^2-r^2)$ / $(3y^2-r^2)$ orbital ordering in the cooperative Jahn Teller distorted phase (probed at 220K), no orbital ordering in the ferromagnetic phase (below 170K)	RXS on the Mn K edge
present work	(x^2-z^2) / (y^2-z^2) orbital ordering in the cooperative Jahn Teller distorted phase (probed at 240K)	XLD on the Mn L edge

4.2.4 Conclusions

In conclusion, we have shown for the first time, that it is possible to probe the type of orbital ordering in *three dimensional CMR manganites* by using x-ray linear dichroism on the Mn L edge. We obtained rather strong indications that the coherently distorted Jahn-Teller phase in $La_{7/8}Sr_{1/8}MnO_3$ is accompanied by a predominantly cross type (x^2-z^2) / (y^2-z^2) orbital ordering. This result can not be explained within the widely used framework of exchange interaction and we find experimental evidence that, besides the widely used electron-phonon interaction, also the electron-hole interaction has to be taken into account in order to understand the fascinating interplay between orbital, charge and spin order in CMR manganites.

Chapter 5

The double perovskite Sr_2FeMoO_6

Recently, huge magnetoresistance (MR) phenomena have been also reported for the double perovskite Sr_2FeMoO_6 [3]. More strictly spoken, Sr_2FeMoO_6 is a tunneling magnetoresistance compound, driven by the tunneling of the charge carriers across insulating barriers [215, 216]. Due to its high Curie temperature of about 420 K and a substantial MR effect even at room temperature in a relatively low field, Sr_2FeMoO_6 is a promising model compound for applications in magnetoelectronics and related industrial fields. In order to optimize the intricate properties this material should be half metallic, meaning that one spin channel is metallic while the other is insulating [5]. In contrast to the manganites it has been shown that Sr_2FeMoO_6 has a ferrimagnetic structure since a small magnetic moment at the Mo site, which is antiferromagnetic with respect to the spin moments of Fe has been found [217]. Sr_2FeMoO_6 crystallizes in the tetragonal $I4/mmm$ space group, the ideally "ordered" double structure $A_2B'B''O_6$ comprises alternating $AB'O_3$ and $AB''O_3$ perovskite units. Particularly, in the case of Sr_2FeMoO_6 the B' and the B'' sites are occupied by Fe and Mo ions, respectively. Figure 5.1 shows this part of the crystal structure.

Although this compound has been studied intensely by various experimental and theoretical approaches a number of essential questions, for instance with respect to the valence states of iron and molybdenum, are controversial. Sarma *et al.* reported an XPS Mo 3*d* core level spectrum which they associate with Mo^{5+} [219]. Furthermore, XMCD measurements revealed the Fe valence state to be 3+, suggesting the system is somewhat more ionic than even $LaFeO_3$ [220]. On the other hand, Douvalis *et al.* found a mixed valent $Fe^{2.5+}$ state by applying Mössbauer spectroscopy [221, 222], and Besse *et al.* found a mixed iron valence state involving 66% Fe^{2+} ions and 34% Fe^{2+} ions [217]. Finally, neutron diffraction and magnetotransport measurements lead to the conclusion of a $Fe^{2+}(3d6)$-$Mo^{6+}(4d0)$ configuration rather than a $Fe^{3+}(3d5)$-$Mo^{5+}(4d1)$configuration [223].

One possible reason for the different experimental results may be the presence of antisite (AS) defects, which means Mo ions are randomly replaced by Fe ions and vice versa. These antisite defects strongly influence the properties of the compound [224]. We present here magnetic measurements and x-ray spectroscopic measurements performed on the same sample, with a well characterized and low antisite defect concentration of around 3%. This means variations due to different antisite defect concentrations can be excluded.

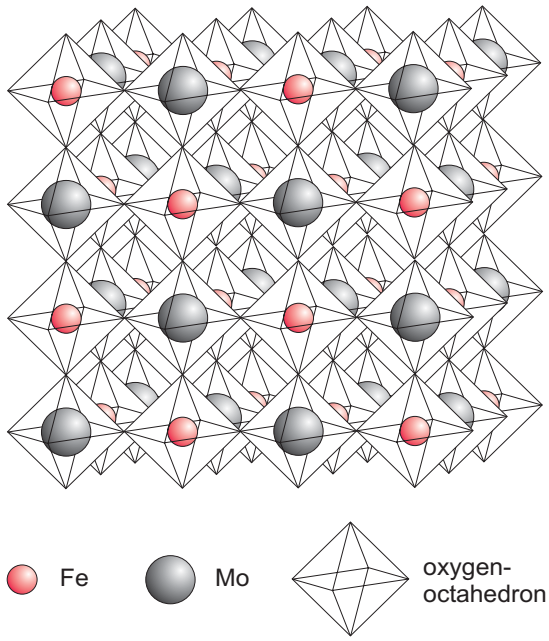

Figure 5.1: A schematic picture of alternating FeO_6 and MoO_6 octahedra in an ordered double perovskite, adapted from [218].

Turning now to the valence band region various attempts to determine the electronic structure and the correlation strength of Sr_2FeMoO_6 have been undertaken but the discussion of this point is still controversial [3, 225, 215, 226, 227]. Very different results have been reported, and the electronic structure of Sr_2FeMoO_6 has been found to be dominated by strong correlation effects [226, 227]. In addition to the Coulomb repulsion U between the metal d orbitals ($U = 4$ eV for the Fe $3d$ electrons) also a term representing Coulomb interactions between the oxygen p orbitals has been introduced into a Hartree-Fock type mean field approach in order to obtain a correct description of the electronic properties [226]. In comparison Saitoh *et al.* have adopted significantly smaller values U for the Fe d ($U = 2eV$) and Mo d orbitals [215], and very recently a magnetic Compton profile study has been reported to be in good agreement with simple FLAPW-GGA calculations [216].

In order to study the ferrimagnetic ground state of Sr_2FeMoO_6 in detail the technique of x-ray magnetic circular dichroism (XMCD) is especially useful. This is because the strong dichroism at the $L_{2,3}$ edges of transition-metal ions provides information about the ground-state magnetic properties. Moreover, by exploiting the chemical sensitivity of X-ray absorption edges, contributions from different transition-metal ions within the compound can be easily separated. Another main interest in performing XMCD measurements is that they give information about the ground state magnetic moments, noticeably the orbital and spin-magnetic moments (see also Chapter 2.4.1).

Up to now two different XMCD studies on Sr_2FeMoO_6 have been reported by

Ray *et al.* [220] and Besse *et al.* [217]. There are some differences in detail. Whereas Ray *et al.* use a bulk poly crystal with about 10 % antisite concentration Besse *et al.* grew up a single crystalline sample showing around 15 % disorder. The measurements of the latter group were performed at a temperature of 15 K and a external magnetic field of 5 T was applied to the sample. In contrast Ray and co-workers carried out their measurements at 77 K, no information about the magnetic field strength is given in their paper. Their XMCD analysis reveals a saturation moment of $1.68\,\mu_B/f.u.$ at the Fe site, compared to a bulk saturation moment of $2.81\,\mu_B/f.u.$ obtained by magnetometry. No considerable moment at the Mo site has been found. The results of Besse *et al.* are essentially different. They revealed a total moment $3.2\,\mu_B/f.u.$ by means of SQUID magnetic measurements, whereas their XMCD spectroscopy reveals spin magnetic moments of $3.05\,\mu_B/f.u.$ at the Fe site and $-0.32\,\mu_B/f.u.$ at the Mo site, respectively. No essential orbital magnetic moments have been found. The deviation of the total magnetic moment derived from the XMCD results ($\sim 2.8\,\mu_B/f.u.$) and the bulk magnetic moment is essentially smaller than that found by Ray *et al.* [220].

5.1 Experimental and theoretical details

Polycrystalline samples of Sr_2FeMoO_6 were produced by standard solid state reaction. The powder was annealed at 1200 °C in 99% Ar / 1% H_2 atmosphere. X-ray diffraction (XRD) was used in order to check the structural quality (in particular anti site defect concentration) and the single phase nature of the specimens. The magnetic measurements were performed in the temperature range 4.2 - 400 K in fields up to 9 T, by using an Oxford Instruments equipment at the Department of Physics at the Babes-Bolyai University in Cluj-Napoca, Romania. Above the Curie temperature, the magnetic susceptibilities were determined with a Faraday type balance equipment in a field of 1 T. All x-ray spectroscopic measurements were performed using the sample showing the lowest antisite defect concentration ($\sim$ 3%).

The XES spectra were measured at room temperature at the Advanced Light Source, beamline 8.0.1 using the x-ray fluorescence end station of the University of Tennessee at Knoxville [119]. Photons with an energy of 450-800 eV were provided to the end station via a spherical 925 lines/mm grating monochromator. The iron L, molybdenum M and oxygen K XES were calibrated using a reference sample of pure Fe metal, Mo metal and MgO, respectively. The excitation energies were set to 800 eV for the Fe L edge, to 600 eV for the O K edge and to 500 eV for the Mo M edge for the measurements on the sample as well as for the corresponding calibration spectra. The overall resolution (beamline plus spectrometer) was set to around 1 eV. The sample was scraped in air with a diamond file in order to reduce surface contamination just before mounting them in the transfer chamber. X-ray emission probes the sample to depths of tens or hundreds of nm and is bulk sensitive in the present study.

The XPS valence band was recorded using a PHI 5600CI multi-technique spectrometer with monochromatic Al Kα ($h\nu$ = 1486.6 eV) radiation of 0.3 eV at full width of half maximum (FWHM), and with the sample at room temperature. The overall resolution of the spectrometer is 1.5% of the pass energy of the analyzer,

0.35 eV in the present case. The spectrometer was calibrated using a Au foil as a reference sample (the binding energy of the Au $f_{7/2}$ core level is 84.0 eV [113]). To get a surface free of contamination, the sample was fractured in situ.

The XMCD experiments at the Fe L edge were performed at beamline 4.0.2 at the ALS, Lawrence Berkeley National Laboratory, Berkeley, USA. For the measurements we used the XMCD chamber (6T, 2K) [124]. In order to saturate the magnetization along the field a field of 5.5 T was applied parallel to the incoming x-ray beam (perpendicular to the sample surface), and the sample was cooled down to a temperature of 15 K. The dichroic spectra were obtained by performing XAS with 90% left and right circularly polarized x-rays in a wide energy range from 670-770 eV. This allows a proper background correction, an essential point if one wants to apply the sum rules [96] correctly. We compare the experimental results with multiplet calculations whicn were carried out with the TT-multiplets based upon the methods described by Thole, van der Laan and de Groot [61, 55].

Regarding the band structure calculations, we used the full-potential linearized augmented plane waves (FLAPW) method as implemented in the WIEN2k code [47]. The lattice parameters of the body-centered tetragonal unit cell used in the calculation were a=5.5706 Å and c=7.8858 Å (i.e. the base diagonal and the doubled length of the prototype perovskite cell), according to Ref. [19]. Muffin-tin radii of 2.0 Bohr (Sr), 1.90 Bohr (Fe, Mo) and 1.6 Bohr (O) were used, with otherwise "default" WIEN2k cutoffs for the basis function and charge density expansions (RK_{max}=7.0, G_{max}=14.0). We did not try to optimize lattice constants or internal coordinates, that would have required checking the convergency of results with respect to these cutoffs. For the exchange-correlation potential, we used the generalized gradient approximation (GGA) "Perdew-Wang 91", as discussed at length by Perdew *et al.* [43]. Moreover, in order to describe the effects of intraatomic correlation (presumably strong within the localized Fe 3d shell) beyond the conventional LDA or GGA treatment, we allowed in some calculations the inclusion of an orbital-dependent potential of the type implementing the "LDA+U" approach by Anisimov *et al.* [228]; in particular (among many known variants thereof), the formalism is outlined in Refs. [228, 45, 229]. The values of the Coulomb (U) and exchange (J) parameters entering this formalism were taken to be J=0.07 Ry, as routinely recommended for Fe in a number of similar calculations, and U= 2 – 4 eV (see the discussion below). The inclusion of spin-orbit interaction was tested and found not to affect the calculated DOS or energy bands in any noticeable way. The DOS discussed below has been calculated with $10 \times 10 \times 10$ divisions of the Brillouin zone.

5.2 Results and discussion

5.2.1 Magnetic properties

Rietveld analysis of the XRD data revealed that all samples crystallized in the $I4/mmm$ lattice. It is well known that Sr_2FeMoO_6 can exist with varying extents of anti-site (AS) disorder between the Fe and Mo sublattices. The diffractive intensity ratio $[I(101)/I(200) + I(112)]$ showed that three samples had the following concentrations of anti site (AS) defects: sample 3.3, 3% AS (highly ordered); sample 3.1, 5% AS (slightly less ordered; and sample 2.4, 7% AS (less ordered). The temperature dependencies of the magnetic susceptibilities for these three Sr_2FeMoO_6 samples are plotted in Fig. 5.2. The sample with the highest degree of order (3% AS) shows Curie-Weiss type behavior. The other two samples, above Curie temperatures, have a small amount (less than 0.1%) of magnetically ordered phase, and consequently, no reliable data can be obtained by paramagnetic measurements.

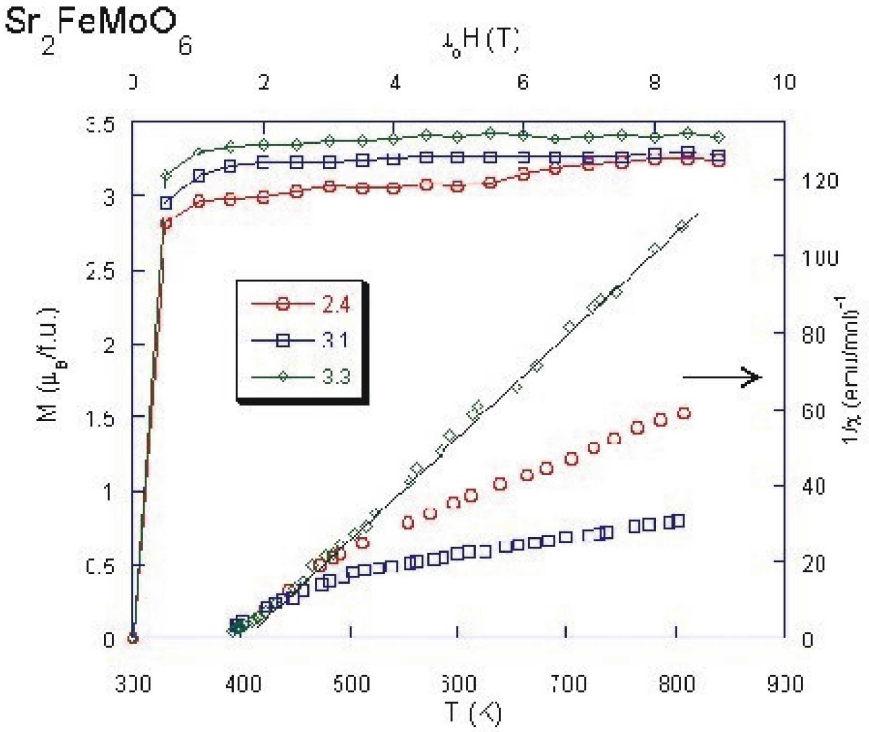

Figure 5.2: Magnetization isotherms at 4.2K, and thermal variations of reciprocal susceptibilities [19].

Fig. 5.3 displays the XAS and XPS results. XAS is known to be sensitive to the chemical environment of the absorbing atom, and we compare the Fe $2p$ XAS spectrum of Sr_2FeMoO_6 with some other iron oxides, namely FeO (Fe^{2+} ions), α-Fe_2O_3 (Fe^{3+} ions) and Fe_3O_4 (33.3% Fe^{2+} and 66.6% Fe^{3+} ions). The lower left panel of Fig. 5.3 shows the XPS Fe $3s$ core level spectra of the double perovskite, FeO

and Fe_2O_3, in the lower right panel of Fig. 5.3 we present the Mo 3*d* XPS spectra of Sr_2FeMoO_6, MoO_3 and MoO_2, respectively.

Information on the iron valence states can be obtained from the Curie constant [230]. We assume that the effective Fe^{2+} and Fe^{3+} moments are given by the spin value only. The analysis of the XMCD spectrum of Mo shows that the Mo moment is very small [217]. The present data suggest that some Fe^{3+} and Mo^{5+} contributions to XPS and XAS spectra cannot be excluded. If we consider that Mo is in the 6+ state, we obtain approximately equal contributions of Fe^{2+} and Fe^{3+} ions to the Curie constant obtained by paramagnetic measurements of the highly ordered sample (3.3). The percentage of Fe^{2+} ions increases up to 60% if around 30% of Mo ions are supposed to be in the +5 valence state. An alternative analysis may be made considering an iron mixed valence state as suggested by Mössbauer effect studies, in this case a +2.5 valence is suggested, in agreement with previous data [221, 222], or by the present XPS measurements on the Fe 3*s* and Mo 3*d* core levels. Mössbauer effect measurements on the same sample used in the present work are now in progress in order to obtain further information on the matter. The magnetization isotherms at 4.2 K, for the three Sr_2FeMoO_6 samples, are also plotted in Fig. 5.2. The saturation magnetizations decrease when increasing the degree of disorder. We note that for the sample having a concentration of 7% AS, at 6T, an increase by $\sim 0.2\,\mu B$ of the magnetization was shown. This metamagnetic transition may be correlated with the reversal of magnetizations of some Fe or/and Mo ions. The diminution of saturation magnetization seen in Fig. 5.2 can be correlated with the increased disorder. Based on the false-site imperfection model [231], for a sample showing around 2% AS concentration, derived from Rietveld refinement, a saturation magnetization of $3.8\,\mu_B/f.u.$ was evaluated for Sr_2FeMoO_6 [224]. This is in agreement with the magnetization determined in the case of the sample showing ∼3% AS concentration, namely $3.5\,\mu_B/f.u.$, as well as the decrease of the magnetization showing a higher concentration of AS.

5.2.2 Valence states of Fe and Mo: XAS and XPS

The Fe 2*p* XAS of Sr_2FeMoO_6 consists of a small shoulder at about 705.5 eV, a shoulder at 707 eV, and the main peak is located at around 708.5 eV, representing excitations from the Fe $2p_{3/2}$ core level. The excitations from the Fe $2p_{1/2}$ level comprise a small shoulder at around 718.5 eV and two main features located at 720.2 eV and 721.8 eV, respectively.

In comparison with the other iron oxides, the Fe 2*p* XAS of the double perovskite is most similar to that of FeO. Multiplet calculations for FeO and α-Fe_2O_3 [133] reveal that the shoulders at 705.5 eV and 718.5 eV can be associated with Fe^{2+} ions. Indeed, these features disappear in the spectrum of $SrFeO_{2.82}$, (see also the 718.5 eV feature, indicated by arrows). Furthermore, for a Fe^{2+} ion in an octahedral crystal field the first main feature (∼720 eV) is more intensive than the second one (∼722 eV), the order of the peaks is reversed for Fe^{3+} [133]. Following these arguments, the iron in Sr_2FeMoO_6 comprises mainly Fe^{2+} ions, but the pronounced shoulder at around 707 eV and the weaker shoulder at 718.5 eV, compared to that of FeO, indicate also that there may be significant Fe^{3+} contributions.

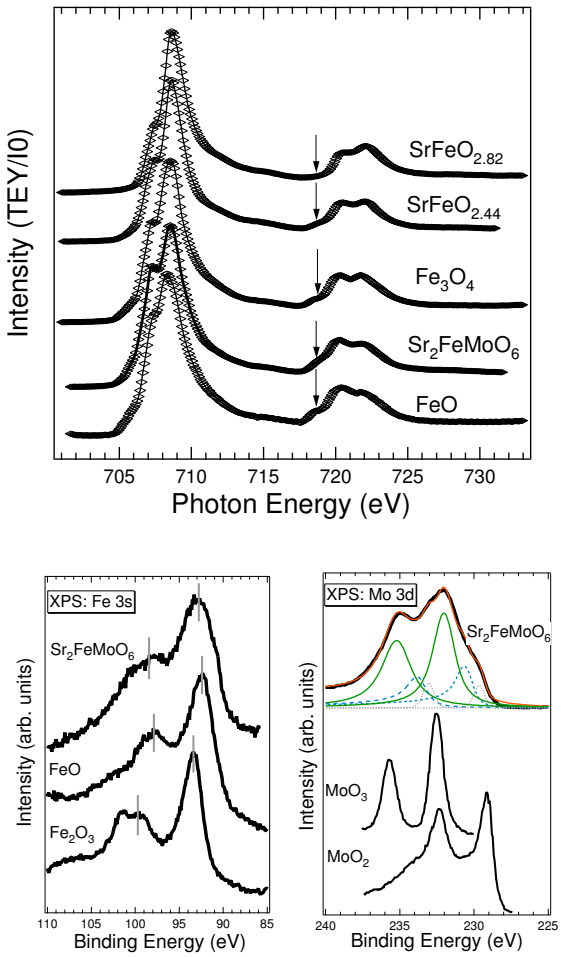

Figure 5.3: Fe 2*p* XAS spectra (upper panel), XPS core level spectra of Fe 3*s* (lower left panel) and Mo 3*d* (lower right panel) of Sr_2FeMoO_6, compared with the spectra of some other compounds, the FeO XAS spectra has been taken from Prince *et al.* [161], the Mo 3*d* spectra of MoO_2 and MoO_3 have been adapted from Colton *et al.* [232].

One may probe the valence state of transition metal (TM) ions in TM compounds by studying the TM 3*s* x-ray photoelectron spectra. Applying a phenomenological model [92], the spectral splitting of the 3*s* core-level x-ray photoemission spectra in transition metals and their compounds originates from the exchange coupling between the 3*s* hole and the 3*d* electrons, and is modified by configuration interaction. The magnitude of the splitting is related to $(2S + 1)$, where S is the local spin of the 3*d* electrons in the ground state. FeO ($3d^6$ configuration) shows an exchange splitting of around 5.4 eV whereas the 3*s* splitting in Fe_2O_3 ($3d^5$ configuration) is 6.4 eV. The XPS Fe 3*s* spectrum of the double perovskite shows a splitting of around 5.7 eV. Assuming a linear relationship between exchange splitting and ratio of valence state, this leads to the conclusion that around 30% of the Fe ions may be in the +3 valence state.

The Mo 3*d* XPS spectrum (Fig. 5.3, lower right panel) consists of two rather broad peaks located at around 232 eV and 235 eV on a binding energy scale. In order to separate the obviously overlapping Mo^{5+} and Mo^{6+} states we fitted the spectra with Doniach-Sunjic functions [83]. The features which can be associated with Mo^{5+} contributions (dashed lines) show a rather pronounced tail (asymmetry) to higher binding energies (∼25%). The analysis of the peak areas after background subtraction reveals 29% Mo^{5+} and 71% Mo^{6+} contributions to the Mo 3*d* spectrum, in very good concurrence with the result for the iron. The two rather small fitted peaks located at around 229.6 eV and 233 eV are likely to be due to surface defect states because firstly, the Fe 3*s* spectrum also shows a weak shoulder on the low binding energy side, and secondly, similar effects of surface defects on XPS spectra have been investigated in other studies of TM compounds, such as TiO [233] or WoO_3 [234].

5.2.3 The valence band: XPS and XES

In Fig. 5.4 the XPS valence band of Sr_2FeMoO_6 is compared with results of different band structure calculations. The experimental valence band region comprises five distinct features labelled $a - e$. Features a and b are located around E_F, -1 eV on an energy loss scale, followed by a shoulder around -3 eV (c), a local maximum around -4 eV (d), finally a rather broad absolute maximum in intensity (feature e) is located between -6.5 and -7.5 eV. We compare the experiment with the results of different *ab initio* band structure approaches, namely the total densities of states from a GGA calculation and LDA calculations using different values for the on site Coulomb potential U (see Fig. 5.4). As the electronic structure of Sr_2FeMoO_6 has been calculated earlier, albeit with less accurate methods, we refer to its main features only briefly.

Our main objective in the present work is to provide an adequate description of observed XPS and X-ray emission spectra, taking into account relevant weighting factors applied to pDOS, and hence offer a plausible interpretation of them. The U parameter of the LDA+U approach is used as adjustable, in the search for the best possible agreement with experiment. We then discuss the calculated results corresponding to U=2 eV, the value apparently yielding the best agreement with experiment, in more detail.

An interesting property of Sr_2FeMoO_6, according to band structure calculations, is that it is a semi-metallic material. Its majority-spin band has an energy gap of about 1.2 eV around the Fermi level whereas the minority-spin band has small but finite density of states in this energy region, although there is a gap in the energy band spectrum of minority-spin states at $\approx$ 1.0 eV below the Fermi level. Such half-metallic behavior is clearly present in a calculation using the GGA for the exchange-correlation, resulting in a strictly integer magnetic moment (4 μ_B) per unit cell; the LDA calculation yields the half-metallicity only approximatively, as the Fermi level cuts the very top of the majority-spin band. The inclusion of the orbital-dependent potential within the LDA+U formalism opens the majority-spin band gap even further and thus "stabilizes" the half-metallic state. Throughout the range of U values we tried, 0 to 4 eV, the band structure changes so that the center of gravity of occupied states of the Fe 3*d* type is shifted downwards and that of vacant states

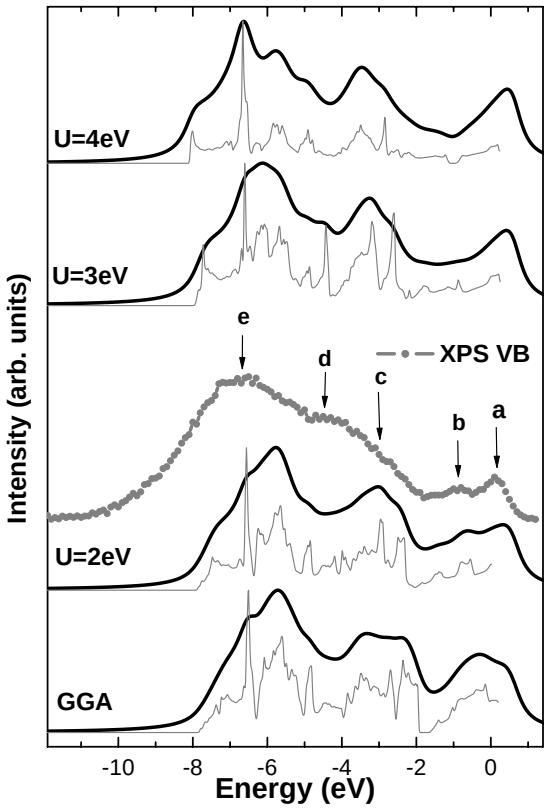

Figure 5.4: The XPS valence band of Sr_2FeMoO_6 (circles), compared with LDA+U calculations for different values of U (thin solid lines) [235]. The calculated total densities of states have been weighted with the corresponding photoionization cross sections [236] and broadened with the spectrometer resolution (bold lines) for direct comparison with the experiment.

upwards, as is common in LDA+U calculations. The majority-spin band gap opens slightly, and the magnetic moment per cell remains equal to 4 μ_B, without pronounced quantitative changes.

Fig. 5.5 shows the pDOS of Fe, Mo and Sr, calculated with U=2 eV. These states hybridize to form a common valence band going down to ∼8 eV below the Fermi level. Sr is largely ionized, so its partial density of states is higher in energy than the 4p semicore (at −17 eV, according to the calculation, and around -17.5 eV in the XPS spectrum) makes no noticeable contribution throughout the valence band. The O 2s states are even lower in energy and will also be excluded from the subsequent discussion.

The valence band, which is probed by x-ray photoelectron spectroscopy, is mainly constituted by Fe 3d, Mo 4d and O 2p states. They have different photoionization cross-sections, which should be taken into account for weighting the corresponding

atom-resolved contributions to the total DOS, as the simplest approximation of the measured spectra. Specifically, we took the relative photoionization cross-section values, corresponding to the excitation energy of 1486.6 eV, from the Ref. [236]: The weights therein tabulated, which refer to each respective electronic shell as a whole, were normalized to a single electron and then multiplied with partial densities of states $g(E)$ and with the number of atoms of each type in the unit cell, giving the calculated spectral intensity function $G_{\mathrm{tot}}(E)$:

$$G_{tot} = 1 \cdot 0.01715 \cdot g_{Fe3d} + 1 \cdot 0.0315 \cdot g_{Mo4d} + 6 \cdot 0.003225 \cdot g_{O2p} + 2 \cdot 0.13 \cdot g_{Sr4p}.$$

The weighted valence band densities, for several trial U values, are those shown in Fig. 5.4 in comparison with the experimental spectrum. All the calculated tDOS spectra reproduce the general structure of the measured XPS valence band correctly and better than previously published results [215, 227] – probably, due to the superior accuracy of the present calculational method. Between the present calculations done with different U values, one notes differences in the positions of spectral features and in their relative intensity. First we use the comparison with the experimental spectrum in order to select the best value of U taking into account relevant intensity and energy.

One notes that the a and b features are rather well reproduced already with the simple GGA (U=0). However, the calculated intensity of band a is higher than that of band b, in contrast to the experimental result. As the opposite extreme, the LDA+U calculation with U=4 eV predicts a much too narrow peak (of mostly Fe 3d character) just below the Fermi level, thus implying "unphysically" localized states. The calculation with the intermediate value of U=2 eV reproduces the a and b features rather well, notably their relative intensities, and offers an acceptable description of features c to e. We note that the c feature seems to be overestimated in the simple GGA calculation, but that this is in part corrected in the LDA+U scheme.

There are still problems with the positions of the lower peaks: the theory predicts that the c, d, e features are 1–1.5 eV less bound, as compared to the experimental values. This trend is common in the Density Functional Theory (DFT) when Kohn–Sham eigenvalues are compared with experimental excitation energies: an emitted electron leaves a hole behind, that enhances its binding energy, an effect which is stronger for more localized states and not accounted for in a conventional band structure calculation. The "+U" correction amends for this effect, although for a different reason: each single correlated electron (which experiences the Coulomb correction to the potential) of the total N electrons feels the repulsion of other $N-1$ electrons. In a conventional DFT treatment, on the contrary, an electron feels the Coulomb repulsion from an charge density corresponding to all N electrons, with just an "average" exchange-correlation hole dig in it. This would usually result in higher energy, due to a spurious self-interaction. The difference in energies between the two cases becomes larger for more localized states. Therefore the LDA+U approach might serve as a tool to model higher localization of relevant states and so to displace them close to energies consistent with spectroscopy. This indeed happens for the lower peaks in the DOS of the current compound, assuming a U value of 4 eV (as shown in Fig. 5.4), or larger.

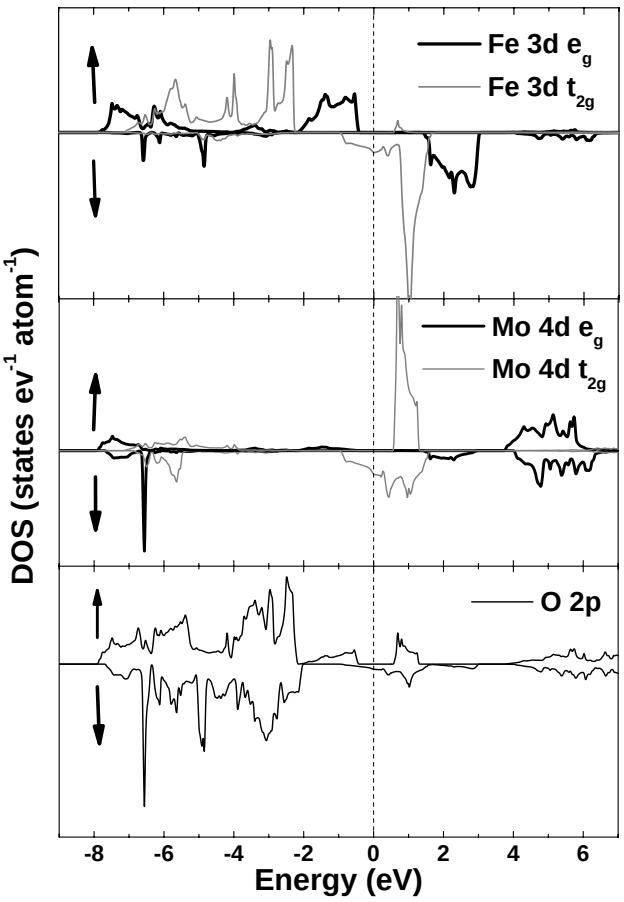

Figure 5.5: The spin-resolved, site-projected densities of states of the LDA + U (U = 2 eV) calculation for Sr_2FeMoO_6 [235].

Apparently the LDA+U treatment with a single, energy-independent U parameter is too simplistic to provide a good overall description of the XPS spectrum. However, we retain a moderate value U=2 eV, which still offers a certain improvement over the conventional DFT description. With this, we come back to calculated pDOS (Fig. 5.5) to discuss the origin of different spectral features.

The gap in the majority-spin band and hence the half-metallicity of Sr_2FeMoO_6, as follows from the calculation, have been mentioned earlier. The minority band around E_F is dominated by the Mo 4d (t_{2g}) states, overlapping with the Fe 3d (t_{2g}) states. Hence, feature a in the XPS valence band can be attributed to overlapping Mo 4d and Fe 3d minority-spin states, which are mixed since they are degenerate in energy. The b peak comprises mainly the majority-spin Fe 3d (e_g) states, while feature c is mainly composed of the majority-spin Fe 3d (t_{2g}) states hybridized with the O 2p. The d feature can also be attributed to overlapping Fe 3d–O 2p states – however, with a strong minority-spin contribution. Finally, the e feature contains both Fe 3d and

Mo $4d$ contributions, the latter becoming gradually enhanced towards the conduction band bottom. A large photoionization cross section for the Mo $4d$ electrons accounts for the strength of the e peak in the resulting XPS valence band spectrum, despite their moderate participation in the total DOS.

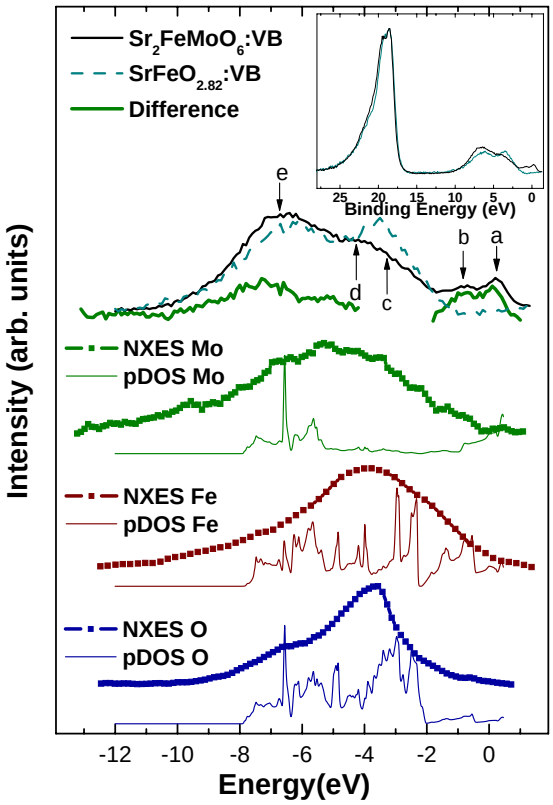

Figure 5.6: The XPS valence band and XES spectra of the Fe L edge, the Mo M and the O K edges of Sr_2FeMoO_6. The calculated densities of states are also shown (thin solid lines). The XPS valence band of $SrFeO_{2.82}$ has been normalized to the Sr $4p$ XPS located around 17.5 eV of binding energy (see inset graph). The "difference spectrum" of Sr_2FeMoO_6 and $SrFeO_{2.82}$ is also shown.

Fig. 5.6 displays the XPS valence band and the XES spectra of the Fe $3d \rightarrow 2p$, Mo $4d \rightarrow 3p$, and the O $2p \rightarrow 1s$ transitions. The XES spectra have been plotted on a common energy scale with the XPS valence band by using the corresponding XPS core level binding energies (710.6 eV for Fe $2p_{3/2}$, 529.4 eV for O $1s$ and 398.0 eV for Mo $3p_{3/2}$) for calibration. Hence, the XES spectra reflect the site-specific partial densities of states of the different elements in the compound which is symmetry-selected by the dipole selection rule, and broadened by the core-hole lifetime Γ_0 and the spectrometer resolution.

According to the XES, Fe $3d$ states are present from the Fermi level to around

−8 eV binding energy, the maximum intensity is reached around −3.5 eV, corresponds to band *c* in the XPS valence band. The Fe *L* edge XES also indicates that the Fe 3*d* states extend over the whole valence band region, hence, the iron states are not extremely localized in energy. Because of this extension in the energy domain, the Fe 3*d* states are certainly not strongly localized in space. Indeed, they exhibit a pronounced hybridization with O 2*p* states and, due to sharing a common oxygen neighbor with Mo atoms, show a number of features at the same energies (around E_F and also at −4 – −8 eV, bands *c*–*e*). The experimental XES results for iron and oxygen are also supported by the calculated (summed up over spin) densities of Fe 3*d* and O 2*p* states, as seen from Fig. 5.6. Finally, the Mo 4*d* XES spans the energy range from E_F to about −9 eV, with a rather broad maximum between −6 and −7 eV. In contrast the calculation suggests the presence of Mo 4*d* contributions around the Fermi level and in the region between −5 and −8 eV with a sharp maximum close to −7 eV. This difference is likely due to the rather high core-hole lifetime Γ_0 of metal 3*p* states, which can be estimated to be 2–4 eV by using the corresponding total atomic transition rates [237]. In contrast one finds a value of around $\Gamma_0 = 0.4$ eV for the Fe $2p_{3/2}$ state [238]. We also compare the XPS valence band of Sr_2FeMoO_6 with that of $SrFeO_{2.82}$ as a reference. Since the amount of Sr is the same in both compounds we can normalize the XPS valence band spectra to the Sr 4*p* peak located around 17.5 eV binding energy scale (inset in Fig. 5.6). By subtracting of the $SrFeO_{2.82}$ valence band from that of Sr_2FeMoO_6, we obtain the curve labelled as "Difference". The residual then mainly reflects the Mo 4*d* contributions to the valence band of Sr_2FeMoO_6. According to theory features *a* and *b* are also formed by Fe 3*d* states and not only by Mo 4*d* states. This is because $SrFeO_{2.82}$ has a stoichiometry close to $SrFeO_3$, an antiferromagnetic insulator, and the Fe 3*d* states in this kind of compound are much more localized between −2 and −3 eV compared to the half metal Sr_2FeMoO_6, although the electronic and magnetic properties of the defect oxide $SrFeO_{3-\delta}$ show strong changes dependent on the oxygen content. The electronic structure of $SrFeO_{3-\delta}$ will be discussed in detail elsewhere [239]. Considering these facts the Mo 4*d* contribution to the valence band of Sr_2FeMoO_6, in particular the states around E_F and the low lying states between −6 and −8 eV are nicely reproduced by the difference spectrum.

5.2.4 XMCD in XAS at the Fe L edge

The upper panel of Fig. 5.7 shows the absorption spectra excited with left and right circularly polarized light at the Fe $L_{2,3}$ edges and their MCD difference, respectively. A standard procedure has been used to subtract a two-step like function from the overall XAS intensity (lower panel) in order to take only into account the $2p-3d$ transitions. The thresholds of the step-function were set to the L_3 and L_2 peaks, and the height of the L_3 (L_2) step was set to 2/3 (1/3) after Chen *et al.* [96].

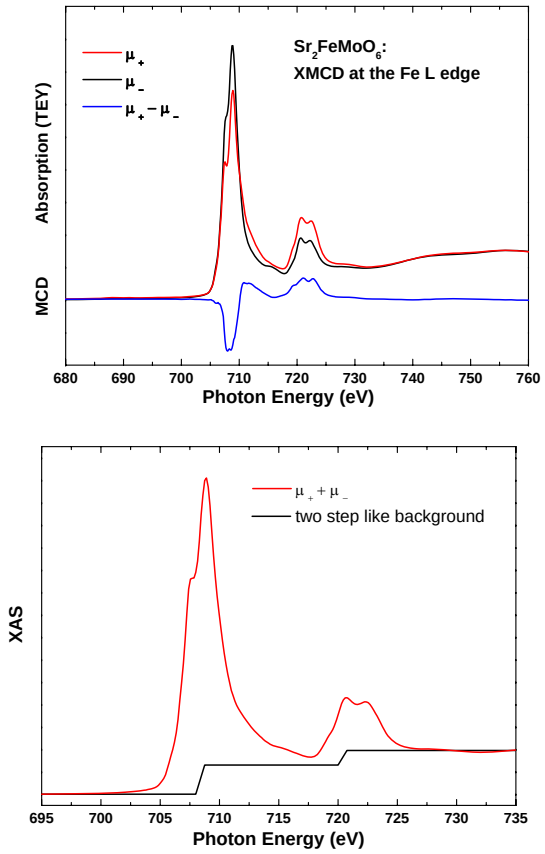

Figure 5.7: Upper panel: the XAS spectra taken with left and right circularly polarized x-rays and the resulting MCD ($\mu_+ - \mu_-$), lower panel: the overall XAS spectrum ($\mu_+ + \mu_-$) and a two step like background function (black line).

From the previous analysis of the Fe L edge XAS, the Fe $3s$ and the Mo $3d$ XPS core levels we are able to reveal that the number of d holes at the Fe site is about 4.35. Using the spin and orbital sum rule for the $2p$ edges of transition metals (Chapter 2.4.1, [96]) we obtain the spin moment of Fe to be $1.61\,\mu_B/f.u$ and the orbital magnetic moment on the Fe site to be $-0.26\,\mu_B/f.u$. We find no considerable contributions of Mo and O. In comparison the bulk magnetic measurement gives an overall saturation magnetization of $3.5\,\mu_B/f.u$. This means the magnetic moment revealed by XMCD is over 50% lower than that determined from magnetometry. This result is similar to that of Ray *et al.* [220]. Nonetheless, we can exclude that

the conditions under which the dichroic spectra have been recorded are responsible for this discrepancy. The only difference remaining compared to the work of Besse *et al.* is that we used a poly crystalline material and they used either a single crystal or a thin film comprising single crystalline grains. Table 5.1 collects the different results. Indeed, the properties of poly crystalline and single crystalline Sr_2FeMoO_6 are quite different. Tomioka *et al.* studied the magnetic properties of a Sr_2FeMoO_6 single crystal in detail and found only a minimal magneto resistance effect in their sample [218], in sharp contrast to the large MR effects in poly ctystals [3]. This is a clear indication that the nature of the MR effect is closely related to so called intergrain tunnelling, or grain boundary effects. Thus, Sr_2FeMoO_6 seems to be more related to tunnelling magneto resistance compounds than to the "classical" CMR manganites. In a recent work the influence of grain boundary effects to the magnetic and electric properties have been investigated in detail [240]. It was found that, if the concentration of grain boundary (GB) barriers is high enough, the resistivity and the MR effects on Sr_2FeMoO_6 are, to large extend, dominated by these small GB barriers.

Table 5.1: Comparison of previously published XMCD results with the one obtained in the present work.

	Ray *et al.* [220]	Besse *et al.* [217]	present work
sample	poly crystal	single crystal	poly crystal
disorder (XRD)	$\approx 10\%$	$\approx 15\%$	$\approx 3\%$
sat. mag.	$2.8\mu_B$(77K)	$3.2\mu_B$(5K)	$3.5\mu_B$(4.2K)
valence state Fe	100% Fe^{3+}	66% Fe^{2+} + 34% Fe^{3+}	65% Fe^{2+} + 35% Fe^{3+}
n_{3d} holes	5	4.34	4.35
XMCD conditions	T= 77K	T= 10K,B= 5T	T= 15K,B= $5,5$T
m_{spin} Fe	$1.71\mu_B$	$3.05\mu_B$	$1.61\mu_B$
m_{orb} Fe	$-0.03\mu_B$	-	$-0.26\mu_B$
m_{spin} Mo	-	$-0.32\mu_B$	-

As to the XMCD signal, the influence of a high concentration of GBs to dichroic spectra has not been studied in a systematic way by now. However, it has been shown that surface boundaries may lead to an essential drop of the MCD [241]. It is also noteworthy that the orbital momentum at the Fe site is obviously not completely quenched in the present measurement. With as an external magnetic field of 5.5 T, far above the saturation magnetization of Sr_2FeMoO_6 ($\sim$ 1T) (Chapter 5.2.1) this is a rather surprising result. However, very recently Sikora *et al.* also reported evidence of significant orbital contributions to the magnetic moment of iron in a related compound, namely Ca_2FeReO_6 [242].

Complementary measurements of the resistivity of our Sr_2FeMoO_6 sample show a similar behavior than that found by Niebieskikwiat *et al.* [240], moreover recently recorded Mössbauer data suggest a noncollinear spin arrangement at the Fe site in our sample, these are further indications that GB barriers may play an essential role

in the sample used for the XMCD experiments presented here. Another sample which shows an essentially lower electrical resistivity is now going to be analyzed by means of Mössbauer spectroscopy as well. One important topic in order to reveal an improved understanding of the intricate magnetic properties of Sr_2FeMoO_6 and other double perovskites is the further study of the interplay between grain boundary and antisite defects.

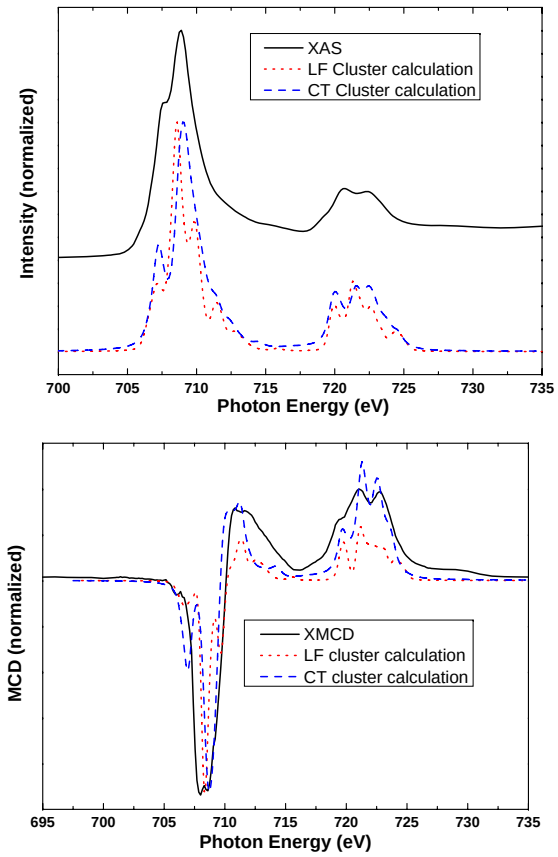

Figure 5.8: The experimental XAS spectrum (upper panel) and the XMCD (lower panel) in comparison with ligand field (LF) (dotted line) and charge transfer (CT) multiplet calculations (dashed line) in O_h symmetry.

In Fig. 5.8 we present multiplet calculations of the Fe $L_{2,3}$ edge XAS and XMCD of Sr_2FeMoO_6. We calculated the absorption multiplets of the iron d^5 and d^6 configurations in octahedral (O_h) symmetry for linear and circularly polarized x-rays. Like for the calculations presented in Chapter 3.2.3 we used the TT-multiplets program based upon the methods described by Thole, van der Laan and de Groot [61, 55].

Table 5.2 sums up the parameters used for the simulation of the Fe $L_{2,3}$ XAS and the corresponding XMCD. For the d^6 configuration the crystal field strength was set to 1.2 eV in the ligand field approach, and for the d^5 configuration to 1.8 eV. For the charge transfer calculations, crystal field parameters of 1.0 eV and 1.5 eV for the d^6 and d^5 configurations were used, respectively. The energy difference Δ between the $3d^n$ and $3d^{n+1}\underline{L}$ configuration was set to about 4.0 eV for both cases. For all

Table 5.2: The crystal field parameters as used in the Fe $L_{2,3}$ XAS and the corresponding XMCD multiplet calculation. The simulations were performed assuming a cubic crystal field (O_h symmetry). For the d^6 calculation, the $3d$ spin-orbit coupling was set to zero.

configuration	Type of calculation	10 Dq (eV)	Δ (eV)	Slater-Condon (% of atomic)
Fe^{2+} (d^6)	ligand field	1.2	-	80 %
Fe^{3+} (d^5)	ligand field	1.8	-	80 %
Fe^{2+} (d^6)	charge transfer	1.0	4.0	80 %
Fe^{3+} (d^5)	charge transfer	1.5	4.0	80 %

calculations the Slater-Condon parameters were reduced to 80% of their calculated Hartree-Fock values in order to account for intra-atomic relaxation effects. The calculated features were convoluted with a 0.3 eV FWHM Lorentzian to take into account the experimental broadening.

The calculated XAS and XMCD were obtained as follows. Firstly, the calculated spectra representing the d^6 and the d^5 configurations had to be shifted relative to each other with respect to the energy axis. This is because the energy positions are calculated from the atomic Hartree-Fock values, without considering any hybridization. Thus, the chemical shift is overestimated by this kind of calculation. We used the experimental spectra of FeO and Fe_2O_3 for calibration of the calculated XAS spectra. Then both, the simulated absorption and the calculated magnetic circular dichroism representing the d^6 and d^5 configuration of iron were summed up considering the valency of Fe in Sr_2FeMoO_6, the Fe^{2+} simulation was weighted by 0.65, and the Fe^{3+} simulation by 0.35, respectively.

Turning now to the comparison of experimental and simulated XAS spectra, the ligand field calculation (red dotted line in Fig. 5.8) simulates the experimental spectrum quite good. Nevertheless, there are some deviations at the shoulder located around 708 eV, the calculated intensity is too low. The charge transfer approach, which also includes the $3d^6\underline{L}$ and $3d^7\underline{L}$ electronic configurations improves the agreement between experiment and theory, although the calculated intensity around 708 eV is still too low. A similar situation is found for the MCD spectrum. The experimental spectrum shows an intense negative peak located between 708 and 709 eV followed by a rather broad positive L_3 contribution located between 710-716 eV on the energy scale. The L_2 dichroism leads to a broad positive peak spanning the energy range from 718-730 eV. Both simulations resemble the general shape of the MCD quite well, however, in the ligand field calculation both L_3 contributions, the negative peak as well as the positive shoulder are narrower compared to the experiment. Also the calculated minimum intensity of the MCD at 721 eV is not seen in the experimental spectrum. Like for the XAS, also here the charge transfer calculation leads to a significant improvement of the simulation. Also the deviations compared to the experimental MCD contributions arising from the L_3 edge are reduced, but there remain some differences. Nevertheless, an overall satisfactory

agreement between the experimental MCD and the corresponding charge transfer multiplet calculation is achieved. In order to further improve the $2p$ absorption and circular dichroism simulations one could perform a more extended series of calculations involving different values of 10 Dq as well as different charge transfer energies. Moreover the calibration of the calculations with the experimental spectra of FeO and Fe_2O_3 must not be perfect. One may try to shift the simulated spectra in a different way to each other in order to find the optimal fit. The MCD spectrum is also very sensitive to the broadening parameter, which can be varied as well. Such an improved charge transfer multiplet calculation may also be used as a starting point for the simulation of the Fe $2p$ RIXS spectra. These experiments, involving measurements with linear and circular polarized x-rays, have been performed very recently. The results will be reported elsewhere [243].

5.2.5 Conclusions

We have presented a combined study of the magnetic and electronic properties of highly ordered Sr_2FeMoO_6. In order to avoid variations due to different antisite defect concentrations all experiments have been performed on the same sample. XRD measurements reveal a low antisite defect concentration of around 3% in the highest quality sample and the saturation magnetization is $3.5\,\mu_B/f.u.$ Paramagnetic measurements suggest a percentage of 60% Fe^{2+} ions while 30% of the Mo ions are in the +5 valence state. This finding is in good agreement with results obtained by means of XAS on the Fe L edge, and Fe $3s$ and Mo $3d$ core level XPS, respectively. The Fe $3s$ splitting and the separation of the overlapping peaks in the Mo $3d$ XPS reveal a mixed iron valence state involving around 30% Fe^{3+} – Mo^{5+} and 70% Fe^{2+} – Mo^{6+} states in highly ordered Sr_2FeMoO_6.

We have presented a detailed x-ray spectroscopic study of the electronic structure of highly ordered Sr_2FeMoO_6 and compared these experimental results with different first principles band structure calculations. The XPS valence band comprises five distinct features. The region near Fermi level is dominated by energetically overlapping Mo t_{2g} $4d$ and Fe $3d$ t_{2g} spin down states, which are also responsible for the half metallic character of Sr_2FeMoO_6. Between -2 eV and -3.5 eV the valence band is dominated by Fe t_{2g} (spin up) states. The lower lying features can be attributed to strongly overlapping Fe $3d$, O $2p$ and Mo $4d$ states. In particular, the Fe $3d$ states are not extremely localized, and we find evidence that charge transfer between Fe $3d$ and O $2p$ states play an essential role. In conclusion, Sr_2FeMoO_6 can be described as a moderately correlated compound. Assuming an effective potential $U_{dd} = 2.0$ eV for the Fe $3d$ electrons and invoking no on-site correlation energy for the Mo $4d$ and O $2p$ states we find a satisfactory overall agreement between experiment and theory.

Regarding the XMCD measurements, we find a spin moment $1.61\,\mu_B/f.u.$ and an orbital magnetic moment of $-0.26\,\mu_B/f.u.$ at the Fe site. The strong drop of the magnetic moment revealed by XMCD compared to magnetometry may be associated with the presence of grain boundary barriers, which obviously play an essential role for the electric and magnetic transport properties in double perovskites. The XMCD spectrum could be resembled by charge transfer multiplet calculations which may be used as a starting point for further theoretical investigations such as the simulation of Fe $2p \rightarrow 3d$ RIXS measurements.

Chapter 6

Defect oxides: The electronic structure of Li_xCoO_2

6.1 Introduction

Defect oxides like oxides Li_xCoO are of special interest for industrial applications and they serve already as cathode materials for Li batteries [244]. Therefore, knowledge about the electronic structure of such compounds is very important. $LiCoO_2$ is a semiconductor with the band gap of 2.7 eV [245] while Li_xCoO_2 at concentrations below $x = 0.75$ is metallic [246], implying that a metal-insulator transition occurs at intermediate Li concentrations. Electrical conduction in $LiCoO_2$ is expected to occur not in the Co e_g conduction band but in the Co t_{2g} valence band by the hopping of Co $3d$ electrons between localized states near the Fermi level [247]. In $LiCoO_2$, the Li and Co ions reside alternatively layered between close-packed planes of oxygen ions (space group $R\bar{3}m$). Extraction of Li from $LiCoO_2$ occurs via several phase transitions. In Li_xCoO_2, two rhombohedral phases co-exist for $0.75 \leq x \leq 0.93$ [248] which has been attributed to the insulator metal transition upon Li extraction. In the defect cobaltites Li_xCoO_2 a coexistence of Co^{3+} and Co^{4+} ions can be expected. Due to a study of Co $2p$ and O $1s$ core levels of Li_xCoO_2 defect oxides by means x-ray absorption spectroscopy (XAS) Montoro *et al.* [249] have concluded that the trivalent Co ions remain unaffected by Li de-intercalation, i.e. in Li_xCoO_2 oxides, doped holes are localized in O $2p$ states. Thus the Co ions in these cobaltites can be regarded as being in the d^6 configuration, as it was shown by the Co $2p$ x-ray spectroscopic measurements of the related compound $NaCo_2O_4$ [250]. On the other hand side, Yoon *et al.* [251] have proposed that the charge compensation for the electron exchange in the Li-ion de-intercalation process could affect both the oxygen site and cobalt site simultaneously.

The electronic structure of $LiCoO_2$ has been studied intensely by applying a combination of x-ray photoelectron and emission spectra [252] and the related defect cobaltites $LiCoO_{2-\delta}$ have been investigated by means of x-ray photoelectron spectroscopy (XPS) [253]. In present work we want to go beyond the research done so far and present the results of a combined x-ray spectroscopic study of Li_xCoO_2 performed by means of x-ray absorption (XAS), x-ray emission(XES), and x-ray photoelectron (XPS) spectroscopy. As one result, it is experimentally shown that in these defect

cobaltites, electronic holes have mainly O $2p$ nature.

Furthermore, it has been shown, that by setting up resonant Raman conditions to the O $1s$ edge one can observe loss features characteristic of excitations from the ground state to a valence excited state for strongly correlated and insulating oxides [169, 170]. Very recently resonant Raman scattering as been also found near the S $2p$ edge of semiconducting FeS_2 [167]. In the present work we apply here resonant Raman conditions to the O $1s$ threshold of the semiconductor $LiCoO_2$.

6.2 Experimental Details

A single-phase, homogeneous sample of $LiCoO_2$ was prepared by sintering a mixture of Co_3O_4 and Li_2CO_3 at the Institute of Metal Physics of the Russian Academy of Sciences in Yekaterinburg, Russia. The synthesis was carried out in two steps in air, firstly at a temperature of 700 °C for 20 h, followed by a second sintering procedure at a temperature of 850 °C for 25 h, finally the compounds were cooled down slowly. The defect samples Li_xCoO_2 ($x = 0.60 - 0.96$) oxides were produced by chemical de-intercalation in 0.7 N H_2SO_4. A de-intercalation time of $\tau = 20$ min corresponds to the oxide with $x = 0.96$, and $\tau = 1.5$ h corresponds to $x = 0.6$. Li concentrations were estimated by means of atom-absorption analysis using a spectrophotometer Perkin-Elmer 503. The phase composition was checked by x-ray diffraction analysis using an x-ray diffractometer STADI-P (STOE). The x-ray photoelectron spectra of the Li_xCoO_2 oxides were obtained with a PHI 5600 CI Multitechnique System XPS spectrometer using monochromatized Al $K\alpha$ radiation at the Department of Physics at University of Osnabrück. The spectrometer was calibrated using Au foil (the binding energy of the Au $4f_{7/2}$ line is 84.0 eV) [113]. The energy resolution was about 0.4 eV. The Co $2p$ and O $1s$ x-ray absorption spectra (XAS) of the Li_xCoO_2 oxides were carried out at the Russian-German Beam Line at BESSY II, Berlin, Germany. The spectra were normalized to the incident current as measured from a gold grid located at the entrance chamber. The O $K\alpha$ resonant x-ray emission (RXES) spectra were measured at the bulk branch line of beamline I511 at MAX II, MAX-lab National Laboratory, Lund, Sweden. The spectra were obtained using a high-resolution Rowland-mount grazing-incidence grating spectrometer with a two-dimensional detector [120].

6.3 Results and discussion

Since the electric dipole-allowed $1s \rightarrow 2p$ transition is dominating oxygen $1s$ x-ray absorption spectra direct information of the unoccupied oxygen density of states as well as about Co–O bonding interaction is provided. The $2p$ orbitals of the oxygen ligand are involved in bonding configuration with Co metal ions. Fig. 6.1 (a) shows the O 1s x-ray absorption spectra (XAS) of $LiCoO_2$, $Li_{0.96}CoO_2$, and $Li_{0.6}CoO_2$. The sharp peak at 530.5 eV corresponds to the transition of oxygen $1s$ electrons to the hybridized state of Co $3d$ (e_g^*) and oxygen $2p\sigma$ orbitals whereas the broad bumps at energies of 538 eV and 542–544 eV reveal O $2p$ states mixed in the Co $4sp$

bands. The small feature at 534 eV in the spectrum of $LiCoO_2$ is formed by Li_2CO_3 contaminations.

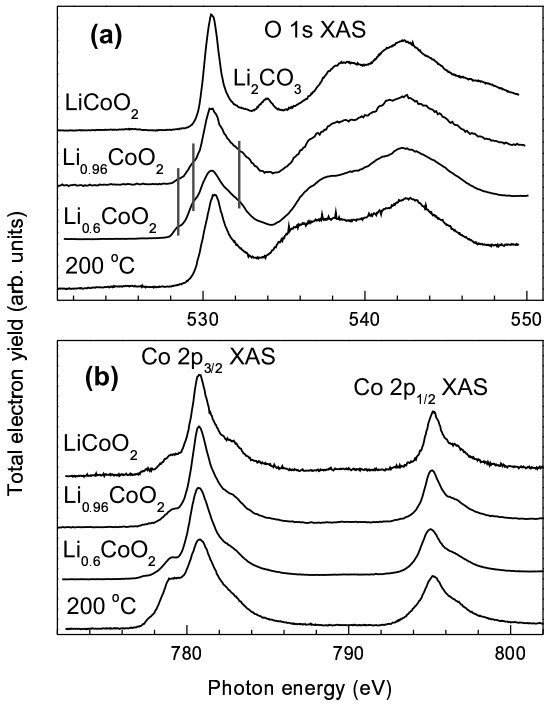

Figure 6.1: Upper panel: O 1s (a), lower panel: Co 2p (b) x-ray absorption spectra of Li_xCoO_2 [254]. The spectra labelled with 200 °C has been measured on the $Li_{0.6}CoO_2$ sample which has been heated at 200 °C for about 20 h.

If an alkali ion removed from $LiCoO_2$, the O 1s XAS spectra of the de-intercalated Li_xCoO_2 compounds show significant changes: the spectra are broadened and three additional features appear (as marked by the vertical bars). In alkali-ion de-intercalated cobaltites, an extra electron hole should be created in the upper t_{2g} valence band. For formally Co^{4+} ions the trigonal field splits the three t_{2g} orbitals into a a_{1g} orbital (with one electron) and two e_g orbitals (with four electrons). The band structure calculations of the reference compound $NaCo_2O_4$ predicts that electronic holes introduced by A-site defects have mainly a_{1g} character [255]. Therefore, the features below the threshold in the O 1s x-ray absorption spectra of defect cobaltites are formed by hybridized Co a_{1g}–O 2$p\pi$ states. These spectral features indicate additional unocuppied O 2p states. Changes in intentsity of the features well correlate with the hole concentration in the Li-sublattice.

In the lower panel of Fig. 6.1 we present the Co 2p x-ray absorption spectra

of Li_xCoO_2. The spectra are characterized by the multiplet structure which can be explained as being due to the Coulomb and exchange interaction between the Co $2p$ core hole and the Co $3d$ electrons, the crystal field splitting, and the spin-orbit interactions. The spectrum of $LiCoO_2$ resembles the multiplet calculation made for the low-spin states of Co^{3+} ions [256]. This confirms the fact that the Co $3d$ states in $LiCoO_2$ are in the low-spin configuration ($S = 0$). Lithium de-intercalation does not change Co $2p$ x-ray absorption spectra significantly, in sharp contrast to the O $1s$ XAS. This is a strong indication that cobalt ions remain in the Co^{3+} state and electronic holes in the defect Li_xCoO_2 cobaltites are mainly of O $2p$ character. A similar effect was found in work by Montoro *et al.* [249], but in distinction to this work, our results also show the effect already for small concentrations of holes.

Heating the defect cobaltides in vacuum leads to dramatic changes of the Co $2p$ and the O $1s$ x-ray absorption spectra. The lowest spectra plotted in Fig. 6.1 (a) and (b) have been measured on $Li_{0.6}CoO_2$ after annealing this sample in vacuum at 200 °C for about 20 h. As to the O $1s$ spectrum, the prepeak structure disappears; the spectrum is more similar to that of $LiCoO_2$ than to the defect oxide O $1s$ XAS. The shape of the Co $2p$ x-ray absorption spectrum also shows significant deviations. One can suggest a degradation process of this compound which can be explained by the appearance of Co^{3+} and also some Co^{2+} ions as a result of a transition of Li_xCoO_2 into $LiCoO_2$ with Co_3O_4 admixtures.

Fig. 6.2 shows O $K\alpha$ resonant x-ray emission spectra (RXES) for $LiCoO_2$ measured at excitation energies of 529.4–548.9 eV. The excitation energies are labelled a_1 (as shown by the solid inclined line), and were chosen based upon the corresponding O $1s$ x-ray absorption spectrum (XAS) measured in total-electron yield (TEY) mode (see inset graph in Fig. 6.2). The vertical bars in the O $1s$ XAS spectrum correspond to the incident photon energies (O $2p \rightarrow 1s$ transition). O $K\alpha$ resonant x-ray emission spectra of $LiCoO_2$ may be explained in terms of both band-like states (main emission band) and localized excitonic states (inelastic scattering). One can associate peak a_2 with Co dd transitions between occupied Co states in the valence and unoccupied Co states in the conduction band, via the hybridization of the Co states with oxygen states. The energy position of feature a_2 is constant in the Raman-shift scale and depends on the excitation energy in the emission-energy scale. This interpretation is supported by optical absorption measurements of Ref. [257] where the absorption peak of ordered $LiCoO_2$ at 2.1 eV is identified as a dd transition from the Co $3d$ (t_{2g}) valence band to the e_g^* conduction band.

Figure 6.3 presents the x-ray photoelectron valence band spectra and the O $1s$ XAS spectra of $LiCoO_2$, $Li_{0.96}CoO_2$, and $Li_{0.6}CoO_2$. For $LiCoO_2$, O $K\alpha$ resonant x-ray emission spectrum excited at 530.5 eV is also shown. The RXES and XAS spectra have been brought to the binding energy scale based upon the O $1s$ binding energies obtained from our x-ray photoelectron experiment. The XPS valence band spectra refelect the total DOS distribution (accurate up to the weight function depending on the atomic photoemission cross-sections [258]). For an excitation energy of 1486.6 eV (Al $K\alpha$), the Co $3d$ to O $2p$ cross-section ratio $\sigma(\text{O } 2p)c(\text{O}) : \sigma(\text{Co } 3d)c(\text{Co})$ is equal to 0.13 : 1 [258]. As a consequence, the main contribution to the XPS valence-band spectrum in the presented energy region results from Co $3d$ states. The XPS region of

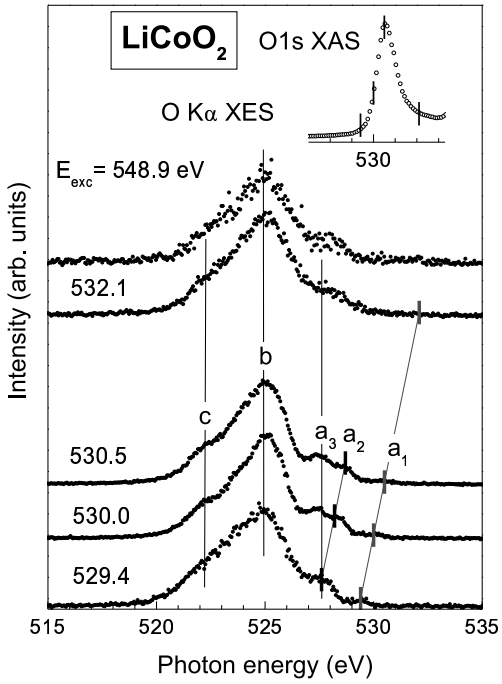

Figure 6.2: X-ray emission O $K\alpha$ emission spectra measured at excitation energies between 529.4 and 548.9 eV. The inset graph shows the corresponding O 1s x-ray absorption spectrum (XAS) measured in total-electron yield mode. The vertical bars in the O 1s XAS and O $K\alpha$ XES spectra mark the incident photon energies [254].

Li_xCoO_2 from 0 to 9 eV (peak A and feature B–E) corresponds to the Co $3d^6\underline{L}$ final-state configuration, while satellite F at about 11.5 eV cannot be interpreted in terms of band structure, but it can be explained as being due to the presence of a poorly screened Co 3d hole (the $3d^5$ final state). Here, $\underline{L}$ denotes a hole in the O 2p states due to the charge-transfer process. The strongest peak A near the Fermi level and feature B can be explained as being due to Co t_{2g} orbitals. According to calculations made by Czyżyk *et al.* [259], feature C mainly formed by t_{1u} orbitals, which derive primarily from the O 2p states with a slight admixture of the Co 4p states. Band D reveals the hybridized O 2p–Co 3d (e_g) states. Finally, band E reflects Co 4s and 4p states (a_{1g} and t_{1u} orbitals), strongly hybridized with O 2p states. Features D and E are nicely reproduced in the O $K\alpha$ RXES spectrum as the main peak b and the shoulder c, respectively. Moreover, feature a_3 in the O $K\alpha$ RXES spectrum coincides well with peak A of the XPS spectrum and can probably be attributed to the presence of some hybridization between the Co t_{2g} and O $2p\pi$ states near E_F.

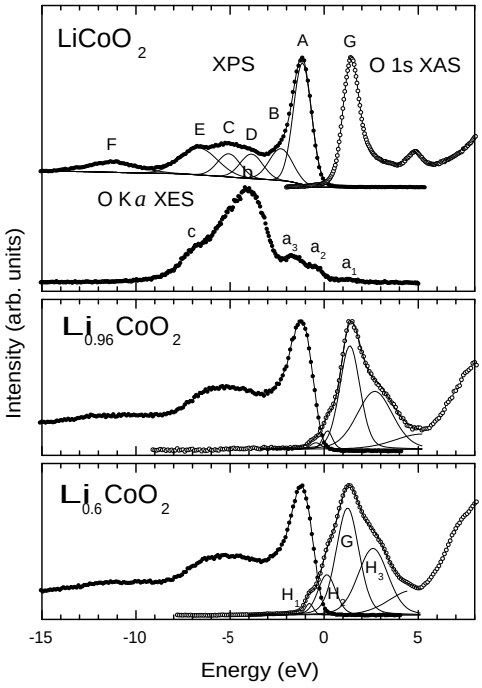

Figure 6.3: Valence band x-ray photoelectron spectrum and O $K\alpha$ resonant x-ray emission (RXES) and O 1s absorption (XAS) spectra of $LiCoO_2$. The XES and XAS spectra are plotted on a common energy scale based on the binding energy of the O 1s levels. The O $K\alpha$ XES spectrum is measured at the excitation energy of 530.5 eV [254].

Although the defect cobaltites Li_xCoO_2 are expected to be hole doped, the Co t_{2g} peak remains sharp. Therefore, one can suggest that the Co^{3+} state remains in the low-spin t_{2g} configuration and that the spectral weight near the Fermi level is dominated by the t_{2g} states.

The combination of the XPS valence bands and O 1s XAS spectra shown in Fig. 6.3 yields clearly the band gap for $LiCoO_2$ and also demonstrates metallic properties of of de-intercalated cobaltites. The distance between peaks A and G for $LiCoO_2$ is about 2.6 ± 0.2 eV is in good agreement to the band gap determined in Ref. [245] by applying a combination of x-ray photoelectron and bremsstrahlung isochromat spectroscopy. For the defect cobaltites Li_xCoO_2, the distance between peak A and feature H_1 (acceptor level) is about 0.5 ± 0.2 eV, and there is certainly some overlap between this peaks. Thus is clear evidence that de-intercalated oxides show metallic properties. Complemantary impedance measurements [246] show that Li_xCoO_2 becomes an electronic conductor for $x \leq 0.9$. However, according to the

results presented in Fig. 6.3, the $Li_{0.96}CoO_2$ compound should already show metallic character. One possible explanation for this discrepancy may be a so-called phase separation effect. A similar effect has been found in manganites [260]. In this case, the lithium de-intercalation leads to the appearance of small metallic clusters with small Li concentrations surrounded by the insulating host material. A decrease in Li-content leads subsequently to an increase of the quantity and the also the size of the metallic clauters. They start to overlap and, as a result, to the appearance of metallic properties of the Li-deintercalated cobaltites.

6.4 Conclusions

In summary we have studied the change in the electronic structure of defect oxides Li_xCoO_2 ($x = 0.6$, 0.96, and 1.0) by means x-ray photoelectron, resonant x-ray emission and x-ray absorption spectroscopy, leading to a number of results. Resonant O $K\alpha$ x-ray emission spectra of $LiCoO_2$ show features which can be associated with Co *dd* transitions. As to the localization of the holes it was established that in defect cobaltites electronic holes are localized mainly in the O $2p$ states. Finally, metallic character of Li_xCoO_2 even for small defect concentrations is suggested by applying a combination of x-ray photoelectron and O $1s$ x-ray absorption spectroscopy.

Chapter 7

Conclusions and outlook / Kurzfassung

The aim of the present work was to develop a detailed picture of the electronic and magnetic properties of a number of very interesting transition metal compounds. A number of complementary experimental and theoretical techniques have been applied, special emphasis was given to x-ray spectroscopies. The studies led to a number of results, and the following conclusions can be drawn:

Wüstite and pyrite

The influence of the magnetic ground state (high-spin (FeO) vs. low-spin (FeS_2)) with respect to the recorded x-ray spectra was investigated. In particular, by performing RXES on the Fe L edge of the two compounds, very different ratios of L_α to L_β integrated intensity for excitation energies close to the L_2 edge have been observed. This effect has been explained in terms of the magnetic structure of FeO (high spin), which inhibits Coster-Kronig processes. One can propose that this is a general rule, for the ratio of L_α intensity for L_3 excitation to L_β intensity for L_2 excitation. Furthermore, by setting up resonant Raman conditions over a narrow energy range near the S $2p$ threshold we are able to probe Fe dd excitations between the valence and conduction band, via the hybridization of the Fe states with sulfur states.

Colossal Magneto Resistance (CMR) manganites

A detailed x-ray spectroscopic study of the A-site doped CMR compounds $La_{1-x}Ba_xMnO_3$ and the A- and B-site doped manganites $La_{0.76}Ba_{0.24}Mn_{0.84}Co_{0.16}O_3$ and $La_{0.76}Ba_{0.24}Mn_{0.78}Ni_{0.22}O_3$ has been performed. XPS and XES data reveal charge transfer between Mn $3d$ states and O $2p$ states in the valence band. Excellent agreement with available theory is found. In $La_{0.76}Ba_{0.24}Mn_{0.84}Co_{0.16}O_3$ the Co $3d$ states mainly contribute at lower binding energies between 0.5-5 eV to the valence band, including the states near E_F. Doping with Ni leads to a lower occupancy of the e_g states near E_F, and the Ni $3d$ states are rather localized between 1.5-5 eV.

RIXS has been performed at the Mn L edge of $La_{1-x}Ba_xMnO_3$. The spectra consist of three main features, which can be associated with the elastic recombination peak and two loss features. A loss peak located around 2.5 eV below the elastic

peak can be associated with a local Mn *dd* transition in agreement with multiplet calculations, the second loss feature can be assigned to charge transfer transitions. With increasing Ba concentration the charge transfer between O $2p$ and Mn t_{2g} bands in the valence band becomes stronger, which can be directly investigated by RIXS: the intensity of the corresponding peak increases with increasing Ba concentration. In summary, we have shown that colossal magneto resistance manganites can be understood as being moderately correlated systems, in which hybridization effects, especially charge transfer between the Mn $3d$ and O $2p$ states for both occupied and unoccupied states play an important role with respect to their unusual phenomena and transport properties.

Special attention has been given to the direct investigation of orbital ordering in a three dimensional CMR manganite, namely $La_{7/8}Sr_{1/8}MnO_3$, by means of x-ray linear dichroism (XLD). We obtained, for the first time, rather strong indications that the coherently distorted Jahn-Teller phase in $La_{7/8}Sr_{1/8}MnO_3$ is accompanied by a predominantly cross type $(x^2 - z^2)$ / $(y^2 - z^2)$ orbital ordering. This result adds new experimental evidence to the re-opened and exciting discussion about the nature of orbital order in manganites, where controversial results were recently reported.

The double perovskite Sr_2FeMoO_6

Turning now to the double perovskite Sr_2FeMoO_6 the combined study by means of x-ray spectroscopies, magnetic measurements and and theoretical band structure calculations could resolve some points discussed controversially in the literature. XRD measurements reveal a low antisite defect concentration of around 3%, in the highest quality sample and the saturation magnetization is $3.5\,\mu_B/f.u.$. Both, paramagnetic measurements as well as core level spectroscopy of the Fe $2p$, Fe $3s$ and the Mo $3d$ states suggest a mixed iron valence state involving around 30% Fe^{3+} - Mo^{5+} and 70% Fe^{2+} - Mo^{6+} states in highly ordered Sr_2FeMoO_6. The XPS valence band comprises five distinct features. The region near Fermi level is dominated by energetically overlapping Mo $4d$ t_{2g} and Fe $3d$ t_{2g} spin down states, which are also responsible for the half metallic character of Sr_2FeMoO_6. Between -2 eV and -3.5 eV the valence band is dominated by Fe e_g (spin up) states. The lower lying features can be attributed to strongly overlapping Fe $3d$, O $2p$ and Mo $4d$ states. In particular, the Fe $3d$ states are not extremely localized, and we find evidence that charge transfer between Fe $3d$ and O $2p$ states plays an essential role.

The defect oxides Li_xCoO_2

In the last chapter the focus moved on a different kind of transition metal compound, namely the defect oxide Li_xCoO_2. A detailed x-ray spectroscopic study involving XPS, XAS and RXES on the O K edge of $LiCoO_2$ was carried out. Resonant O $K\alpha$ x-ray emission spectra of $LiCoO_2$ shows features whichcan be explained as being due to Co *dd* transitions. It was established that in defect cobaltites, electronic holes are localized mainly in O $2p$ states. Metallic character of defect cobaltites Li_xCoO_2 is confirmed by a combination of x-ray photoelectron spectroscopy and O $1s$ XAS measurements.

Outlook

In order to develop a more detailed picture of the L_β/L_α emission ratio for resonant x-ray emission at the L_2 edge of iron oxides an extension of the presented example on FeO and FeS_2 would be highly desirable. More experiments on other iron oxides like Fe_2O_3, Fe_3O_4 and more complex iron compounds would be helpful to provide detailed information about the magnetic state of materials. These studies could also be extended to cobaltites like $LaCoO_3$ or the defect oxides Li_xCoO_2. For Co based oxides the magnetic ground state is often an open question. Sr_2FeMoO_6 is just one of hundreds of double perovskites. One may try to produce samples with even better magnetic properties and higher Curie temperatures. Up to now only a few single crystals of Sr_2FeMoO_6 exist which are mostly not of very high (structural) quality. Furthermore a thorough comparison of the properties of poly crystals and single crystals seems to be necessary. The presented discrepancy in the XMCD is maybe an indication that the transport properties of Sr_2FeMoO_6 may depend very much on grain boundary effects. In case of the defect oxides the present study is just a beginning of more intense studies. For example, other defect oxides, like $SrFeO_{3-x}$ or $LaMnO_{3-x}$ show a fascinating variety of magnetic properties in dependence of the oxygen content, up to now no systematic study of the electronic structure of these and many other defect oxides is available. Finally the investigation of orbital ordering in transition metal compounds has regained a huge interest since much more direct experimental probes of orbital ordering at the transition metal L edges are now available. One possibility is the study by means of x-ray linear dichroism (XLD), another possibility is to perform resonant x-ray scattering (RXS) on the transition metal L edges of interesting compounds. However, it shall be noted that these experiments require highest quality and well characterized single crystals.

Kurzfassung

Die vorliegende Arbeit beschäftigt sich mit der Untersuchung von elektronischen und magnetischen Eigenschaften einiger interessanter Übergangsmetallverbindungen. Um dieses Ziel zu erreichen wurden mehrere sich ergänzende experimentelle und theoretische Methoden angewandt, wobei ein besonderes Augenmerk auf verschiedene Röntgenspektroskopien gelegt wurde. Die Experimente führten zu einigen Ergebnissen, die im Folgenden kurz zusammengefasst werden.

Wüstit and Pyrit

Diese beiden Materialien wurden mittels verschiedenen Röntgenspektroskopien eingehend untersucht, insbesondere im Hinblick auf die unterschiedlichen magnetischen Grundzustände (FeO ist ein high-spin System, hingegen ist FeS_2 eines der wenigen low-spin Materialien). Ein wichtiges Ergebnis wurde mittels resonanter Röntgenemission nahe und an der Eisen L_2 Kante erzielt, wo sehr unterschiedliche L_α/L_β Intensitätsverhältnisse in der Emission beobachtet wurden. Dieser Effekt kann durch Coster-Kronig Prozesse erklärt werden, welche insbesondere durch den high-spin Zustand in FeO unterdrückt werden. Desweiteren wurden die Schwefel $2p$ Zustände von FeS_2 mittels resonanter Röntgenemission untersucht. Dabei konnten Eisen dd Übergänge zwischen dem Valenz- und dem Leitungsband von Pyrit über die Eisen-Schwefel Hybridisierung beobachtet werden.

Manganite

Eine Reihe von A- und B-Platz dotierten Manganiten, welche wegen dem kolossalen magnetoresistiven Widerstand (CMR) von hohem wissenschaftlichen und technologischen Interesse sind, wurden eingehend hinsichtlich ihrer elektronischen Struktur untersucht. Das Valenzband und die partiell besetzten Zustandsdichten von $La_{1-x}Ba_xMnO_3$ ($0 \leq x \leq 0.55$), $La_{0.76}Ba_{0.24}Mn_{0.84}Co_{0.16}O_3$ und $La_{0.76}Ba_{0.24}Mn_{0.78}Ni_{0.22}O_3$ wurden mittels XPS und XES untersucht. Dabei stellte sich heraus, dass charge transfer zwischen den Sauerstoff $2p$ Zuständen und den Mangan $3d$ Zuständen im Valenzband eine entscheidende Rolle zukommt, in sehr guter Übereinstimmung mit vorhandenen theoretischen Bandstrukturrechnungen. Das Kobalt in $La_{0.76}Ba_{0.24}Mn_{0.84}Co_{0.16}O_3$ trägt hauptsächlich in dem Bereich vom Fermi-Niveau bis zu etwa 5 eV Bindungsenergie zum Valenzband bei. Im Gegensatz dazu sind die Ni $3d$ Zustände in $La_{0.76}Ba_{0.24}Mn_{0.78}Ni_{0.22}O_3$ recht lokalisiert, zwischen 1.5 und 5 eV auf der Bindungsenergieskala.

Zudem wurde an $La_{1-x}Ba_xMnO_3$ ($0 \leq x \leq 0.55$) zusätzlich resonante Röntgenemission an der Mn L Kante durchgeführt. Die Spektren bestehen aus drei Peaks, dem elastischen Rekombinationspeak und zwei Verluststrukturen. Davon kann ein Peak, etwa 2.5 eV unterhalb des elastischen Peaks lokalisiert, Mn dd Übergängen zugeordnet werden, in Übereinstimmung mit Multiplettrechnungen. Eine weitere Struktur befindet sich etwa 5-8 eV unterhalb des elastischen Peaks und kann mit charge transfer Anregungen erklärt werden. Es konnte beobachtet werden, dass mit steigender Ba-Konzentration auch die Intensität des charge transfer Peaks in den RIXS-Spektren

deutlich zunimmt, ein weiterer Beweis für den charge transfer Charakter von CMR-Manganiten.

Ein besonderes Experiment wurde an einem $La_{7/8}Sr_{1/8}MnO_3$ Einkristall durchgeführt. Mittels linearem Dichroismus an der Mn L Kante konnte die bevorzugte Besetzung des Mn e_g Orbitals (orbitale Ordnung) in der kooperativ Jahn-Teller verzerrten Phase dieses Kristalls bestimmt werden. Es wurden starke Indizien für eine bevorzugte Besetzung der $(x^2 - z^2)$ / $(y^2 - z^2)$ Orbitale gefunden. Die orbitale Ordnung in Manganiten wird zur Zeit sehr intensiv und kontrovers in der Literatur diskutiert, und dieses Ergebnis bringt einen neuen Aspekt in diese hochspannende Thematik ein.

Das Doppelperowskit Sr_2FeMoO_6

Neben den Manganiten wurde ein weiteres sehr interessantes magnetisches Oxid, Sr_2FeMoO_6, eingehend untersucht. Verschiedene röntgenspektroskopische Methoden wurden in Kombination mit magnetischen Messungen durchgeführt. Zudem wurden die Ergebnisse mit einer ganzen Serie von Bandstrukturrechnungen verglichen. Die strukturelle Qualität der Proben wurde mit Hilfe von XRD Messungen bestimmt. Die beste Probe wies nur eine sehr kleine Konzentration von sogenannten Antisite Defekten auf ($\sim 3\%$), was durch das hohe magnetische Moment von $3.5\,\mu_B/f.u.$ bestätigt wird. Zudem konnte mit paramagnetischen Suszeptibilitätsmessungen sowie XPS und XAS Messungen an den Fe $2p$, Fe $3s$ und Mo $3d$ Linien der Valenzzustand von Eisen und Molybdän in Sr_2FeMoO_6 eingehend untersucht werden. Diese Experimente führen zu der Schlussfolgerung das Eisen und Molybdän in gemischt valenter Form vorliegen, mit etwa 70 % Fe^{2+}-Mo^{6+} und 30 % Fe^{3+}-Mo^{5+}. Das XPS Valenzband besteht aus fünf auflösbaren Bändern, wobei der Bereich nahe dem Fermi-Niveau aus energetisch überlappenden Mo $4d$ t_{2g} und Fe $3d$ t_{2g} (spin-down) Zuständen besteht. Diese sind auch verantwortlich für den halbmetallischen Charakter von Sr_2FeMoO_6. Zwischen -2 eV und -3.5 eV werden die Eisen $3d$ e_g (spin-up) Zustände dominant, während die energetisch tiefer liegenden Strukturen energetisch überlappenden Fe $3d$ and Mo $4d$ Zuständen zugeordnet werden können, welche mit O $2p$ Zuständen hybridisieren. Zusammenfassend kann gesagt werden, dass die Eisen $3d$ Zustände in Sr_2FeMoO_6 nicht allzu lokalisiert sind und dieses Material als moderat korreliert beschrieben werden kann.

Die Defektoxide Li_xCoO_2

Das letzte Kapitel dieser Arbeit beschäftigt sich intensiv mit den Defektoxiden Li_xCoO_2 ($0.6 \leq x \leq 1.0$). Diese Materialien werden schon seit einiger Zeit als Kathodenmaterial in Li-Akkus eingesetzt. Die elektronische Struktur von Li_xCoO_2 wurde mittels XPS und XAS untersucht. An der O K Kante von $LiCoO_2$ wurde zudem RXES durchgeführt. Die Kombination von XPS und XAS zeigt den metallischen Charakter der Defektproben. Ausserdem wird gezeigt, dass die Defekte sich als Löcher in den O $2p$ Zuständen manifestieren. Mit Hilfe der resonanten Emission an der O K Kante können zudem Co dd Übergänge in $LiCoO_2$ beobachtet werden.

Acknowledgement / Danksagung

This work was made in the framework of the PhD program "Synthesis and Characterisation of Surfaces and Interfaces assembled from Clusters and Molecules" of Lower Saxony. The financial support is gratefully acknowledged.

In first place I want to thank apl. Prof. Dr. Manfred Neumann for making possible this work in his research group. His constant organizational and scientific support and his encouragement during insight discussions with special respect to the interpretation of experimental data have been always a very valuable help.

I am indebted to Dr. Kevin C. Prince for a continuous, constructive and very fruitful collaboration. He is acknowledged for showing me a lot of things regarding the usage of synchrotron radiation experiments as well as for many very interesting and substantial discussions. I also want to thank Dr. Maurizio Matteucci for a steady collaboration, especially regarding the work on Sr_2FeMoO_6 this was ever the case, even during difficult times.

A special thank to the group of Prof. Dr. Fulvio Parmigiani which did a great job during all the experiments at ELETTRA. Dr. Federica Bondino, Dr. Marco Zangrando and Dr. Michele Zacchigna are the kind of supporter anyone would like to meet at such a facility. Dr. Jonathan D. Denlinger, Dr. Antony T. Young, and Dr. Cintia Piamonteze are acknowledged for a lot of excellent technical assistance during the measurements performed at the ALS.

During my studies I had the opportunity to work together with several visitors of apl. Prof. Dr. Neumann. It was a fortune to meet Dr. Vadim R. Galakhov for several times in Osnabrück and at BESSY II in Berlin. The collaboration on defect oxides was fruitful and the discussions helped me to clarify a lot of questions with respect to x-ray emission spectroscopy. I am indebted to Prof. Dr. Emil Burzo and Istvan Balasz for performing magnetic measurements on Sr_2FeMoO_6. Furthermore it was a pleasure to work with Dr. Antoni Winiarski on several XRD data.

I was lucky to meet Dr. Frank de Groot. I want to thank him for providing the TT-Multiplets program. He has been an important dialog partner during the last year of my studies. The discussion with him helped to get a clearer view on excitonic states in the x-ray spectra of transition metals.

Dr. Hartmut Hesse is acknowledged for growing a very good Sr_2FeMoO_6 crystal. Without this sample I would not have been able to perform an important part of this work. I want to thank also his co-workers Bernd Lemme and Werner Geisler for providing their support regarding various sample characterizations and preparations.

Furthermore I want to thank Prof. Dr. Gunnar Borstel und Dr. Andrei V. Postnikov. The discussions Dr. Andrei V. Postnikov were a great help in order to reveal a better understanding of the relationship between magnetism, x-ray spectroscopies and

theoretical electronic structure calculations. Special thanks to Mehmet Kadiroğlu for performing band structure calculations on Sr_2FeMoO_6 in the framework of his diploma thesis with great engagement and excellent success.

I want to thank former and actual members of the research group for a pleasant work atmosphere, their assistance and advises, namely: Dr. Markus Bach, Stefan Bartkowski, Dr. Sorin G. Chiuzbăian, Traian Crainic, Dr. Mihaela C. Falub, Franz "Anti" Fangmeier, Daniela Hartmann, Dr. Ingo Karla, Thorsten Meyer, Dr. Stefan Plogmann, Manuel Prinz, Michael Räkers, Stefan Robin, Dr. Bolormaa Sanduijav, Dr. Bernd Schneider, Dr. Helmut Schürmann, Andreas Selinger, Stefan Stiene, Albert F. Takács, Cristian Taubitz and Bernd J. Zimmermann. Special thanks to Dr. Bernd Schneider for all his advisory during my diploma thesis and also in the beginning of my PhD thesis, and to Dr. Markus Bach and Thorsten Meyer for a lot funny and exciting discussions in the k-room about different aspects of life. Werner Dudas is acknowledged for technical and computational assistance during all the years. Furthermore, I want to thank Marion von Landsberg and Birgit Guss for assistance with all the administrative work.

Dr. Jürgen Schnack and Dr. Wolfgang Mikosch are acknowledged for leading and coordinating the PhD program, and I want to thank all the students for the pleasant atmosphere during the lectures, seminars and workshops.

Last but not least I want to thank my parents. Without their constant support I would not be able to present this work.

Danksagung

Diese Arbeit entstand im Rahmen des Promotionsprogrammes "Synthesis and Characterisation of Surfaces and Interfaces assembled from Clusters and Molecules" des Landes Niedersachsen.

An erster Stelle möchte ich apl. Prof. Dr. Manfred Neumann danken, durch dessen Betreuung diese Arbeit erst ermöglicht wurde und der stets mit hilfreichen Ratschlägen zur Verfügung stand. Besonders wertvoll waren dabei die wissenschaftlichen Diskussionen, welche insbesondere bei der Auswertung der vielen experimentellen Daten weiterhalfen.

Ein besonderer Dank gebührt Dr. Kevin C. Prince für eine konstante und ergiebige Zusammenarbeit während meiner gesamten Dissertation. Ich möchte mich für die vielen wichtigen Hinweise im Umgang mit Synchrotron-basierten Experimenten und die vielen sehr grundlegenden wissenschaftlichen Diskussionen bedanken. Auch Dr. Maurizio Matteucci möchte ich für eine stetige Kooperation danken, welche auch gelegentliche Rückschläge gut überstand. Im Speziellen gilt das für die Arbeit an Sr_2FeMoO_6.

An dieser Stelle möchte ich auch ausdrücklich die sehr gute Zusammenarbeit mit der Gruppe von Prof. Dr. Fulvio Parmigiani bei ELETTRA erwähnen. Dr. Federica Bondino, Dr. Marco Zangrando und Dr. Michele Zacchigna sind Kooperationspartner mit denen man jederzeit gern zusammenarbeitet. Dr. Jonathan D. Denlinger, Dr. Antony T. Young und Dr. Cintia Piamonteze will ich für ihre hervorragende Unterstützung danken, die mir während all den Messungen an der ALS zuteil wurde.

Während meiner Zeit in Osnabrück hatte ich Gelgenhheit mit diversen Gästen von apl. Prof. Dr. Neumann zu arbeiten. Dr. Vadim R. Galakhov sei für die erfolgreiche Zusammenarbeit auf dem Gebiet der Defektoxide ebenso wie für hilfreiche Diskussionen über Röntgenemissionsspektroskopie gedankt. Gleicher Dank gilt Prof. Dr. Emil Burzo and Istvan Balasz für die Durchführung magnetischer Messungen an Sr_2FeMoO_6. Zudem will ich mich an dieser Stelle bei Dr. Antoni Winiarski für einige XRD Messungen bedanken.

Dr. Frank de Groot war eine große Hilfe bei der Interpretation von angeregten Zuständen. Er hat zudem das TT-Multiplet Computerprogramm zur Verfügung gestellt.

Ein besonderer Dank gilt Dr. Hartmut Hesse für die Herstellung eines sehr guten Sr_2FeMoO_6 Kristalls. Auf dieser Probe basiert ein wichtiger Teil der vorliegenden Arbeit. Ein Dank geht auch an seine Mitarbeiter Bernd Lemme und Werner Geisler für ihre Unterstützung bei vielen Präparationsfragen.

Desweiteren möchte ich Prof. Dr. Gunnar Borstel und Dr. Andrei V. Postnikov danken. Die Diskussionen mit Dr. Andrei V. Postnikov waren sehr hilfreich um die Brücke zwischen Magnetismus, Spektroskopie und Bandstrukturrechnung schlagen zu können. Mein besonderer Dank gilt dabei Mehmet Kadiroḡlu, welcher unter großem Engagement die Bandstrukturrechnungen an Sr_2FeMoO_6 im Rahmen seiner Diplomarbeit durchführte und sich dabei auch von manch auftretender Schwierigkeit nicht aufhalten lies.

Früheren und jetzigen Mitgliedern der Arbeitsgruppe Photoelektronenspektroskopie sei für die angenehme Arbeitsatmosphäre und so einige Unterstützung gedankt: Dr. Markus Bach, Stefan Bartkowski, Dr. Sorin G. Chiuzbăian, Traian Crainic, Dr. Mihaela C. Falub, Franz "Anti" Fangmeier, Daniela Hartmann, Dr. Ingo Karla, Thorsten Meyer, Dr. Stefan Plogmann, Manuel Prinz, Michael Räkers, Stefan Robin, Dr. Bolormaa Sanduijav, Dr. Bernd Schneider, Dr. Helmut Schürmann, Andreas Selinger, Stefan Stiene, Albert F. Takács, Christian Taubitz und Bernd J. Zimmermann. Insbesondere möchte ich mich bei Dr. Bernd Schneider für die Betreuung meiner Diplomarbeit, welche auch während der Startphase meiner Promotion anhielt, bedanken. Ein Dank geht auch an Dr. Markus Bach und Thorsten Meyer für die vielen abwechslungsreichen Diskussionen im k-Raum. Werner Dudas stand über all die Jahre oft mit technischer Unterstützung und im EDV-Bereich zur Verfügung. Zudem möchte ich mich bei Marion von Landsberg und Birgit Guss für Hilfe bei administrativen Fragen bedanken.

Zu danken habe ich auch Dr. Jürgen Schnack und Dr. Wolfgang Mikosch für ihre Arbeit im Rahmen des Promotionsprogrammes. Den studentischen Mitgliedern sei für die stets angenehme Atmosphäre in den Vorlesungen, Seminaren und Workshops gedankt.

Zu guter Letzt möchte ich mich an dieser Stelle bei meinen Eltern bedanken, die durch ihre kontinuierliche Unterstützung dieses Studium möglich machten.

Bibliography

[1] R. von Helmolt and J. Wecker and B. Holzapfel and L. Schultz and K. Samwer, "Giant negative magnetoresistance in perovskitelike $La_{2/3}Ba_{1/3}MnO_x$ ferromagnetic-films," *Phys. Rev. Lett.*, vol. **71**, pp. 2331–2334, 1993.

[2] S. Jin, T. H. Tiefel, M. McCormack, R. A. Fastnacht, R. Ramesh, and L. H. Chen, "Thousandfold change in Restivity in Magnetoresistive La-Ca-Mn-O films," *Science*, vol. **264**, pp. 413–415, 1994.

[3] K. L. Kobayashi, T. Kimura, H. Sawada, K. Terakura, and Y. Tokura, "Room-temperature magnetoresistance in an oxide material with an ordered double-perovskite structure," *Nature*, vol. **395**, pp. 677–680, 1998.

[4] W. E. Pickett and J. S. Moodera, "Half metallic magnets," *Physics Today*, vol. **54**, pp. 39–44, 2001.

[5] J. H. Park, E. Vescovo, H. J. Kim, C. Kwon, R. Ramesh, and T. Venkatesan, "Direct evidence for a half-metallic ferromagnet," *Nature*, vol. **392**, pp. 794–796, 1998.

[6] J. Zaanen, G. A. Sawatzky, and J. W. Allen, "Band gaps and electronic structure of transition-metal compounds," *Phys. Rev. Lett.*, vol. **55**, pp. 418–421, 1985.

[7] C. Zener, "Interaction between the D-shells in the Transition Metals .2. Ferromagnetic Compounds of Manganese with Perovskite Structure," *Phys. Rev.*, vol. **82**, pp. 403–405, 1951.

[8] M. N. Baibich, J. M. Broto, A. Fert, N. V. Dau, F. Petroff, P. Etienne, G. Creuzet, A. Friederich, and A. Chazelas, "Giant magnetoresistance of (001)Fe/(001)Cr magnetic superlattices," *Phys. Rev. Lett.*, vol. **61**, pp. 2472–2475, 1988.

[9] G. Binasch, P. Grünberg, F. Saurenbach, and W. Zinn, "Enhanced magnetoresistance in layered magnetic structures with antiferromagnetic interlayer exchange," *Phys. Rev. B*, vol. **39**, pp. 4828–4830, 1989.

[10] J. S. Moodera, L. R. Kinder, T. M. Wong, and R. Meservey, "Large magnetoresistance at room temperature in ferromagnetic thin film tunnel juntions," *Phys. Rev. Lett.*, vol. **74**, pp. 3273–3276, 1995.

[11] A. Urushibara, Y. Moritomo, T. Arima, A. Asamitsu, G. Kido, and Y. Tokura, "Insulator to metal transition and giant magnetoresistance in $La_{1-x}Sr_xMnO_3$," *Phys. Rev. B*, vol. **51**, pp. 14103–14109, 1995.

[12] A. J. Millis, "Lattice effects in magnetoresistive manganese perovskites," *Nature*, vol. **392**, pp. 147–150, 1998.

[13] M. B. Salamon and M. Jaime, "The physics of manganites: Structure and transport," *Rev. Mod. Phys.*, vol. **73**, pp. 583–628, 2001.

[14] B. Dabrowski, X. Xiong, Z. Bukowski, R. Dybzinski, P. W. Klamut, J. E. Siewenie, O. Chmaissem, J. Shaffer, C. W. Kimball, J. D. Jorgensen, and S. Short, "Structure-properties phase diagram for $La_{1-x}Sr_xMnO_3$ ($0.1 \leq x \leq 0.2$)," *Phys. Rev. B*, vol. **60**, pp. 7006–7017, 1999.

[15] R. Klingeler, J. Geck, L. Pinsard-Gaudart, A. Revcolevschi, S. Uhlenbruck, and B. Büchner, "Magnetism and the charge order transition in lightly doped $La_{1-x}Sr_xMnO_3$," *Phys. Rev. B*, vol. **65**, p. 174404, 2002.

[16] Y. Moritomo, A. Asamitsu, H. Kuwahara, and Y. Tokura, "Giant magnetoresistance of manganese oxide with a layered perovskite structure," *Nature*, vol. **380**, pp. 141–144, 1996.

[17] Y. Moritomo, A. Asamitsu, H. Kuwahara, and Y. Tokura, "Colossal magnetoresistance in Cr-based chalcogenide spinels," *Nature*, vol. **386**, pp. 156–159, 1997.

[18] E. Z. Kurmaev, A. V. Postnikov, H. M. Palmers, C. Greaves, S. Bartkowski, V. Tsurkan, M. Demeter, M. Neumann, D. A. Zatsepin, V. R. Galakhov, S. N. Shamin, and V. Trofimova, "Electronic structure of FeCr2S4 and $Fe_{0.5}Cu_{0.5}Cr_2S_4$," *J. Phys.: Cond. Mat.*, vol. **12**, pp. 5411–5421, 2000.

[19] K. Kuepper, I. Balasz, H. Hesse, A. Winiarski, K. C. Prince, M. Matteucci, D. Wett, R. Szargan, E. Burzo, and M. Neumann, "Electronic and magnetic properties of highly ordered Sr_2FeMoO_6," *phys. stat. sol. (a)*, vol. **201**, pp. 3252–3255, 2004.

[20] E. Riedel, *Anorganische Chemie*. 4. Auflage, de Gruyter Verlag, 1999.

[21] G. F. Koster, J. O. Dimmock, R. G. Wheeler, and H. Statz, *Properties of the thirty-two Pointgroups*. Cambridge, Massachusetts: M.I.T. Press, 1963.

[22] J. Hubbard, "Electron Correlations in narrow Energy Bands," *Proc. R. Soc. London, Ser. A*, vol. **276**, p. 238, 1963.

[23] S. Hüfner, F. Hulliger, J. Osterwalder, and T. Riesterer, "On the interpetation of valence band photoemission spectra of nio," *Solid State Commun.*, vol. **50**, pp. 83–86, 1984.

[24] P. W. Andersen, "Localized Magnetic states in Metals," *Phys. Rev.*, vol. **124**, pp. 41–53, 1961.

[25] S. Hüfner, *Photoelectron spectroscopy*. Berlin Heidelberg: Springer-Verlag, 1995.

[26] J. Hubbard, "Electron Correlations in narrow Energy Bands .2. Degenerate Band Case," *Proc. R. Soc. London, Ser. A*, vol. **277**, p. 237, 1964.

[27] J. B. Goodenough, "Theory of the role of covalence in the Perovskite-type Manganites [La,M(II)]MnO_3," *Phys. Rev.*, vol. **100**, pp. 564–573, 1955.

[28] J. Kanamori, "Superexchange Interaction and Symmetry Properties of Electron orbitals," *J. Phys. Chem. Solids*, vol. **10**, pp. 87–98, 1959.

[29] G. H. Jonker and J. H. van Santen, "Ferromagnetic Compounds of Manganese with Perovskite Structure," *Physica*, vol. **16**, pp. 337–349, 1950.

[30] P. W. Anderson and H. Hasegawa, "Considerations on Double Exchange," *Phys. Rev.*, vol. **100**, pp. 675–681, 1955.

[31] P.-G. de Gennes, "Effects of Double Exchange in Magnetic Crystals," *Phys. Rev.*, vol. **118**, pp. 141–154, 1960.

[32] K. I. Kugel and D. I. Khomskii, "Jahn-Teller Effect and Magnetism - Transition-Metal Compounds," *Uspekhi Fizicheskikh Nauk*, vol. **136**, pp. 621–664, 1982.

[33] Y. Murakami, J. Hill, D. Gibbs, M. Blume, I. Koyama, M. Tanaka, H. Kawata, T. Arima, Y. Tokura, K. Hirota, and Y. Endoh, "Resonant X-ray scattering from orbital ordering in $LaMnO_3$," *Phys. Rev. Lett*, vol. **81**, pp. 582–585, 1998.

[34] M. Mostovoy and D. Khomskii, "Orbital ordering in charge transfer insulators," *Phys. Rev. Lett*, vol. **92**, p. 167201, 2004.

[35] S. Ishihara and S. Maekawa, "Theory of Anomalous X-Ray Scattering in Orbital-Ordered Manganites," *Phys. Rev. Lett.*, vol. **80**, pp. 3799–3802, 1998.

[36] M. Benfatto, Y. Joly, and C. R. Natoli, "Critical reexamination of the experimental evidence of orbital ordering in $LaMnO_3$ and $La_{0.5}Sr_{1.5}MnO_4$," *Phys. Rev. Lett.*, vol. **83**, pp. 636–639, 1999.

[37] H. B. Huang, T. Shishidou, and T. Jo, "Strong linear dichroism in Mn $L-2$,$L-3$ absorption predicted for orbital ordering in $LaMnO_3$," *J. Phys. Jpn.*, vol. **69**, pp. 2399–2402, 2000.

[38] P. Hohenberg and W. Kohn, "Inhomogenous Electron Gas," *Phys. Rev.*, vol. **136**, pp. B864–B871, 1964.

[39] W. Kohn, "Nobel Lecture: Electronic structure of matter–wave functions and density functionals," *Rev. Mod. Phys.*, vol. **71**, no. 5, pp. 1253–1266, 1999.

[40] W. Kohn and L. J. Sham, "Self-Consistent Equations including Exchange and Correlation Effects," *Phys. Rev.*, vol. **140**, pp. A1133–A1138, 1965.

[41] M. Imada, A. Fujimori, and Y. Tokura, "Metal-insulator transitions," *Rev. Mod. Phys.*, vol. **70**, pp. 1039–1263, 1999.

[42] D. C. Langreth and J. P. Perdew, "Theory of Nonuniforn Electronic Systems .1. Analysis of the Gradient Approximation and a Generalization that works," *Phys. Rev. B*, vol. **21**, pp. 5469–5493, 1980.

[43] J. P. Perdew, J. A. Chevary, S. H. Vosko, K. A. Jackson, M. R. Pederson, D. J. Singh, and C. Fiolhais, "Atoms, Molecules, Solids, and Surfaces - Applications of the Generalized Gradient Approximation for Exchange and Correlation," *Phys. Rev. B*, vol. **46**, pp. 6671–6687, 1992.

[44] V. I. Anisimov, J. Zaanen, and O. K. Andersen, "Band Theory and Mott Insulators - Hubbard-U instead of Stoner-I," *Phys. Rev. B*, vol. **44**, pp. 943–954, 1991.

[45] V. I. Anisimov, M. A. Korotin, J. Zaanen, and O. K. Andersen, "Spin Bags, Polarons, and Impurity Potentials in $La_{2-x}Sr_xCuO_4$ from 1st Principles," *Phys. Rev. Lett.*, vol. **68**, pp. 345–348, 1992.

[46] D. Singh, *Plane waves, pseudopotentials and the LAPW method*. Kuwer Academic, 1994.

[47] P. Blaha, K. Schwarz, and J. Luitz, "Full-potential, linearized augmented plane wave programs for crystalline systems," *WIEN2k (Vienna University of Technology, Vienna, 2000). Improved and updated version of original copyrighted WIEN code; P. Blaha, K. Schwarz, P. Sorantin and S. B. Trickey, Comput Phys. Commun.*, vol. **59**, pp. 399–415, 1990.

[48] J. Hubbard, "Electron Correlations in narrow Energy Bands .3. Improved Solution," *Proc. R. Soc. London, Ser. A*, vol. **281**, p. 401, 1964.

[49] A. Fujimori, F. Minami, and S. Sugano, "Multielectron satellites and spin polarization in photoemission from Ni compounds," *Phys. Rev. B*, vol. **29**, pp. 5225–5227, 1984.

[50] A. Fujimori and F. Minami, "Valence-band photoemission and optical absorption in nickel compounds," *Phys. Rev. B*, vol. **30**, pp. 957–971, 1984.

[51] A. Kotani and S. Shin, "Resonant inelastic x-ray scattering spectra for electrons in solids," *Rev. Mod. Phys.*, vol. **73**, pp. 203–246, 2001.

[52] A. Giesekus and L. M. Falicov, "Theory of pressure-induced magnetic and metal-insulator transitions," *Phys. Rev. B*, vol. **44**, pp. 10449–10454, 1991.

[53] V. J. Emery, "Theory of high-T_c superconductivity in oxides," *Phys. Rev. Lett.*, vol. **58**, pp. 2794–2797, 1987.

[54] M. Matsubara, Y. Harada, S. Shin, T. Uozumi, and A. Kotani, "Resonant X-ray emission spectroscopy in scandium halides," *J. Phys. Soc. Jpn.*, vol. **73**, pp. 711–718, 2004.

[55] F. M. F. de Groot, "High resolution x-ray emission and x-ray absorption spectroscopy," *Chem. Rev.*, vol. **101**, pp. 1779–1808, 2001.

[56] R. D. Cowan, *The Theory of Atomic Structure and Spectra*. Berkeley: University of California Press, 1981.

[57] B. T. Thole, R. D. Cowan, G. A. Sawwatzky, J. Fink, and J. C. Fuggle, "New probe for the ground state electronic structure of narrow band and impurity states," *Phys. Rev. B*, vol. **31**, pp. 6856–6858, 1985.

[58] B. T. Thole, G. van der Laan, and P. H. Butler, "Spin-mixed ground state of Fe phthalocyanine and the temperature depenent branching ratio in X-ray absorption spectroscopy," *Chem. Phys. Lett.*, vol. **149**, pp. 295–299, 1988.

[59] F. M. F. de Groot, J. C. Fuggle, B. T. Thole, and G. A. Sawatzky, "X-ray absorption of 3*d* transition metal compounds: an atomic multiplet description including the crystal field," *Phys. Rev. B*, vol. **42**, pp. 5459–5468, 1990.

[60] K. Okada, A. Kotani, B. T. Thole, and G. A. Sawatzky, "Evidence of local singlet state in $NaCuO_2$ from Cu 2p X-ray photoemission and photoabsorption spectra," *Solid State Commun.*, vol. **77**, pp. 835–838, 1991.

[61] G. van der Laan, M. S. M. A. Hoyland, C. J. F. Flipse, B. T. Thole, Y. Seino, H. Ogasawara, and A. Kotani, "Resonant photoemssion at the ni 2*p* edge core level as a probe of electron correlation effects in nickel," *Phys. Rev. B*, vol. **46**, pp. 9336–9340, 1992.

[62] H. Hertz, "Über den Einflu des ultravioletten Lichtes auf die elektrische Entladung," *Wiedemannsche Annalen*, vol. **31**, pp. 983–1000, 1887.

[63] W. Hallwachs, "Über den Einflu des Lichtes auf elektrostatisch geladene Körper," *Wiedemannsche Annalen*, vol. **33**, pp. 301–312, 1888.

[64] A. Einstein, "Über einen die Erzeugung und Verwandlung des Lichtes betreffenden heuristichen Gesichtspunkt," *Annalen der Physik*, vol. **17**, pp. 132–148, 1905.

[65] K. Siegbahn, D. Hammond, H. Fellner-Feldegg, and E. F. Barnett, "Electron spectroscopy with monochromatized Xrays," *Nature*, vol. **176**, pp. 245–252, 1972.

[66] P. Auger, "Sur l'Effect Photoelectrique Commpose," *Le Journal de Physique et le Radium*, vol. **6**, pp. 205–208, 1925.

[67] M. C. Demeter, *Spectroscopic study of transition metal compounds*. Universität Osnabrück: PhD Thesis, 2001.

[68] M. O. Krause and J. H. Oliver, "Natural widths of atomic K-Levels and L-Levels, K-Alpha X-ray-lines and several KLL Auger lines," *J. Phys. Chem. Ref. Data*, vol. **8**, pp. 329–338, 1979.

[69] E. J. Nordgren, S. M. Butorin, L. C. Duda, J. H. Guo, and J. E. Rubensson, *Soft X-ray Flourescence Spectroscopy for Materials Science and Chemical Physics: In Advanced Series of Physical Chemistry - Vol. 12A - Chemical Applications of Synchrotron Radiation*. World Scientific, 2002.

[70] H. A. Kramers and W. Heisenberg, "Über die Streuung von Strahlung durch Atome," *Z. Phys.*, vol. **31**, pp. 681–708, 1925.

[71] edited by G. Materlik, C. J. Sparks, and K. Fischer, *Resonant Anomalous X-ray Scattering*. Amsterdam: Elsevier Science B.V., 1994.

[72] S. M. Butorin, J.-H. Guo, M. Magnuson, P. Kuiper, and J. Nordgren, "Low-energy d-d excitations in MnO studied by resonant x-ray fluorescence spectroscopy," *Phys. Rev. B*, vol. **54**, pp. 4405–4408, 1996.

[73] L. C. Duda, J. Nordgren, G. Dräger, S. Bocharov, and T. Kirchner, "Polarized resonant inelastic X-ray scattering from single-crystal transition metal oxides," *J. Electr. Spectr. Rel. Phenom.*, vol. **110-111**, pp. 275–285, 2000.

[74] G. P. Zhang, T. A. Callcott, G. T. Woods, L. Lini, B. Sales, D. Mandrus, and J. He, "Electron correlation effects in resonant inelastic x-ray scattering of NaV_2O_5," *Phys. Rev. Lett.*, vol. **88**, p. 077401, 2002.

[75] S. G. Chiuzbăian, *Electronic structure and magnetism of selected materials.* Universität Osnabrück: PhD Thesis, 2003.

[76] G. Borstel, "Theoretical aspects of photoemission," *Applied Physics A*, vol. **38**, pp. 193–204, 1985.

[77] T. Koopmans, "Über die Zuordnung von Wellenfunktionen und Eigenwerten zu den einzelnen Elektronen eines Atoms," *Physica*, vol. **1**, pp. 104–113, 1933.

[78] C. N. Berglund and W. Spiecer, "Photoemission studies of copper and silver: Theory," *Physical Review*, vol. **136**, pp. A1030–A1044, 1964.

[79] S. Tanuma, C. J. Powell, and D. R. Penn, "Proposed formula for electron inelastic mean free paths based on calculations for 31 materials," *Surface Science*, vol. **192**, pp. L849–L857, 1987.

[80] A. Jablonski, "Universal energy dependence of the inelastic mean free path," *Surface and Interface Analysis*, vol. **20**, pp. 317–321, 1993.

[81] S. Uhlenbrock, *Theorie der spinpolarisierten CoreLevel Spektroskopie für Photo und Auger Elektronen.* Universität Osnabrück: PhD Thesis, 1999.

[82] D. Briggs and J. C. Rivière, *Spectral Interpretation, in Practical Surface Analysis by Auger and X-ray Photoelectron spectroscopy.* Chichester: John Willey & Sons, 1983.

[83] S. Doniach and M. Sunjic, "Many-Electron Singularity in X-ray Photoemission and X-ray Line Spectra from Metals," *J. Phys. C: Solid State Phys.*, vol. **3**, pp. 285–291, 1970.

[84] D. A. Shirley, "High-resolution x-ray photoemission spectrum of the valence band of gold," *Phys. Rev. B*, vol. **5**, pp. 4709–4714, 1972.

[85] S. Tougaard, "Inelastic background correction and quantitative surface analysis," *J. Electron. Spectr. Rel. Phen.*, vol. **52**, pp. 243–271, 1990.

[86] A. C. Simonsen, S. Yubero, and S. Tougaard, "Analysis of angle-resolved electron energy loss in XPS spectra of Ag, Au, Co, Cu, Fe and Si," *Surf. Science*, vol. **436**, pp. 149–159, 1999.

[87] P. K. Ghosh, *Introduction to photoelectron spectroscopy.* New York/ Chicester/ Brisbane/ Toronto/ Singapore: John Willey & Sons, 1983.

[88] S. Uhlenbrock, *Untersuchungen zur elektronischen Struktur einfacher ÜbergangsmetallOxide unter besonderer Berücksichtigung des NickelOxids.* Universität Osnabrück: PhD Thesis, 1994.

[89] J. M. Hollas, *High resolution spectroscopy.* London: Butterworths & Co, 1982.

[90] J. H. van Vleck, "The Dirac Vector Model in Complex Spectra," *Phys. Rev.*, vol. **45**, pp. 405–419, 1934.

[91] C. S. Fadley and D. A. Shirley, "Multiplet splitting of metal-atom electron binding energies," *Phys. Rev. A*, vol. **42**, pp. 1109–1120, 1970.

[92] V. R. Galakhov, M. Demeter, S. Bartkowski, M. Neumann, N. A. Ovechkina, E. Z. Kurmaev, N. I. Lobachevskaya, Y. M. Mukovskii, J. Mitchell, and D. L. Ederer, "Mn 3*s* exchange splitting in mixed-valence manganites," *Phys. Rev. B*, vol. **65**, p. 113102, 2002.

[93] P. S. Bagus, A. J. Freeman, and F. Sasaki, "Prediction of New Multiplet Structure in Photoemission Experiments," *Phys. Rev. Lett.*, vol. **30**, pp. 850–853, 1973.

[94] B. W. Veal and A. P. Paulikas, "X-Ray Photoelectron Final State Screening in Transition Metal Compounds," *Phys. Rev. Lett.*, vol. **51**, pp. 1995–1998, 1983.

[95] L. Sangaletti, L. E. Depero, P. S. Bagus, and F. Parmigiani, "A proper Anderson Hamiltonian treatment of the 3s photoelectron spectra of MnO, FeO, CoO and NiO," *Chem. Phys. Lett.*, vol. **245**, pp. 463–468, 1995.

[96] C. T. Chen, Y. U. Idzerda, H.-J-Lin, N. V. Smith, G. Meigs, E. Chaban, G. H. Ho, E. Pellegrin, and F. Sette, "Experimental Confirmation of the X-Ray Magnetic Circular Dichroism Sum Rules for Iron and Cobalt," *Phys. Rev. Lett.*, vol. **75**, pp. 152–155, 1995.

[97] J. Stöhr, *NEXAFS Spectroscopy*. Berlin: Springer, 1992.

[98] G. Schütz, W. Wagner, W. Wilhelm, P. Kienle, R. Zeller, R. Frahm, and G. Materlik, "Absorption of circularly polarized x-rays in iron," *Phys. Rev. Lett.*, vol. **58**, pp. 737–740, 1987.

[99] H. Ebert, "Magneto-optical effects in transition metal systems," *Rep. Prog. Phys.*, vol. **59**, pp. 1665–1735, 1996.

[100] S. Plogmann, *Untersucheungen der elektronischen und magnetischen Eigenschaften manganhaltiger Heusler Legierungen mittels Photoelektronen- und Röntgenspektroskopie*. Universität Osnabrüuck: Ph.D. thesis, 1999.

[101] B. T. Thole, P. Carra, F. Sette, and G. van der Laan, "X-ray circular dichroism as a probe of orbital magnetization," *Phys. Rev. Lett.*, vol. **68**, pp. 1943–1946, 1992.

[102] P. Carra, B. T. Thole, M. Altarelli, and X. Wang, "X-ray circular dichroism and local magnetic fields," *Phys. Rev. Lett.*, vol. **70**, pp. 694–697, 1993.

[103] J. Stöhr and M. G. Samant, "Liquid crystal alignment by rubbed polymer surfaces: a microscopic bond orientation model," *J. Electr. Spectr. Rel. Phenom.*, vol. **98-99**, pp. 189–207, 1999.

[104] M. Taguchi and M. Altarelli, "Orbital ordering in $LaMnO_3$: Cluster model calculation of resonant X-ray scattering and X-ray absorption at the Mn L_2, L_3 edge," *Surf. Rev. Lett.*, vol. **9**, pp. 1167–1171, 2002.

[105] C. R. Brundle and A. D. Baker, *Electron Spectroscopy: Theory, Techniques and Applications*. Bristol: John Willey & Sons, 1979.

[106] J. Jiménez-Mier, J. van Eck, D. L. Ederer, T. A. Callcott, J. Jia, J. Carlisle, L. Terminello, A. Asfaw, and R. C. Perera, "Dynamical behavior of x-ray absorption and scattering at the L edge of titanium compounds: Experiment and theory," *Phys. Rev. B*, vol. **59**, pp. 2649–2658, 1999.

[107] J. A. Carlisle, E. L. Shirley, E. A. Hudson, L. J. Terminello, T. A. Callcott, J. J. Jia, D. L. Ederer, R. C. C. Perera, and F. J. Himpsel, "Probing the Graphite Band Structure with Resonant Soft-X-Ray Fluorescence," *Phys. Rev. Lett.*, vol. **74**, pp. 1234–1237, 1995.

[108] Y. Kayanuma and A. Kotani, *Core-level Spectroscopy in Condened Systems*. (Springer, Heidelberg): edited by J. Kanamori A. Kotani, 1988.

[109] S. Tanaka, Y. Kayanuma, and A. Kotani, "Theory of the resonant $5p \rightarrow 3d$ X-ray-emission spectra in CeO_2," *Journ. Phys. Soc. Japan.*, vol. **59**, pp. 1488–1495, 1990.

[110] L. D. Finkelstein, E. Z. Kurmaev, M. A. Korotin, A. Moewes, B. Schneider, S. M. Butorin, J.-H. Guo, J. Nordgren, D. Hartmann, M. Neumann, and D. L. Ederer, "Band approach to the excitation-energy dependence of x-ray fluorescence of TiO_2," *Phys. Rev. B*, vol. **60**, pp. 2212–2217, 1999.

[111] A. Kotani, "Theory of resonant X-ray emission spectra in strongly correlated electron systems," *J. Electr. Spectr. Rel. Phen.*, vol. **110-111**, pp. 197–212, 2000.

[112] J.-E. Rubensson, J. Lüning, S. Eisebitt, and W. Eberhardt, "It's always a one-step process," *Appl. Phys. A*, vol. **65**, pp. 91–96, 1997.

[113] J. Chastain, *Handbook of X-ray Photoelectron Spectroscopy*. Eden Prairie: Perkin Elmer Coorporation , 1992.

[114] I. Karla, *Various energy scales in rare earth compounds: multimples, band energy gaps and crystal fields in RE nickel antimonides*. University of Osnabrüuck/ Université Joseph Fourier of Grenoble: Ph.D. thesis, 1999.

[115] D. Attwood, *Soft X-rays and Extreme Ultraviolet Radiation*. Cambridge: Cambridge University Press, 1999.

[116] http://www.bessy.de.

[117] W. B. Peatman, *Gratings, Mirrors and Slits: Beamline Design for Soft X-ray Synchrotron Radiation Sources*. Amsterdam: Gordon and Reach Science Publishers, 1997.

[118] http://www-als.lbl.gov/als/techspecs/bl8.0.1.html.

[119] J. J. Jia, T. A. Callcott, J. Yurkas, A. W. Ellis, F. J. Himpsel, M. G. Samant, G. Stöhr, D. L. Ederer, J. A. Carlisle, E. A. Hudson, L. J. Terminello, D. K. Shuh, and R. C. C. Perera, "First experimental results from IBM/TENN/TULANE/LLNL/LBL undulator beamline at the advanced light source," *Rev. Sci. Instrum.*, vol. **66**, pp. 1394–1397, 1995.

[120] J. Nordgren, G. Bray, S. Gramm, R. Nyholm, J.-E. Rubensson, and N. Wassdahl, "Soft x-ray emission spectroscopy using monochromatized synchrotron radiation (invited)," *Rev. Sci. Instrum.*, vol. **60**, pp. 1690–1696, 1989.

[121] D. Cocco, M. Matteucci, K. C. Prince, and M. Zangrando, "ComIXS: a compact inelastic x-ray spectrometer," *SPIE*, vol. **4506**, pp. 46–55, 2001.

[122] M. Zangrando, M. Finazzi, G. Paolucci, G. Comelli, B. Diviacco, R.P.Walker, D. Cocco, and F. Parmigiani, "BACH, the beamline for advanced dichroic and scattering experiments at ELETTRA," *Rev. Sci. Instrum.*, vol. **72**, pp. 1313–1319, 2001.

[123] http://www.elettra.trieste.it/experiments/beamlines/bach/index.html.

[124] http://www-als.lbl.gov/als/techspecs/bl4.0.2.html.

[125] http://www.bessy.de/lab_profile/04.rglab/.RGLab/index.html.

[126] I. I. Mazin and V. I. Anisimov, "Insulating gap in FeO: Correlations and covalency," *Phys. Rev. B*, vol. **55**, pp. 12822–12825, 1997.

[127] M. Takahashi and J. Igarashi, "Local approach to electronic excitations in MnO, FeO, CoO, and NiO," *Phys. Rev. B*, vol. **54**, pp. 13566–13574, 1996.

[128] P. Wei and Z. Qi, "Insulating gap in the transition-metal oxides: A calculation using the local-spin-density approximation with the on-site Coulomb U correlation correction," *Phys. Rev. B*, vol. **49**, pp. 10864–10868, 1994.

[129] I. Balberg and H. L. Pinch, "Oprical-Absorption of Iron-Oxides," *J. Magn. Magn. Mater.*, vol. **7**, pp. 12–15, 1978.

[130] H. K. Bowen, D. Adler, and B. H. Auker, "Electrical and Optical-Properties of FeO," *J. Solid State Chem.*, vol. **12**, pp. 355–359, 1973.

[131] J. Hugel and M. Kamal, "Electronic ground state of MnO, FeO, CoO and NiO within the LSDA+U approximation," *Solid State Commun.*, vol. **100**, pp. 457–461, 1996.

[132] S. Gota, F. Jollet, J. P. Crocombette, Z. Y. Wu, M. Pollak, N. Thromat, M. Gautier-Soyer, and C. R. Natoli, "Characterization of iron oxides by XAS at the Fe L-2,L-3 and O K edges," *J. Phys. IV*, vol. **7**, pp. 507–508, 1997.

[133] J. P. Crocombette, M. Pollak, F. Jollet, N. Thromat, and M. Gautier-Soyer, "X-ray-absorption spectroscopy at the Fe $L_{2,3}$ threshold in iron oxides," *Phys. Rev. B*, vol. **52**, pp. 3143–3150, 1995.

[134] Z. Y. Wu, S. Gota, F. Jollet, M. Pollak, M. Gautier-Soyer, and C. R. Natoli, "Characterization of iron oxides by x-ray absorption at the oxygen K edge using a full multiple-scattering approach," *Phys. Rev. B*, vol. **55**, pp. 2570–2577, 1997.

[135] F. de Groot, M. Grioni, J. Fuggle, J. Ghijsen, G. A. Sawatzky, and H. Petersen, "Oxygen 1s x-ray-absorption edges of transition-metal oxides," *Phys. Rev. B*, vol. **40**, pp. 5715–5723, 1989.

[136] C. Colliex, T. Manoubi, and C. Ortiz, "Electron-energy-loss-spectroscopy near-edge fine structures in the iron-oxygen system," *Phys. Rev. B*, vol. **44**, pp. 11402–11411, 1991.

[137] P. S. Bagus, C. R. Brundle, T. J. Chuang, and K. Wandelt, "Width of the *d*-Level Final-State Structure Observed in the Photoemission Spectra of Fe_xO," *Phys. Rev. Lett.*, vol. **39**, pp. 1229–1232, 1977.

[138] R. J. Lad and V. E. Henrich, "Photoemission study of the valence-band electronic structure in Fe_xO, Fe_3O_4, and α-Fe_2O_3 single crystals," *Phys. Rev. B*, vol. **39**, pp. 13478–13485, 1989.

[139] S. L. Finklea, L. Cathey, and E. L. Amma, "Investigation of Bonding Mechanism in Pyrite using Mössbaur-Effect and X-ray Crystallography," *Acta Cryst. A*, vol. **32**, pp. 529–537, 1976.

[140] R. W. G. Wyckoff, *Crystal Structures.* New York: Interscience Publishers, second edition, 1963.

[141] E. D. Stevens, M. L. Delucia, and P. Coppens, "Experimental-Observation of the Effect of Crystal-Field Splitting on the Electron-Density Distribution of Iron Pyrite," *Inorg. Chem.*, vol. **19**, pp. 813–820, 1980.

[142] A. Schlegel and P.Wachter, "Optical properties, phonons and electronic structure of iron pyrite (FeS_2)," *Journ. of Phys. C: Solid State Phys.*, vol. **9**, pp. 3363–3369, 1976.

[143] J. F. W. Mosselmans, R. A. D. Pattrick, G. V. der Laan, J. M. Charnock, D. J. Vaughan, C. M. B. Henderson, and C. D. Garner, "X-Ray-Absorption Near-Edge Spectra of Transition-Metal Disulfides FeS_2 (Pyrite and Marcasite), CoS_2, NiS_2 and CuS_2, and their Isomorphs FeAsS and CoAsS," *Phys. and Chem. of Minerals*, vol. **22**, pp. 311–317, 1995.

[144] J. M. Charnock, C. M. B. Henderson, J. W. Mosselmans, and R. A. D. Pattrick, "3*d* transition metal *L*-edge X-ray absorption studies of the dichalcogenides of Fe, Co and Ni," *Phys. Chem. Minerals*, vol. **23**, pp. 403–408, 1996.

[145] B. T. Thole and G. van der Laan, "Branching ratio in x-ray absorption spectroscopy," *Phys. Rev. B*, vol. **38**, pp. 3158–3171, 1988.

[146] G. L. Zhaoa, J. Callaway, and M. Hayashibara, "Electronic structures of iron and cobalt pyrites," *Phys. Rev. B*, vol. **48**, pp. 15781–15786, 1993.

[147] Y. Zeng and N. A. W. Holzwarth, "Density-functional calculation of the electronic structure and equilibrium geometry of iron pyrite (FeS_2)," *Phys. Rev. B*, vol. **50**, pp. 8214–8220, 1994.

[148] E. Z. Kurmaev, J. van Ek, D. L. Ederer, L. Zhou, T. A. Callcott, R. C. C. Perera, V. M. Cherkashenko, S. N. Shamin, V. A. Trofimova, S. Bartkowski, M. Neumann, A. Fujimori, and V. P. Moloshag, "Experimental and theoretical investigation of the electronic structure of transition metal sulphides: CuS, FeS_2 and $FeCuS_2$," *J. Phys.: Condens. Matter*, vol. **10**, pp. 1687–1697, 1998.

[149] V. Eyert, K.-H. Höck, S. Fiechter, and H. Tributsch, "Electronic structure of FeS_2: The crucial role of electron-lattice interaction," *Phys. Rev. B*, vol. **57**, pp. 6350–6359, 1998.

[150] S. Suga, A. Kimura, T. Matsushita, A. Sekiyama, S. Imada, K. Mamiya, A. Fujimori, H. Takahashi, and N. Mori, "2*p* resonance photoemission and Auger features in NiS_2 and FeS_2," *Phys. Rev. B*, vol. **60**, pp. 5049–5054, 1999.

[151] F. Parmigiani and L. Sangaletti, "Fine structures in the X-ray photoemission spectra of MnO, FeO, CoO, and NiO single crystals," *J. Electr. Spectr. Rel. Phenom.*, vol. **98-99**, pp. 287–302, 1999.

[152] R. Zimmerman, P. Steiner, R. Claessen, R. Reiner, S. Hüfner, P. Blaha, and P. Dufcek, "Electronic structure of 3*d*-transition-metal oxides: on-site Coulomb repulsion versus covalency," *J. Phys.: Condens. Matter*, vol. **11**, pp. 1657–1682, 1999.

[153] M. Taguchi, L. Braicovich, F. Borgatti, G. Ghiringhelli, A. Tagliaferri, N. B. Brookes, T. Uozumi, and A. Kotani, "Resonant Raman scattering at the L thresholds with final $3s$ hole in $3d^{2+}$ systems. I. Configuration interaction with two $3p$ hole final states in different systems," *Phys. Rev. B*, vol. **63**, p. 245114, 2001.

[154] A. E. Bocquet, T. Mizokawa, T. Saitoh, H. Namatame, and A. Fujimori, "Electronic structure of $3d$-transition-metal compounds by analysis of the $2p$ core-level photoemission spectra," *Phys. Rev. B*, vol. **46**, pp. 3771–3784, 1992.

[155] A. G. Schaufuss, H. W. Nesbitt, I. Kartio, K. Laajalehto, G. M. Bancroft, and R. Szargan, "Incipient oxidation of fractured pyrite surfaces in air," *J. Electr. Spectr. Rel. Phen.*, vol. **96**, pp. 69–82, 1998.

[156] H. W. Nesbitt, G. M. Bancroft, A. R. Pratt, and M. J. Scaini, "Sulfur and iron surface states on fractured pyrite surfaces," *Am. Mineral.*, vol. **83**, pp. 1067–1076, 1998.

[157] G. van der Laan, C. M. B. Henderson, R. A. D. Pattrick, S. S. Dhesi, P. F. Schofield, E. Dudzik, and D. J. Vaughan, "Orbital polarization in $NiFe_2O_4$ measured by Ni-$2p$ x-ray magnetic circular dichroism," *Phys. Rev. B*, vol. **59**, pp. 4314–4321, 1999.

[158] M. V. Yablonskikh, Y. M. Yarmoshenko, V. I. Grebennikov, E. Z. Kurmaev, S. M. Butorin, L.-C. Duda, J. Nordgren, S. Plogmann, and M. Neumann, "Origin of magnetic circular dichroism in soft x-ray fluorescence of Heusler alloys at threshold excitation," *Phys. Rev. B*, vol. **63**, p. 235117, 2001.

[159] M. Magnuson, N. Wassdahl, and J. Nordgren, "Energy dependence of Cu $L_{2,3}$ satellites using synchrotron excited x-ray-emission spectroscopy," *Phys. Rev. B*, vol. **56**, pp. 12238–12242, 1997.

[160] L. I. Yin, I. Adler, M. H. Chen, and B. Crasemann, "Width of Atomic L_2 and L_3 Vacancy States near $Z = 30$," *Phys. Rev. A*, vol. **7**, pp. 897–903, 1973.

[161] K. C. Prince, M. Matteucci, K. Kuepper, S. G. Chiuzbaian, S. Bartkowski, and M. Neumann, "Core-level spectroscopic study of FeO and FeS_2," *Phys. Rev. B*, vol. **71**, p. 085102, 2005.

[162] Y. Luo, H. Ågren, F. Gel'mukhanov, J. Guo, P. Skytt, N. Wassdahl, and J. Nordgren, "Symmetry-selective resonant inelastic x-ray scattering of C_{60}," *Phys. Rev. B*, vol. **52**, pp. 14479–14496, 1995.

[163] F. Gel'mukhanov and H. Ågren, "Channel interference in resonance elastic x-ray scattering," *Phys. Rev. A*, vol. **50**, pp. 1129–1132, 1994.

[164] D. W. Bullett, "Electronic structure of $3d$ pyrite- and marcasite-type sulphides," *J. Phys. C: Solid State Phys.*, vol. **15**, pp. 6163–6174, 1982.

[165] I. Opahle, K. Koepernik, and H. Eschrig, "Full-potential band-structure calculation of iron pyrite," *Phys. Rev. B*, vol. **60**, pp. 14035–14041, 1999.

[166] J. Muscat, A. Hung, S. Russo, and I. Yarovsky, "First-principles studies of the structural and electronic properties of pyrite FeS_2," *Phys. Rev. B*, vol. **65**, p. 054107, 2002.

[167] K. C. Prince, K. Kuepper, M. Neumann, D. Cocco, F. Bondino, M. Zangrando, M. Zacchigna, M. Matteucci, and F. Parmigiani, "Resonant Raman x-ray scattering at the S $2p$ edge of iron pyrite," *J. Phys.: Condens. Matter*, vol. **16**, pp. 7397–7404, 2004.

[168] D. Li, G. M. Bancroft, M. Kasrai, M. Fleet, X. Feng, and K. Tan, "S-K-Edge and L-Edge X-Ray-Absorption Spectroscopy of Metal Sulfides and Sulfates - Applications in Mineralogy and Geochemistry," *Canadian Mineralogist*, vol. **33**, pp. 949–960, 1995.

[169] P. Kuiper, J.-H. Guo, C. Såthe, L.-C. Duda, J. Nordgren, J. J. M. Pothuizen, F. M. F. de Groot, and G. A. Sawatzky, "Resonant X-Ray Raman Spectra of Cu dd Excitations in $Sr_2CuO_2Cl_2$," *Phys. Rev. Lett.*, vol. **80**, pp. 5204–5407, 1998.

[170] Y. Harada, K. Okada, R. Eguchi, A. Kotani, H. Takagi, T. Takeuchi, and S. Shin, "Unique identification of Zhang-Rice singlet excitation in $Sr_2CuO_2Cl_2$ mediated by the O 1*s* core hole: Symmetry-selective resonant soft x-ray Raman scattering study," *Phys. Rev. B*, vol. **66**, p. 165104, 2002.

[171] L.-C. Duda, T. Schmitt, J. Nordgren, G. Dhalenne, and A. Revcolevschi, "Resonant inelastic soft X-ray scattering of insulating cuprates," *Surf. Rev. and Lett.*, vol. **9**, pp. 1103–1108, 1998.

[172] M. V. Yablonskikh, Y. M. Yarmoshenko, E. G. Gerasimov, V. S. Gaviko, M. A. Korotin, E. Z. Kurmaev, S. Bartkowski, and M. Neumann, "Local magnetic moments at X-ray spectra of 3*d* metals," *J. Magn. Magn. Mat.*, vol. **256**, pp. 396–403, 2003.

[173] Y. D. Chuang and A. D. Gromko and D. S. Dessau and T. Kimura and Y. Tokura, "Fermi surface nesting and nanoscale fluctuating charge/orbital ordering in colossal magnetoresistive oxides," *Science*, vol. **292**, pp. 1509–1513, 2001.

[174] H. L. Ju, Y. S. Nam, J. E. Lee, and H. S. Shin, "Anomalous magnetic properties and magnetic phase diagram of $La_{1-x}Ba_xMnO_3$," *J. Magn. Mag. Mat.*, vol. **219**, pp. 1–8, 2000.

[175] B. Dabrowski, K. Rogacki, X. Xiong, P. W. Klamut, R. Dybzinski, J. Shaffer, and J. D. Jorgensen, "Synthesis and properties of the vacancy-free $La_{1-x}Ba_xMnO_3$," *Phys. Rev. B*, vol. **58**, pp. 2716–2723, 1998.

[176] C. Roy and R. C. Budhani, "Raman, infrared and x-ray diffraction study of phase stability in $La_{1-x}Ba_xMnO_3$ doped manganites," *J. Appl. Phys.*, vol. **85**, pp. 3124–3131, 1999.

[177] P. Murugavel, J. H. Lee, J. G. Yoon, T. W. Noh, J. S. Chung, M. Heu, and S. Yoon, "Origin of metal-insulator transition temperature enhancement in underdoped lanthanum manganite films," *Appl. Phys. Lett.*, vol. **82**, pp. 587–589, 2003.

[178] P. Mandal and B. Ghosh, "Transport, magnetic, and structural properties of $La_{1x}M_xMnO_3$ (M = Ba, Sr, Ca) for $0 \leq x \leq 0.20$," *Phys. Rev. B*, vol. **68**, p. 014422, 2003.

[179] T. Chatterji, L. P. Regnault, and W. Schmidt, "Spin dynamics of $La_{0.7}Ba_{0.3}MnO_3$," *Phys. Rev. B*, vol. **66**, p. 214408, 2002.

[180] A. Maignan, F. Damay, A. Barnabe, C. Martin, M. Hervieu, and B. Raveau, "The effect of Mn-site doping on the magnetotransport properties of CMR manganites," *Philos. Trans. Roy. Soc. A*, vol. **356**, pp. 1635–1658, 1998.

[181] D. D. Khalyavin, M. Pekala, G. I. Bychkov, S. V. Shiryaev, S. N. Barilo, I. O. Troyanchuk, J. Mucha, Misiorek, R. Szymczak, M. Baran, and H. Szymczak, "Magnetotransport properties of flux melt grown single crystals of Co-substituted manganites with perovskite structure," *J. Phys.: Condens. Matter*, vol. **15**, pp. 925–936, 2003.

[182] M. Demeter, M. Neumann, V. R. Galakhov, N. A. Ovechkina, E. Z. Kurmaev, and N. I. Labachevskaya, "Electronic structure of doped La-Mn-O perovskites," *Acta Physica Polonica A*, vol. **98**, pp. 587–591, 2000.

[183] M. C. Falub, V. Tsurkan, M. Neumann, I. O. Troyanchuk, V. R. Galakhov, E. Z. Kurmaev, and H. H. Weitering, "Electronic structure of cobalt-doped manganites," *Surf. Sci.*, vol. **532**, pp. 488–491, 2003.

[184] J. H. Park, C. T. Chen, S. W. Cheong, W. Bao, G. Meigs, V. Chakarian, and Y. U. Idzerda, "Electronic Aspects of the Ferromagnetic Transition in Manganese Perovskites," *Phys. Rev. Lett.*, vol. **76**, pp. 4215–4218, 1996.

[185] T. Saitoh, A. E. Bocquet, T. Mizokawa, H. Namatame, A. Fujimori, M. Abbate, Y. Takeda, and M. Takano, "Electronic structure of $La_{1-x}Sr_xMnO_3$ studied by photoemission and x-ray-absorption spectroscopy," *Phys. Rev. B*, vol. **51**, pp. 13942–13951, 1995.

[186] N. Hamada and H. Sawada and K. Terakura, "Electronic band structure of $La_{1-x}Ba_xMnO_3$," *J. Phys. and Chem. of Solids*, vol. **56**, pp. 1719–1720, 1995.

[187] S. J. Youn and B. I. Min, "Effects of doping and magnetic field on the half-metallic electronic structures of $La_{1-x}Ba_xMnO_3$," *Phys. Rev. B*, vol. **56**, pp. 12046–12049, 1997.

[188] P. Ravindran, A. Kjekshus, H. Fjellvåg, A. Delin, and O. Eriksson, "Ground-state and excited-state properties of $LaMnO_3$ from full-potential calculations," *Phys. Rev. B*, vol. **65**, p. 064445, 2002.

[189] S. M. Butorin, C. Såthe, F. Saalem, J. Nordgren, and X.-M. Zhu, "Probing the Mn^{3+} sublattice in $La_{0.5}Ca_{0.5}MnO_3$ by resonant inelastic soft X-ray scattering at the Mn L_2,L_3 edge," *Surf. Rev. Lett.*, vol. **9**, pp. 989–992, 2002.

[190] E. Z. Kurmaev, M. A. Korotin, V. R. Galakhov, L. D. Finkelstein, E. I. Zabolotzky, N. N. Erfremova, N. I. Lobachevskaya, S. Stadler, D. L. Ederer, T. A. Callcott, L. Zhou, A. Moewes, S. Bartkowski, M. Neumann, J. Matsuno, T. Mizokawa, A. Fujimori, and J. Mitchell, "X-ray emission and photoelectron spectra of $Pr_{0.5}Sr_{0.5}MnO_3$," *Phys. Rev. B*, vol. **59**, pp. 12799–12806, 1999.

[191] L.-C. Duda, "Magnetic circular dichroism in soft X-ray emission of itinerant and localized magnets," *J. Electr. Electr. Spectr.*, vol. **110-111**, pp. 287–304, 2000.

[192] F. Bondino, M. Platé, M. Zangrando, D. Cocco, A. Comin, I. Alessandri, L. Malavasi, and F. Parmigiani, "Doping dependence of the electronic structure of $La_{1-x}Na_xMnO_3$ by resonant X-ray emission and X-ray absorption spectroscopy," *J. Phys. Chem. B*, vol. **108**, pp. 4018–4023, 2004.

[193] O. Wessely, P. Roy, D. Åberg, C. Andersson, S. Edvardsson, O. Karis, B. Sanyal, P. Svedlindh, M. I. Katsnelson, R. Gunnarsson, D. Arvanitis, and O. Eriksson, "Initial and final state effects in the x-ray absorption process of $La_{1-x}Sr_xMnO_3$," *Phys. Rev. B*, vol. **68**, p. 235109, 2003.

[194] K. Kuepper, M. C. Falub, K. C. Prince, V. R. Galakhov, I. O. Troyanchuk, S. G. Chiuzbaian, M. Matteucci, D. Wett, R. Szargan, N. A. Ovechkina, Y. M. Mukovskii, and M. Neumann, "Electronic structure of A- and B- site doped Lanthanum manganites: A combined x-ray spectroscopic study," *J. Phys. Chem. B*, vol. **109**, pp. 9354–9361, 2005.

[195] C. W. M. Castleton and M. Altarelli, "Orbital ordering in the manganites: Resonant x-ray scattering predictions at the manganese L_{II} and L_{III} edges," *Phys. Rev. B*, vol. **62**, pp. 1033–1038, 2000.

[196] M. Abbate, F. M. F. de Groot, J. C. Fuggle, A. Fujimori, O. Strebel, F. Lopez, M. Domke, G. Kaindl, G. A. Sawatzky, M. Takana, Y. Takeda, H. Eisaki, and S. Uchida, "Controlled-valence properties of $La_{1-x}Sr_xFeO_3$ and $La_{1-x}Sr_xMnO_3$ studied by soft-x-ray absorption spectroscopy," *Phys. Rev. B*, vol. **46**, pp. 4511–4519, 1992.

[197] Z. Yang, L. Yie, and X. Xie, "Electronic and magnetic properties of the perovskite oxides: $LaMn_{1-x}Co_xO_3$," *Phys. Rev. B*, vol. **59**, pp. 7051–7057, 1999.

[198] I. Solovyev, N. Hamada, and K. Terakura, "t_{2g} versus all $3d$ localization in LaMO$_3$ perovskites (M=TiCu): First-principles study," *Phys. Rev. B*, vol. **53**, pp. 7158–7170, 1996.

[199] Z. Q. Yang, L. Ye, and X. D. Xie, "Theoretical Studies of Electronic and Magnetic Properties of Mn-Site-Doped Perovskites $LaMn_{1-x}Ni_xO_3$," *Phys. Stat. Sol. B*, vol. **220**, pp. 885–895, 2000.

[200] Y. Tokura and N. Nagaosa, "Orbital physics in transition-metal oxides," *Science*, vol. **288**, pp. 462–468, 2000.

[201] M. Ziese, "Extrinsic magnetotransport phenomena in ferromagnetic oxides," *Rep. Prog. Phys.*, vol. **65**, pp. 143–249, 2002.

[202] B. B. V. Aken, O. D. Jurchescu, A. Meetsma, Y. Tomioka, Y. Tokura, and T. T. M. Palstra, "Orbital-Order-Induced Metal-Insulator Transition in $La_{1-x}Ca_xMnO_3$," *Phys. Rev. Lett*, vol. **90**, p. 066403, 2003.

[203] H. Nojiri, K. Kaneko, M. Motokawa, K. Hirota, Y. Endoh, and K. Takahashi, "Two ferromagnetic phases in $La_{1-x}Sr_xMnO_3$ ($x \sim 1/8$)," *Phys. Rev. B*, vol. **60**, pp. 4142–4148, 1999.

[204] M. Korotin, T. Fujiwara, and V. Anisimov, "Long-period orbital order with hole stripes in $La_{7/8}Sr_{1/8}MnO_3$," *Phys. Rev. B*, vol. **62**, pp. 5696–5699, 2000.

[205] G. Alejandro, M. C. G. Passeggi, D. Vega, C. A. Ramos, M. T. Causa, M. Tovar, and R. Senis, "Temperature evolution of crystal field interactions across the Jahn-Teller transition in a $La_{7/8}Sr_{1/8}MnO_3$ single crystal," *Phys. Rev. B*, vol. **68**, p. 214429, 2003.

[206] Y. Endoh, K. Hirota, S. Ishihara, S. Okamoto, Y. Murakami, A. Nishizawa, T. Fukuda, H. Kimura, H. Nojiri, K. Kaneko, and S. Maekawa, "Transition between Two Ferromagnetic States Driven by Orbital Ordering in $La_{0.88}Sr_{0.12}MnO_3$," *Phys. Rev. Lett*, vol. **82**, pp. 4328–4331, 1999.

[207] J. Geck, P. Wochner, D. Bruns, B. Bchner, U. Gebhardt, S. Kiele, P. Reutler, and A. Revcolevschi, "Rearrangement of the orbital-ordered state at the metal-insulator transition of $La_{7/8}Sr_{1/8}MnO_3$," *Phys. Rev. B*, vol. **69**, p. 104413, 2004.

[208] H. B. Huang and T. Jo, "Orbital degeneracy, orbital polarization and x-ray absorption linear dichroism in transition-metal oxides," *J. Phys. Jpn.*, vol. **73**, pp. 2480–2486, 2004.

[209] D. Huang, W. Wu, G. Guo, H.-J. Lin, T. H. anbd C F. Chang, C. Chen, A. Fujimori, T. Kimura, H. Huang, A. Tanaka, and T. Jo, "Orbital Ordering in $La_{0.5}Sr_{1.5}MnO_4$ Studied by Soft X-Ray Linear Dichroism," *Phys. Rev. Lett*, vol. **92**, p. 087202, 2004.

[210] M. Zangrando, M. Zacchigna, M. Finazzi, D. Cocco, R. Rochow, and F. Parmigiani, "Polarized high-brilliance and high-resolution soft x-ray source at ELETTRA: The performance of beamline BACH," *Rev. Sci. Instrum*, vol. **75**, pp. 31–36, 2004.

[211] K. Kuepper, F. Bondino, K. C. Prince, M. Zangrando, M. Zacchigna, A. F. Takács, T. C. snd M. Matteucci, F. Parmigiani, V. R. Galakhov, Y. M. Mukovskii, A. Winiarski, and M. Neumann, "Investigation of orbital ordering in $La_{7/8}Sr_{1/8}MnO_3$ by means of x-ray linear dichroism at the Mn L edge," *submitted to J. Phys. Chem. B*, 2005.

[212] N. Stojic. Private communication, 2004.

[213] S. Wilkins, P. Spencer, P. Hatton, S. Collins, M. D. Roper, D. Prabhakaran, and A. T. Boothroyd, "Direct observation of orbital ordering in $La_{0.5}Sr_{1.5}MnO_4$ using soft x-ray diffraction," *Phys. Rev. Lett*, vol. **91**, p. 167205, 2003.

[214] S. Dhesi, A. Mirone, C. D. Nadai, P. Ohresser, P. Bencok, N. B. Brookes, P. Reutler, A. Revcolevschi, A. Tagliaferri, O. Toulemonde, , and G. van der Laan, "Unraveling Orbital Ordering in $La_{0.5}Sr_{1.5}MnO_4$," *Phys. Rev. Lett*, vol. **92**, p. 056403, 2004.

[215] T. Saitoh, N. Nakatake, A. Kakizaki, H. Nakajima, O. Moritomo, S. Xu, Y. M. N. Hamada, and Y. Aiura, "Half-metallic density of states in Sr_2FeMoO_6 due to Hund's rule coupling," *Phys. Rev. B*, vol. **66**, p. 035112, 2002.

[216] A. Deb, N. Hiraoka, M. Ituo, Y. Sakurai, A. Koizumi, Y. Tomioka, and Y. Tokura, "Evidence of negative spin polarization in ferromagnetic Sr_2FeMoO_6 as observed in a magnetic Compton profile study," *Phys. Rev. B*, vol. **70**, p. 104411, 2004.

[217] M. Besse, V. Cros, A. Barthélémy, H. Jaffrès, J. Vogel, F. Petroff, A. Mirone, A. Tagliaferri, P. Bencok, P. Decorse, P. Berthet, Z. . Szotek, W. M. Temmerman, S. S. Dhesi, N. B. Brookes, A. Rogalev, and A. Fert, "Experimental evidence of the ferrimagnetic ground state of Sr_2FeMoO_6 probed by X-ray magnetic circular dichroism," *Europhys. Lett.*, vol. **60**, pp. 608–614, 2002.

[218] Y. Tomioka, T. Okuda, Y. Okimoto, R. Kumai, K.-I. Kobayashi, and Y. Tokura, "Magnetic and electronic properties of a single crystal of ordered double perovskite Sr_2FeMoO_6," *Phys. Rev. B*, vol. **61**, pp. 422–427, 2000.

[219] D. D. Sarma, P. Mahadevan, T. Saha-Dasgupta, S. Ray, and A. Kumar, "Electronic Structure of Sr_2FeMoO_6," *Phys. Rev. Lett.*, vol. **85**, pp. 2549–2552, 2000.

[220] S. Ray, A. Kumar, D. D. Sarma, R. Cimino, S. Turchini, S. Zennaro, and N. Zema, "Electronic and magnetic structures of Sr_2FeMoO_6," *Phys. Rev. Lett.*, vol. **87**, p. 097204, 2001.

[221] A. P. Douvalis, M. Venkatesan, J. M. D. Coey, M. Grafoute, J. M. Greneche, and R. Suryanarayanan, "Mössbauer, magnetization and crystal structure studies of the double perovskites $Sr_2FeMo_{1-x}W_xO_6$, $x = 0$, 0.1, 0.2, 0.3 and 0.4," *J. Phys: Condens. Matter*, vol. **14**, pp. 12611–12627, 2002.

[222] J. Linden, T. Yamamoto, M. Karppinen, H. Yamauchi, and T. Pietari, "Evidence for valence fluctuation of Fe in Sr_2FeMoO_{6-w} double perovskite," *Appl. Phys. Lett.*, vol. **76**, pp. 2925–2927, 2000.

[223] B. Garcia-Landaa, C. Ritter, M. R. Ibarra, J. Blasco, P. A. Algarabel, R. Mahendirana, and J. García, "Magnetic and magnetotransport properties of the ordered perovskite Sr_2FeMoO_6," *Solid State Commun.*, vol. **110**, pp. 435–438, 1999.

[224] J. Navarro, J. Nogues, J. S. Munoz, and J. Fontcuberta, "Antisites and electron-doping effects on the magnetic transition of Sr_2FeMoO_6 double perovskite," *Phys. Rev. B*, vol. **67**, p. 174416, 2003.

[225] I. V. Solovyev, "Electronic structure and stability of the ferrimagnetic ordering in double perovskites," *Phys. Rev. B*, vol. **65**, p. 144446, 2002.

[226] S. Ray, P. Mahadevan, A. Kumar, D. D. Sarma, R. Cimino, M. Pedio, L. Ferrari, and A. Pesci, "Strong correlation effects in the electronic structure of Sr_2FeMoO_6," *Phys. Rev. B*, vol. **67**, p. 085109, 2003.

[227] T. Saha-Dasgupta and D. D. Sarma, "*Ab initio* study of disorder effects on the electronic and magnetic structure of Sr_2FeMoO_6," *Phys. Rev. B*, vol. **64**, p. 064408, 2001.

[228] V. I. Anisimov, A. I. Poteryaev, M. A. Korotin, A. O. Anokhin, and G. Kotliar, "First-principles calculations of the electronic structure and spectra of strongly correlated systems: dynamical mean-field theory," *J. Phys.: Condens. Matter*, vol. **9**, pp. 7359–7367, 1997.

[229] A. I. Liechtenstein, V. I. Anisimov, and J. Zaanen, "Density-functional theory and strong interactions: Orbital ordering in mott-hubbard insulators," *Phys. Rev. B*, vol. **52**, pp. R5467–R5470, 1995.

[230] A. H. Morrish, *The physical principles of magnetism*. New York: Huntington, Krieger, 1980.

[231] L. Balcells, J. Navarro, M. Bibes, A. Roig, B. Martinez, and J. Fontcuberta, "Cationic ordering control of magnetization in Sr_2FeMoO_6 double perovskite," *Appl. Phys. Lett.*, vol. **78**, pp. 781–783, 2000.

[232] R. J. Colton, A. M. Guzman, and J. W. Rabalais, "Electrochromism in some thin-film transition-metal oxides characterized by x-ray electron spectroscopy," *J. Appl. Phys.*, vol. **49**, pp. 409–416, 1978.

[233] S. Bartkowski, M. Neumann, E. Z. Kurmaev, V. V. Federenko, S. N. Shamin, V. M. Cherkashenko, S. N. Memnonov, A. Winiarski, and D. C. Rubie, "Electronic structure of titanium monoxide," *Phys. Rev. B*, vol. **56**, pp. 10656–10667, 1997.

[234] C. Cantalini, L. Lozzi, A. Passacantando, and S. Santucci, "The comparative effect of two different annealing temperatures and times on the sensitivity and long-term stability of WO_3 thin films for detecting NO_2," *IEEE Sensors Journal*, vol. **3**, pp. 171–179, 2003.

[235] K. Kuepper, M. Kadirogˉlu, A. V. Postnikov, K. C. Prince, M. Matteucci, V. R. Galakhov, H. Hesse, G. Borstel, and M. Neumann, "Electronic structure of highly ordered Sr_2FeMoO_6: XPS and XES," *submitted to J. Phys.: Condens. Matter*, 2005.

[236] J. H. Scofield, "Hartree-Slater subshell photoionization cross-sections at 1254 and 1487 eV," *J. Electron. Spectr. Rel. Phenom.*, vol. **8**, pp. 129–137, 1976.

[237] E. J. McGuire, "Atomic M-Shell Coster-Kronig, Auger, and Radiative Rates, and Fluorescence Yields for Ca-Th," *Phys. Rev. A*, vol. **5**, pp. 1043–1047, 1972.

[238] E. J. McGuire, "Atomic L-Shell Coster-Kronig, Auger, and Radiative Rates and Flourescence Yields for Na-Th," *Phys. Rev. A*, vol. **3**, pp. 587–594, 1971.

[239] V. R. Galakhov *et al.* manuscript in preperation, 2005.

[240] D. Niebieskikwiat, F. Prado, A. Caneira, and R. D. Sánchez, "Antisite defects versus grain boundary competition in the tunneling magnetoresistance of the Sr_2FeMoO_6 double perovskite," *Phys. Rev. B*, vol. **70**, p. 132412, 2004.

[241] J.-H. Park, E. Vescovo, H.-J. Kim, C. Kwon, R. Ramesh, and T. Venkatesan, "Magnetic Properties at Surface Boundary of a Half-Metallic Ferromagnet $La_{0.7}Sr_{0.3}MnO_3$," *Phys. Rev. Lett.*, vol. **81**, p. 132412, 1998.

[242] M. Sikora, D. Zajac, C. Kapusta, M. Borowiec, C. J. Oates, V. Prochazka, D. Rybicki, J. M. D. Teresa, C. Marquina, and M. R. Ibarra, "Direct evidence of the orbital contribution to the magnetic moment in $AAFeReO_6$ double perovskites," *Arxiv:*, vol. cond-mat-0503358, 2005.

[243] K. Kuepper, M. Raekers, K. C. Prince, F. Bondino, M. Zangrando, M. Zacchigna, F. Parmigiani, A. F. Takács, C. Piamonteze, A. T. Young, S. George, S. Robin, H. Hesse, and M. Neumann, "Investigation of Sr_2FeMoO_6 by means of MCD in XAS and RXES at the Fe L edge," *manuscript in preparation*, 2005.

[244] K. Mizushima, P. C. Jones, P. J. Wiseman, and J. B. Goodenough, "Li_xCoO_2 ($0 < x \leq 1$): A new cathode material for batteries of high energy density," *Mater. Res. Bull.*, vol. **15**, pp. 783–789, 1980.

[245] J. van Elp, J. L. Wieland, H. Eskes, P. Kuiper, G. A. Sawatzky, F. M. F. de Groot, and T. S. Turner, "Electronic structure of CoO, Li-doped CoO, and $LiCoO_2$," *Phys. Rev. B*, vol. **44**, pp. 6090–6103, 1991.

[246] J. Molenda, A. Stoklosa, and T. Bak, "Modification in the Electronic-Structure of Cobalt Bronze Li_xCoO_2 and the resulting Electrochemical Properties," *Solid State Ionics*, vol. **36**, pp. 53–58, 1989.

[247] K. Kushida and K. Kuriyama, "Mott-type hopping conduction in the ordered and disordered phases of $LiCoO_2$," *Solid State Commun.*, vol. **129**, pp. 525–528, 2004.

[248] J. N. Reimers and J. R. Dahn, "Electrochemical and in situ X-ray-Diffraction studies of Lithium intercalation in Li_xCoO_2," *Journ. Electrochem. Soc.*, vol. **139**, pp. 2091–2097, 1992.

[249] L. A. Montoro, M. Abbate, and J. M. Rosolen, "Changes in the electronic structure of chemically deintercalated $LiCoO_2$," *Electrochemical and Solid State Letters*, vol. **3**, pp. 410–412, 2000.

[250] T. Matsushita, M. Mizumaki, N. Ikeda, M. Nakazawa, A. Agui, Y. Saitoh, T. Nakatani, A. Yoshigoe, and S. Nakamura, "X-ray absorption spectroscopy in $NaCo_2O_4$, $LaCoO_3$ and $SrCoO_3$," *Surf. Rev. Lett.*, vol. **9**, pp. 1327–1331, 2002.

[251] W.-S. Yoon, K.-B. Kim, M.-G. Kim, M.-K. Lee, H.-J. Shin, and J.-M. Lee, "Oxygen contribution on Li-ion intercalation-deinterealation in $LiCoO_2$ investigated by O K-edge and Co L-edge X-ray absorption spectroscopy," *J. Phys. Chem. B*, vol. **106**, pp. 2526–2532, 2002.

[252] V. R. Galakhov, E. Z. Kurmaev, S. Uhlenbrock, M. Neumann, D. G. Kellerman, and V. S. Goshkov, "Degree of covalency of $LiCoO_2$: X-ray emission and photoelectron study," *Solid State Commun.*, vol. **99**, pp. 221–224, 1996.

[253] V. R. Galakhov, V. V. Karelina, D. G. Kellerman, V. S. Gorshkov, N. A. Ovechkina, and M. Neumann. Fizika Tverdogo Tela, 2002.

[254] V. R. Galakhov, N. A. Ovechkina, A. S. Shkvarin, S. N. Shamin, E. Z. Kurmaev, K. Kuepper, A. F. Takács, M. Raekers, S. Robin, M. Neumann, G.-N. Gavrilă, A. S. Semenova, D. G. Kellerman, T. Käämbre, and J. Nordgren, "Electronic structure and x-ray spectra of defect Li_xCoO_2," *submitted to Phys. Rev. B*, 2005.

[255] D. J. Singh, "Electronic structure of $NaCo_2O_4$," *Phys. Rev. B*, vol. **61**, pp. 13397–13402, 2000.

[256] M. Abbate, J. C. Fuggle, A. Fujimori, L. H. Tjeng, C. T. Chen, R. Potze, G. A. Sawatzky, H. Eisaki, and S. Uchida, "Electronic structure and spin-state transition of $LaCoO_3$," *Phys. Rev. B*, vol. **47**, pp. 16124–16130, 1993.

[257] K. Kushida and K. Kuriyama, "Narrowing of the Co-3*d* band related to the order-disorder phase transition in LiCoO2," *Solid State Commun.*, vol. **123**, pp. 349–352, 2002.

[258] J. J. Yeh and I. Lindau, "Atomic subshell photoionization cross sections and asymmetry parameters: $1 \leq Z \leq 103$," *At. Data Nucl. Data Tables*, vol. **32**, pp. 1–155, 1985.

[259] M. T. Czyżyk, R. Potze, and G. A. Sawatzky, "Band-theory description of high-energy spectroscopy and the electronic structure of $LiCoO_2$," *Phys. Rev. B*, vol. **46**, pp. 3729–3735, 1992.

[260] J. M. D. Teresa, M. R. Ibarra, P. A. Algarabel, C. Ritter, C. Marquina, J. Blasco, J. Garcia, A. D. Moral, and Z. Arnold, "Evidence for magnetic polarons in the magnetoresistive perovskites," *Nature*, vol. **386**, pp. 256–259, 1997.

Curriculum Vitae

I was born in Lengerich (Westf.), on March 5, 1975. At the end of my studies (1994 − 2001) at the Department of Physics, Universität Osnabrück, I obtained the Diplom in Physics. Since January 2002 I have worked as PhD student in the group Photoelectron Spectroscopy advised by apl. Prof. Dr. Manfred Neumann.

List of publications

Publications in refereed journals

- K. Kuepper, B. Schneider, V. Caciuc, M. Neumann, A. V. Postnikov, A. Ruediger, A. A. Grabar and Yu. M. Vysochanskii, *Electronic structure of $Sn_2P_2S_6$*, Phys. Rev. B **67**, (2003), 11501

- K. C. Prince, K. Kuepper, M. Neumann, D. Cocco, F. Bondino, M. Zangrando, M. Zacchigna, M. Matteucci and F. Parmigiani, *Resonant Raman x-ray scattering at the S 2p edge of iron pyrite*, J. Phys.: Condens. Matter **16**, (2004), 7397

- K. Kuepper, A. V. Postnikov, A. Moewes, B. Schneider, M. Matteucci, H. Hesse and M. Neumann, *The electronic structure of $KTaO_3$: a combined x-ray spectroscopic investigation*, J. Phys.: Condens. Matter **16**, (2004), 8213

- K. Kuepper, I. Balasz, H. Hesse, A. Winiarski, K. C. Prince, M. Matteucci, D. Wett, R. Szargan, E. Burzo, and M. Neumann, *Electronic and magnetic properties of highly ordered Sr_2FeMoO_6*, phys. stat. sol. (a) **201**, (2004), 3252

- K. C. Prince, M. Matteucci, K. Kuepper, S. G. Chiuzbăian, S. Bartkowski, and M. Neumann *A core level spectroscopic study of iron monoxide (FeO) and pyrite (FeS_2)*, Phys. Rev. B **71**, (2005), 085102

- K. C. Prince, F. Bondino, M. Zangrando, M. Zacchigna, F. Parmigiani, K. Kuepper and M. Neumann, *Dichroic O 1s photoabsorption and resonant x-ray scattering in haematite (Fe_2O_3)*, Journ. Electr. Spectr. Rel. Phenom., **144-147** (2005), 719

- K. Kuepper, M. C. Falub, K. C. Prince, V. R. Galakhov, I. O. Troyanchuk, S. G. Chiuzbaian, M. Matteucci, D. Wett, R. Szargan, N. A. Ovechkina, Ya. M. Mukovskii, and M. Neumann, *Electronic structure of A- and B- site doped Lanthanum manganites: A combined x-ray spectroscopic study*, J. Phys. Chem. B **109**, (2005), in production

- K. Kuepper, F. Bondino, K. C. Prince, M. Zangrando, M. Zacchigna, A. F. Takács, T. Crainic, M. Matteucci, F. Parmigiani, V. R. Galakhov, Ya. M. Mukovskii, A. Winiarski and M. Neumann, *Investigation of orbital ordering in* $La_{7/8}Sr_{1/8}MnO_3$ *by means of x-ray linear dichroism at the Mn L edge*, J. Phys. Chem. B , (2005), submitted

- V. R. Galakhov, N. A. Ovechkina, A. S. Shkvarin, S. N. Shamin, E. Z. Kurmaev, K. Kuepper, A. F. Takács, M. Raekers, S. Robin, M. Neumann, G.-N. Gavrilă, A. S. Semenova, D. G. Kellerman, T. Käämbre and J. Nordgren, *Electronic structure and x-ray spectra of defect* Li_xCoO_2, Phys. Rev. B , (2005), submitted

- K. Kuepper, M. Kadirog̈lu, A. V. Postnikov, K. C. Prince, M. Matteucci, V. R. Galakhov, H. Hesse, G. Borstel, and M. Neumann, *Electronic structure of highly ordered* Sr_2FeMoO_6*: XPS and XES*, J. Phys.: Condens. Matter , (2005), submitted

Non refereed publications (Annual Reports, etc.)

- K. Kuepper, K. C. Prince, M. Matteucci and M. Neumann, *Investigation of an A- and B- site doped Lanthanum Manganite by means of RIXS*, ALS compendium (2002)

- M. Neumann, K. Kuepper, V.R. Galakhov, and M.C. Falub, *Colossal magnetoresistance materials investigated by x-ray spectroscopic techniques*, Proceedings of the Fifth General Conference of the Balkan Physical Union, invited contribution (2003)

- K. Kuepper, V. R. Galakhov, A. F. Takács, M. Neumann, and Ya. M. Mukowskii, *Electronic structure of* $La_{1-x}Sr_xMnO_3$*: Resonant Inelastic X-ray Scattering (RIXS)*, BESSY Annual Report (2003)

- A. F. Takács, K. Kuepper, M. Neumann, T. Crainic, D. Wett, R. Szargan, R. W. Saalfrank and A. Scheurer, *Electronic structure of* $[Fe(FeL_2)]*4CHCl-3$ *where* $L=NO_2$*: Normal X-ray emission (XES)*, BESSY Annual Report (2003)

- K. Kuepper, F. Bondino, K. C. Prince, M. Zangrando, M. Zacchigna, A. F. Takács, T. Crainic, M. Matteucci, F. Parmigiani, V. R. Galakhov, Ya. M. Mukovskii, A. Winiarski and M. Neumann , *Investigation of orbital ordering in* $La_{7/8}Sr_{1/8}MnO_3$ *by means of x-ray linear dichroism at the Mn L edge*, ELETTRA Science Highlights (2004)

Eidesstattliche Erklärung

Hiermit erkläre ich an Eides Statt, die vorliegende Abhandlung selbständig und ohne unerlaubte Hilfe verfasst, die benutzten Hilfsmittel vollständig angegeben und noch keinen Promotionsversuch unternommen zu haben.

Osnabrück, 06.06.2005
Karsten Küpper